The University Of Sheffield.

Department Of Mechanical Engineering

Effects of Compression applied to Gas Diffusion Layers in PEM Fuel Cells

By:

Fahad A J M A Aldakheel

A thesis submitted in partial fulfilment of the requirements for the degree of Doctor of Philosophy

The University of Sheffield

Faculty of Engineering

Department of Mechanical Engineering

Energy 2050

July 2021

ABSTRACT

There is a global and urgent need to embrace alternative renewable power sources to mitigate the detrimental environmental effects of the greenhouse gases, in particular carbon dioxide. Proton electrolyte membrane (PEM) fuel cells have been an attractive clean technology to decarbonise a multitude of applications, particularly those in the automotive sector. Although PEM fuel cells have, compared to other types of fuel cells, high efficiency and low-operating temperature, there are still some very important challenges that need to be overcome so that the PEM has a wider application. One of the main issues that affect the lifetime of PEM fuel cells is the mechanical degradation of the gas diffusion layers (GDLs). Since GDLs are responsible for the transport of reacting gases, heat and electronic charge from/to the catalyst layers, any damage to their structure may have detrimental consequences on the above transport processes and, subsequently, the performance of the fuel cell. Typically, GDLs are subject to two types of compressive stresses: assembling and cyclic stresses. The assembling stress occurs due to the clamping pressure applied to assemble the various components of the fuel cell. The cyclic stress is due to the hydration/dehydration cycles of the membrane as it swells or shrinks. In this thesis, a novel and carefully designed compression test (mimicking the assembling and cyclic stresses that the GDL is subjected to within the fuel cell) has been performed on a set of commercially available GDLs. This was followed by a series of tests to examine the effects of compression on the mass transport (gas permeability test), morphology (SEM

analysis), thermal stability (TGA analysis), and wettability (contact angle test) of the tested GDLs. Such tests and the related outcomes are of much importance to the researchers in the field, especially those who model PEM fuel cells as these tests provide much more accurate and realistic data for the physical properties being investigated. The same investigation was then performed in the presence of sealing gaskets in order to explore how the effects of compression are mitigated with the sealing gaskets. Finally, the experimental values for the GDL gas permeability and contact angle (before and after compression) were fed into a comprehensive three-dimensional PEM fuel cell model to investigate their effects on the overall performance of the cell. The key findings of the study are as follows: (i) the MPL-coated GDLs are more resistive to mechanical deformation than uncoated GDLs, (ii) the contact angle of the GDLs reduce by 3° - 15° after compression, (iii) GDLs are less deformed in presence of sealing gaskets, (iv) GDLs lose around 40% of its PTEF content after compression and (v) the performance of the modelled fuel cell is hardly affected by variation in GDL gas permeability.

ACKNOWLEDGEMENTS

First and foremost, my deep gratitude goes to my God Allah for providing me all the blessings and strength for my entire life, and through my PhD journey. Also, I would like to thank the Kuwait Institute for Scientific Research (KISR) for their financial support by funding my PhD study at the University of Sheffield, specifically in the Energy 2050 group.

Secondly, a special thanks and a sincere gratitude goes to my supportive supervisors; Professor Mohamed Pourkashanian, Professor Derek B. Ingham, Dr. Kevin J Hughes, Professor Lin Ma, and Dr. Mohammed Ismail. I wouldn't make it without your guidance and positive feedbacks in our weekly meetings. Our group discussions made this PhD journey more thoughtful and fuller of ideas and constructive encouragement. A special thanks to my mentor in the fuel cells group Dr. Mohammed Ismail, without your advices, support, and all the comments, I won't be able to achieve all these accomplishments.

Moreover, I would like to appreciate the opportunity that my supervisors gave me to join the collaboration research conducted between the university of Sheffield- (Energy 2050), and Kyushu University- (ICNER^2). Thank you, Dr. Stephen Lyth, for giving me the opportunity to work in your laboratory at Kyushu University in Japan. Also, I would like to thank Dr. Albert Mufundirwa for his guidance and support and the time he spent to teach me new experimental techniques. Thank you all for giving me good advices and suggestions during my visit.

Finally, I would like to thank my family for their support through all the past difficult years, and their continuous encouragement. A special acknowledgement to my

lovely parents: Ahamd J. Aldakheel and Seham. A. Almassad for their great support and prayers, May god bless you. I would like to dedicate this thesis to my brother Abdullah A. Aldakheel, may you rest in peace!

PUBLICATIONS, CONFERENCES AND WORKSHOPS

A) Publications

The work in **Chapter 5** of the thesis has appeared in the publication as follows:

1) **F. Aldakheel**, M.S. Ismail, K.J. Hughes, D.B. Ingham, L. Ma, M. Pourkashanian, D. Cumming, R. Smith,*"Gas permeability, wettability and morphology of gas diffusion layers before and after performing a realistic ex-situ compression test",* Renewable Energy, Volume 151, 2020, Pages 1082-1091.

The work in **Chapter 6** of the thesis has appeared in the publication as follows:

2) **F. Aldakheel,** M.S. Ismail, K.J. Hughes, D.B. Ingham, L. Ma, M. Pourkashanian, *"Effects of compression on mechanical integrity, gas permeability and thermal stability of gas diffusion layers with/without sealing gaskets"*, International Journal of Hydrogen Energy, Volume 46, Issue 44, 2021, Pages 22907-22919

B) Poster Presentations

1) **F. Aldakheel**, M.S. Ismail, D.B. Ingham, L. Ma, K.J. Hughes and M. Pourkashanian. *"Gas permeability, wettability and morphology of gas diffusion layers before and after performing a realistic ex-situ compression test."* At the Mechanical Engineering Poster event. 27/June/2019

C) Workshops and Presentations

1) Attended and presented at three workshops as part of the " Sheffield-Kyushu Workshop Joint on Electrochemical Energy Conversion (SKWEEC), Sheffield, UK"
2) An exchange PhD student at Kyushu University for the fourth workshop between University of Sheffield and Kyushu University (SKWEEC), Japan, July-August, 2019

CONTENTS

LIST OF FIGURES

LIST OF TABLES

NOMENCLATURE

Roman symbols	Definition	Units
a	Specific area	m^{-1}
ac	Water activity	–
D	Diffusion coefficient	–
D_{eff}	Effective diffusion coefficient	–
E_c	Compression Young's modulus	Pa
K	Permeability	m^2
L	Thickness of porous medium	m
M	Molecular weight	kg/mol
$\dot{m}$	Mass flow rate	kg/s
m'	Mass flux	$kg/m^2/s$
P	Pressure	Pa
P_{in}	Inlet pressure	Pa
P_{out}	Outlet pressure	Pa
$\bar{R}$	Universal gas constant	$J.K.mol^{-1}$
T	Temperature	K

t	Time	s
u	Velocity	m/s

Greek symbols	Definition	Units
β	Inertial coefficient	m^{-1}
ε	Porosity	–
ρ	Density	Kg/m^3
μ	Dynamic viscosity	Pa.s

Abbreviations	Definition
AFC	Alkaline fuel cell
CL	Catalyst layer
FEP	Fluorinated-ethylene-propylene
FFP	Flow field plate
GDE	Gas diffusion electrode

GDL	Gas diffusion layer
MCFC	Molten carbonate fuel cell
MEA	Membrane electrode assembly
MIP	Mercury intrusion porosimetry
MPL	Micro porous layer
PAFC	Phosphoric acid fuel cell
PAN	Polyacrylonitrile
PEMFC	Proton electrolyte membrane fuel cell
PTFE	Polytetrafluoroethylene
SEM	Scanning electron microscope
SOFC	Solid oxide fuel cell

Chemical symbols	Definition
CH_4	Methane
CO	Carbon monoxide
CO_2	Carbon dioxide
CO_3^{2-}	Carbonate ion

Cr	Chromium
H_2	Hydrogen molecule
H_2O	Water molecule
H_3PO_3	Phosphoric acid
Ni	Nickel
O_2	Oxygen molecule
Pt	Platinum

1 INTRODUCTION

1.1 Background and motivation

Fossil fuels and green energy

Energy production and finding different types and sources are considered to be one of the most important topics worldwide. No one can dispense the usage of energy in all aspects of our daily lives. Generally, energy is one of the key factors that without it, no work can be done, i.e. all means of transportation cannot work without energy, no lighting, no heating and ventilation systems, no factories and industry etc. Diverse energy sources are an essential factor in the development and prosperity of any nation. Thus, energy sources are different, depending on the type of source that it comes from [1], [2].

The classification of energy sources is associated to the type of its source, mainly it can be divided into three main categories: fossil fuels, nuclear energy, and alternative energy. Each type of these three energy sources has its advantages and disadvantages in terms of the abundancy, efficiency and environmental impact. For instance, nuclear energy is low in carbon dioxide and other forms of emissions, however radiation issues can arise and environmental issues [3]. The same concept with burning fossil fuels such as oil, natural gas, and coal which has a dramatic impact on the environment and greenhouse emissions. Moreover, the depletion of fossil fuels as an energy source is a worldwide issue. As a result, an alternative energy is emerging that

dramatically minimises the dependency on traditional energy sources, as well as to eliminate the environmental impacts associated to it.

Alternative energy has been the trend and focus of most countries worldwide, many policies and legislations have been introduced to mitigate the environmental impact of the traditional sources of energy, as well as finding efficient and sustainable energy sources. For instance, much work has been done to exploit and develop some of the natural sources such as wind, solar, biofuels and hydrogen gas in order to convert them to efficient and sustainable energy [4].

The future of energy is obscure as the global economy expands, more energy will be required to provide the higher levels of activity and living standards. International Energy Outlook [5] projects that world energy consumption will grow by about 28% between 2015 and 2040. The dominant source of energy production is still fossil fuels; however, they are finite resources. Over-consumption of these resources will naturally cause their depletion and have catastrophic effect on the environment. The combustion of hydrocarbon fuels for transportation and heating contributes over half of all greenhouse gas emissions and a large fraction of air pollutant emissions. Alternative sources must be considered in this case where there is an international trend to use renewable energy, such as solar energy, wind, rain, tides, waves, and hydrogen, which is one the most promising technology.

Hydrogen as a Clean Source of Energy

Hydrogen has several criteria that makes it the perfect candidate to generate our future energy. Its inexhaustibility, low density, cleanliness and it is suitable for both transportation and stationary applications. The dilemma of the hydrogen economy that the cost of producing hydrogen as an alternative fuel has been higher than the cost of the energy used to make it. However, now it can be easily manufactured by splitting water molecules into hydrogen and oxygen using renewable sources of energy. Another potential factor that hydrogen outperforms the conventional energy sources by having zero emissions and therefore is environmentally friendly when used.

Climate change and pollution is considered as one of the major and most vital problems worldwide. Our planet is exposed to many environmental issues on a daily basis, and some of these issues occur naturally, such as volcanoes and flooding. However, the major contribution of these environmental issues is made by human activities, such as burning fossil fuels like coal and oil. Therefore, rates of atmospheric CO_2 emissions have increased dramatically over the decades [6]–[8]. A statistical study, conducted by the International Energy Agency (IEA) [9], showed the global emissions trends from 1990-2019. Figure 1.1 shows the CO_2 in gigatonnes (Gt) emissions for both advanced economies and the rest of the world over the last 30 years. Higher rates of greenhouse gases, such as CO_2, play a crucial role in the environmental system. Consequently, by 2050, according to estimates, the average global temperature will dramatically increase by 2-3 °C [10].

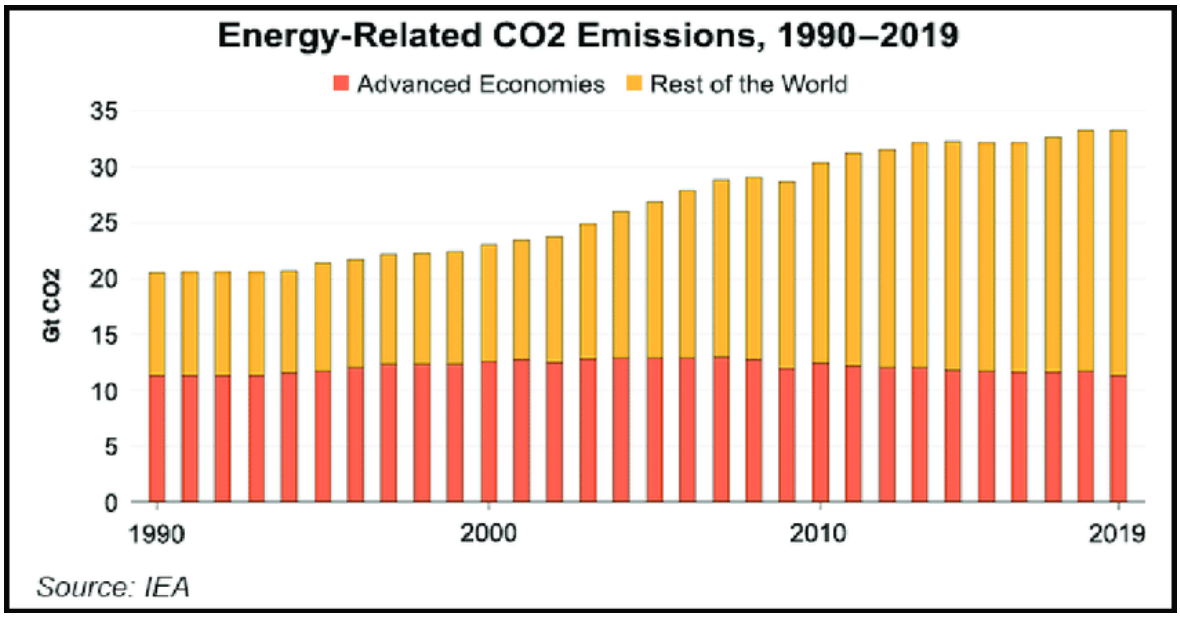

Figure 1.1 The CO_2 emissions in [Gt CO_2/yr] for advanced economies, and the rest of the world from 1990-2019 [9].

The huge impact of the damage to our environment is mainly attributed to the dependency of fossil fuels as the main source of energy. Recently, much effort in research has been conducted to resolve many environmental problems. One of the main solutions is to find alternatives to fossil fuels to support the high demand of energy, as well as to decrease the environmental impacts of the burning of fossil fuels. All the new policies worldwide are heading towards sustainable and renewable energy, such as solar, wind, tidal and fuel cells. Researchers and developers worldwide are focusing on alternative energies and working towards making such alternative energies more efficient, sustainable, with less cost and being more environmentally friendly.

A very promising solution is the proton electrolyte membrane fuel cells (PEMFCs or PEM fuel cells), in which they have zero emissions and use

hydrogen as the main fuel. In other words, implementing the usage of fuel cells will support the reduction in many issues related to climate change and global warming. Moreover, using hydrogen as the main fuel will reduce the dependency on fossil fuels as the main source of energy, while, in turn producing a valuable alternative source of energy. The PEM fuel cell is a perfect emerging power source for many applications. Due to its extraordinary properties, such as low temperature operation, fast start-up time, noiseless and having a zero emission operation, makes it suitable for stationary applications i.e. power generators, and portable applications related to transportation engines [11], [12]. Therefore, in order to mitigate the serious problems related to fossil fuels, alternative solutions to energy have to be found.

1.2 Fuel cells overview

The aim of this chapter is to outline the recent developments in Proton Electrolyte Membrane Fuel Cells (PEMFC). Also, to emphasize the significance of the proposed study in the Fuel Cells field. This literature survey begins with an overview of the fuel cell technology and how it starts, as well as the different types of fuel cells and their advantages and disadvantages. Then, an overview of PEM fuel cells' main components is briefly outlined. Finally, the emphasis of this literature survey will be on the Gas Diffusion Layers' properties, materials, and characterization techniques.

1.3 Fuel cell technology

1.3.1 Brief history

A fuel cell is an electrochemical device that converts a chemical reaction to energy (electricity). In general, an electrical current can be produced through an oxidation-reduction reaction between a fuel and oxygen (or different oxidising agent), respectively. The term and the concept of "Fuel Cell" was first discovered by Sir William Robert Grove, an English scientist, who presented the idea of the electrochemical reaction between hydrogen and oxygen [13]. The first experiment involved two platinum electrodes immersed in electrolyte media (dilute sulfuric acid) but then, much research has been performed in developing and improving this concept. Moreover, many developments in this field have been proposed and conducted in the last two decades.

1.3.2 Main components in fuel cells

In general, a fuel cell consists of three main parts namely anode, cathode, and electrolyte. Each component has a specific function in the process of producing energy from of the fuel cell and Figure 1.2 shows the main components of the fuel cell.

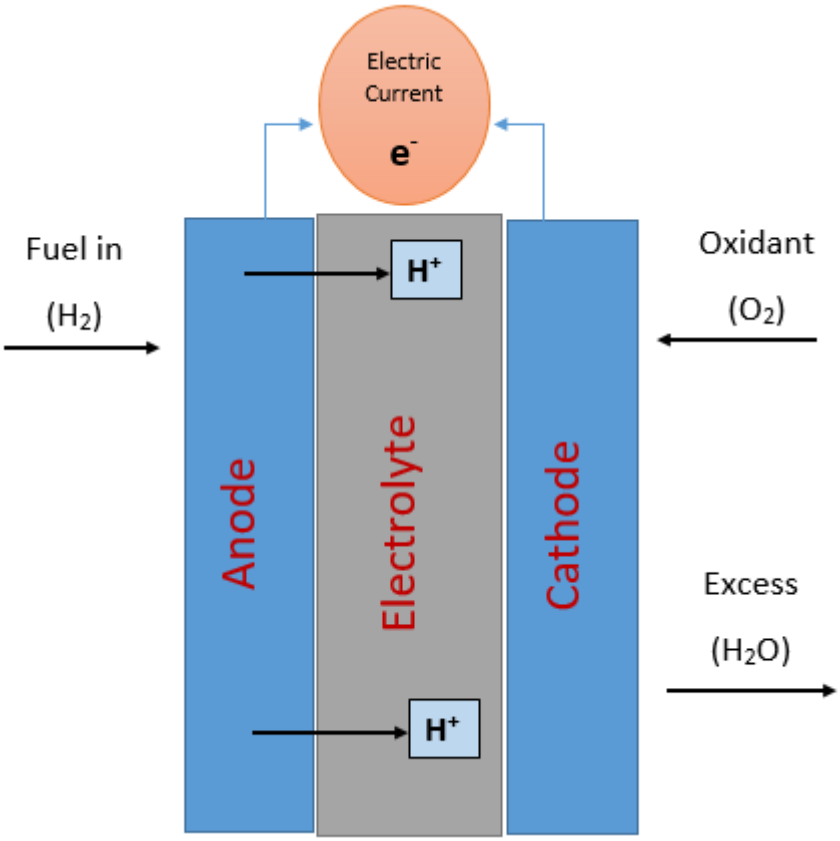

Figure 1.2 Schematic of the different components in a hydrogen fuel cell.

1.3.3 Functionality of a fuel cell

As shown in Figure 1.2, the three main components of a fuel cell together is called a membrane electrode assembly (MEA). Basically, the process starts with a fuel (hydrogen atoms, H_2) entering at the anode side, and an oxidant (oxygen atoms, O_2) entering at the cathode side. Typically, the hydrogen atoms become separated, and the electrons move to an electrical circuit producing an electrical current (energy), while the protons pass through the electrolyte to migrate to the oxygen atoms, thus producing water (H_2O). As opposed to the different power sources such as the conventional ones, for instance, internal combustion engines and batteries, fuel cells are considered to be

sustainable clean power source with zero emissions. In addition, they can produce energy continuously without interruptions as long as the reactants (fuel and oxidant) are provided [14].

1.3.4 Types of fuel cells

The classification of the different types of fuel cells depends on the type of electrolyte they employ. Based on that classification, each fuel cell type has its advantages, limitations, fuel required and a cell operating temperature. Primarily, there are five main types of fuel cells and these are classified according to their electrolyte and each type of these five fuel cells is explained briefly in the following subsections.

1.3.4.1 Solid oxide fuel cell (SOFC)

A solid oxide fuel cell employs a solid ceramic polymer as an electrolyte to operate in a high temperature range (600-1000 °C). Typically, the type of fuel used for SOFC is methane (CH_4,) or carbon monoxide (CO), or hydrogen (H_2) and therefore, the mobile ion produced through the process is O^{-2}. The electrodes used in the SOFC should be highly conductive to air such as perovskite oxides and the efficiency of a SOFC is about 45-60% [15] . As a result, it can be used in a combined heat and power systems from 2 kW to multi MW [14]. A schematic of the SOFC components and the way it is utilised is presented in Figure 1.3.

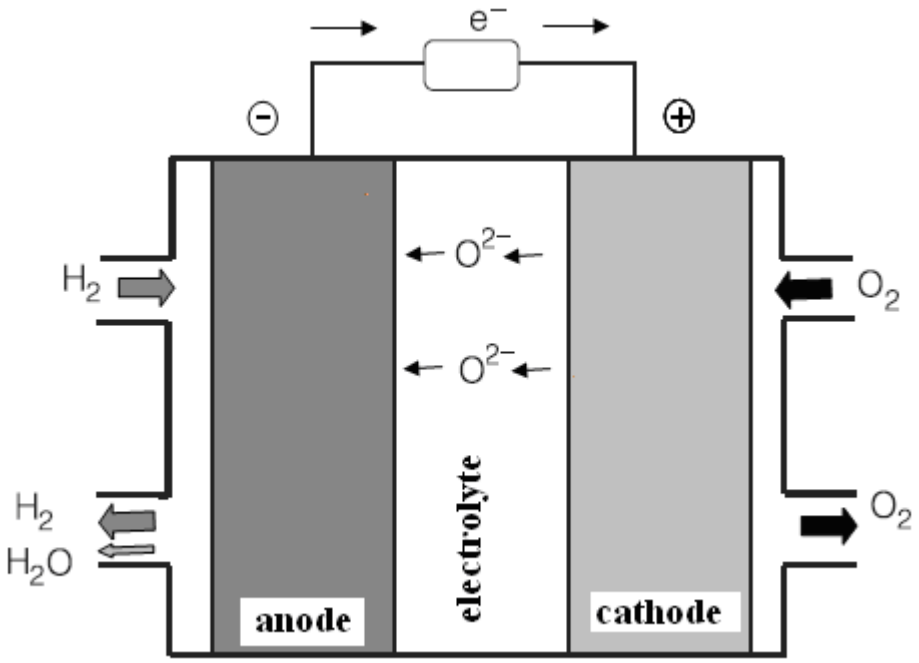

Figure 1.3 A schematic of the different components of a SOFC [16].

The anode and cathode reactions for SOFCs are given as follows [16]:

At the anode:

$$H_2 + O^{2-} \longrightarrow H_2O + 2e^- \qquad (1.1)$$

At the cathode:

$$\frac{1}{2}O_2 + 2e^- \longrightarrow O^{2-} \qquad (1.2)$$

1.3.4.2 Alkaline fuel cell

The alkaline fuel cell (AFC) is a low operating temperature fuel cell with a temperature in the range of 65-220 °C, and it employs a platinum as a catalyst to enhance the reaction. AFCs use transition metals for its electrodes, such as

nickel, and recently carbon-based electrodes have been used. The electrodes are separated by an aqueous alkaline solution, such as sodium hydroxide and potassium hydroxide solutions. The efficiency of this type of fuel cell is 50-70% and it is used mainly in vehicles, spacecraft and mobile applications [14]. Figure 1.4 depicts the different components in an AFC and how it functions.

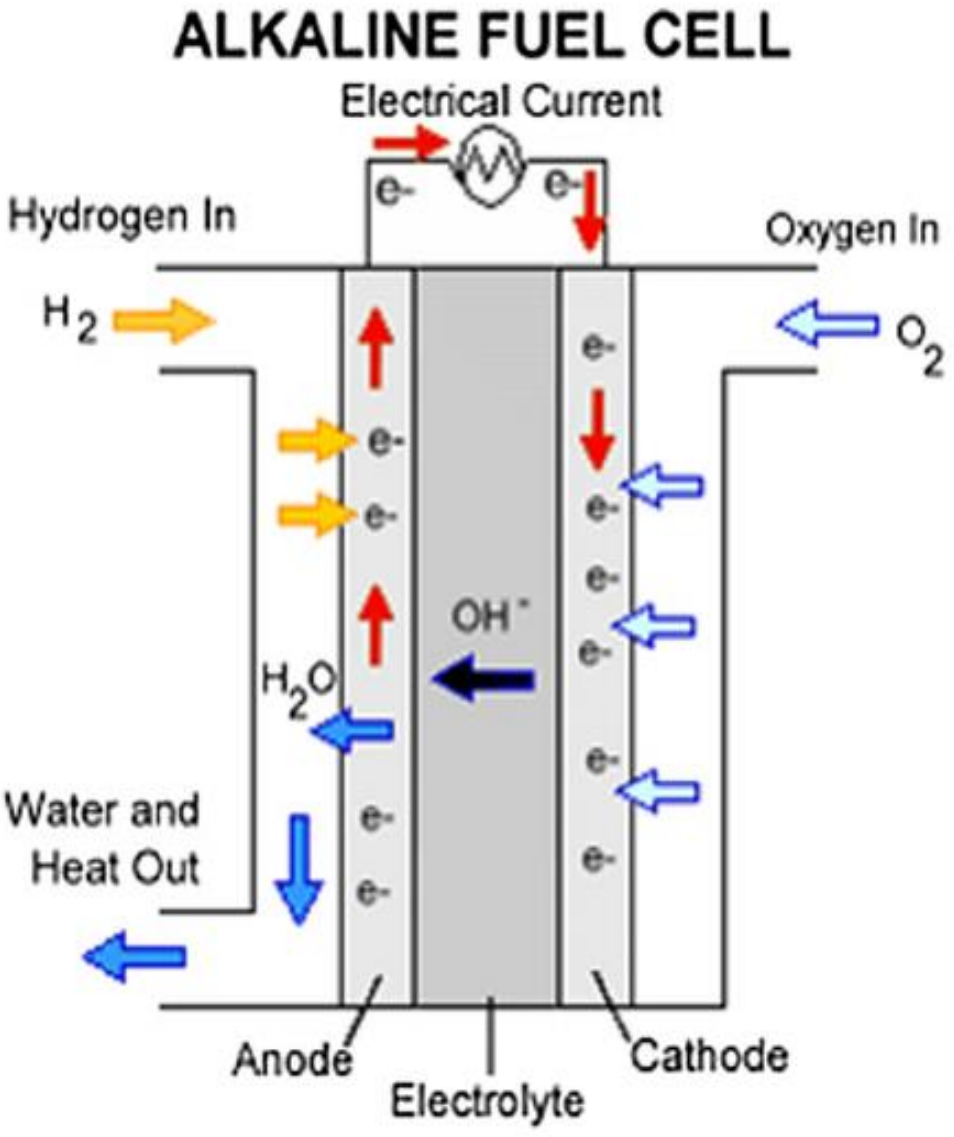

Figure 1.4 Schematic of the different components in AFCs and the way the AFC is utilised [17].

The anode and cathode reactions for AFCs are given as follows [17] :

At the anode:

$$H_2 + 2OH \longrightarrow 2H_2O + 2e^- \quad (1.3)$$

At the cathode:

$$\frac{1}{2}O_2 + H_2O + 2e^- \longrightarrow 2OH^- \quad (1.4)$$

1.3.4.3 Phosphoric acid fuel cell

The phosphoric acid fuel cell (PAFC) employs a proton conducting membrane such as phosphoric acid (H_3PO_4) and platinum (Pt) supported on carbon as the catalysts. It is considered as a low operating temperature fuel cell operating in a temperature range of 180-250 °C. Typically, the fuel used in this type of fuel cell is hydrogen (H_2) and the mobile ion is H^+. The PAFCs efficiency ranges between 35-50%, which is considered to be a low efficiency compared to other types of fuel cells. Therefore, applications using PAFCs are combined heat and power systems in a range of 2000KW [14]. Figure 1.5 shows a schematic of the PAFC and its main components.

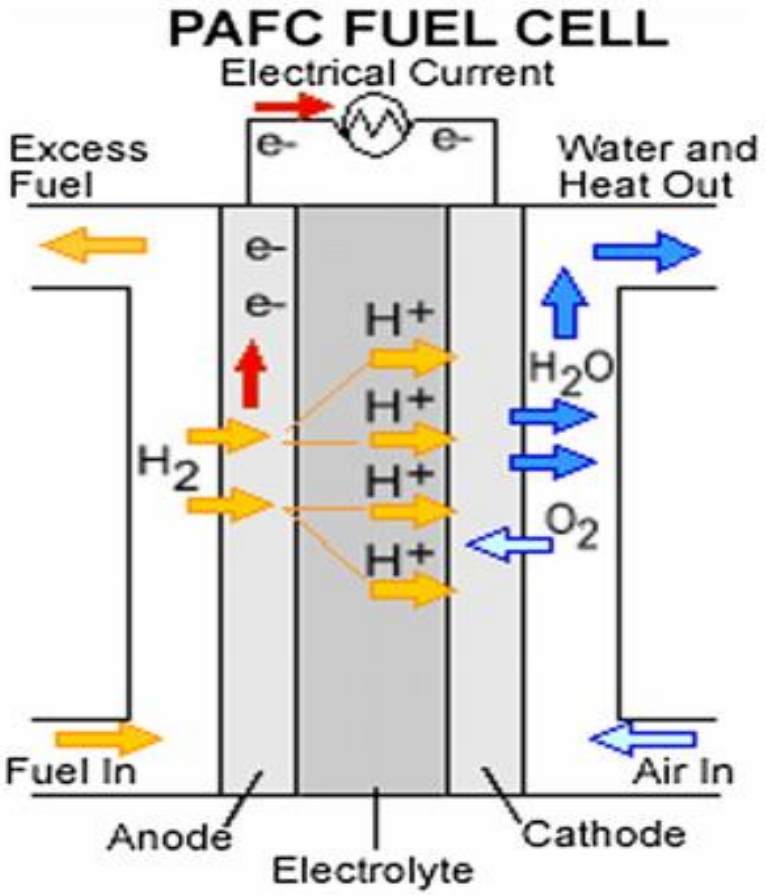

Figure 1.5 Schematic of the different components of a PAFC and the way it functions [17].

The anode and cathode reactions for PAFCs are given as follows [17]:

At the anode:

$$H_2 \longrightarrow 2H^+ + 2e^- \qquad (1.5)$$

At the cathode:

$$\frac{1}{2}O_2 + 2H^+ + 2e^- \longrightarrow 2H_2O \qquad (1.6)$$

1.3.4.4 Molten carbonate fuel cell

The Molten Carbonate Fuel Cell (MCFC) usually employs a carbonate mixture of lithium and potassium or sodium carbonates. The anode is made from a Ni-Cr/Ni-Al alloy with a pore size 3-6 μm, while the cathode is made from NiO with a pore size 7-15 μm. The main fuel for this type of fuel cell is methane (CH_4) or carbon monoxide (CO) with hydrogen (H2) and therefore the mobile ion due to the reaction is CO_3^{2-}.This type of fuel cell operates in the high temperature range between 600-700 °C. Typically, the efficiency of MCFCs is in the range 40-50%, and the main applications that these fuel cells can be used in are medium to large scale combined heat and power systems [14]. Figure 1.6 shows a schematic of the MOFC and the way it operates.

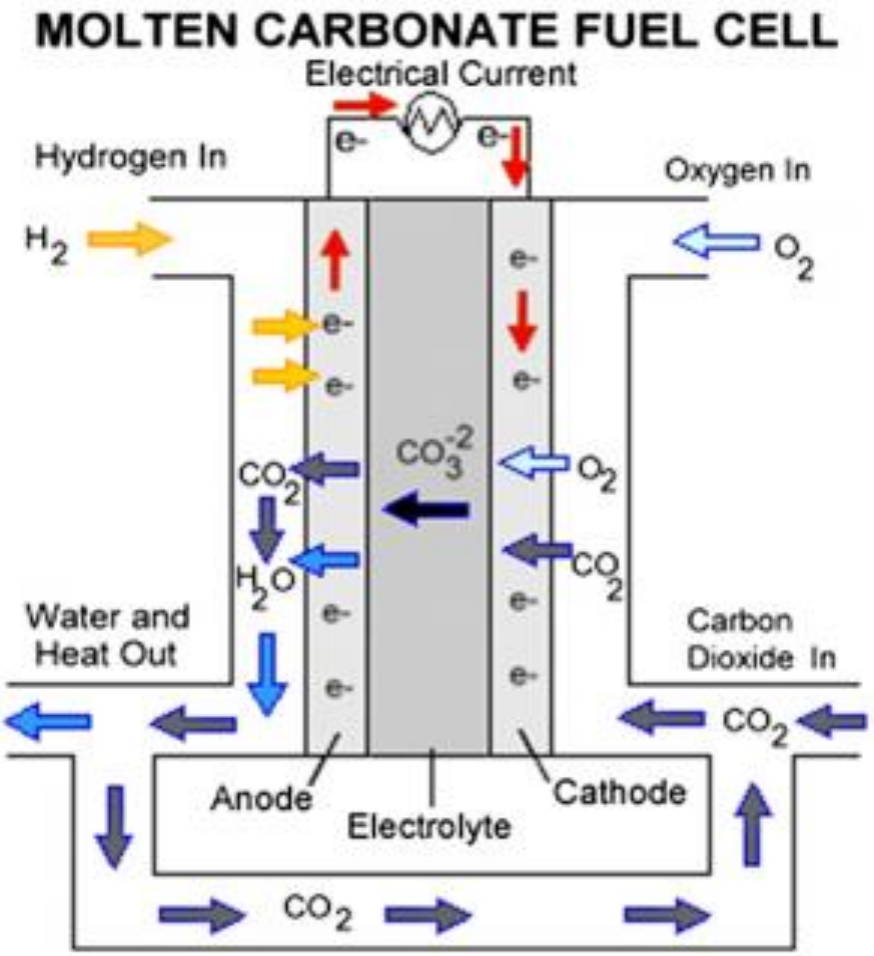

Figure 1.6 Schematic of the main components of a MCFC and the way it operates [17].

The anode and cathode reactions for MCFCs are given as follows [17]:

At the anode:

$$H_2 + CO_3^{3-} \longrightarrow 2H_2O + CO_2 + 2e^- \qquad (1.7)$$

At the cathode:

$$\frac{1}{2}O_2 + CO_2 + 2e^- \longrightarrow CO_3^{2-} \qquad (1.8)$$

1.4 Gap in knowledge and overall objective

Mechanical degradation of the gas diffusion layer or GDL (which is a key component in PEM fuel cells as will be shown in Chapter 3) is one of the key issues that could significantly affect the overall performance of a PEM fuel cell. GDL is responsible for the transport of reacting gases, charge, heat and liquid water. It also acts as a mechanical support for the delicate catalyst layers. Any mechanical damage to the GDL due to for example excessive compression could badly impact some or all the above functions and as such the overall performance of the fuel cell. The GDL is normally subjected to two types of compression: (i) assembling compression that is applied to the fuel cell to seal it and minimise the contact resistance between the various components of the fuel cells and (ii) cyclic compression which is due to swelling/shrinkage of the membrane electrolyte as it hydrates/dehydrates.

Surveying the open literature, there have been no studies that account for both assembling and cyclic compressions when investigating the impact of compression on the physical properties of the GDL and/or the overall performance of PEM fuel cells; the focus of the relevant studies is either on the impact of assembling (or clamping) compression or the above-described cyclic compression. The present work, for the first time, investigates the impact of both assembling and cyclic compressions on the mass transport, morphology, thermal stability and wettability of some commercially-available GDLs in the absence or presence of sealing gaskets. To achieve the above goal, a carefully designed compression test mimicking the assembling and cyclic compressions is performed. The data obtained out of the relevant tests (i.e.

gas permeability, contact angle SEM analysis and TGA analysis) are accurate and realistic and they are therefore of significant importance to the researchers in the field, particularly the PEMFC modellers and designers. Feeding the fuel cell model with more accurate data for the physical properties of the GDL will undoubtedly enhance the prediction of the model.

1.5 Scope of the thesis

The thesis is divided into 8 chapters. Chapter 1 is an introduction on the importance of renewable energy and the need for a variety of different energy resources. The gas in knowledge and the overall objective are stated in this chapter. Chapter 2 briefly introduces the various types of fuel cells, with a particular emphasis on the PEM fuel cell and its main components. This leads to Chapter 3 which focuses on the gas diffusion layers and their key physical properties. Also, it contains an overview of the mechanical degradation and the two main mechanisms of compression (i.e. assembling and cyclic). The chapter ends with listing the main sealing gaskets used in the PEM fuel cell and their main properties. Chapter 4 describes all the experimental procedures and data analysis that have been adopted in the thesis to obtain: the mechanical behaviour, the gas permeability, the contact angle, the morphology and the thermal stability of the tested GDLs. Chapter 5 is the first "technical" chapter and it investigates the effect of the combined compression (i.e. assembling compression plus cyclic compression) on the mechanical integrity, gas permeability and the wettability of the tested GDLs. Chapter 6 is the second technical chapter that investigates the effects of combined compression in the

presence of commonly used sealing gaskets on all the above-mentioned properties of the GDLs (i.e. mechanical integrity, the gas permeability, the wettability and the thermal stability). Chapter 7 is the third technical chapter that theoretically investigates the impact of the gas permeability and the contact angle (before and after compression) on the overall PEM fuel cell performance employing a comprehensive three-dimensional model. Finally, Chapter 8 summarises the key findings of the experimental and modelling work presented in Chapters 5, 6 and 7 and lists some recommendations for future work.

2 LITERATURE REVIEW ON FUEL CELLS

2.1 Proton electrolyte membrane fuel cell (PEMFC)

The PEM fuel cell was first developed by General Electric in the 1960s, and this was first used by NASA in their space-craft. It employs an ion conductive membrane as an electrolyte in the middle with two layers of catalysts for the anode and cathode sides. This type of fuel cells operates at low temperatures in the range 40-200 °C and the main fuel for PEM fuel cells is hydrogen (H_2), and the mobile ion is H^+. The efficiency of PEM fuel cells is 30-60%, and it has no corrosive elements, therefore the cell can operate in any direction. Many applications can benefit from the advantages of the PEM fuel cells, such as portable applications like vehicles or stationary power generation applications [18]. Figure 2.1 shows the main components of a PEM fuel cell and the way it operates.

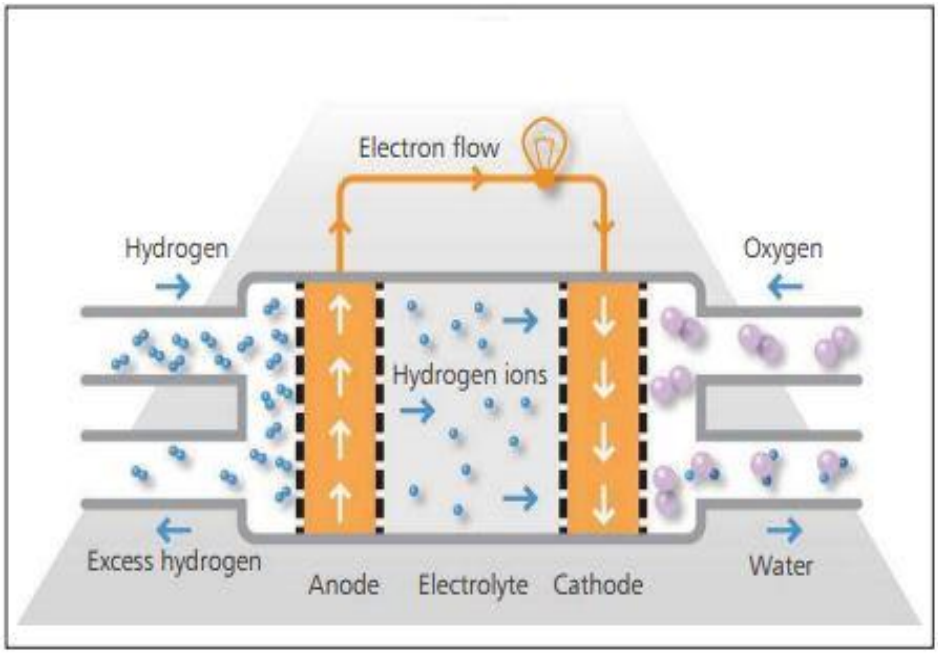

Figure 2.1 Schematic of the main components of a PEM fuel cell and the way it operates [19].

The anode and cathode reactions for PEMFCs are given as follows [19]:

At the anode:

$$H_2 \longrightarrow 2H^+ + 2e^- \quad (2.1)$$

At the cathode:

$$\frac{1}{2}O_2 + 2H^+ + 2e^- \longrightarrow H_2O \quad (2.2)$$

In the next sections, an overview of the main components of a PEM fuel cell are discussed in more detail.

2.1.1 Why PEM fuel cells?

PEM fuel cells have gained much attention due to their capability of being operated at lower temperatures. In addition, they have the ability to be operated for a wide range of applications, including portable or stationary uses and this is attributed to the solid polymer electrolyte used, as well as the absence of any corrosive fluids [20]. The main components of a PEM fuel cell are the polymer electrolyte, catalyst layers, gas diffusion electrodes (GDE), and flow field plates. Flow field plates are placed at both ends of a PEM fuel cell, and their main functionality is to supply the reactant gases and operate as flow channels. The gas diffusion electrodes (GDE) consist of a gas diffusion layer (GDL) and a catalyst layer at one side of it. Together the electrolyte and the

two porous electrodes are called a membrane electrode assembly (MEA). Therefore, the two flow field plates are placed at both ends with the MEA being placed in between, thus forming a single cell. Due to the high power requirements for some application, a series of cells are connected together to form a multi-cell stack of fuel cells [14], [17], [21]. Figure 2.2 shows the main components of the PEM fuel cell in detail and with the role of each component summarised.

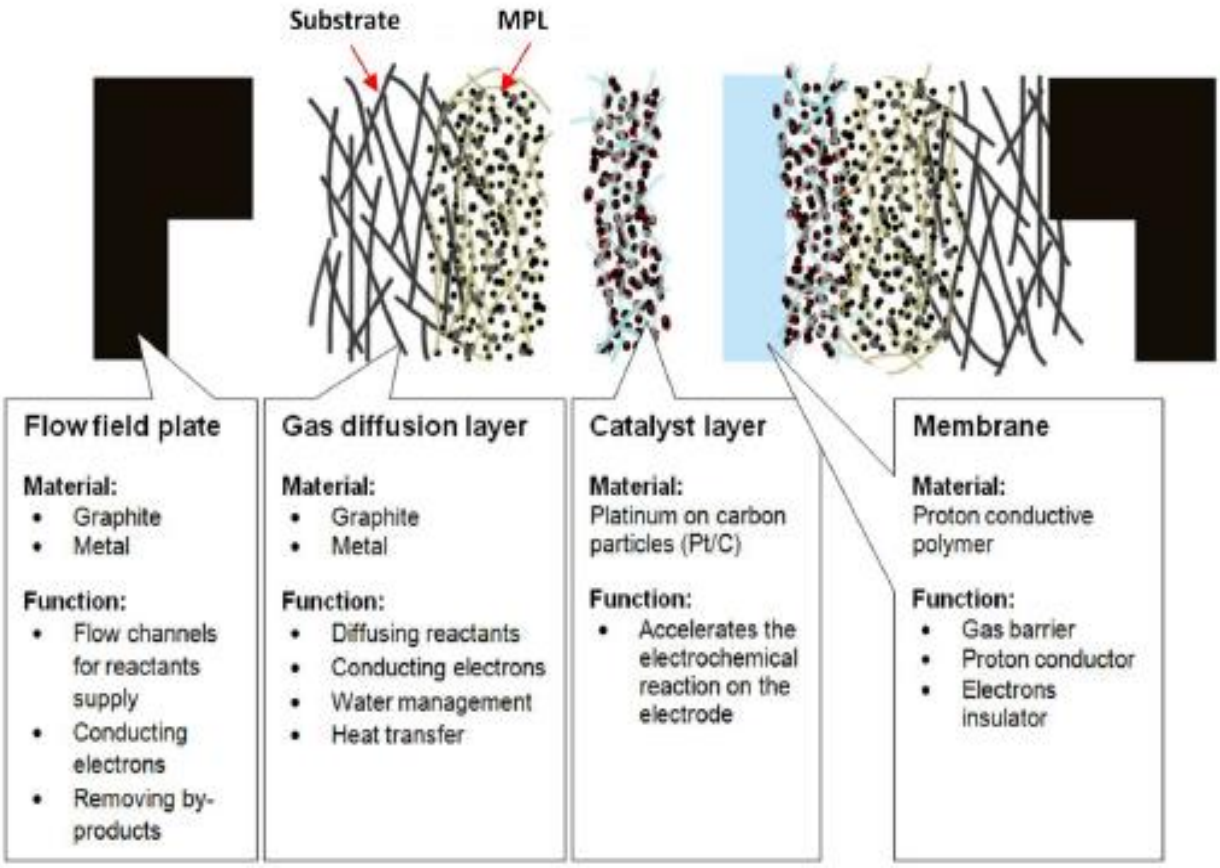

Figure 2.2 The main components of a single PEM fuel cell and with the role of each component [14].

In the next sections of this chapter, an overview of the main components, their functionality, and the materials used in a PEM fuel cell are presented.

2.1.2 Solid polymer electrolyte

A solid polymer electrolyte is one of the essential components in a PEM fuel cell. The materials used for the electrolyte component in a PEM fuel cell have to be highly ionic conductive, with high durability and resistive to other chemical reactions. The first membrane used by General Electric was polystyrene sulfonic acid [22], and recently this was replaced by a perfluorosulfonic acid membrane (Nafion ®) made by DuPont. The structure of Nafion membrane is illustrated in Figure 2.3. This membrane is comprised of polytetrafluoroethylene back-bone (PTFE) and sulfonic acid chains connected to it. PTFE is mechanically and chemically stable and has a hydrophobicity advantage to repel excess water from the membrane. On the other hand, the sulfonic acid has a hydrophilic properties to maintain hydration in the membrane [23].

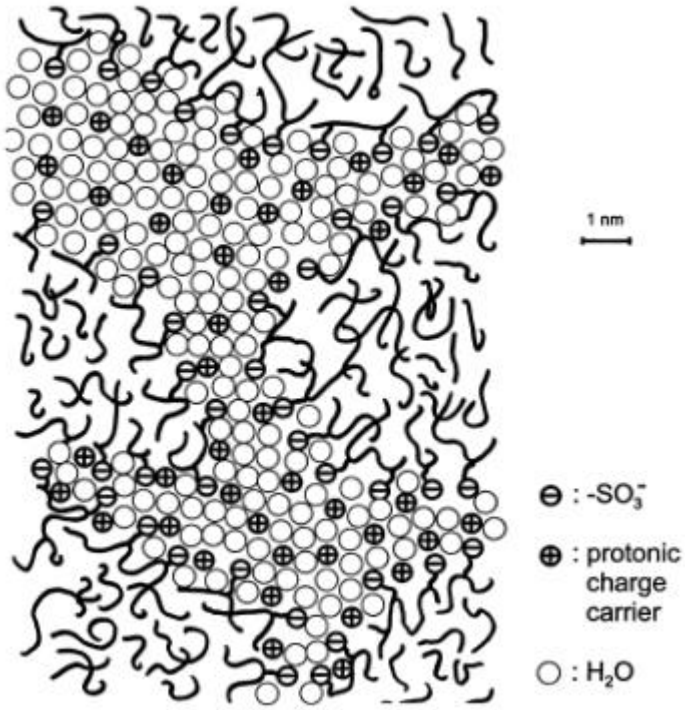

Figure 2.3 Schematic of the structure of Nafion comprised of hydrophilic and hydrophobic materials [15].

Typically, in a Nafion membrane, water is clustered in the sulfonic acid region due its hydrophilic effect. Once the membrane is fully hydrated, the H^+ ions can be repelled by the PTFE hydrophobic effect. Therefore, the power density of PEM fuel cells has increased dramatically since the replacement of traditional membranes of polystyrene sulfonic acid (PSSA) with the perfluorosulfonic acid (PFSA) membranes [21], [23].

2.1.3 The electro-catalyst layer

An important component of a PEM fuel cell is the catalyst layer at the anode and cathode electrodes. Typically, a PEM fuel cell comprises of two electrodes (anode and cathode) supported with a catalyst layer. Generally, at the anode side, the catalyst layer plays a crucial role in the disassociation of the hydrogen

atom and enhances the oxygen reduction reaction at the cathode side. As a result, the electrons pass through an external circuit to initiate an electrical current, and the protons pass through the membrane to unite with the oxygen molecules to form a by-product of water [24], [25]. The structure of the electrode and catalyst layer consists of platinum (Pt) nano particles deposited onto a carbon cloth or paper (carbon supported catalyst). As shown in Figure 2.4, the carbon plays a critical role in supporting the Pt nano particles mechanically, as well as enhancing the diffusion of the gases to the catalyst particles. Then, this electro catalyst layer is placed at the interface of the electrolyte as shown in Figure 2.5.

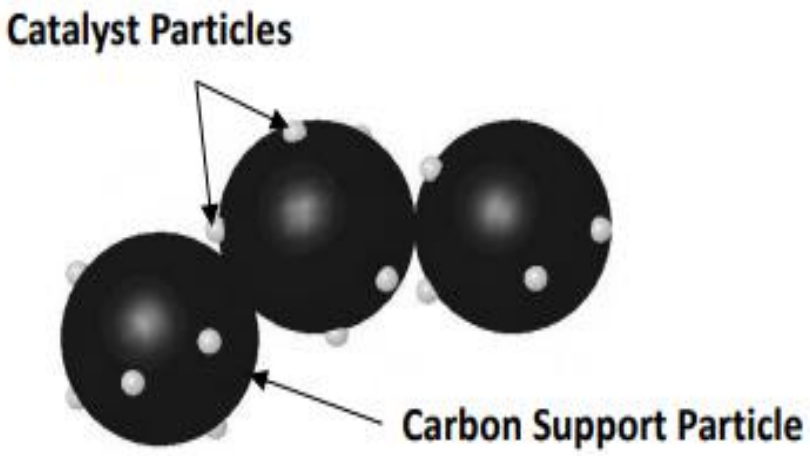

Figure 2.4 Schematic of the carbon supported catalyst of Pt used in PEM fuel cells [14].

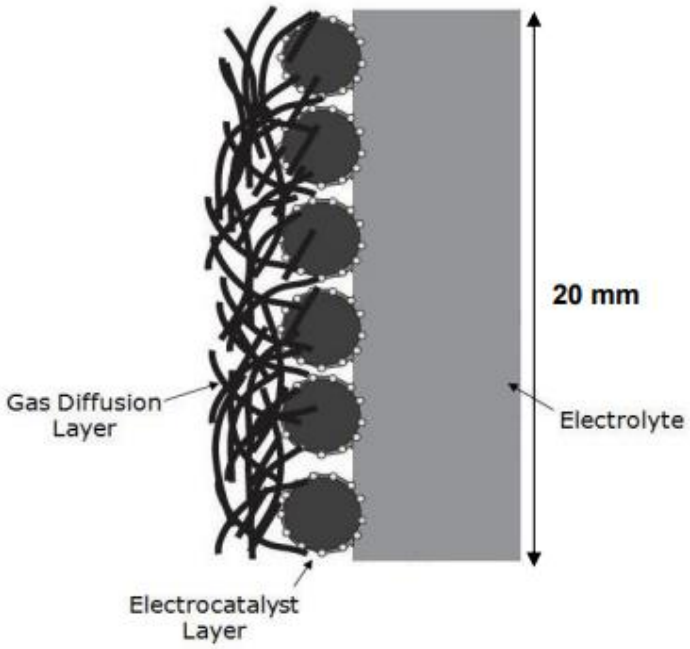

Figure 2.5 schematic of the electro-catalyst layer placed at the interface of the membrane electrolyte [14].

2.1.4 Flow field plates

Flow field plates are mainly used in PEM fuel cells to distribute the reactant gases to the electro-catalyst layers from the flow channels through the gas diffusion media. In addition, these flow field plates (FFP) operate as a current collector at the anode side of the fuel cell. Moreover, the FFP is used to hold a fuel cell stack in which they are called bi-polar plates. They have to be durable with a high strength, as well as chemically and corrosively resistant due to the exposed environment [14], [26], [27]. The bipolar plates are usually exposed to the corrosive environment in the fuel cell and this environment has a 2-4 pH level and a temperature in the range 60-80 °C. Therefore, the materials that are used to fabricate the bipolar plates should have high electrical conductivity and be resistant to corrosion. The most suitable candidates are metals coated with graphite due to their high electrical conductivity and their ability to

withstand the corrosive environment. There are different types of design for the flow field plates based on the shape of the channels that are usually parallel, interdigitated, or serpentine. The serpentine FFP is the most widely used in PEM fuel cells due to its advantages in removing some of the excess water compared to the other designs [28].

2.1.5 Gas diffusion layer

The main role of the gas diffusion layer is to permit the reactant gases to diffuse through the catalyst layer onto the membrane electrode assembly. A GDL has to be made from a porous and high electrically conductive material. Typically, GDLs are made from carbon fibre-based materials divided into two groups, namely non-woven carbon paper and woven carbon cloth. Usually, the carbon papers are surrounded by a carbonised thermoset resin, but on the other hand; due to the woven structure of the carbon cloth then no binder is needed. Therefore, there is much interest on using carbon cloth due to the ability of coating a Micro Porous Layer (MPL) on them [29], [30]. In the next chapter an overview of the GDL developments and degradation processes will be discussed in more details.

3 GAS DIFFUSION LAYER

3.1 Background

As briefly discussed in the previous chapter on the main components of a PEM fuel cell, the gas diffusion layer (GDL) is an intrinsic part in a PEM fuel cell and this is due to its important roles and functionalities. The next sections cover more details about the importance of the GDL and the various factors that are involved in the GDL degradation. Typically, a GDL is placed between two other components, namely the flow field plate (FFP) and the catalyst layer (CL). The process of feeding the reactant gases starts from the gas flow channels in the FFP through the GDL to be delivered efficiently and sufficiently to the CL in the MEA. Therefore, the structure of the GDL is highly important in the fabrication process. The structure of the GDL must act as a mass transporter for both reactant and the by-product fluids. Hence, there are some factors that have to be considered in the materials selection for the GDL [31]. The materials used in the GDL must be (i) electrically and thermally conductive to effectively transfer the electrons and (ii) they must be porous and have both hydrophobic and hydrophilic characteristics. Hydrophobic and hydrophilic effects play an essential role in controlling the hydration/dehydration in GDLs. In order to consider all these functionalities of a GDL, then it is necessary to have some trade-offs in the material selection. For instance, water management is one of the most crucial issues since it leads to a loss in power density occurring at the GDL. Consequently, excessive water leads to flooding in the MEA and drastically affects the electrochemical reaction process. The issues of loss in

power density on the GDL and water flooding in the MEA requires special material treatments in specific amounts in order to effectively utilise the performance of the fuel [32][33]. Therefore, understanding the behaviour of such materials used in the PEM fuel cell and their mechanical properties can help modellers in the design process and optimisation. A typical GDL is made of carbon-based materials; either a woven carbon cloth or a non-woven carbon paper as mentioned in Section 2.2.9. Usually, these carbon-based materials that are used for GDLs have some additives in order to overcome water management issues and generally, carbon-based materials, such as woven carbon cloth have a hydrophilic nature in their structure. As a result, polytetrafluoroethylene (PTFE) loadings are used to enable the hydrophobicity effect in the GDL; in order to overcome any excess water or any blockage in the GDL pores. Also, another way to mechanically enhance the GDL substrate is by adding a micro porous layer (MPL). Usually, MPLs are coated on the GDL at the catalyst layer side in order to improve the mass transfer of reactants [34], [35]. To have a better insight of the GDL characteristics, the next sections cover the main properties and factors related to the GDL structure and its effect due to the clamping forces and the hygrothermal effect.

3.2 GDL Structure

3.2.1 Porosity

The GDL has a porous structure made of multi layered carbon, typically a macro-porous substrate or backing substrate, and a micro-porous layer (MPL). Generally, the macro-porous backing is made of carbon cloth or paper as mentioned in section 2.2.9. The pore size of this macro layer is usually in the range 1-100 μm and the pore size distribution of the carbon substrate measurement can be affected by adding an MPL [36], [37].Therefore, the effective diffusion coefficient of a porous medium can be identified via a Mercury Intrusion Porosimetry (MIP) and calculated using the following equation [36]:

$$D_{eff} = \frac{\varepsilon}{\tau D} \tag{3.1}$$

where D_{eff} is the effective diffusion coefficient, ε is the porosity, τ is the tortuosity, and D is the diffusion coefficient of the gas.

The concept of a pore size analysis using a MIP method is by intruding mercury over a range of pore diameters to identify the pore volume and pore size distribution. The porosity is one of the most important factors that affects the mass transfer in the GDLs. In general, the porosity is the void space or volume found in a material. In a typical gas diffusion layer, that is made of carbon paper or cloth, the pore size and volume is different for each type, and it significantly affects the electrical and thermal conductivities in a PEM fuel cell. Many studies

in the literature [38]–[47] have related the volume of the pores in the GDL to the overall performance of the fuel cell as well as the electrical and thermal conductivities. Nabovati et al. [38] studied the effect of the porosity of different loadings of PTFE on the GDLs. They investigated GDLs by adding different percentages of PTFE and a binder material. They found that there is an inverse relation between the increment of fibre volume percentage and the in/through-plane permeability due to the heterogeneity in the porosity. Farmer et al. [39] studied the porosity of different carbon and PTFE loadings on different GDL samples. They compared the porosity of a treated and untreated GDL samples using two different techniques, namely 2D SEM micrographs to mathematically construct a 3D volume structure; and they used the mercury intrusion porosity method to compare their results with a 2% error margin. Hinebaugh et al. [40] investigated the porosity of GDL samples to form a fibrous network simulated model using x-ray computed tomography and they presented a very detailed view of the water distribution in different GDL samples. Rajalakshmi et al. [42] studied different loadings of carbon black on MPL coated GDL samples. They investigated the thickness, pore size and porosity properties and related to the electrical conductivity and the fuel cell performance. They found that as the thickness of the MPL later increases, due to carbon loadings, the electrical conductivity at the MEA decreases, which in turn affects the fuel cell performance. Hiramitsu et al. [43] studied the issue of water flooding in GDL samples under different humidity conditions with different carbon paper treatments. They related the water flooding phenomena in GDLs to the differences in the pore size. Also, they showed that

reducing the thickness of the GDL, and controlling the pores sizes, played an essential role in controlling the flooding issues. Yan et al. [45] conducted a study on the flow distributor and the GDL geometries. They linked their conclusion on the GDL geometry to the overall performance of a PEM fuel cell and they concluded that the higher is the porosity of a GDL structure then this enhances the mass transport during the operation. On the other hand, some studies [48], [49] suggest that a low porosity GDLs enhances the PEM fuel cell performance. Jorden et al. [49] conducted a study on the morphology of a GDL sample with different carbon black types, namely Vulcan XC-72R and Acetylene Black with 10 % PTFE. They found that, due to the lower porosity of Acetylene Black, water hindered the flooding of the MEA, which implies a better mass transport.

3.2.2 Fibre orientation

The carbon fibre orientation in the GDLs is an essential factor in characterising its mass transport properties since the fibre to fibre contact through the pores is responsible for delivering the reactants from/to the CL [50]. Moreover, it affects the electrical and thermal conductivities through the GDL. Approximately 80 % of the porous structure is comprised of randomly orientated carbon fibres [17] and the carbon fibres are typically made of a copolymer consisting of more than 90 % of polyacrylonitrile (PAN) [29]. However, based on the type of carbon substrate used as GDL, the physical proprieties will be affected. Figure 3.1 Micrographs of (a) non-woven carbon paper structure, and (b) woven carbon cloth structure [52].

A study was conducted by Frey and Linardi [51], on the differences between the carbon cloth and carbon paper structures of different GDLs. They concluded that the GDL structure and the fibre orientation play an essential role on the fluctuation of the PEM fuel cell performance. Wang et al. [52] supported the latter study by explaining the reasons behind the performance fluctuations, and they found that carbon cloth based GDL is better under high humidity operation. Due to its fibrous structure, carbon cloth GDLs have the ability to decrease the ohmic losses and increase the hydration level in the MEA. Therefore, woven GDLs are relatively better than non-woven GDLs in the flexibility and the mechanical properties hence, the structure and morphology of GDLs play an intrinsic role in determining many physical properties. Fishman et al. [41] investigated the tomography of several GDLs, and it was found that the lower the roughness of the surface of the GDL then the more effort is required to transport water through it.

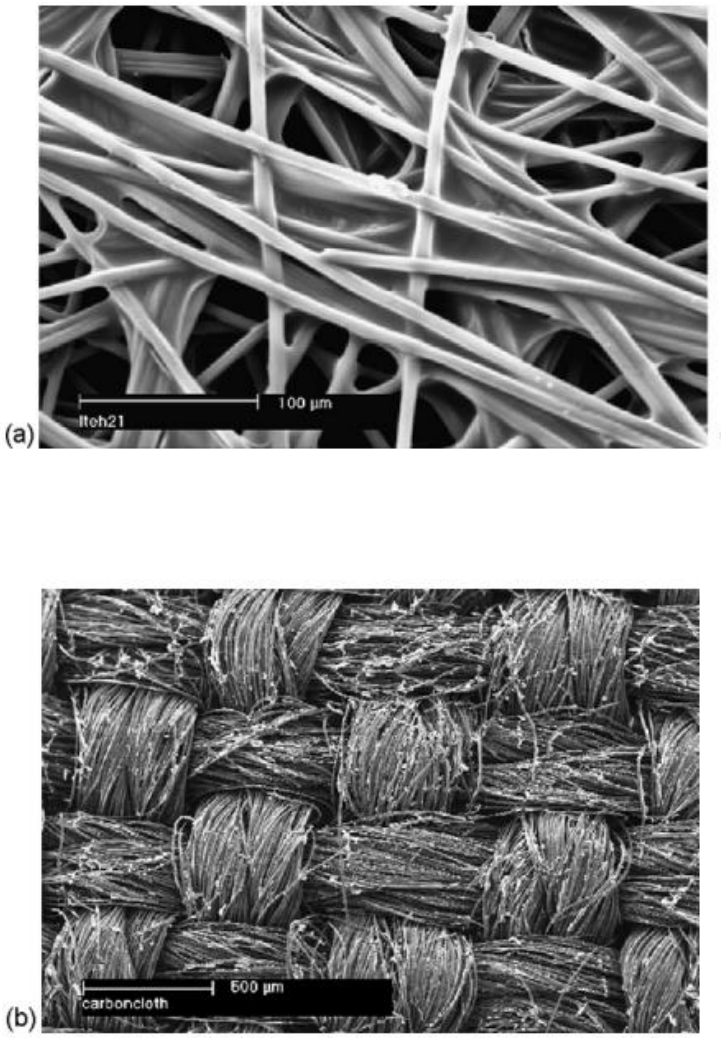

Figure 3.1 Micrographs of (a) non-woven carbon paper structure, and (b) woven carbon cloth structure [52].

Therefore, with all these studies regarding the structure and morphology of the GDLs, it is essential to focus on the changes in GDLs due to compression effects. Compressive stresses in a fuel cell can lead to severe changes in the porosity and carbon fibre orientation.

3.2.3 Surface wettability and Contact Angle

Water management in the GDL is one of the main factors that is dependent on the surface structure of the pores. A surface wettability test through

measuring the contact angle, in which contact angles less than 90° indicate a hydrophilic surface and contact angles greater than 90° a hydrophobic surface. Therefore, a contact angle of a solid surface can give an indication of the surface nature, as well as the roughness of the fibres in the case of GDLs. Obeisun et al. [53] conducted an experimental study to correlate the wettability of heated GDL samples in order to study the effect of the evaporation dynamics of the droplets contact angle. It was found that increasing the temperature leads to a small contact angle on the surface. The latter method was mainly performed to study the external surface property and how it changes based on the content of the hydrophobic and hydrophilic pores. On the other hand, Gurau et al. [54] proposed a different method of measuring the internal wettability of the GDL, where they used the ‘’Washburn method‘’ that has been used only to determine the internal contact angle of hydrophilic materials. Basically, this method uses different fluid droplets that have very low contact angles to be absorbed through the GDL surface and the assumption is that water can’t be used for this test due to the inhomogeneous nature of the surface of the GDLs.

Therefore, for structural analyses of the GDL, the external wettability test is a good indication of the nature of the surface and the changes that may occur due to any type of degradation. Since, compression stresses can affect the GDL properties, it is necessary to study such changes on the surface. Comparing the results obtained for the wettability of the uncompressed and compressed GDL samples then can give an indication on the surface changes and effects due to compression, and will provide a data set for the tested GDL types for

modellers. Moreover, it can give an insight regarding the behaviour of water droplets on the GDL surface.

3.2.4 Hydrophobic agent loading on GDL

Water management in a PEM fuel cell is mainly related to the GDL structure. As mentioned in Section 3.1, enhancing the water management properties in the GDLs require some hydrophobic additives. There are many studies in the literature that investigate the GDL structure by adding different hydrophobic agents. For instance, different studies related to the type of hydrophobic agent were conducted, for instance, the use of polytetrafluoroethylene (PTFE), polyvinylidene fluoride agent [55], and fluorinated ethylene propylene (FEP) [30], [56], [57]. The focus will be more on the PTFE hydrophobic agent due to its common use as a GDL hydrophobic treatment. Many studies suggest that there is a relation between the PTFE loadings and the overall performance of the PEM fuel cell, as well as some opposing effects on the porosity and permeability [30], [58]–[62]. In a study conducted by Sow et al. [63] on different GDL samples with different PTFE loadings, they found that there is a relation between the bulk and the contact resistance on GDL samples due to the PTFE loadings. It was attributed to the fractional insulation in PTFE conductive material. In other words, it means that there is some noticeable difference in pore size distribution of the GDL structure, which in turn plays a significant role in water management. Despite of the number of studies [30], [60], [64] that suggest that there is an optimum loading content of PTFE on GDL. It was found

that different operation conditions can contribute significantly to the permeability of the GDL with different loadings of PTFE.

3.2.5 Dual layer GDL

A dual layer GDL is a two-layer component that comprise of back substrate (which is usually a single layer GDL with or without hydrophobic agent), and a micro porous layer (MPL). Typically, a thin layer that comprises of carbon black material and hydrophobic agent; namely the MPL, added to the macro porous layer (back substrate gas diffuser). The role of this layer is to mitigate the mass transport losses, and to improve the mechanical properties of the GDL in the MEA [60]. Many studies [34], [65]–[70] suggest that the MPL plays a crucial role in enhancing the performance of a PEM fuel cell. For instance, Park et al. [65], in their study about the two different types of GDLs namely carbon paper and carbon cloth substrates, found that adding an MPL layer on carbon paper substrate improves the water management. It was noticed that due to the pore volume presented by the MPL, accumulation of water significantly reduced, and some enhancement of oxygen transport reaction was observed. Since the MPL comprises of a hydrophobic agent, such as: PTFE, and carbon black powder. The change in the content and composition of the PTFE or carbon black loading, respectively, can affect the performance as well. Qi and Kaufman [67] have conducted an experimental work on the MPL with different PTFE and carbon black loadings. In their work, they concluded that these layers enhanced the mechanical strength and improve the water management in GDLs. On the other hand, some simulation work has been conducted by

different research groups to study the effect of the MPL. For example, Weber and Newman [70] performed a simulation model to study the MPL effect and role in PEM fuel cells performance. They found that the MPL works as a water valve that repels any excess water from the GDL and membrane. It was concluded that the MPL helps to reduce the effect of water flooding in the MEA. Therefore, the role of the hydrophobic agent is crucial in controlling the hydration level in the MEA and avoiding any excess water which lead to membrane swelling and performance issues.

3.3 GDL degradation

Due to its structure, the GDL is considered to have the highest tendency in deformation in a PEM fuel cell stack [71]. Gas diffusion layers are susceptible to different types of degradation. These degradation effects can be categorized into two main types namely, chemical degradation and mechanical degradation. Chemical degradation can be attributed to the carbon corrosion or the wetting behaviour of PTFE on the GDL. On the other hand, mechanical degradation of the GDL can be comprised of different effects and phenomena [72]. Figure 3.2 shows a schematic of different types of GDL degradation due to both chemical and mechanical effects. However, in this literature investigation, mechanical degradation will be the focal point. The lifetime and durability of a PEM fuel cell is mainly affected by the GDL mechanical degradation. Hence, understanding the mechanical effects that lead to degrade the GDL performance, which in turn determines the overall performance of the fuel cell, is essential [73].

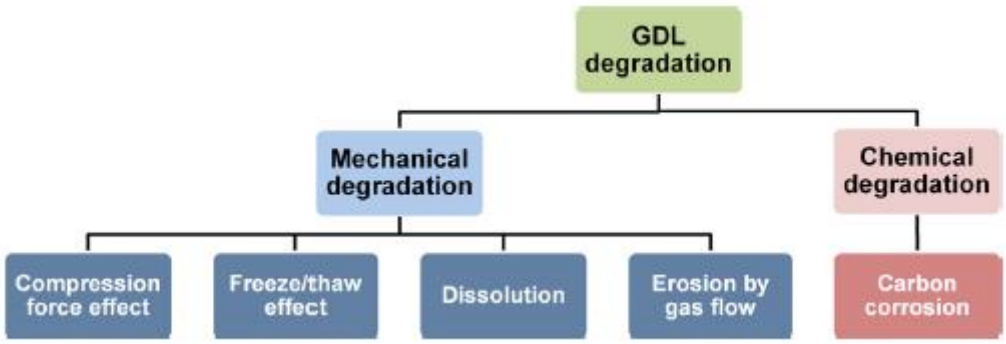

Figure 3.2 An illustration of the different types of degradation on GDLs [72].

3.3.1 Mechanical degradation on the GDL

Generally, there are numerous researches conducted on the overall degradation of PEM fuel cells. PEM fuel cells are subjected to different types of mechanical effects during operation. For commercialization purposes and different types of applications; different types of stresses can exist. The main stress mode that all PEM fuel cells can experience is the compression stresses due to the hygrothermal effect of the membrane due to the membrane swelling. This change in humidity and temperature plays an intrinsic role in adding more stresses to the GDL. Moreover, the clamping torque on the end plates will add pressure; due to the fuel cell assembly which can lead to compression stresses on the GDL as well. On the other hand, for instance, fuel cells used for transportation purposes are subjected to vibrational stresses due to movement and road structures [74]. Therefore, cyclic compression stresses can be experienced during the fuel cell operation.

The interfacial contact between the flow field plate (FFP) and the GDL is an important aspect of the PEM fuel cell design. There are many studies conducted on the contact resistance between the components of the fuel cell and compression effect [75]. The operational voltage of a PEM fuel cell is directly related to the interfacial electrical contact resistance between the FFP and the GDL. As a result, the PEM fuel cell performance will be considerably affected [76]. Zhou et al. [75] for example, studied the effect of the clamping forces on the contact resistance and the porosity of the GDL. They found that as the clamping force increases; the contact resistance decreases and the porosity of the GDL reduces due to its deformation and change in void volume.

Other studies by different groups [77]–[79] also support this correlation between the contact resistance of the GDL/FFP and the reduction of GDL porosity. Some of these studies went further in the analysis by adding different parameters that can be affected by the clamping pressure in the fuel cell assembly. Lai et al. [80] emphasised in their study that there are two types of contact activities that affect the performance and create more losses in power, such as ohmic losses. They investigated the GDL/FFP contact resistance and studied the electrical resistance effect. They found that mechanical stresses significantly affect the electrical contact resistance. Therefore, it's very important to understand the modes and effects of stresses acting on the gas diffusion layer separately. The structure of the channel/rib in the FFP in contact with the GDL can lead to significant changes in the compression mode. Nitta et al. [81] in their experimental study took into account the inhomogeneous compression on the GDL due the interfacial contact of the channel/rib structure with the GDL. Similarly, a study conducted by García-Salaberri et al. [82] on the inhomogeneous pressure as a result of the fuel cell assembly/disassembly process. This pressure enhances both electrical and thermal properties and decreases the contact resistance. However, in contrast, extra pressure can hinder mass transport through the GDL, which in turn can lead to a reduction in delivering the reactant gases. A different simulation study was conducted by Sun et al. [83], and their assumption was that GDL thickness varies with its location, i.e. areas exposed to the rib channel in the FFP. They assumed that the structure of the rib/channel interface with GDL will decrease 15 % in thickness due to the compression effect. Figure 3.3

shows a schematic of the rib/channel interface with GDL. Therefore, it is well noted in the literature that in order to achieve a better performance and output of a fuel cell, the applied compression pressure has to be significantly measured and studied to find an ideal pressure for each setup [76], [77], [84].

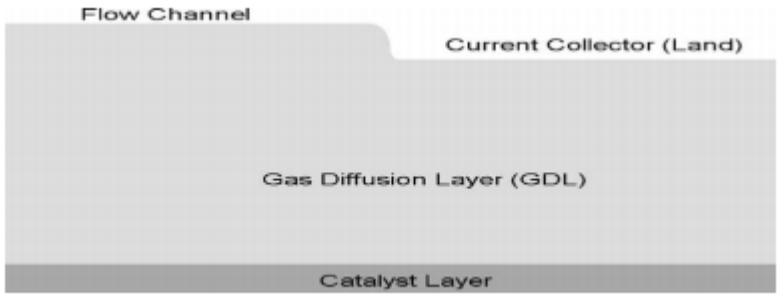

Figure 3.3 A schematic of a compressed GDL due to the interference of rib/channel [83].

Other studies by different research groups [85]–[87] have studied the effect of excessive compression and the way it significantly affect the carbon fibre structure, thus leading to the different properties during fuel cell operation. Furthermore, compression often leads to the loss of some PTFE and/or carbon particles as a result of the breakage of the carbon fibres of the GDL material. One of the efficient ways to quantify the amount of lost PTFE due to compression is to use Thermogravimetric Analysis (TGA) for uncompressed and compressed GDLs.

3.3.2 Types of Stresses on GDL

There are a number of studies that suggest the occurrence of the compression force exerted on the GDL due to the interfacial contact resistance between the rib/channel structure and the GDL. Lu et al. [88] conducted a simulated and

experimental study on three GDL samples under two types of stresses namely, steady state stress of 1 MPa and a loading/unloading compression stress due to the hygrothermal cycle of the MEA. The purpose of their investigation is to relate the effect of the GDL modulus under compression. On one hand, this compression force is attributed to the fuel cell assembly; in which it significantly affects the thickness of the GDL material. On the other hand, the cyclic compression pressure is due to the effect of swelling in the membrane. It is important to distinguish between the two types of compressions that the GDL is subjected to within the polymer electrolyte fuel cells (PEFCs): (i) the assembly compression which is "permanent" (around 1 MPa) and applied to bring the various components of the fuel cell together and (ii) the cyclic compression which varies depending on whether the membrane electrolyte expands (as a result of hydration) or shrinks (as a result of dehydration). With this in mind, it is evident that the cyclic compression (which could be anything between 0 and 2 MPa [89], [90]) is additive to the assembly compression. It should be noted that the above cyclic compression is different to potential cycles of compression/decompression that occur as a result of vibration and may loosen the assembly bolts [74], leading eventually to less assembly compression and lower performance. However, such vibrational cycles of compression/decompression are unlikely to take place in stationary applications. Therefore, it is well documented that there are two types of stresses to be considered in evaluating the properties of a GDL for real-life operations.

Steady-state compression pressure & Cyclic compression pressure

PEM fuel cell components require a relatively high compression stress to be held in position during assembly. The compression stress exerted on the PEM fuel cell due to the clamping force is mainly to reduce the interfacial contact resistance and avoid any gas leakage. However, these clamping forces play a crucial role in mitigating the overall performance of a PEM fuel cell [72]. Reducing the contact resistance between PEM fuel cell components is well achieved by a clamping force. This will assist in a better electrical conductivity through the GDL. However, overloading the fuel cell with compression can lead to degradation; mechanical degradation, in which it can affect the performance of the fuel cell and damage the GDL structure [88]. Practically, a PEM fuel cell undergoes a compressive stress in the range of 1 MPa and above during assembly [91], and based on the US Department of Energy (DoE) targets, a value of 1.4 MPa is the region of interest for fuel cell developers [92]–[94]. Therefore, for a better contact resistance in the MEA, a target of 1-1.4 MPa is desired. However, due to the assembly/disassembly the GDL is subjected to stresses in different ranges, which can affect their structure, which in turn can affect the overall performance of a fuel cell. Many researchers have studied the effect of the assembly compression pressure due to the clamping force [95]–[100]. Taymaz and Benli [99] have suggested an ideal value of assembly compression in their numerical simulation study at a temperature 65 °C and 30 % relative humidity for better electrical conductivity. Based on a range of 0-3 MPa, they claimed that a range of 0.5-1 MPa compression is ideal for better performance. Another finite element modelling study, conducted by Mehboob et al. [101], to

study the effect of the clamping forces based on two different numbers of bolts namely: 4 bolts and 8 bolts for an assembly in the range of 1.55 MPa and 8.48 MPa, respectively. They found that the usage of 4 bolts results in a desirable fuel cell performance. However, the 8 bolt compression force reduced the mass transport through the GDL due to over compression. Therefore, it is well documented that over compression due to clamping forces can lead to undesirable fuel cell performance. Hence, it is vital to understand the structural behaviour of such compression exerted on GDLs. Different methods in analysing the effect of compression pressure on the GDL structure will be discussed in Chapter 4.

PEM fuel cells have gained much attention due to their wide range of applications. Therefore, the environmental impact due to vibrations and sudden shocks in such applications, e.g. transportation and spacecraft and vehicles. These vibrational modes can range between 0.9-40 Hz, which can result in degrading the fuel cell performance. On the other hand, the hygrothermal cyclic effect in the MEA, due to hydration/dehydration in the membrane, contributes in adding more stresses on the GDL. All these factors can result in a cyclic compression pressure that significantly affects the GDL, which in turn can affect the overall performance of the fuel cell. Dry conditions of MEA and room temperature don't imitate a running fuel cell. In a running fuel cell from the start-up period, the MEA undergoes in different stages that result in swelling/hydration. Consequently, this swelling induces a hygrothermal stress that affects the GDL and increases the applied pressure on it [71]. Solasi et al. [102] have conducted a numerical study on a cyclic

compression on the MEA due to the hygrothermal effect. In their study, they found that a stabilisation of the plastic strain was after the sixth compressive cycle.

3.3.3 Effect of Gas Permeability in GDLs

Permeability is an important physical factor that is responsible for the mass transport in designing a GDL. Since the GDL functions as a mechanical support to the MEA, as well as deliver/remove reactants and water to/from the MEA, respectively [86]. It is vital to understand the changes in permeability due to any structural changes in the GDL, such as compression. Many studies have been conducted in correlating the GDL compression with permeability and porosity. There are some studies, for example [103], that show an opposing effect of GDL compression with permeability, electrical and thermal conductivities. Notably, as the GDL permeability decreases due to compression, nevertheless the electrical and thermal conductivities significantly increase. Radhakrishnan and Haridoss [104] studied the effect of the permeability of a commercial GDL Toray-H-120 under two different compressed thicknesses. As a result, increasing the compression on the GDL increases the pressure drop between the inlet and outlet of the serpentine flow channel. All this is attributed to the reduction in the pore size and permeability due to the compression. Also, in the same study, they compared the latter result with a parallel flow channel configuration. They observed that with compression, there was no significant pressure drop when using the parallel flow channel, which means that the convective mass transport is

negligible. Therefore, there has to be a trade-off in designing GDLs in order to control the physical properties in a fuel cell. There are two directions in which the permeability needs to be taken into account whilst designing the GDL, namely the in-plane permeability, and the through-plane permeability [105]. It is very important to emphasize that the structure of the GDL fibres is anisotropic. Therefore, many research groups have studied the effect of the permeability in different directions, i.e. it is not the same in all directions. Hence, some studies [106], [107] suggest that adding the dual layer to the backing substrate of the GDL, such as the MPL will not affect the in-plane permeability, and it will only be affected in the through-plane direction. Therefore, permeability can be altered due to its fibre orientation. The through-plane direction of a GDL is very important, it allows reactants through the diffusion mode to transport from flow channels to the catalyst layers. However, the in-plane direction due to the forced convective mass transport also plays an essential role as well. It is well documented that convection mass transport in the plane direction of GDL enhance the fuel cell performance due to the pressure difference between two neighbouring flow channels [29], [108].

3.4 Gaps in the literature related to compression stresses in a GDL

The majority of research studies in the literature regarding the GDL mechanical characterisation is due to steady-state and cyclic compression effects that are mainly focused in two main approaches. First, quite a number of studies are experimental investigations into different GDLs with different ranges of clamping pressures during the fuel cell operation. In other words, in-situ experimental work on different operating conditions, including a clamping pressure, in order to investigate the overall performance of a running fuel cell and the GDL stability. On the other hand, numerous numerical studies, including the effect of steady-state and cyclic compression on GDLs have been conducted. However, to the best of the author's knowledge, very few studies have been conducted as ex-situ measurements of the GDL structure under compression. Escribano et al. [86] have conducted an experimental study on three different types of GDL samples namely, cloth, felt and paper. All these samples were subjected to a pressure in the range 0-10 MPa for two cycles. The result was that a felt GDL has no significant effect in the second compression cycle compared with the cloth and paper GDL samples. The microstructure of the felt GDL comprises of an entangled fibrous structure in both the in/through plane directions, with no polymeric binder. This composition and structure assist in withstanding higher compression rates compared to the paper and cloth GDLs. El-kharouf et al. [36] investigated the mechanical, physical and the electrical properties for a variety of GDL materials. As part of the mechanical test, the GDL samples were "conditioned" at 3 MPa (5 times), in order to minimise the irreversibility of the GDL

deformation and thickness. Following the conditioning procedure, three different clamping pressure (i.e. 0.5, 1.5 and 2.5 MPa) were applied on the GDLs and different characteristics were estimated at these clamping pressures. The gas permeability of the tested GDLs were measured using a mercury intrusion porosimetry. Likewise, the gas permeability of some commercial GDL materials was measured in the present work; however, an in-house setup was used to achieve this before and after performing a realistic compression. Further, in the present work, other parameters including the contact angle, the thermal stability, the thickness and the morphology of the GDLs were measured and/or investigated before and after the compression test. Whereas, very little attention has been focused on the structural analysis on the ex-situ characterisation of GDLs; including different parameters, i.e. pore size distribution, porosity, gas permeability, thermal stability, surface contact angle and scanning electron microscope before and after a realistic compression test. In order to obtain a better visualization and information related to the GDL structure, it is essential to include all these parameters and determine a correlation between them. Moreover, and more importantly, is to have such a stress-strain curves for different GDLs to assist the modellers and provide them with very critical data on compressed GDL stress-strain curves and their physical properties. Figure 3.5 [81] shows the effect of increasing the compression on the gas diffusion layer.

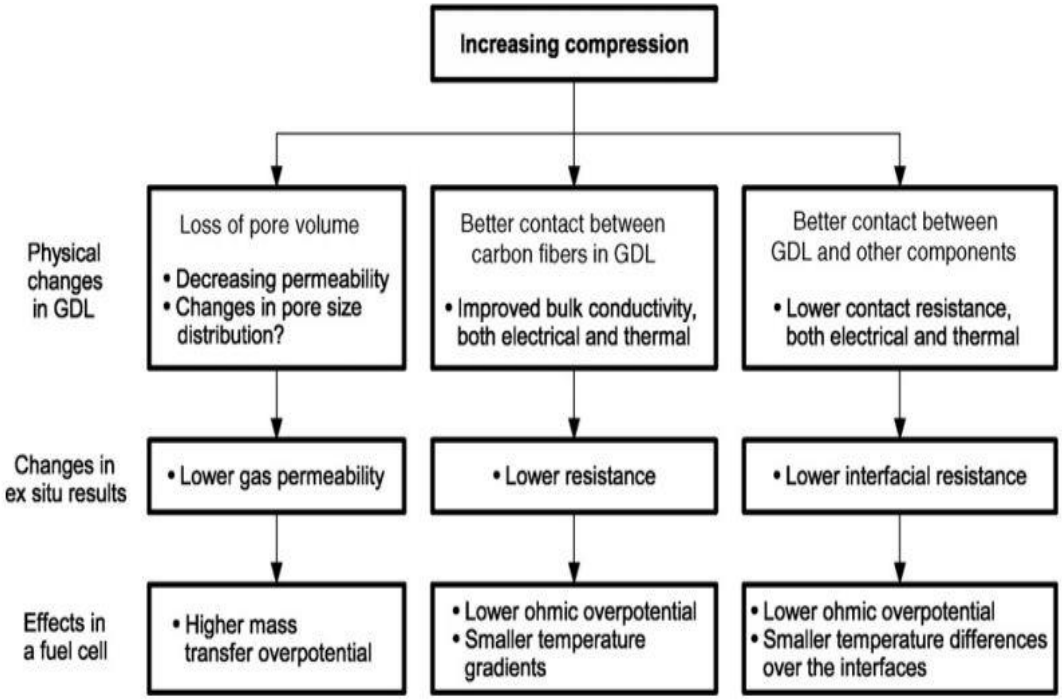

Figure 3.4 The effect of the compression on the gas diffusion layer and the PEM fuel cell performance [81].

From Figure 3.4, it is important to note that over-compression of the gas diffusion layer can cause more losses in the PEM fuel cell performance. Therefore, over-compressed GDLs in the fuel cell are considered one of the main issues that hinders a better performance of the fuel cell due to changes in the physical properties, mass transport and contact resistance.

In conclusion, Table 3.1 shows different studies related to the mechanical characterisation methods employed in GDL investigations, and the major experimental techniques that have been used.

Table 3.1 The different methods employed for the mechanical characterisation of GDLs.

Method used	Type of compression	Stacking	Range of stress	Reference
Universal testing machine (INSTRON 5566)	Clamping force	No	0-3.4 MPa	Ismail et al. [109]
Universal testing machine (INSTRON 4465)	Clamping force + bipolar plates effect	10 samples	0-10 MPa	Escribano et al. [86]
Single cell fixture	Clamping forces	No	Different compression ratios.	Lin et al. [110]
Controlled compression unit cell	Clamping forces+ cyclic compression	No	0.2-2.5 MPa	Mason et al. [111]
Aluminium and graphite plate fixture	Cyclic compression due to PEMFC serviceability	No	At two different values 1.7 and 3.4 MPa	Radhakrishnan and Haridoss [112]

Mathematical modelling	Clamping forces due to bipolar plates contact		0-1.4 MPa	Kleemann et al. [97]
Five cells fixture	Clamping forces	5 Samples	Two different compression ratios (15% and 30%)	Yim et al. [113]
Aluminium plates with steel gage	Clamping forces due to bipolar palate contact	No	Controlled thickness	Nitta et al. [81]
Copper and graphite plates with thickness gage	Clamping forces	No	0-35 bar	Chang et al. [95]
Tensile-compression apparatus for thickness measurement.	Cyclic compression	No	0-1.5 MPa	Sadeghi et al. [50]
In-situ characterization	Clamping forces	No	Different compression ratios	Han et al. [114]

by controlling the thickness			(15%,26%,36% and 46%)	
In-situ characterization of the performance	Clamping forces	No	Different torque values (100,125, and 150 lb_f)	Lee et al. [76]
Dynamic mechanical analysis test machine	Clamping forces+ cyclic compression	No	0-12 MPa	Gigos et al. [115]
Small tester (No details)	Clamping forces due to the bipolar plate contact	10 samples	0-20 MPa	Matsuura et al. [87]

In summary, all the investigation work on the mechanical behaviour and its effect on the GDL has either considered the clamping forces during assembly or the cyclic compression due to the hygrothermal effect or serviceability, i.e. assembling/disassembling the fuel cell stack. However, no experimental work has considered the combination of the steady-state compression due to the clamping forces of assembly and the hygrothermal effect on the MEA which in turn induces more stresses on the GDL during operation (start-up/shutdown).

Therefore, a more realistic representation of a combined mode of compression will be investigated in this thesis.

3.5 The sealing gasket

3.5.1 Introduction

Sealing gaskets are one of the most important components used in PEM fuel cell stacks. Using proper sealing gaskets ensures better performance of the fuel cell. The main advantages of sealing gaskets is to provide an insulation of any gas leakage. There are many issues related to safety and reliability of gaskets, which in turn affects the commercialisation of the PEM fuel cells.

Each component of the PEM fuel cell stack can be affected by a chemical or mechanical degradation. There are many factors that can contribute to adding more damage to these components, which in turn can affect the overall performance of the cell. Therefore, the design and the assembly of the PEM fuel cell stack play an important role in its performance. For instance, any failure related to the sealing gaskets can lead to gas mixing of the reactants, and consequently affect and degrade the performance of the fuel cell.

Typically, the PEM fuel cell stack comprises of a membrane electrode assembly (MEA), a gas diffusion layer, gaskets placed in the perimeter of the GDL and MEA, catalyst layer, flow field plate (FFP) and an end plates for assembly. Figure 3.5 shows the different components of the PEM fuel cell stack with the position of the sealing gaskets in the cell [116].

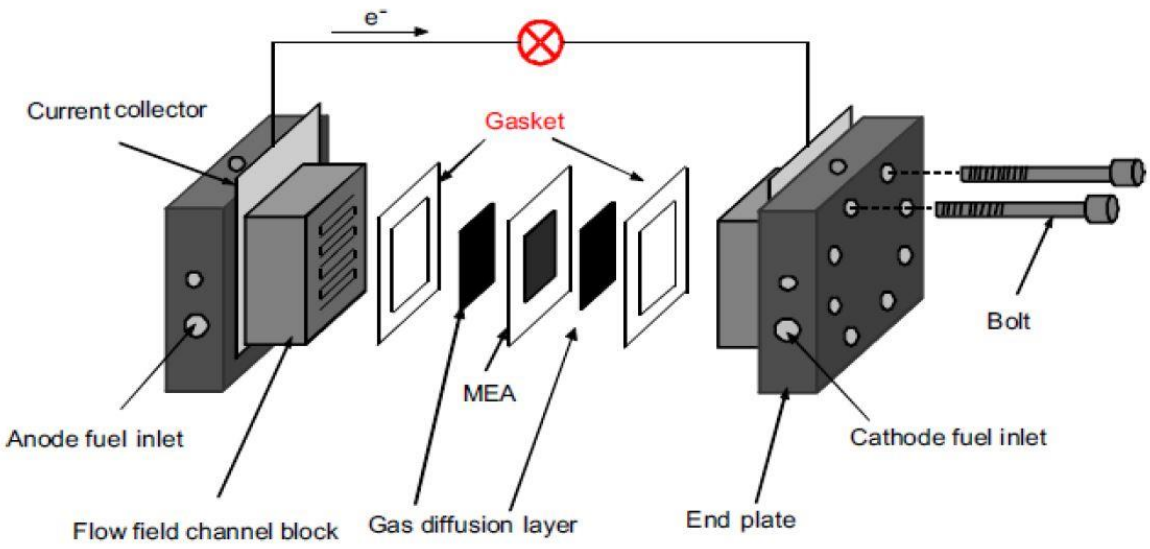

Figure 3.5 schematic of the PEM fuel cell components [114].

One of the main requirements for a PEM fuel cell commercialisation is to have a good sealing gasket due to its crucial role in preventing any gas leakage. Each component in the PEM fuel cell has its own limitations and durability during operation. The durability of the fuel cell components is associated with the durability of the used materials. There have been many studies on different materials of the PEM fuel cell components such as: GDLs, bipolar plates, and MEA, however, the effect of the sealing gaskets have been neglected [117]–[119]. The sealing gaskets considered as one of the main components in the fuel cell stack.

Typically, there are two types of leakages that occur inside the fuel cell, cross over leaks and overboard leaks. Cross over leaks happen in the cathode or the anode side when some of the reactant gases divert to the outside atmosphere. However, the overboard leaks occur during the transfer of the gas inside the membrane (from side to side). Therefore, the main functionality of using a good sealing gasket is to prevent both types of leaks. Gas leakage considered

as one of the vital issues inside the cell due to its direct correlation with safety issues [120]–[122] .

In order to consider a good sealing material, it has to be durable and able to maintain and survive the harsh conditions inside the fuel cell. There are many conditions that the sealing gasket has to be tested for in order to be considered as a sealing material. Some of the main effects on the gasket's failure are described briefly in the next section. Typically, the gasket is subjected to different types of mechanical, electrochemical and thermal conditions. Mechanical stresses in the form of compressive loads are subjected on the gaskets and could lead to mechanical failures. Humidity and temperature play an important role in deteriorating the functionality of the gaskets as well. Operating temperature from the range between -40 and 80 °C or even higher (i.e. high-temperature PEMFC), and 100% relative humidity can lead to some types of failure as well. Finally, the chemical factor of the acidic nature in the MEA and the fuel cell structure which can lead to a corrosive impact on the gasket. Also, the chemical reactions of the reactant gases and the by-products.

3.5.2 Sealing gasket properties

3.5.2.1 Mechanical stresses and stability

The mechanical forces acting inside the cell is one of the important properties that is crucial for the sealing gasket. Providing sufficient amount of pressure assist in safely sealing the cell with no leakage. Moreover, it ensures better electrical and thermal conductivities to the cell [123]. Considering most of the

sealing gasket materials used are elastomers, which have a special rubber-like materials which is called hyperelasticity. They can withstand higher loads of pressure and return to its initial state without being mechanically failed or losing its mechanical properties.

3.5.2.2 Temperature and electrochemical properties

One of the important properties of the sealing gaskets is to withstand the fluctuation of low and high temperatures and the acidic environment in the cell. In some cases, and especially for cold start-up fuel cells, i.e. automobiles and other transportation applications, experience a cyclic and rapid change in temperature from -30 to 80 °C. The electrochemical reactions that occur inside the cell could increase the possibility of the gasket deterioration. Using some types of elastomer materials can react with the reaction process leading to some distinct damage to the gaskets and therefore, deteriorating the PEM fuel cell performance dramatically [124].

3.5.2.3 Sealing material compatibility and gas permeability.

The sealing gasket can be in contact with different components in the fuel cell stack due its importance of existence. The compatibility of the materials between among each other is crucial. This can lead to a chemical degradation in the seal materials due to the chemical nature and the reactions of the membrane, catalysts and GDLs. Also, making sure that the materials used for the sealing gaskets don't interfere with the catalyst, which can lead to side reactions. Therefore, choosing the right elastomer material for a sealing gasket is vital to the overall performance and other safety issues [121], [124]. The

interference between the sealing gasket and the GDL and its effect on the gas permeability due to compression is studied in Ch6

3.5.2.4 Resistivity

There are different types of resistances that a sealing gasket requires to survive the inside cell environment. Moisture resistance for sealing gasket materials is important due the nature of the vapour water by-product and the high relative humidity for the membrane conductivity. Super hydrophobic gaskets are favourable, in order to lower the degradation process and avoiding any adsorption of excess water [26], [125].The assembly of the fuel cell stack requires essential components that assist in a better performance. Sealing gaskets used in PEM fuel cells have different types and designs in which they can improve the conductivity and resistance between various elements. As well as, different sealing gaskets parameters can affect other components in the cell. Some of the important parameters are the type of the material used, and the thickness of the sealing gasket [120][126].

3.5.2.5 Sealing gasket materials

Suitable gasket design requires materials that withstand the different and rapid changes that occur inside the cell, i.e. temperature change, humidity, and swelling/contraction of the membrane. As mentioned earlier that the sealing gaskets can assist in decreasing the internal resistance of the different components. Elastomer materials are used widely for sealing gaskets purposes in fuel cells due to their flexibility and durability. However, different types of gasket materials can act differently under applied compressive loads during

assembly and temperature change, i.e. expansion and contraction of the membrane. Recently, there has been a focus on the development of appropriate gasket designs and solutions to prevent leakage and overcome compressibility effects. The main property of elastomer materials is that they have a mechanical resistance under compression. They can return to their thickness and shape due to their viscoelastic property. Typically, compounds that contains elastomers are produced to form sealing materials for PEM fuel cells gaskets. Crosslinks and fillers of elastomer materials and other types of compounds forming these polymer chains to create better sealing gaskets. Additionally, assist in adding more durability to the sealing materials during curing. Chemical degradation analysis of different gasket materials has been tested in different environments that is shown in Chapter 6. Due to its viscoelastic properties, the difference between the loading/unloading is negligible compared to GDLs. Therefore, testing different types of gaskets with different uncoated and MPL-coated GDLs in order to investigate the effect of the compression on mass transport properties.

4 METHODOLOGY

4.1 Introduction

This chapter covers the materials and methods that are implemented in this thesis. The study focuses on the structural analysis and the techniques used on the GDL samples under a combined mode of compression that was stated in previous chapters. For a better insight into the GDL behaviour, measurements of various tests, including: (i) universal testing machine, (ii) scanning electron microscopy, (iii) contact angle measurements for wettability measurements, (iv) through plane permeability are obtained before and after compression, and (v) thermal stability analysis (TGA) before and after compression with/without different types of gaskets. This will assist modellers to have more precise data on the structural aspect, gas permeability, and thicknesses of the GDL before and after a steady state and cyclic compression. Preliminary investigation was studied with the collaboration of I^2CNER in Japan to study MIP, electrical resistance, thermal stability, and the catalyst layer is shown in the appendix.

4.2 Gas diffusion layer samples

For the purpose of this study, a set of five different samples will be experimentally measured to determine their physical properties with a range of techniques. The GDL samples will be three different uncoated GDLs from different commercial companies. However, the second set of samples will be the same samples with MPL-coated GDL. All these samples will be subjected to a compression stress in the range 0-3 MPa. The sample size will be 1 inch

diameter. Also, the GDL samples used in the experiments were provided from two commercial GDL manufacturers namely Toray International UK Ltd, and SGL Technologies GmbH, Meitingen, Germany. All thicknesses were measured at four different locations of the GDL sample using a micrometre before and after compression as shown in Figure 4.1. All measurements were averaged with a 95% confidence interval.

Figure 4.1 Micrometre used to measure the thickness of the GDL samples before and after compression.

4.3 Mechanical characterisation

4.3.1 Compression test

In order to determine the behaviour of a material under different loads, a compression test provides a good understanding of the mechanical properties and materials strength. There are different machines and apparatus that have been used for GDL compression as mentioned in Chapter 3. In this thesis, a universal testing machine is used to conduct the compressibility testing on

different GDL samples. The compression test comprises of two modes of compression namely, steady state compression and cyclic compression.

4.3.2 Universal testing machine apparatus

Universal testing machines are widely used in the mechanical characterization of materials including tensile, compressive and a fatigue testing. A Shimadzu EZ-LX is used to perform a compression test on the GDL samples. Figure 4.2 shows the setup of the universal testing machine (Shimadzu-EZ-LX).

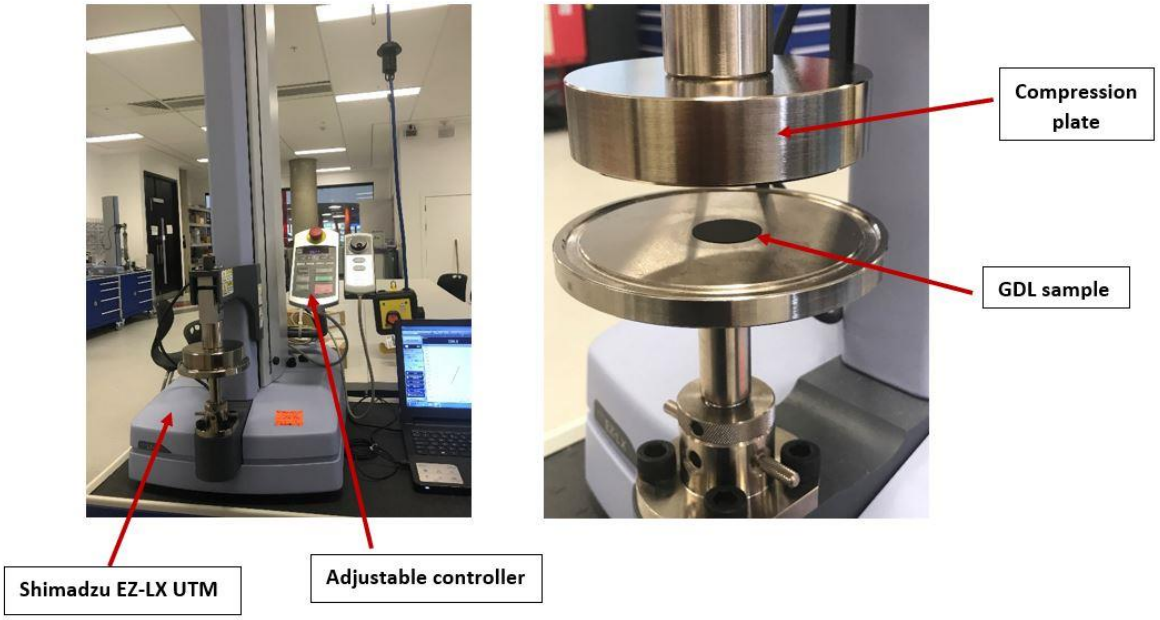

Figure 4.2 Shimadzu EZ-LX universal testing machine setup and the compression plate with the tested GDL sample.

4.3.3 Test conditions

The compression test used on the GDL samples was by applying two types of compression, namely steady-state compression due to the clamping forces during assembly, and a cyclic compression for ten cycles due to the hydration cycle in the membrane and the hygrothermal effect during the start-

up/shutdown process of the fuel cell operation. Figure 4.3 shows the applied force as a function of time for all GDL samples in order to realistically measure the impact of all types of compression acting on the GDL surface simultaneously. It should be noted that this frequency of cycling (i.e. 10 cycles) has been selected as no further deformation is expected to happen to the GDL materials after the 9^{th} or the 10^{th} cycle (see Figure 5.3). This is corroborated by similar investigations in which a good number of cyclic compression was implemented to ensure saturation in deformation; see for example [111], [127]. The conditions of the compression test in the universal testing machine, in terms of sample size and applied load, are presented in Table 4.1.

Table 4.1 The testing conditions of the GDL samples and the machine universal testing machine setup.

GDL sample size	Steady-state compression	Cyclic compression
1 inch diameter (25.4 mm)	Force: 0-506.71 N Stress: 0-1 MPa	Force: 506.71-1520.13 N Stress: 1-3 MPa

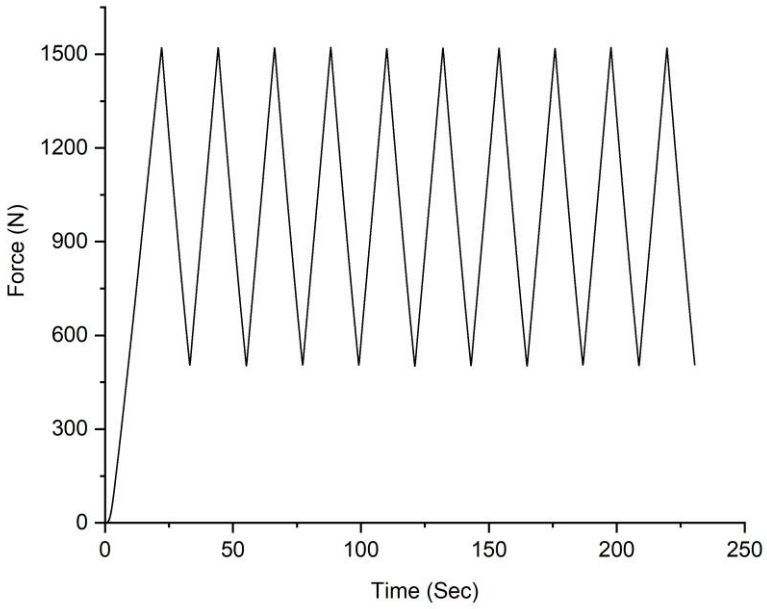

Figure 4.3 The applied load as a function of the time of the compression stress test on all the GDL samples.

4.3.4 Machine compliance

Using universal testing machines for testing the strength, tensile, compression, and fatigue of any material is vital for the physical properties and the lifetime of such a material. The data produced for the tested materials using a universal testing machine give important properties of the materials. However, using universal testing machines for characterising thin materials, which in our case are the gas diffusion layer materials, is not straightforward. These thin materials can interfere with the compression plates during the test, which requires a machine compliance for measurement accuracy. Typically, a machine compliance is obtained by conducting a compression test without any material to measure the machine stress-strain curve. This compression test

enhances the measurements by subtracting the slope of the stress-strain of the machine from the measured stress-strain curve of the tested materials.

4.4 Through plane permeability

4.4.1 Main setup and procedure

The gas permeability is often obtained by experimentally investigating how well the GDL is capable of permitting reactants through its pores in order to efficiently reach the CL. Therefore, as mentioned in Section 3.3.3, the through-plane permeability can give a clear indication of the gas transport properties from the flow channels through the GDL pores. Generally, high gas transportation in the through-plane direction leads to a better operation of the fuel cell, in which more reactants can be permitted to flow through the pores via the diffusion effect [29], [108]. However, there are some factors that lead to the degradation of the gas permeability through the GDL, i.e. decrease the flow of fluids through the pores of the GDL. The main factor that leads to this degradation is the compression effect on the GDL during operation due to the hygrothermal effects. Therefore, it is crucial to investigate the changes in the through plane permeability before and after a cyclic compression. In order to measure the gas permeability of the GDL samples, an in-house permeability test setup was used. Figure 4.4 shows the main components of the through-plane permeability setup.

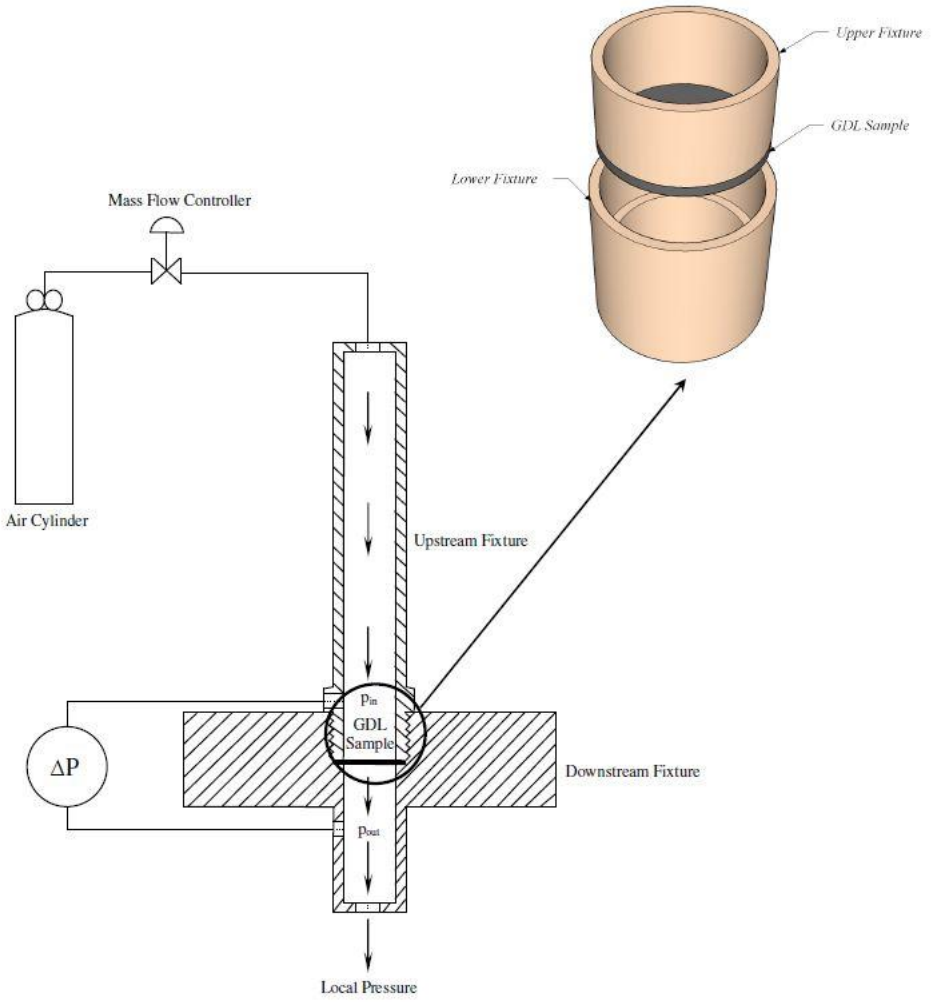

Figure 4.4 A schematic of the through-plane permeability experimental setup [128].

In general, the experimental setup is comprised of two main fixtures namely; the upstream and downstream fixtures. The GDL samples are placed and tightened in between the upper and lower fixtures. A differential pressure sensor is employed to measure the pressure drop whilst the air flows through the GDL sample at constant rate. For this setup, the samples used are circular in shape with a diameter of 25.4mm (1 inch), however the active area of the

sample is 20 mm due to the placement of the sample between the two fixtures as shown in Figures 4.5(a) and 4.5(b).

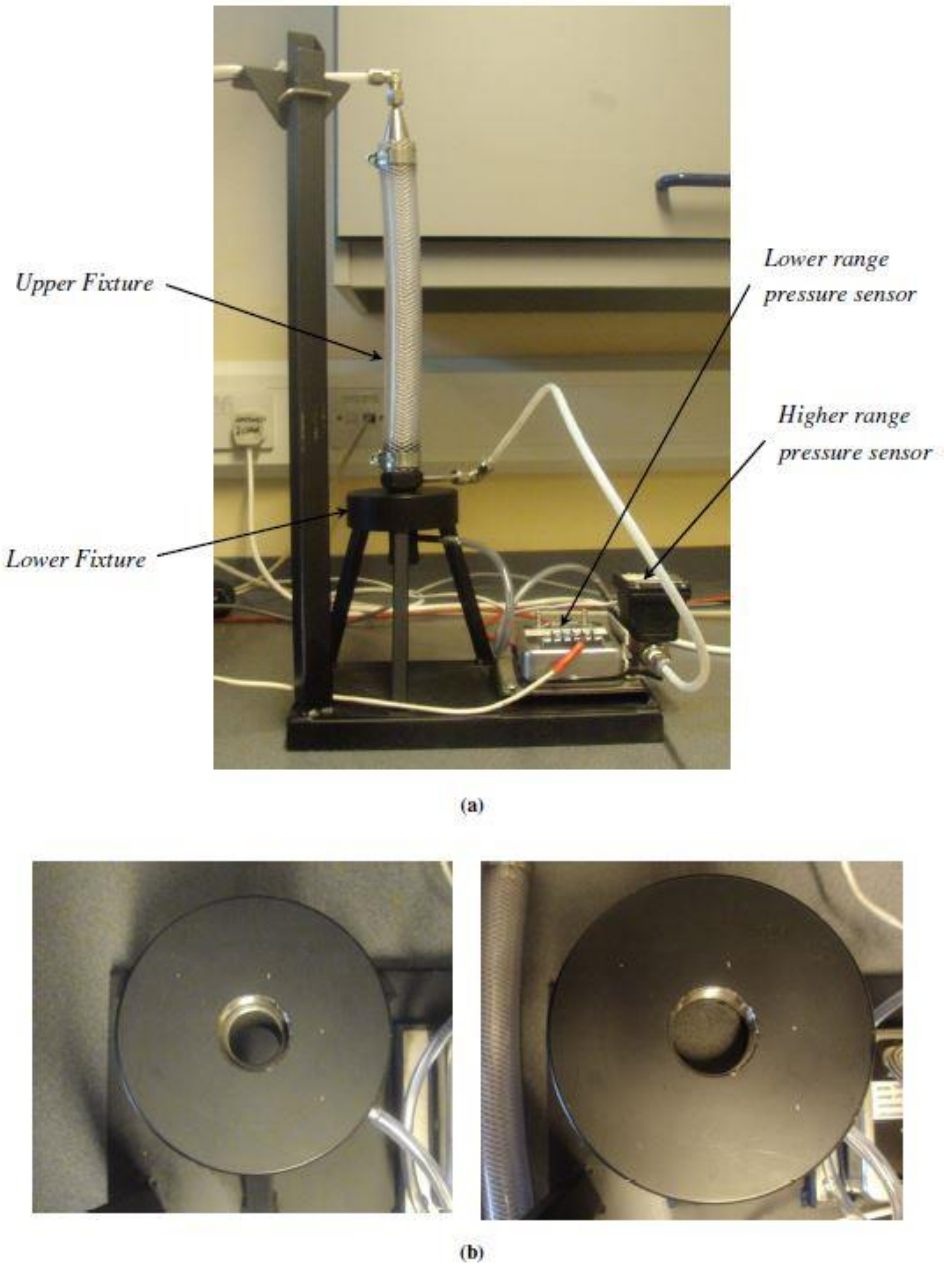

Figure 4.5 (a) The main components of the experimental setup of the through-plane permeability, and (b) the upstream and downstream fixtures [128].

4.4.2 Data analysis

Using a relatively low gas velocity for the porous material leads to the most drop in pressure caused by the viscous resistance of the fluid flow. Therefore, Darcy's law can express this flow through the porous materials as follows [128]:

$$-\nabla p = \frac{\mu}{k} u \tag{4.1}$$

where p is the pressure, k is the permeability of the GDL sample, μ is the dynamic viscosity of nitrogen, and u is the velocity of nitrogen. However, it should be noted that some additional terms have to be added to the equation (4.1) when higher velocities are used, and this additional term accounts for the inertial losses. This term is called the Forchheimer or the non-Darcy term, namely:

$$-\nabla p = \frac{\mu}{k} u + \beta \rho u^2 \tag{4.2}$$

where β is the inertial or the Forchheimer or the non-Darcy coefficient, and ρ is the density of the nitrogen. Therefore, by using Equation (4.1) the Darcy's law, the through-plane permeability can be obtained by solving for the other parameters. In order to solve for the velocity of nitrogen in Equation (4.1), the velocity can be expressed as follows:

$$u = \frac{\dot{m}}{\rho A} = \frac{m'}{\rho} \tag{4.3}$$

where $\dot{m}$ is the mass flow rate of nitrogen, m' is the mass flux of nitrogen, and A is the active area of the GDL sample placed between the fixtures. Also, since

nitrogen is compressible, thus its density can easily be calculated by using the ideal gas law:

$$\rho = \frac{pM}{\overline{R}T} \tag{4.4}$$

where M is the molecular weight of nitrogen, $\overline{R}$ is the universal gas constant (8.314 J.K.mol^{-1}), and T is the absolute temperature in Kelvin. By substituting Equation (4.4) into Equation (4.3) yields:

$$u = \frac{\overline{R}\,Tm'}{pM} \tag{4.5}$$

Now, by substituting Equation (4.5) into Equation (4.3), with the assumption of one- dimensional and low flow, yields:

$$-\frac{dp}{dx} = \frac{\mu \overline{R} T m'}{KpM} \tag{4.6}$$

By using the separation of variables and integrating both sides of Equation (4.6) from the inlet pressure P_{in}, to the outlet pressure P_{out}, across the thickness of the GDL sample L, yields:

$$P_{in}^2 - P_{out}^2 = \frac{\mu}{K}\frac{2\overline{R}TL}{M}m' \tag{4.7}$$

Typically, before conducting the permeability test, a thickness measurement of the GDL sample is taken using a micrometer with a resolution of 1 μm. As mentioned in Equation (4.2) about the non Darcy's law or the (Forchheimer equation), when using higher velocity of nitrogen gas, it is important to

consider the inertial effect in which it can significantly affect the calculations, thus this yields:

$$P_{in}^2 - P_{out}^2 = \frac{\mu}{K}\frac{2\overline{R}TL}{M}m' + \beta\frac{2\overline{R}TL}{M}(m')^2 \tag{4.8}$$

Generally, Equation (4.7) is used to calculate the through-plane permeability when the relationship of the pressure gradient of the flow rate as a function of velocity is linear. Afterwards, the GDL samples are averaged with 95% confidence interval of the mean value.

4.4.3 Effect of Forchheimer term for gas permeability measurements

Using Darcy's law to calculate for the gas permeability of a fluid through a porous medium has its own limitation. In order to assure the validity of the proposed law, the flow of the nitrogen gas has to be sufficiently low (Reynold's number <10). Therefore, assuming the validation of the negligible inertial coefficients, a scaling analysis of the non-darcy's term is investigated. From equation (4.2), one can separate the Darcy's and non-Darcy's term in the following equations:

$$\text{Darcy term} = \frac{\mu}{k}u \tag{4.9}$$

$$\text{Non-Darcy term} = \beta\rho u^2 \tag{4.10}$$

In order to non-dimensionlise the following terms: velocity (u), and the density of nitrogen (ρ) in which they become:

$$u = u_{\circ} u' \tag{4.11}$$

$$\rho = \rho_{\circ} \rho' \tag{4.12}$$

Substituting the non-dimensionless terms in Eq(4.11) Eq (4.12) into Eq (4.9) , and Eq(4.10):

$$\text{Darcy term} = \left(\frac{\mu}{k} u_{\circ}\right) u' \tag{4.13}$$

$$\text{Non-Darcy term} = (\beta \rho_{\circ} u_{\circ}^2) \rho' (u')^2 \tag{4.14}$$

Where $u_{\circ}$ is taken to be the average inlet velocity, or reference velocity, and $\rho_{\circ}$ is the reference density, and v and ρ are the nondimensionalised velocity and density, respectively.

Now, one can calculate the sensitivity of each term by estimating the relative error associated to the non-dimensionlised terms. Assuming that the effect of inertial terms is more significant at the higher velocities and flowrates. In the case of our permeability setup, the maximum flowrate, for instance, for Toray-90-H, is 0.06 L/min. Density of Nitrogen gas (the flowing gas) at atmospheric pressure (1 atm) and room temperature (298 K) is $\rho_{\circ}$ [1.17 Kg/m^3]. The viscosity of Nitrogen at the same conditions of atmospheric pressure and room temperature is 1.80 × 10^{-5} Pa s. The permeability of Toray-H-90 was experimentally calculated to be

6.62×10^{-12} m^2. Now one can calculate β, which is the inertial coefficients using the following relationship:

$$\beta = 2.88 \times 10^{-6} \frac{\tau}{\varepsilon K} \tag{4.15}$$

The tortuosity τ, and the porosity ε, can be calculated using the following equations:

$$\tau = \frac{1}{\varepsilon^{0.5}} \tag{4.16}$$

$$\varepsilon = 1 - \frac{areal\ weight\ (\frac{g}{m^2})}{GDL\ thickness\ (\mu m) \times 1.8\ (\frac{g}{cm^3})} \tag{4.17}$$

Therefore, for the case of Toray-H-90, the porosity, thickness, and the areal weight is given by the manufacturer. Now, one can easily substitute the values into the equations 4.13 and 4.14 and to ensure the validity of Darcy's law. Continuing the example of Toray-H-90, the results for the Darcy and non-Darcy terms are $5.1 \times 10^3\ v'$ and $2.5\ \rho'(v')^2$, respectively. Therefore, the sensitivity analysis of ignoring the non-Darcy terms is 0.05%, which is very minimal to be accounted for in the calculation of the gas permeability for the specified velocities and flowrates. Table 4.2 shows all the GDL samples and the maximum error % of ignoring the non-darcy terms.

Table 4.2 The error due to neglecting the non-darcy term based on the maximum flowrate for the calculation of GDLs gas permeability

GDL type	Maximum error (%)
Toray-90-H	0.05
SGL-24-BA	0.04
SGL-10-BA	0.04
SGL-34-BA	0.05
SGL-34-BC	0.01
SGL-35-BC	0.01
SGL-39-BA	0.04
SGL-39-BC	0.05

4.5 Scanning electron microscope

The morphology and structure of the gas diffusion layer samples were investigated using a scanning electron microscopy (SEM) unit by JEOL model (JBM-BO10LA) shown in Figure 4.6.

Figure 4.6 Photograph of the scanning electron microscope facility used in the morphological investigation of the gas diffusion layer.

4.6 Mercury intrusion porosimetry

Generally, mercury intrusion porosimetry (MIP) is used to determine the pore size distribution (PSD), connectivity and porosity for porous materials. Some of the characteristics of the microstructure of the GDL can be determined using a mercury intrusion porosimetry method. It has been mainly used for characterising the physical properties of cement-based materials. Due the structure of the GDL surface and pores, which has irregular pores geometry, this method has its limitation. Therefore, different assumptions have to be considered when applying this method, especially for irregular pore geometries [129], [130]. Consequently, the results obtained by applying the mercury intrusion method on the GDL structure will not be accurate due to the structure. However, it can give a clear insight about the microstructure of

porous materials, especially pore size distribution, porosity percentage, and the permeability. The MIP method is still used for a wide range of porous materials especially for cement and GDLs.

4.6.1 Main setup and procedure

Mercury intrusion porosimetry (MIP) is one the most powerful techniques that gives an insight into the characteristics of the surface of porous materials. Generally, the main concept behind the MIP technique is to use a non-wetting fluid which has a contact angle greater than 90°. In this case, this fluid cannot penetrate the surface of the tested material unless an external pressure is applied. Typically, mercury is used to penetrate the porous structure by applying a capillary pressure in order to force it through the pores. The structure of the GDL can be affected due to the compression applied during the fuel cell assembly and operation. To gain a better insight into the structural changes, the MIP technique can provide a wide range of characteristics on the compressed GDL samples. In order to conduct a mercury intrusion test, the GDL samples have to be cut into small shaped pieces and placed into the glass bulb penetrometer. The process starts by evacuating the cell. Then, filling the cell with mercury by increasing the pressure of mercury steadily, in which the large pore volume fills first at low pressure and smaller pore volume fills at higher pressure.

4.7 Drop shape instrumentation

4.7.1 Main setup and procedure

Surface wettability is an important physical property of the diffusion layer surface. Contact angle droplets on the GDL surface provide an indication of the hydrophobicity and hydrophilicity of the tested surface. In other words, hydrophobicity and hydrophilicity is an indication of the ability of the surface to repel or absorb the required amount of water. Typically, water management during the PEM fuel cell operation is a vital concern in terms of maintaining sufficient water content in the MEA without any flooding or blockage. In order to measure the water contact angle of the GDL surface, a video drop shape system FTA200 goniometer is used, provided by First Ten Angstroms, Inc. Portsmouth, Virginia. Figure 4.7 shows the main setup of the FTA200 goniometer.

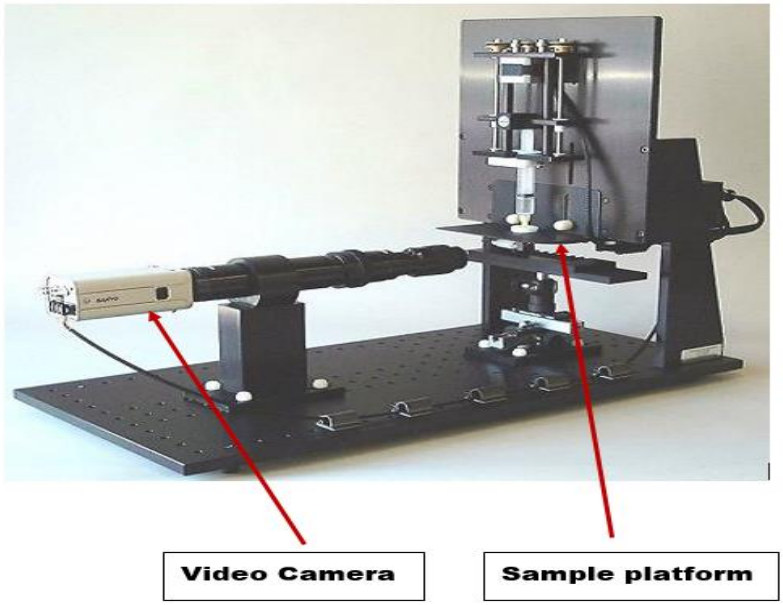

Figure 4.7 Photograph of the drop shape machine for measuring the contact angle of the GDL samples.

4.8 Thermogravimetric Analysis (TGA)

Fig 4.8 shows Pyris 1 TGA Thermogravimetric Analyzer (PerkinElmer, USA). It was used at a heating rate of 10 °C/min and under a nitrogen flow rate of 20 ml/min. This step was conducted to ensure that oxidation of the tested samples does not take place. The samples were initially exposed to nitrogen flow for 15 minutes at a temperature of 30 °C. The TGA analysis is then performed as the sample is heated from 30°C to 900°C at the above-mentioned rate (i.e., 10 °C/min).

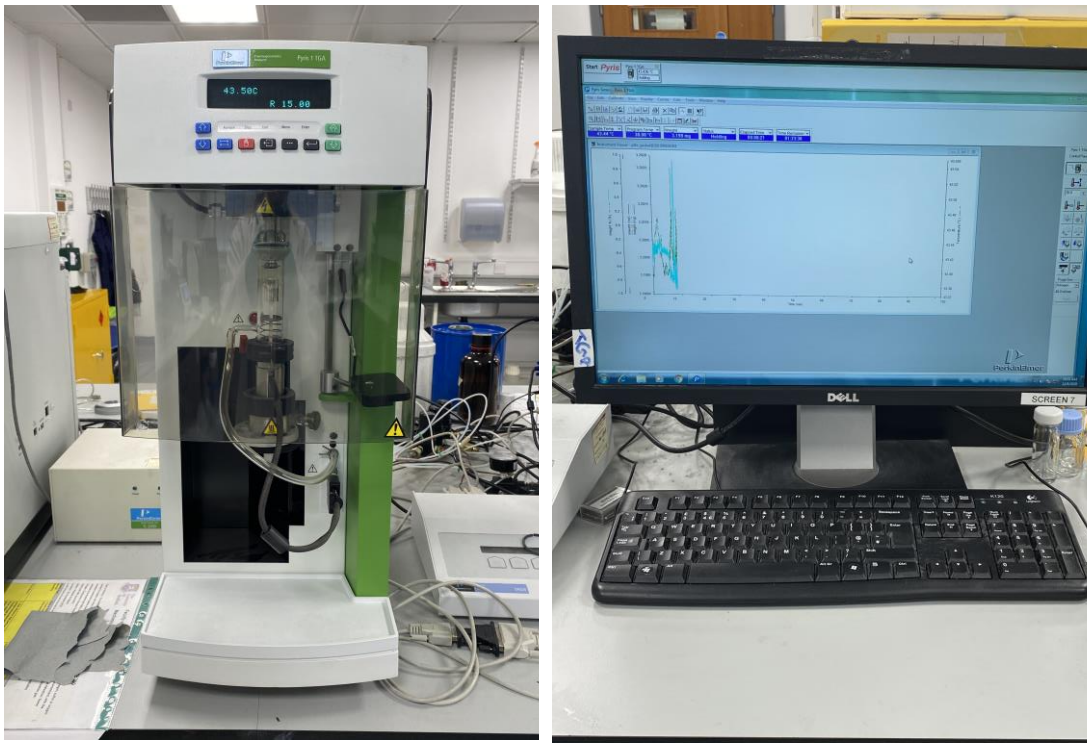

Figure 4.8 Pyris 1 TGA Thermogravimetric Analyzer, and the instrument manging software.

5 EFFECTS OF COMPRESSION ON GDLS

5.1 Introduction

Proton exchange membrane (PEM) fuel cells (or Polymer Electrolyte Fuel Cells (PEFCs)) are energy converters that directly convert chemical energy stored in hydrogen fuel into electrical energy. In the last two decades, PEM fuel cell technology has gained a good deal of attention and this is primarily due to its high efficiency, low operating temperature, and consequent rapid start-up [131]–[134]. Gas diffusion layers, placed between the flow field plates and the catalyst layers, are key components in PEM fuel cells; they enhance the uniformity of the distribution of the reacting gases over the catalyst layer and assist in removing excess liquid water [135], [136]. Typically, GDLs are made of either woven carbon or non-woven carbon fibers. Each type of GDL has its own characteristics and limits with regards to the porosity, diffusivity, mechanical properties and gas permeability.

The lifetime and the durability of the GDL is an important aspect that affects the overall performance of the PEM fuel cell and is closely correlated to the properties of its main components [57]. Generally, there are two types of degradation that significantly deteriorate the functions of the GDL and in turn the performance of the PEM fuel cell namely, chemical degradation and mechanical degradation. Briefly, the chemical degradation is attributed to the corrosion and erosion of the carbon loading, as well as the wetting characteristics of the polytetrafluoroethylene (PTFE) available in the GDL. On the other hand, the mechanical degradation is attributed to two main sources,

namely; (i) the compression while assembling the fuel cell, and (ii) the cyclic compression due to the hygrothermal effects [72]. Much research has been conducted on the compression effects on the overall performance of PEM fuel cells [137]–[140], and the electrical contact resistance between various fuel cell components [111], [141]–[144]. For instance, Escribano et al. [86] conducted an experimental investigation to evaluate the compressibility of different types of GDL samples using a universal testing machine (INSTRON 4450). They used a stack of 10 GDL samples in order to minimise the error associated with the measurement of the GDL thickness during compression. However, using a stack of multiple GDL samples can lead to inaccuracy in determining the actual thickness of each GDL sample after compression.

The clamping force used to assemble the fuel cell significantly affects its performance and it needs to be optimized to ensure (i) good electrical contact between the various components of the fuel cell and (ii) adequate supply of reacting gases to the catalyst layer. Xing et al. [98] conducted a numerical study to determine the optimum clamping pressure value under different operating voltages. They found that a range of 1.0-1.5 MPa of clamping pressure is optimum as it results in reasonably low contact resistance and an adequate supply of reactants to the catalyst layer. This is in line with the recommendation of the US Department of Energy (DoE) that the compression on the fuel cell be 1.4 MPa [94], [145]. There has been a number of studies that have investigated the effects of the mechanical compression on the dynamics of liquid water and, consequently, on the fuel cell performance. Kulkarni et al. [146] studied how two different compression ratios, namely 25 and 35%, affect

the dynamics of liquid water and, subsequently, fuel cell performance. Their results showed that the increase in the compression ratio from 25 to 35% results in higher mass transport resistance, leading to lower fuel cell performance. Similarly, Wu et al. [147], using in-operando neutron radiology, conducted a study to investigate the effect of 3 different compression ratios on the transport and distribution of liquid water. The results showed that relatively high compression ratios could cause serious limitations in mass transfer and this is due to the increased water accumulation. Therefore, it was recommended to use an optimum assembly compression which ensure gas-tightness, reasonably low contact and mass transport resistances.

However, at low fuel cell voltages, the rate of chemical reactions is higher and therefore higher amounts of reactants are required. In this case, the clamping pressure needs to be relatively low (e.g. 0.8 MPa) to allow more reactant gases to reach the reactive areas in the catalyst layer especially under the areas beneath the ribs of the flow-field plates [98]. Notably, only a few studies have investigated the effects of cyclic compression, arising as a result of the hygrothermal effects, on the GDL material. For instance, Gigos et al. [115] experimentally and numerically investigated the effects of cyclic compression in the range of 0-12 MPa on 3 different types of GDL materials. They found that the deformation is irreversible after the first loading.

Radhakirshnan and Haridoss [127] conducted an experiment to analyse the impact of cyclic compression on the GDL material at two different ranges: 0-1.7 MPa and 0-3.4 MPa. The GDL material used in their study was Toray paper

(TGP-H-120), and it was compressed using a pair of aluminum end plates with two graphite plates between which the GDL is sandwiched. They found that, as a result of the applied cyclic compression, a permanent deformation in the GDL structure occurs. This change in the structure has a direct impact on other GDL properties: surface roughness, electrical resistance, GDL thickness and in-plane permeability. Mason et al. [111] similarly conducted a study on the effect of cyclic compression on a Toray GDL material using a commercial compression-controlled unit cell. They studied the effects of cyclic compression on the thickness and the electrical resistance of the GDL materials. It was found that the deformation of the tested GDL becomes permanent after 10 cycles. The compression, either steady-state or cyclic, affects the microstructure and, consequently the transport properties of the GDLs. One of the key mass transport properties of the GDL that are influenced by compression is the gas permeability which is important to be determined in order to estimate the contribution of the convective flow and the distribution of saturation within the GDL [148], [149]. Also, the wettability, normally represented by the surface contact angle of the GDL, is another important characteristic that is expected to be influenced by compression, and significantly affects the dynamics of liquid water on and within the surface of the GDL.

Gostick et al. [108] investigated the in-plane and through-plane permeability of several GDL materials. The in-plane permeability was measured under different compression ratios. They found that by compressing the GDL sample to half of its initial thickness, the permeability is reduced by an order of

magnitude. El-kharouf et al. [150] investigated the in-plane and through-plane permeability under different steady-state compressions using a Mercury Intrusion Porosimetry (MIP). They investigated woven and non-woven GDL materials, and found that the high fibre density of GDLs tends to lower the permeability. Also, there are a number of experimental investigations on the effect of the PTFE loading, carbon loading, microporous layer (MPL) coating and sintering on the permeability of several GDL materials [148], [149], [151]–[155]. For example, for a given PTFE loading, the permeability was found to decrease with increasing carbon loading and this is mainly due to the increase in the thickness of the MPL [154]. Fuel cell performance wise, the benefit of the MPL becomes apparent in the intermediate current density region, i.e. the ohmic loss controlled region, since the conformability of this layer minimises the contact resistance between the GDL and the catalyst layer. Such a benefit outweighs the negative effects associated with the concentration loss controlled region, i.e. long diffusion paths and reduced mass transport properties [155].

Likewise, there have been similar investigations in the literature which attempt to correlate the wettability of the GDL to the contact resistance between the GDL and the bipolar plates [156], thermal characteristics of the GDL surface [53], PTFE loading [157][158], MPL composition [159][160] and GDL compression [127][158]. Radhakirshnan and Haridoss [127] measured the contact angle for TGP-H-120 GDL material before and after five cycles of compression. They found that the contact angle decreases after each cycle of compression and this was attributed to the loss of PTFE particles as a result of compression.

They also compared the wettability of GDLs after compression and after a 96-hour electrochemical aging. They found that the cyclic compression tends to affect the hydrophobicity of the sample more than the electrochemical aging. Kumar et al. [158] found that PTFE-treatment of the GDL material in stages reduces the hydrophobicity loss of the GDL after being subject to cyclic compression.

As demonstrated above, very few experimental works have been conducted to investigate the effect of compression on the gas permeability and the wettability of the GDL materials. Equally, previous compression tests appear to neglect the fact that the GDL inside the fuel cell is subjected to two types of compression: (i) assembling compression, arising as a result of the forces used to clamp and assemble the fuel cell components, and (ii) cyclic compression induced by the swelling (caused by the hydration) and shrinkage (caused by the dehydration) of the membrane electrolyte. The level of hydration/dehydration depends on how much water is produced at the cathode electrode and/or the moisture content of the oxidant and fuel gases. The compression on the GDL due to swelling of the membrane could be up to 2 MPa [161]. Therefore, in this study, we experimentally investigate the through-plane permeability and the contact angle of the GDL materials, which are subjected to the above two types of compressions, in order to obtain more accurate and realistic values for the permeability and the contact angle. Subsequently, these values could be fed into the mathematical models of PEM fuel cells to obtain better model predictions of cell performance before and

after compression. To the best of the authors' knowledge, there are no similar studies in the open literature.

5.2 Methodology and Materials

This section explains the experimental methods employed to perform compression and through-plane permeability tests on the GDL materials. Five different commercial GDL materials have been used in this investigation; Table 5.1 shows their properties, as provided by the manufacturers, i.e. Toray International (UK), and SGL Technologies GmbH (Germany). The morphology and the gas permeability were investigated before and after performing the compression tests. In addition, scanning electron microscope (SEM) images obtained from a JEOL instrument (Model JBM-BO10LA) have been used to investigate the morphology. SEM cross-section images were obtained by cutting the samples in the middle and placing them vertically using a cross-sectional sample holder which enables the user to observe the top view of the edges of the samples, thus allowing for the determination of the thickness of the GDL.

Table 5.1 Manufacturers physical properties of the tested carbon paper substrates.

Manufacturer type	Initial Thickness[a] (μm)	PTFE Loading (%)	PTFE Loading of MPL (%)
Toray-H-90	282.5 ± 1.0	5	NA
SGL-24-BA	210 ± 3.1	5	NA
SGL-10-BA	397.5 ± 1.0	5	NA
SGL-34-BC	317.5 ± 2.4	5	25
SGL-35-BC	322.5 ± 1.0	5	25

(a) Thickness measurements are based on 95% confidence.

For the findings of the study to be as generic as possible, several factors were considered when selecting the GDL materials investigated in this study. Namely: (i) they are supplied from two different well-known suppliers (i.e. Toray and SGL Carbon Group), (ii) they are structurally different as their fibres are either randomly distributed (e.g. Toray-H-90) or felt-like (e.g. SGL 10 BA) and (iii) they are uncoated (e.g. SGL 10 BA) or MPL-coated (e.g. SGL 35BC). Further, the selected GDL materials are commonly used for lab-scale or large-scale industrial applications and this is due to their proven high performance and durability.

5.2.1 Compression test

A universal testing machine, Shimadzu EZ-LX, was used to perform the compression tests on the investigated GDL samples as described in Chapter 4. The machine was corrected for compliance as described in [109]; such a procedure ensures the mitigation of the inaccuracies associated with the estimation of the thickness of the samples undergoing the compression test. The compression test was designed in such a way that simulates an initial assembling compression of 1 MPa (0-1 MPa), followed by 10 cycles of loading and unloading in the range between 1 and 3 MPa, thus simulating the compression arising as a result of hydration/dehydration of the membrane electrolyte. This cyclic range (i.e. 1-3 MPa) covers the extreme cases of fully dry and fully hydrated membrane electrolytes. The conservative value of 3 MPa was selected in order to cover the highest possible compression the GDL material may be subjected to inside the fuel cell. The ambient temperature and relative humidity in the laboratory at the time that the compression tests were performed were about 20°C and 40%, respectively. As shown in Fig. 4.3 the applied load on the tested GDL samples is conducted as a function of time. The GDL samples are circular and the diameter of each is 25.4 mm. To conform to the size and shape of the sample holder of the gas permeability setup, the GDL samples were made circular with a diameter of 25.4 mm.

5.2.2 Through-plane gas permeability test

The in-house built setup described in Chapter 4.4 was used in this investigation. Typically, five different samples of each GDL material was measured before and after the steady-state and cyclic compression test. Nitrogen gas is forced to flow through the sample, and measurements were taken by obtaining the pressure drop across the GDL for at least 5 flowrates. A flow controller (HFC-202, Teledyne Hastings, UK) with a range of 0.0–0.1 SLPM is used to control the flowrate of the nitrogen gas. A differential pressure sensor (PX653, Omega, UK) with a range of ±12.5 Pa, was used to measure the pressure difference across the GDL sample.

The assumption of negligible inertial losses is valid due to the sufficiently low flow rates used. Therefore, Darcy's law could be used to calculate the gas permeability of the GDL samples, i.e.

$$\frac{\Delta P}{L} = \frac{\mu}{K} u \tag{5.1}$$

$$u = \frac{Q}{\pi D^2/4} \tag{5.2}$$

where ΔP is the pressure difference across the GDL sample, L is the measured thickness of the sample, μ is the dynamic viscosity of the flowing gas (i.e. nitrogen) which is about 1.8×10^5 Pa.s at 20 °C, K is the gas permeability of the

GDL sample, u is the velocity of the flowing gas, Q is the volumetric flow rate and D is the diameter of the GDL sample.

Fig 5.1 shows typical pressure gradients as a function of the velocity of the flowing gas for: (a) Toray-H-90 (uncoated), (b) SGL-24-BA (uncoated), (c) SGL-10-BA (uncoated), (d) SGL-34-BC (MPL-coated), and (e) SGL-35-BC (MPL-coated). As it can be seen from the figure 5.1, different ranges of gas flow rates were used for the presented GDL materials. The reason behind this is that the SGL GDL material (i.e. 34BC and 35BC) is MPL-coated and therefore it is much more resistive to the transport of the flowing gas compared to the uncoated GDL material of Toray-H-90. To this end, much lower flow rates must be used when testing SGL 34BC in order not to exceed the maximum limit of the pressure sensor which is as low as 12.5 Pa. The presented set of data are measured before and after the compression of 5 samples of each GDL material. The error bars represent the 95% confidence intervals. The data were linearly curve-fitted to obtain the slope of the curve, i.e. $\frac{\mu}{K}$, and subsequently calculate the gas permeability of the GDL material.

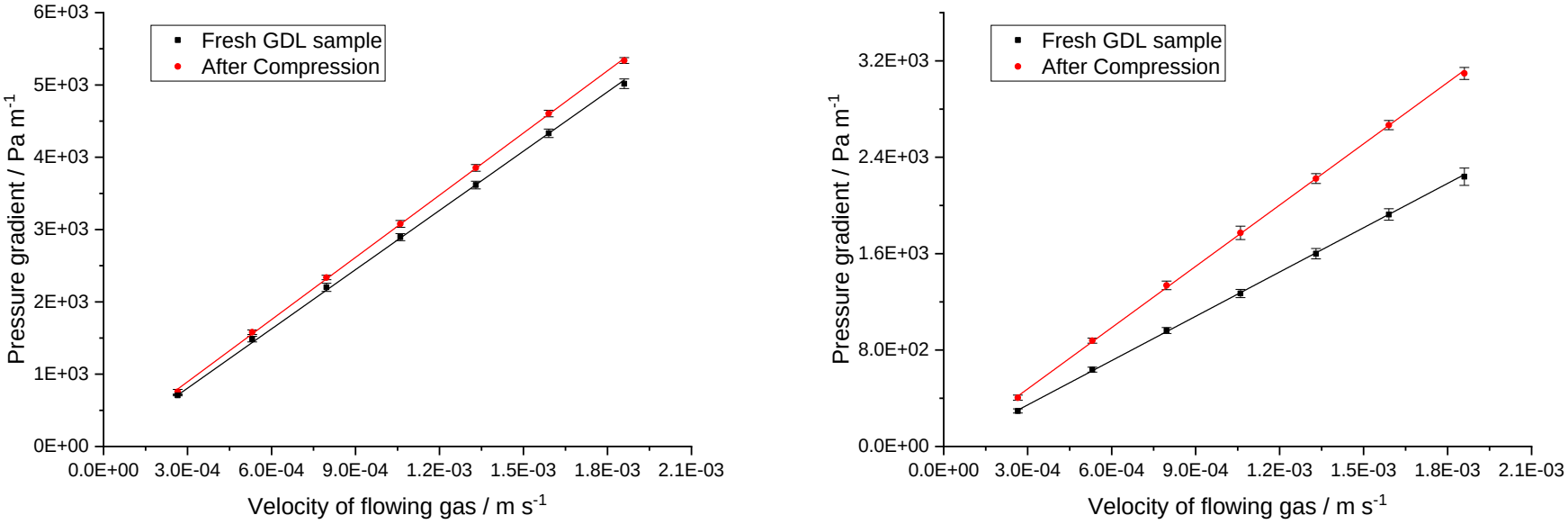

(a) (b)

Figure 5.1 The pressure gradient as a function of the flowing gas velocity for (a) Toray-H-90 and (b) SGL-24-BA before and after compression.

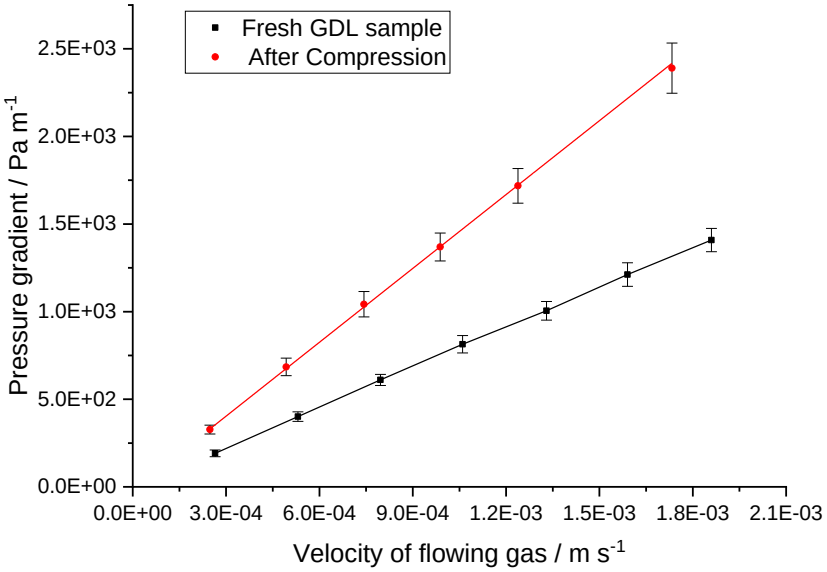

(c)

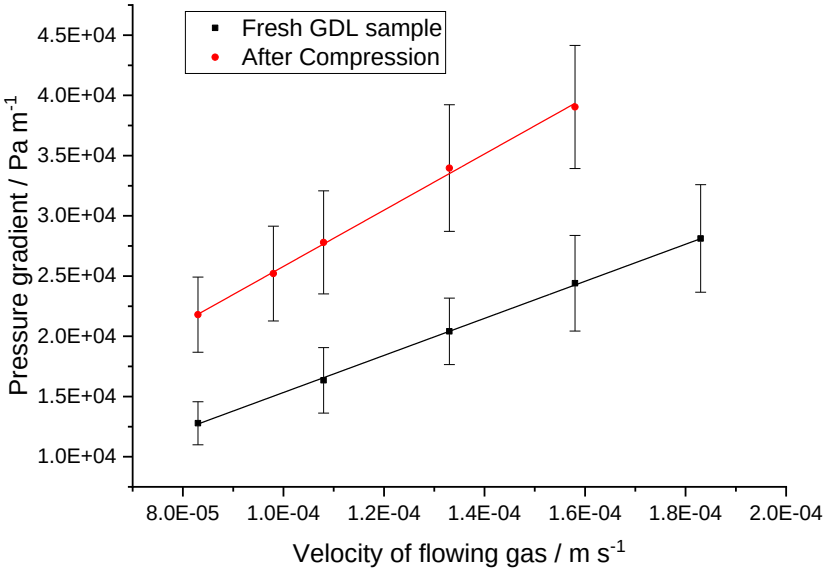

(d)

Figure 5.1 The pressure gradient as a function of the flowing gas velocity for (c) SGL-10-BA and (d) SGL-34-BC before and after compression.

(e)

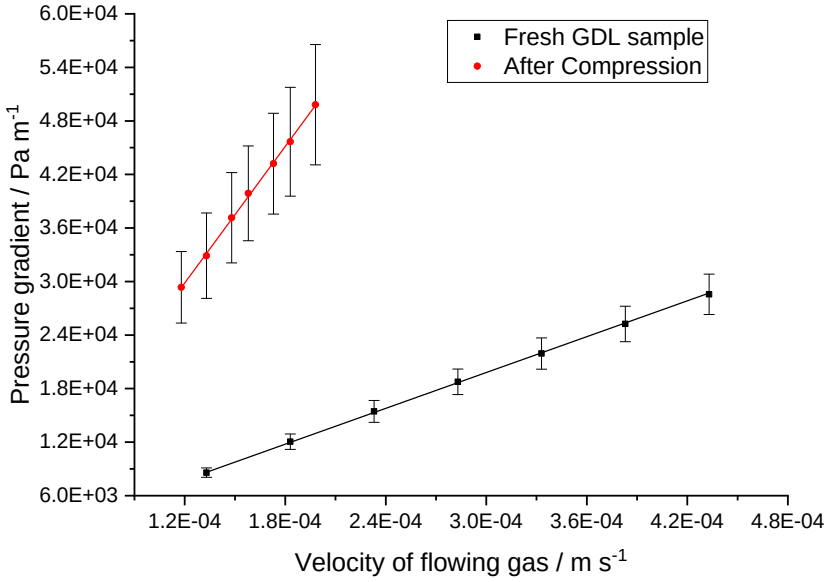

Figure 5.1 The pressure gradient as a function of the flowing gas velocity for (e) SGL-35-BC before and after compression.

5.3 Results and Discussion

5.3.1 Stress-strain curves

The mechanical characterization of the tested GDLs is presented in the form of stress-strain curves. Fig. 5.2 shows typical stress-strain curves of (a) Toray-H-90 (uncoated), (b) SGL-24-BA (uncoated), (c) SGL-10-BA (uncoated), (d) SGL-34-BC (MPL-coated), and (e) SGL-35-BC (MPL-coated) samples. All the stress-strain curves of the tested GDL samples demonstrate the same trend: hysteresis, i.e. the difference between the forward curve (loading) and backward curve (unloading), is significant for the first cycle and then becomes much less significant for the subsequent cycles. This implies that the very first compression caused by the assembly of the fuel cell is responsible for most of the deformation of the GDL. Subsequent cycles of the compression (or loading), due to the membrane hydration and non-compression (i.e. unloading) due to the membrane dry-out contributes much less to the GDL deformation. Although not clear from Fig. 5.2, the reduced thickness of the uncoated GDL materials (i.e. Toray-H-90, SGL-10-BA, SGL-24-BA) tend to saturate faster than those of the coated GDL materials (i.e. SGL-34-BC and SGL-35-BC). To elaborate further on this point, Fig. 5.3 was generated, and it shows the relative change in the strain from one cycle to another at 1.5 MPa for all the GDL sample materials. It could be inferred from the latter figure, for instance 5.3(d), and 5.3(e) that the MPL-coated GDL materials show slightly more mechanical resistance to deformation than the uncoated GDL materials. This is evidenced from the observation that the thickness of the uncoated

Toray-H-90 visually becomes saturated after the 8th cycle whereas the MPL-coated SGL-34 BC GDL appear to be visually saturated after the 9th cycle. This observation is in accordance with the idea that the addition of MPL to the GDL improves the mechanical resistance of the GDL [86], [109], [153], [162]. It could be seen from Figure 5.2 that there are no significant differences in strain between the 8th and the 9th cycles. As such, for such GDL materials, the number of cycles could be limited to 8 as the saturation in deformation is ensured.

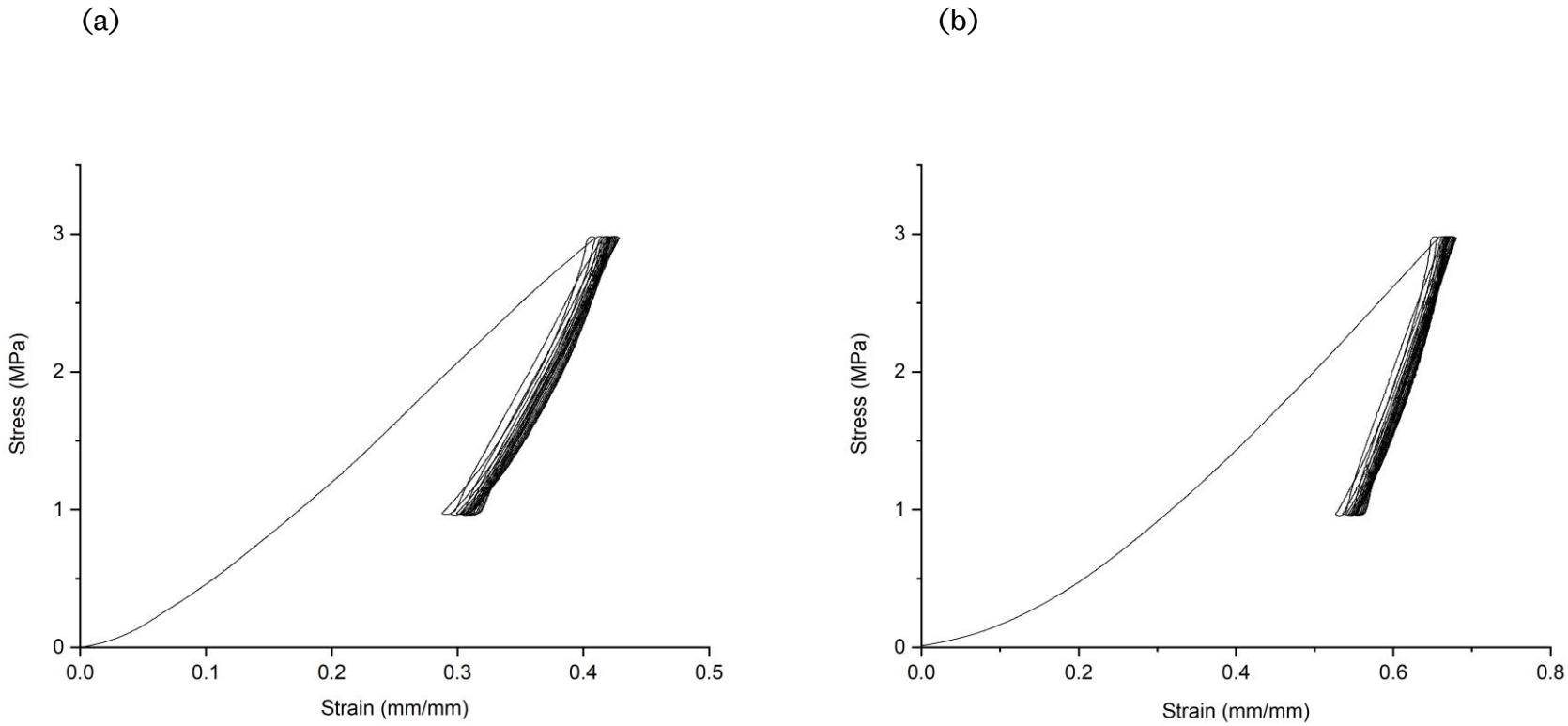

Figure 5.2 Typical stress-strain curves of (a) uncoated Toray-H-90 and (b) uncoated SGL-24-BA GDL samples during steady-state and cyclic compression for 10 cycles.

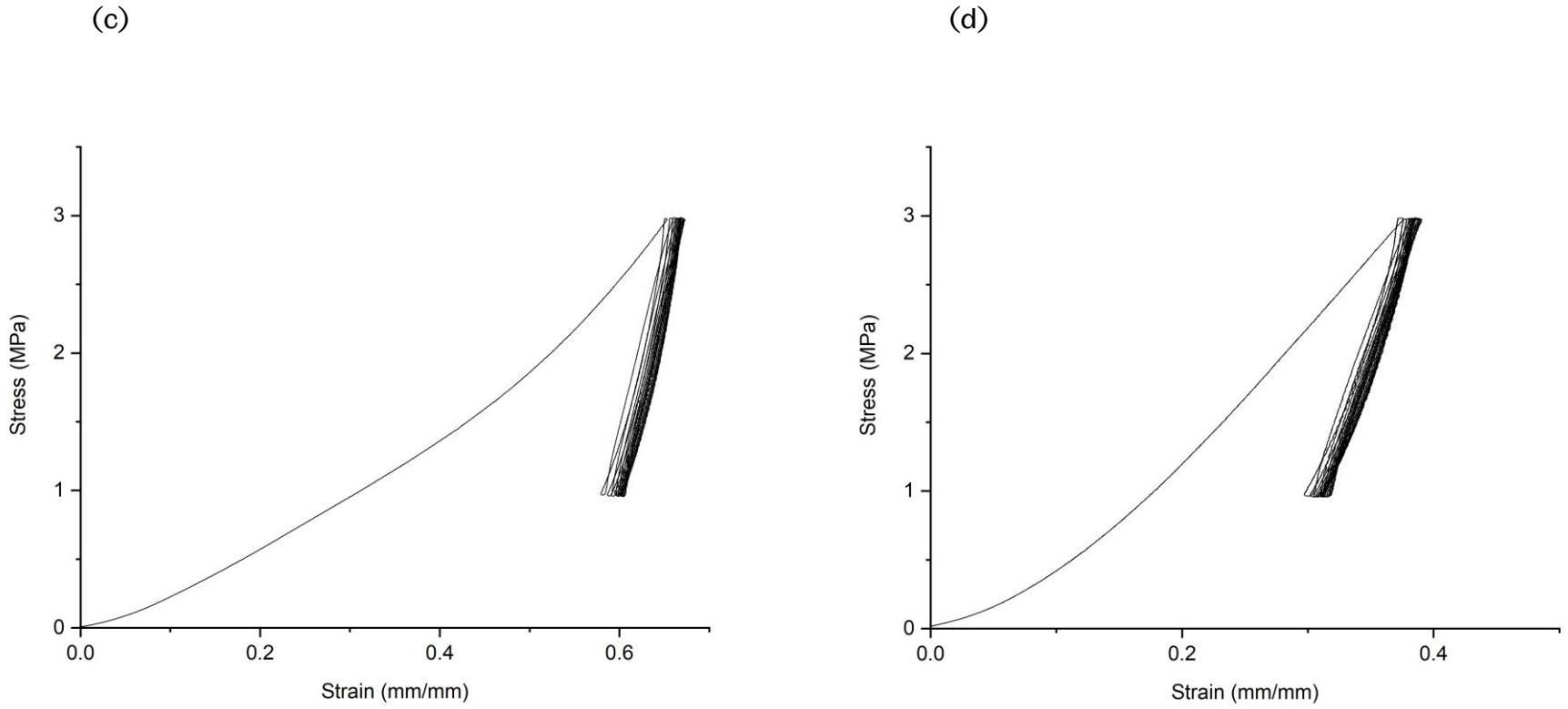

Figure 5.2 Typical stress-strain curves of (c) uncoated SGL-10-BA and (d) MPL-coated SGL-34-BC GDL samples during steady-state and cyclic compression for 10 cycles.

(e)

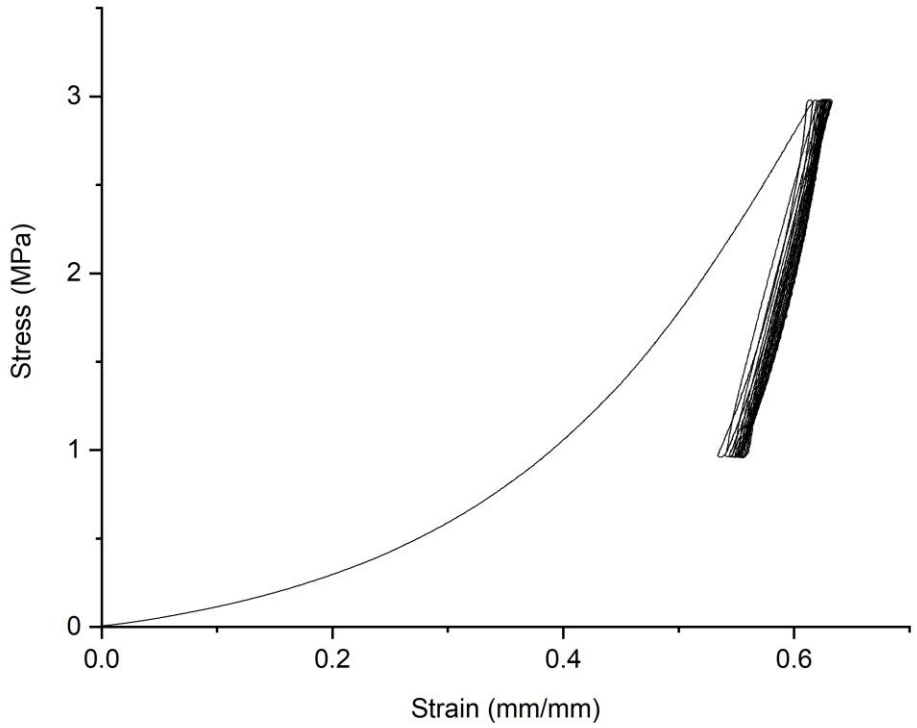

Figure 5.2 Typical stress-strain curves of (e) MPL-coated SGL-35-BC GDL samples during steady-state and cyclic compression for 10 cycles.

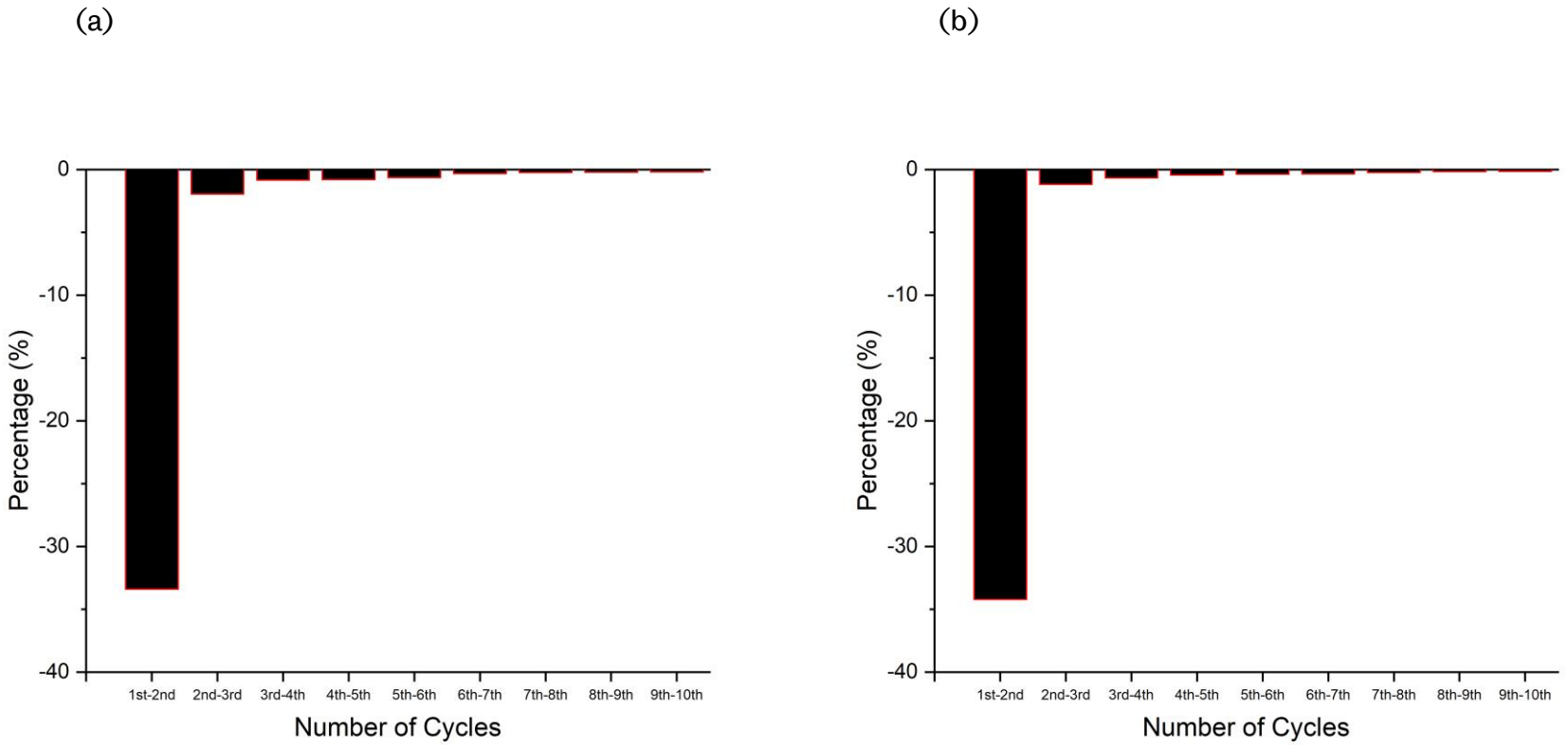

Figure 5.3 The percentage difference of the strain at 1.5 MPa for all the compression cycles of (a) Toray-H-90 and (b) SGL-24-BA.

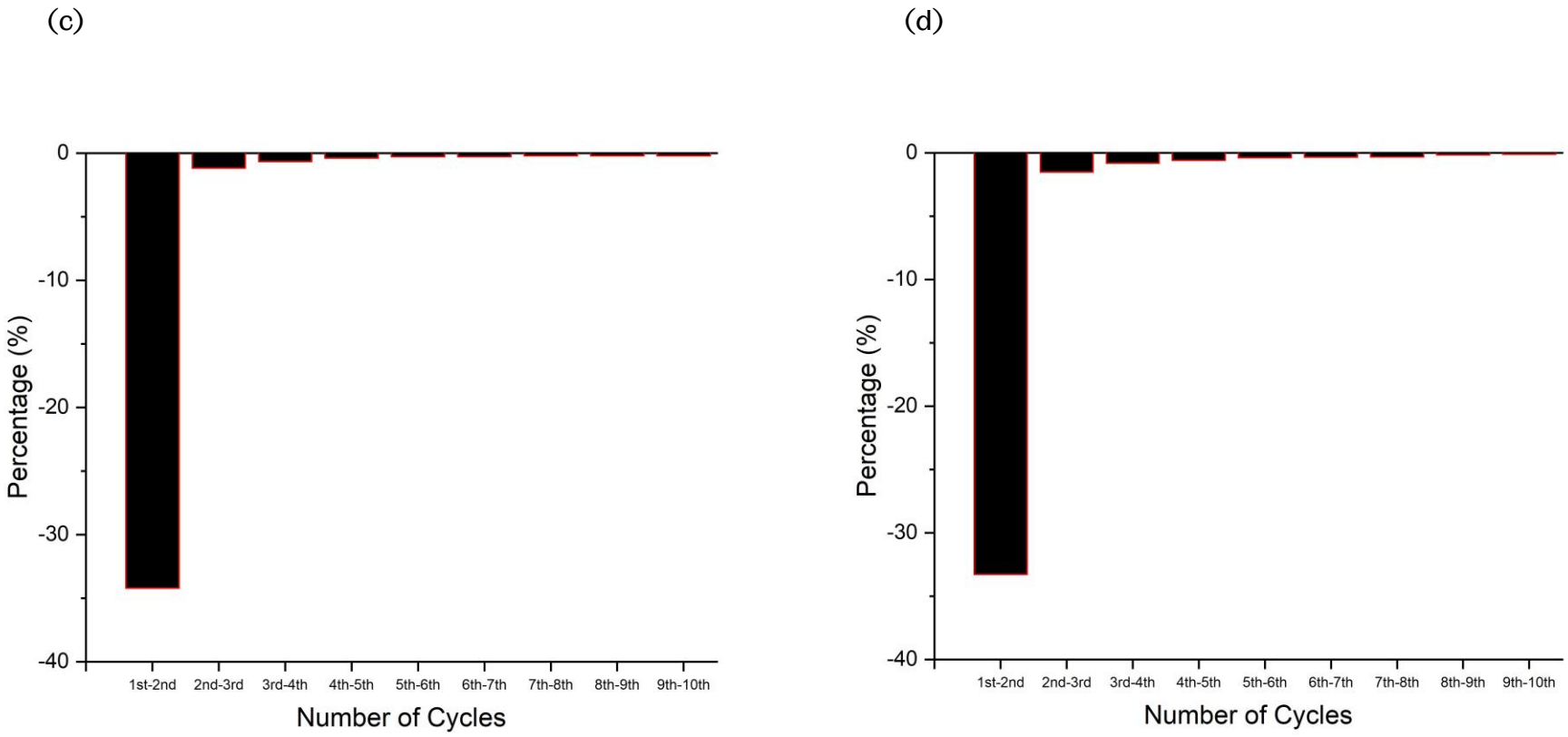

Figure 5.3 The percentage difference of the strain at 1.5 MPa for all the compression cycles of (c) SGL-10-BA and (d) SGL-34-BC.

(e)

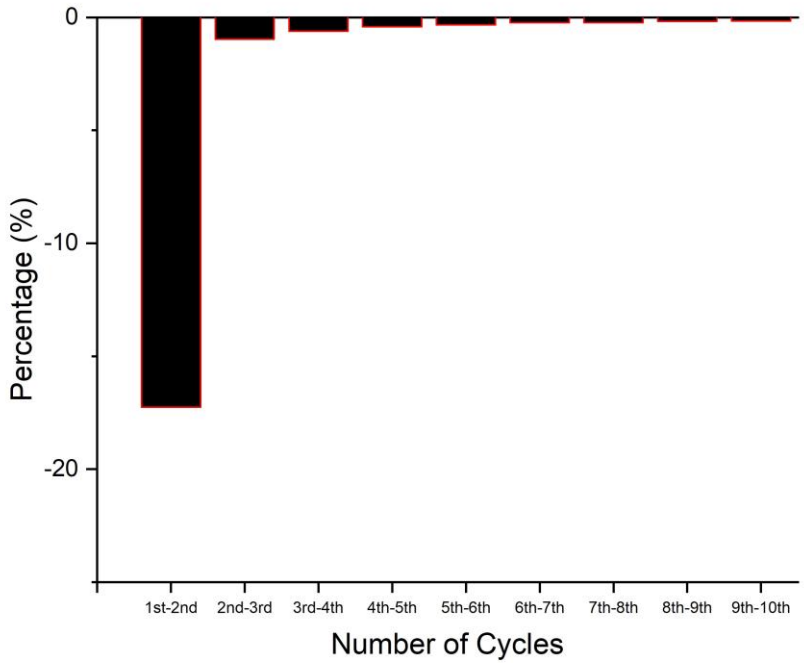

Figure 5.3 The percentage difference of the strain at 1.5 MPa for all the compression cycles of (e) SGL-35-BC

5.3.2 Gas permeability, wettability and morphology

The permeability of the gas diffusion layer in both the through-plane an in-plane directions can provide an essential information of the porosity and how well the gas is flowing from the flow field plates into the gas diffusion layer and the MEA. In this matter, and especially for the GDL, the convective mass transport of the reactant gases is the main source of transporting gases in the through-plane direction. The pore size distribution for fresh GDL samples and compressed samples can differ due to the changes in the structure including the wettability of the GDL surface, as well as the pore size distribution and the change in the structure. Therefore, an experimental study conducted in the through-plane permeability of the gas diffusion layer samples before and after two modes of compression namely, steady-state and cyclic stresses. Figure 5.4 shows the reduction in gas permeability after the steady-state and cyclic compression.

Table 5.2 shows the measured thicknesses of the tested GDL samples before and after applying the cyclic compression test, and Table 5.3 shows the through-plane permeability values of the tested GDL materials before and after compression. It is observed from the latter table that there exists a correlation between the reduction in thickness and the reduction in the gas permeability for either the uncoated and MPL-coated GDL materials: as the reduction in thickness increases, the reduction in the through-plane permeability increases. The reduction in the thickness of the GDL, caused by compression signals that the porosity of the GDL decreases. Subsequently, the gas

permeability, which is a strong function of the porosity, as evidenced from the Kozney-Carman equation [108], decreases.

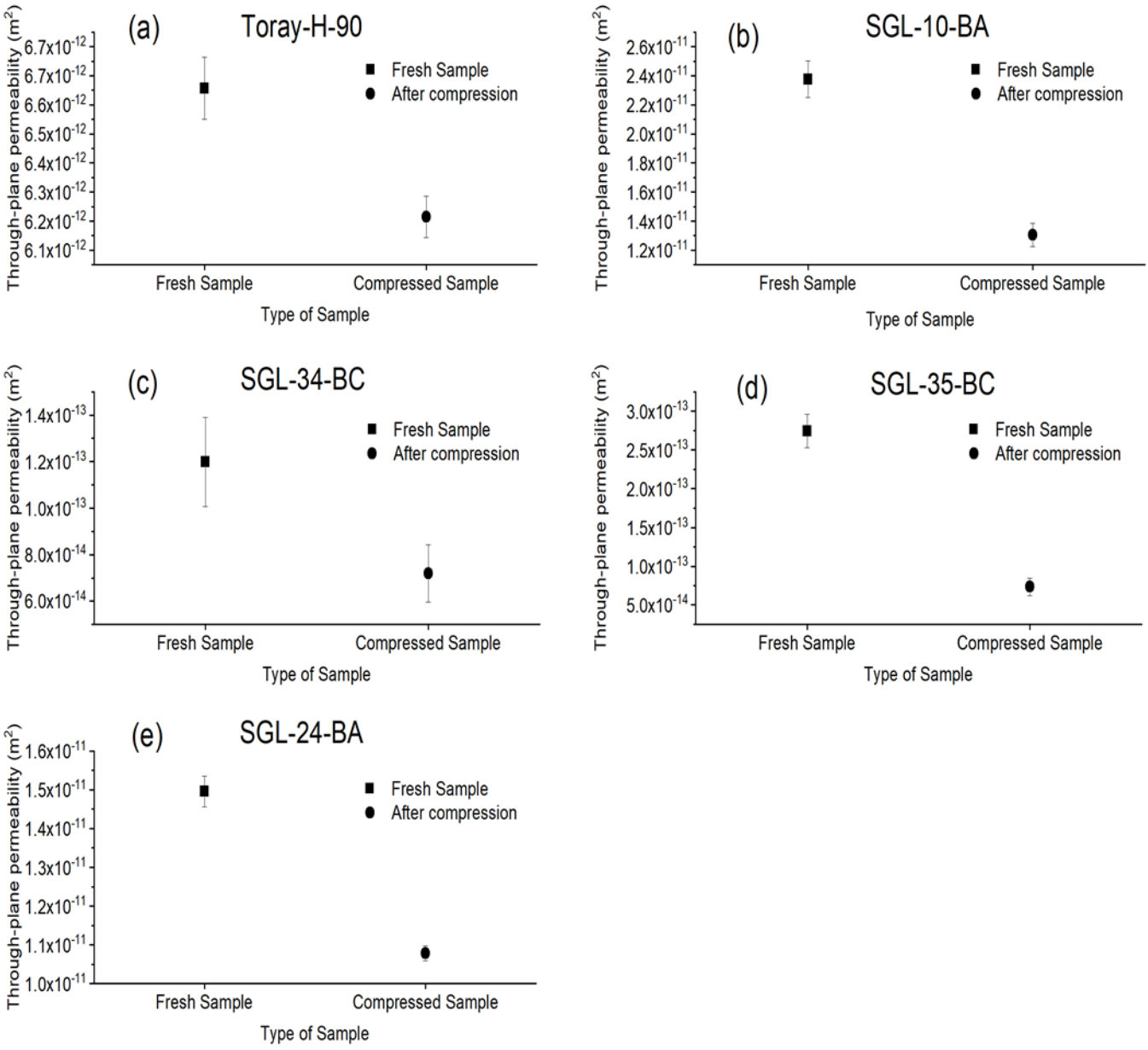

Figure 5.4 The reduction in gas permeability after the steady-state and cyclic compression for the tested GDL samples.

Table 5.2 Thickness measurements of the tested GDL samples before and after compression.

Manufacturer type	Thickness of Fresh sample(μm)	Thickness after steady-state and cyclic compression(μm)
Toray-H-90	282.5 ± 1.0	272.5 ± 1.0
SGL-24-BA	210.0 ± 3.1	165 ± 2.1
SGL-10-BA	397.5 ± 1.0	285 ± 2.0
SGL-34-BC	317.5 ± 2.4	283 ± 3.0
SGL-35-BC	322.5 ± 1.0	222.5 ± 1.0

Table 5.3 Through-plane permeability before and after compression, and the percentage of both reduction in thickness and permeability of the tested samples.

GDL Type	Through-plane permeability before compression (m^2)	Through-plane permeability after compression (m^2)	Reduction in thickness (%)	Reduction in permeability (%)
Toray-H-90	$(6.62 \pm 0.10) \times 10^{-12}$	$(6.22 \pm 0.06) \times 10^{-12}$	3.5	5.0
SGL-24-BA	$(1.50 \pm 0.04) \times 10^{-11}$	$(1.08 \pm 0.02) \times 10^{-11}$	21.4	27.9
SGL-10-BA	$(2.38 \pm 0.13) \times 10^{-11}$	$(1.31 \pm 0.08) \times 10^{-11}$	28.3	45.1
SGL-34-BC	$(1.20 \pm 0.19) \times 10^{-13}$	$(7.19 \pm 1.23) \times 10^{-14}$	10.9	39.6
SGL-35-BC	$(2.74 \pm 0.22) \times 10^{-13}$	$(7.33 \pm 1.17) \times 10^{-14}$	31.0	73.3

It should be noted that the reduction in thickness shown in Table 5.3 is measured after performing the full cyclic compression in order to ensure that

the mechanical deformation to the GDL materials is almost permanent; see Fig. 5.3. This mimics the situation inside the fuel cell where the GDL material is subject to cycles of compression and decompression as a result of membrane hydration/dehydration, thus eventually leading to permanent GDL deformation. To elaborate more on how the structure and thickness change with compression, cross-sectional SEM images of the tested uncoated and MPL-coated GDL materials have been generated, see Fig. 5.5 and Fig. 5.6. It is seen from the latter figures that the original thicknesses of the tested GDLs have, in general, reduced after performing the compression test. Notably, the difference in the thickness of Toray-H-90 before and after compression is very small, see Fig. 5.5(a-b). This observation is in line with the relatively small value reported in Table 5.3 for the reduction in thickness of the above mentioned GDL material, i.e. 3.5%. The high resistance to deformation (or compliance) shown by Toray-H-90 GDL could be attributed to its relatively high density of carbon fibres compared to those of SGL-10-BA and SGL-24-BA GDLs; see Fig.5.7. This observation is in accordance with the density and porosity values reported for the above GDL materials [150], [151], [163]. Namely, the density and porosity of Toray-H-90 (i.e. 0.45 g cm^{-3} and 0.62) are respectively higher and lower than those of SGL-10-BA (0.21 g cm^{-3} and 0.88), and SGL-24-BA (i.e. 0.28 g cm^{-3} and 0.74), thus imparting a higher degree of stiffness to the Toray GDL material. Equally, compared to Toray-H-90 and SGL-24-BA GDLs, SGL-10-BA GDL material shows the highest level of reduction in thickness and gas permeability as it has the lowest density and the highest porosity, respectively.

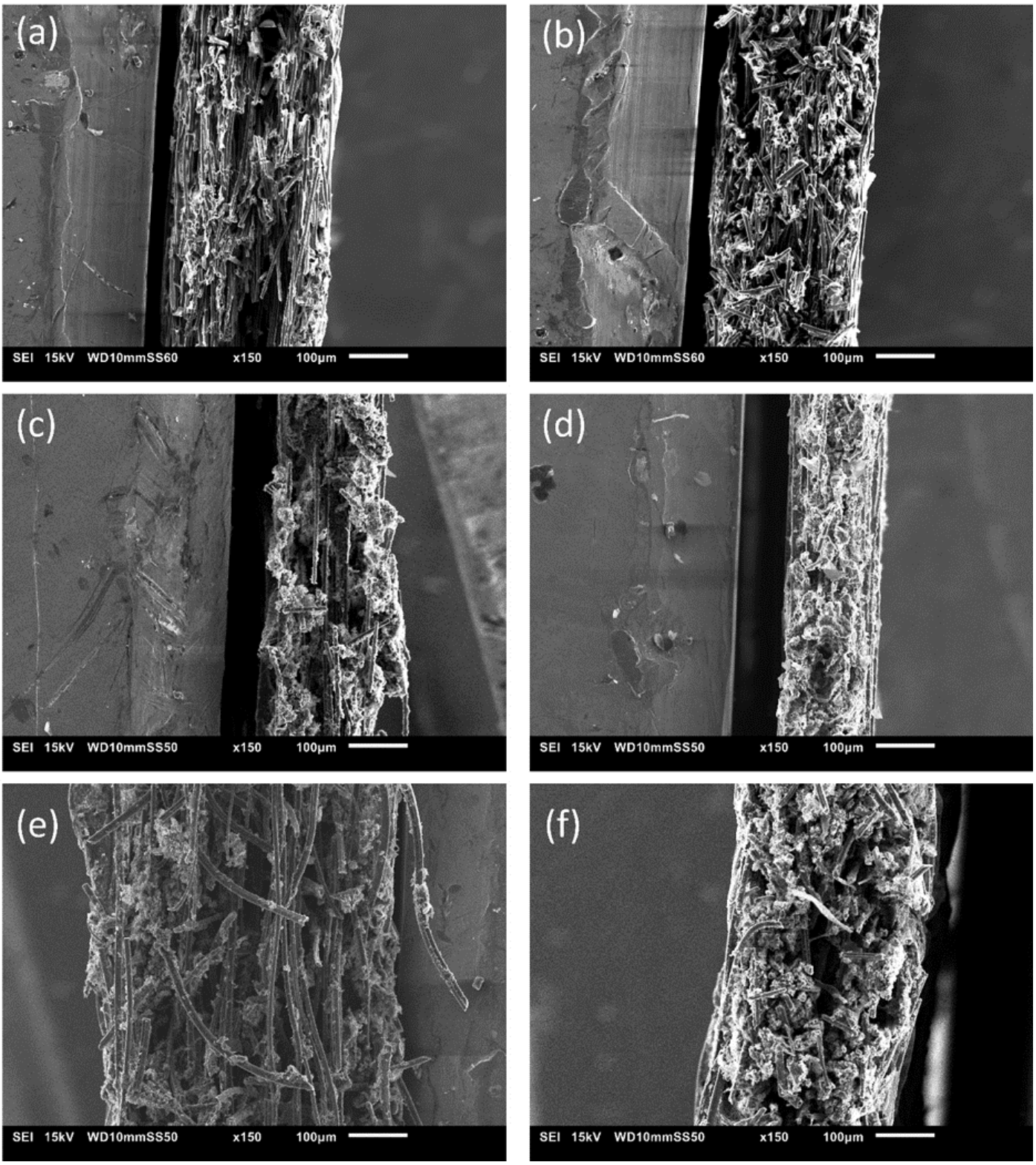

Figure 5.5 Cross-sectional SEM images at 150x for uncoated GDL samples before and after compression, (a) uncompressed Toray-H-90, (b) Compressed Toray-H-90, (c) Uncompressed SGL-24-BA, (d) Compressed SGL-24-BA, (e) Uncompressed SGL-10-BA, and (f) Compressed SGL-10-BA

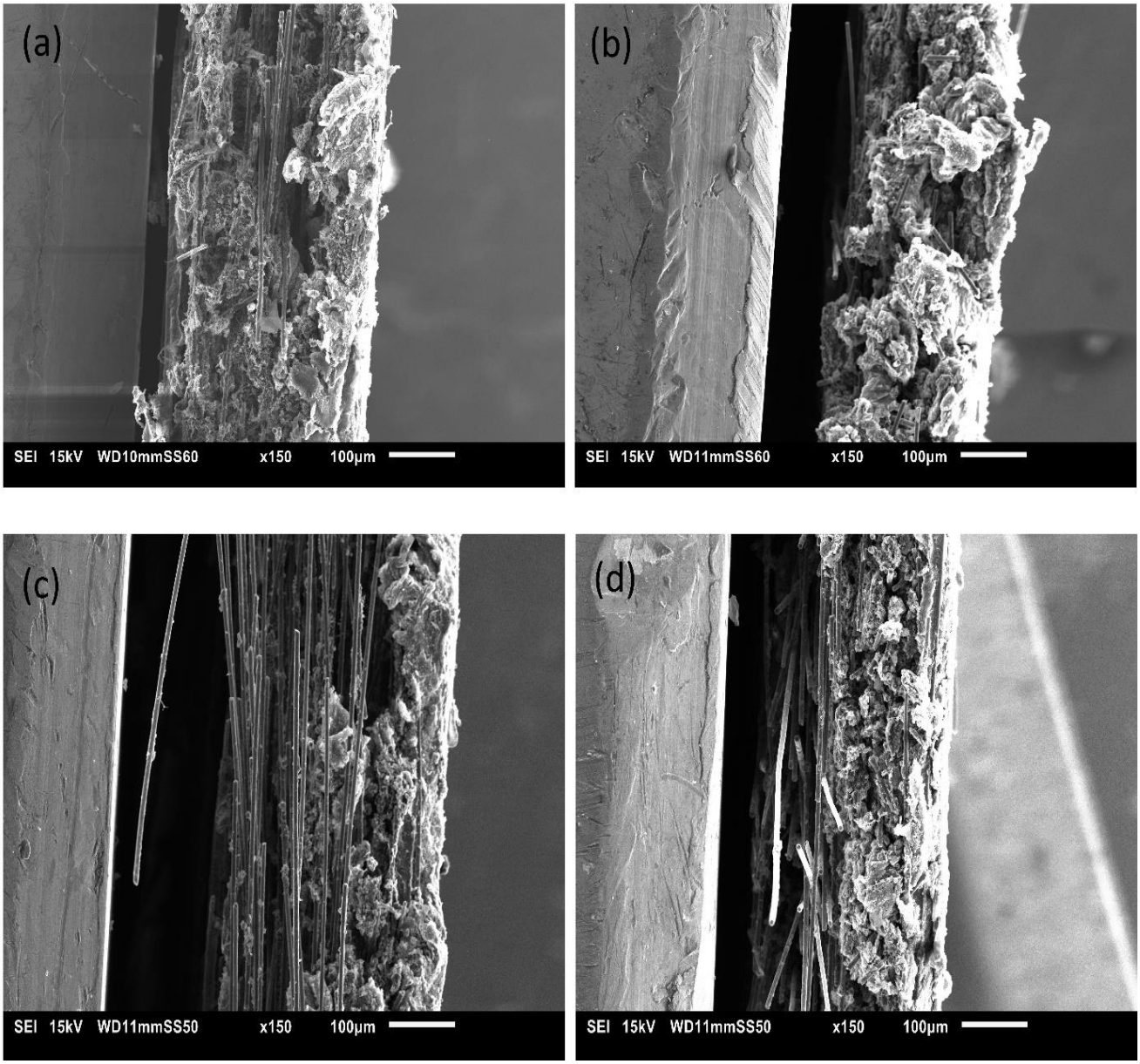

Figure 5.6 Cross-sectional SEM images at 150x for MPL-coated GDL samples before and after compression, (a) uncompressed SGL-34-BC, (b) compressed SGL-34-BC, (c) uncompressed SGL-35-BC, and (d) compressed SGL-35-BC.

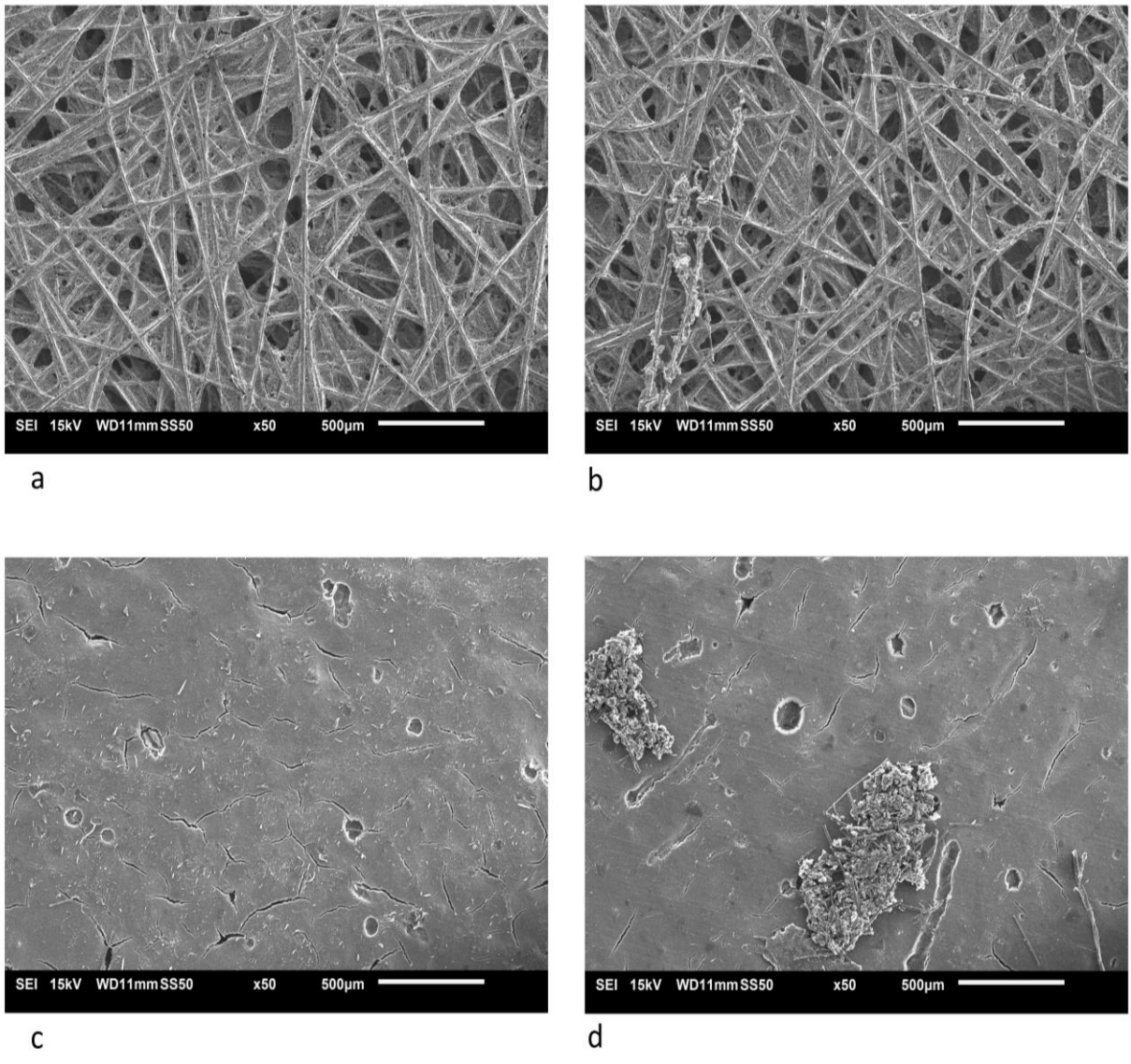

Figure 5.7 SEM micrographs of (a) SGL 24 BA before compression (b) after compression (c) SGL 34 BC before compression (d) after compression

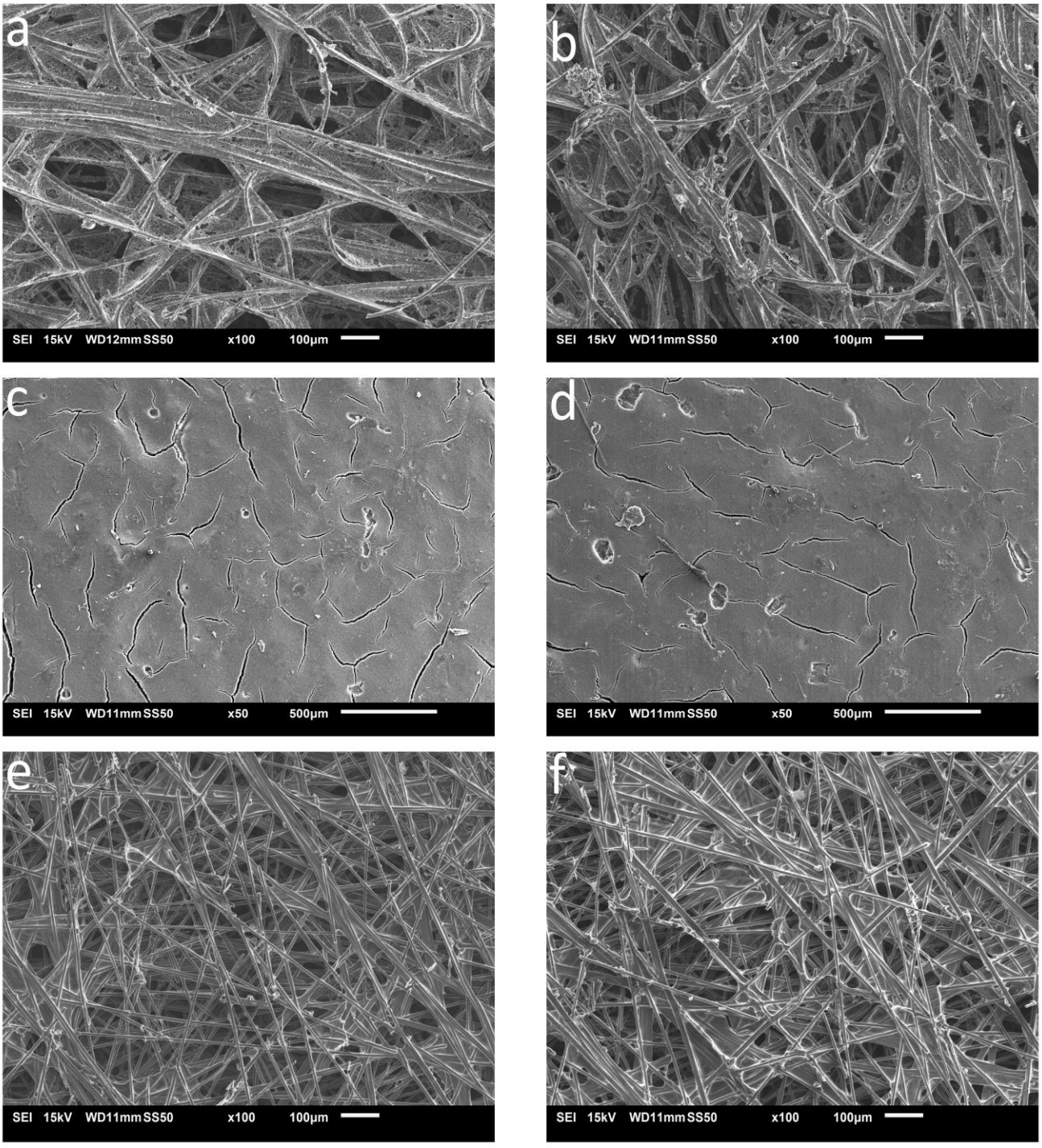

Figure 5.8 SEM micrographs of (a) SGL 10 BA before compression, (b) after compression, (c) SGL 35 BC before compression, (d) after compression, (e) Toray-H-90 before compression, and (f) after compression.

The morphology of the samples' surface was studied before and after compression using a scanning electron microscope. The micrographs shown in Figures 5.7 and 5.8 give an insight of the top view of the GDL surface before and after compression for Toray-H-90, SGL-24-BA, SGL-34-BC, SGL-35-BC, and SGL-10-BA. It is shown from the micrographs that after compression there was a slight change on the top surface of the GDLs. This is could be attributed to the change of roughness and thickness of the tested surfaces. Also, there are some residual particles on the some of the GDL surfaces that prove some kind of particles crushing.

Therefore, further investigation in the direction of the compression requires a more thorough analysis. Figure 5.5 shows the cross-sectional SEM images of the tested uncoated GDL samples before and after compression. To elaborate more on how the structure and thickness change with compression, cross-sectional SEM images of the tested uncoated and MPL-coated GDL materials were generated, see Fig. 5.5 and Fig. 5.6. It can be seen from the latter figures that the original thicknesses of the tested GDLs have in general reduced after performing the compression test. Notably, one could hardly see the difference in the thickness of Toray-H-90 before and after compression, see Fig. 5.5(a-b). This observation is in line with the relatively small value reported in Table 5.2 for the reduction in thickness for the above mentioned GDL material, i.e. 3.5%. The high resistance to deformation (or compliance) shown by Toray-H-90 GDL could be attributed to the fact that its carbon fibres are straight and randomly distributed, see Fig. 5.8(e) imparting a high degree of stiffness to the GDL material. Similarly, SGL-24-BA has a straight and randomly distributed carbon

fibres, however when comparing the latter two GDL materials, they have different reduction in thickness which can be attributed to the density of the connected carbon fibres. It is well observed from Fig. 5.8(e-f), that Toray-H-90 is more dense in terms of the connected carbon fibres compared to SGL-24-BA in Fig. 5.7 (a-b). Therefore, this fibre density attributes in adding more mechanical resistance and stiffness when being under compression. As the density of the GDL material increases, its porosity decreases, hence a GDL with higher density is more capable to withstand reduction in thickness under compression [163].

5.3.3 The wettability of the GDL surface

The wetting behaviour of the GDL surface can be measured using a goniometer with water droplets. Typically, the interaction of solid surface and liquid droplets, in this case water droplets plays an important role in determining the contact angle of the GDL surface. Thus, contact angle is a vital parameter in determining the wettability of the surface and how it behaves during operation [164]. The hydrophobicity of the GDL surface and its content of PTFE or other hydrophobic agents were measured before and after the applied mode of compression. A water droplet of the uncoated GDL samples is shown in Fig. 5.9 (a) Toray-H-90 fresh sample, (b) Toray-H-90 after compression, (c) SGL 24 BA fresh sample, (d) SGL 24 BA after compression, (e) SGL 10 BA fresh sample, and (f) SGL 10 BA after compression. Also, Figure 5.10 shows the water droplets of the MPL-coated GDLs measurements of (a) SGL-34-BC fresh sample, (b) SGL-34-BC after compression, (c) SGL-35-BC fresh sample, (d)

SGL-35-BC after compression. It could be seen from Figures 5.9 and 5.10 that, for almost all the drops, the edges of the drop contacting the surface is rather blurry and the automatic detection (using the red lines) is often, as a result of this blurriness, not accurate. Therefore, more accurate tangent lines (black lines in Figures 5.9 and 5.10) were made manually and a protractor was used to measure the contact angles. Ten drops were made for each sample and the contact angle for each drop was measured manually as described above. Table 5.4 lists the values of the contact angle of the tested GDLs before and after compression. As expected, the surfaces of all the tested GDL materials, either before or after compression, were found to be hydrophobic (the respective contact angles are all greater than 90°). Also, the values of the surface contact angle for the uncompressed SGL-34-BC (126.7° ± 3.4) and SGL-35-BC (122.1° ± 4.1) are in good agreement with those reported by El-kharouf et al. [150] for SGL-34-BC (126° ± 7), and SGL-35-BC (118° ± 11). The contact angle changes with the roughness of the surface; the rougher is the surface, the greater is the surface contact angle [150]. Typically, the internal contact angles of GDLs depend on how the fibres and the pores separating them are connected. On the other hand, the external (or the surface) contact angles of the GDL depend on the morphology and the roughness of the surface, normally resulting in higher values compared to those of the internal contact angles [54]. One may see from Table 5.4 that the contact angles of all the tested GDL materials reduce after compression. Also, Figure 5.9 and 5.10 clearly show that the contact angles for all the tested GDL samples before compression is greater than that after compression. The reason behind this reduction in the contact

angle after compression is that the surface of the GDL sample becomes smoother after compression, as evidenced from the cross-section images of the tested GDL materials shown in Fig.5.5 and Fig.5.6. This is corroborated with the results that show that the contact angle of the GDL surface generally reduces as the surface roughness decreases [165].

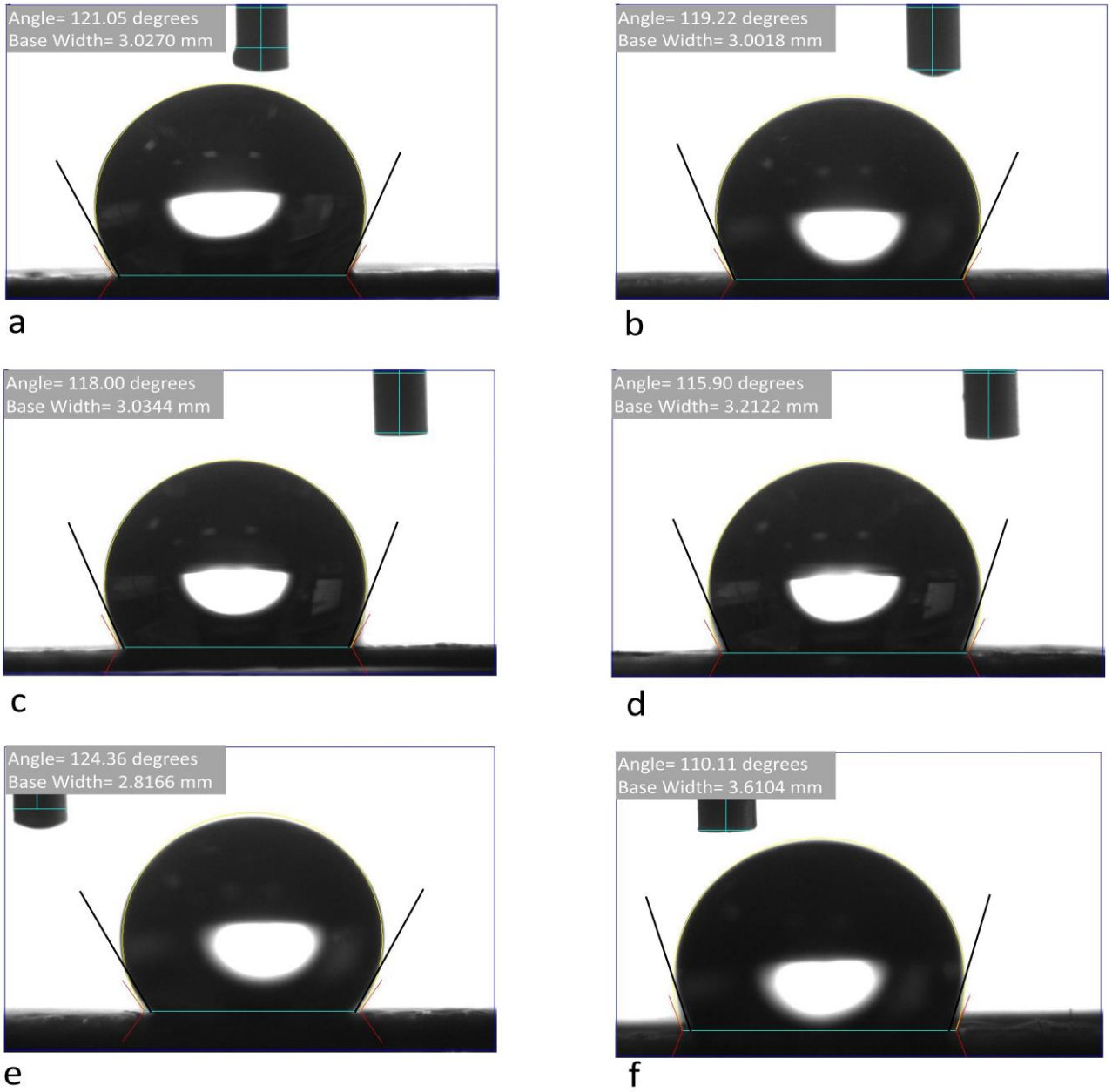

Figure 5.9 contact angle measurements of (a) Toray-H-90 fresh sample, (b) Toray-H-90 after compression, (c) SGL 24 BA fresh sample, (d) SGL 24 BA after compression, (e) SGL 10 BA fresh sample, and (f) SGL 10 BA after compression.

Ten water droplets were taken for each GDL type before and after compression with a 95 % percentage confidence interval shown in Table 5.4.

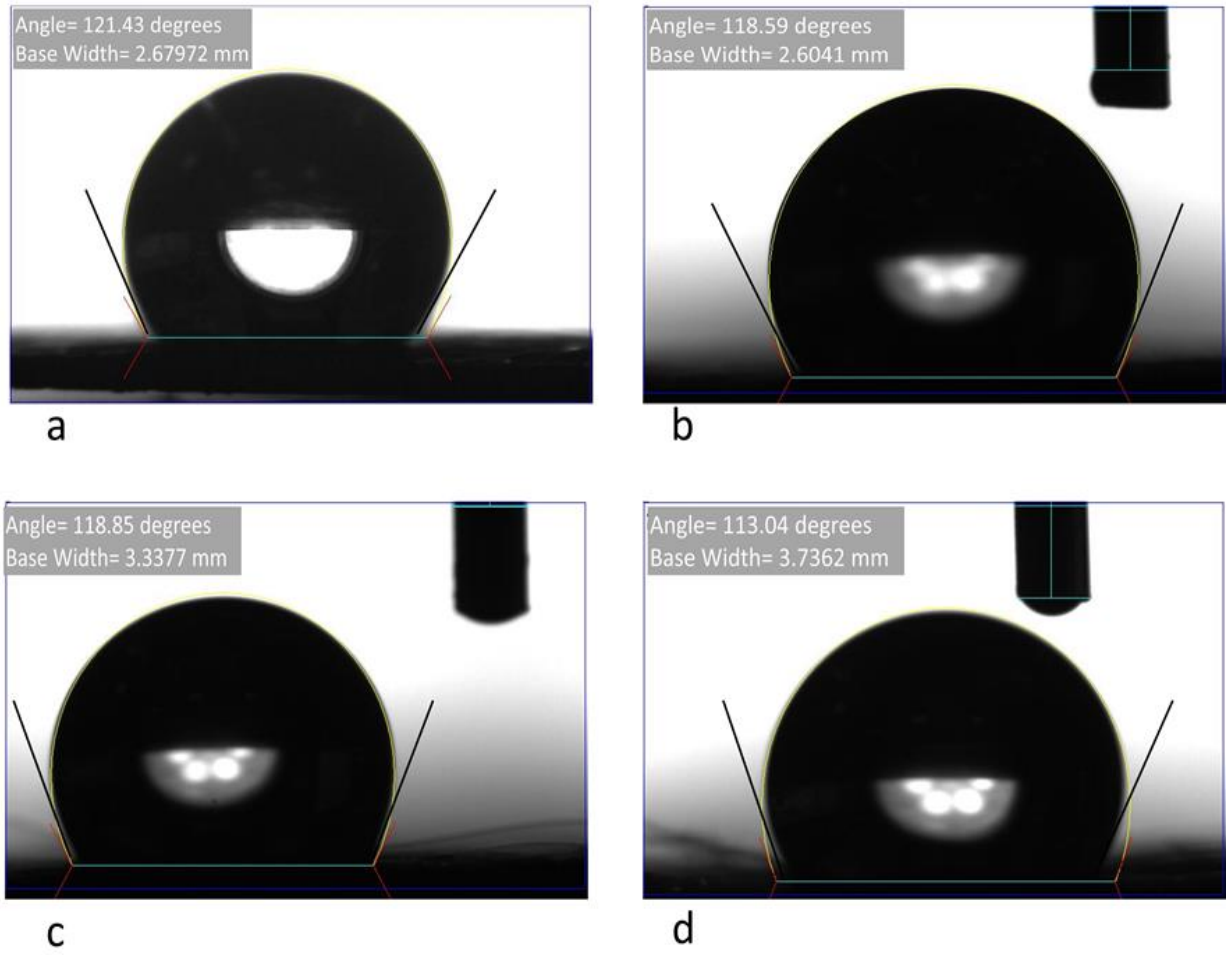

Figure 5.10 contact angle measurements of (a) SGL-34-BC fresh sample, (b) SGL-34-BC after compression, (c) SGL-35-BC fresh sample, (d) SGL-35-BC after compression.

Table 5.4 Contact angle measurements of fresh and compressed GDL samples

Manufacturer type	Contact angle ° Fresh sample	Contact angle ° Compressed Sample
Toray-H-90	124.3° ± 2.3°	120.1° ± 3.5°
SGL-24-BA	122.7° ± 2.6°	120.5° ± 2.4°
SGL-10-BA	121.5° ± 3.2°	112.6° ± 1.7°
SGL-34-BC (MPL-coated)	B.S[1]: 121.3° ± 1.3°	B.S[1]: 119.4° ± 0.9°
	MPL[2]: 122.0° ± 1.6°	MPL[2]: 109.8° ± 2.2°
SGL-35-BC (MPL-coated)	B.S[1]: 118.7° ± 1.5°	B.S[1]: 113.7° ± 4.2°
	MPL[2]: 117.4° ± 2.2°	MPL[2]: 114.1° ± 3.8°

(1) B.S: contact angle measurement taken from the backing substrate side.

(2) MPL: contact angle measurement taken from the micro porous layer side.

5.4 Conclusions

In this chapter, different types of GDL materials were ex-situ compressed using a universal testing machine. The compression test was designed in such a way that simulates an initial assembling compression, followed by a number of cycles of loading and unloading, thus simulating the compression arising as a result of hydration/dehydration of the membrane. The thickness, the through-plane permeability, the contact angle, and the morphology of the tested GDL materials were examined before and after performing the compression test. The obtained values of the above variables after compression are of use for PEFC models as they are more realistic and subsequently enhance the predictions of the models. The following are the main findings of the study;

- The coated GDL materials appear to be slightly more resistive to deformation than the uncoated GDL materials, and this is due to the enhanced mechanical strength of the coated GDLs as a result of the addition of relatively dense material, i.e. the MPL, to the carbon substrate.
- The tested Toray carbon substrate is mechanically stronger than the tested SGL carbon substrates and this is due to the higher density and lower porosity demonstrated by the former carbon substrate. This translates into a smaller reduction in thickness and gas permeability for the Toray carbon substrate after performing the compression test.
- One of the tested coated GDL materials (i.e. SGL-35-BC) shows substantially much higher reduction in thickness and gas permeability compared to the other tested coated GDL material (i.e. SGL-34-BC).

This is attributed to the higher level of MPL penetration demonstrated by the former coated GDL material.

- The contact angle of all the tested GDL materials were found to decrease by about 3°-15° after compression, and this is due to the increased surface smoothness after compression.

6 EFFECTS OF COMPRESSION ON GDLS IN PRESENCE OF SEALING GASKETS

6.1 Introduction

Polymer electrolyte membrane (PEM) fuel cells are energy converters that directly and efficiently produce electricity, with zero-emission at the point of use. Owing to its high efficiency (~ 50%), noise-free operation and clean by-products (only pure water), the PEM fuel cell is one of the most promising power conversion technologies for a multitude of portable, automotive and stationary applications. One of the essential components inside PEM fuel cells is a gas diffusion layer (GDL). GDLs are mainly responsible for supplying the reactants (i.e. O_2 and H_2) from the flow channels grooved in the flow-field plates to the active areas in the catalyst layers as uniformly as possible [166]–[168]. Additionally, GDLs transport electronic charge and heat between the catalyst layers and the flow field plates and act as a mechanical support to the delicate catalyst layers. Further, they are typically coated with hydrophobic microporous layers (MPLs) to improve the electrical contact with the catalyst layers and to assist in rejecting excess water generated at the cathode side of the fuel cell [169], [170].

There are different factors that play a significant role in affecting the mass transport properties of the GDLs (e.g. gas permeability and diffusivity). The GDL is subject to two types of degradation: mechanical degradation (due to the stresses acting on the GDLs) and chemical degradation (due to the erosion

and corrosion taking place within the environment of the fuel cell). It should be noted that these forms of degradation are not limited to the GDLs and could be seen with the other components of the fuel cell such as the bipolar plates. For example, Li et al. [171] found that, through conducting durability tests for a high-temperature PEM fuel cell, the degradation in fuel cell performance reduces to almost zero if the used stainless steel plates are coated with stacked layers of chromium nitride and chromium. This is evidently due to the reduction in the chemical degradation of these plates that were coated with corrosion-resistant layers. On the other hand, the degradation in fuel cell performance in the case of bare stainless steel or graphite bipolar plates is around 16%.

There are two types of mechanical stresses (or compressions or pressures) that the GDL normally undergoes: a constant stress dictated by the assembly of the fuel cell, and a cyclic stress arising from the cycles of swelling (in the case of membrane hydration) and shrinkage (in the case of membrane dehydration) [72].

The level of compression that the GDL undergoes is somewhat regulated by the presence of the sealing gaskets and this is obviously due the relatively high porosity of the GDL which could be as high as 90% [120], [172]. This regulation of compression induced by the sealing gasket could prove useful as the mass transport of the GDL material are, with sealing gaskets, not badly affected due to compression. The primary function of the sealing gaskets are, as implied by their name, to seal the fuel cell and prevent gas leakage at either side of the

fuel cell. The sealing gaskets should be sufficiently strong to withstand the compressive pressures applied to the fuel cell and should ideally at the same time allow for good contact between the flow field plates and the gas diffusion layers [173] .They should also be chemically stable to resist for example the corrosive environment at the cathode side [174]. The literature shows a good number of research studies that have been conducted to investigate the mechanical or the chemical properties of the sealing gasket materials used in PEM fuel cells. Li et al. [118] studied the chemical degradation of the silicone rubber gaskets using five different aging solutions with different concentrations. The aging process was up to 2500 hours. The XPS and ATR-FTIR spectroscopy showed that the surface of the silicone rubber gaskets experienced significant changes (e.g. cracks) as a sign of the deterioration of the material of the sealing gasket.

Tan et al. [119] investigated the chemical and mechanical durability of four different commercial sealing gaskets (Silicone S, Silicone G, EPDM, and FL) under fuel cell operating conditions. A regular (98% H_2SO_4 dissolved in reagent grade water) and accelerated durability test or ADT (48% HF dissolved in reagent grade water) solutions and three bending angles (0, 90 and 120°) were used for the test. Tan et al. showed that both silicone gaskets have a mass loss and cracks in the regular and ADT solutions. However, the EPDM and FL gaskets only showed degradation after 45 days of their exposure to the ADT solution at a bending degree of 120°. On another study, Tan et al. [175] found that degradation rate of the silicone gaskets increases with increasing temperature as evidenced by the weight loss measurements at 60 °C (~ 1 %) and 80% (~ 3%)

after a 12-week durability test. Ghosh et al. [176] investigated different clamping forces with two types of gaskets using contact pressure distribution films. The purpose of the study was to identify the influence of gaskets, varying in material and thickness, on the contact between the GDL and the flow field plate. The results showed that the spacing between the gasket and the GDL should be reasonable (≤ 0.2 mm) in order to achieve a good contact between the GDL and the flow field plate. Lin et al. [110] experimentally investigated the effect of the gasket thickness (0.05 – 0.48 mm) with two different types of carbon cloth GDLs (NC14 and OC14) on the overall performance of the cell. The results showed that the optimum compression ratios for NC14 and OC14 GDLs that maximises the fuel cell performance are 59% and 64%, respectively.

Another important, but related, topic is the effect of the compression on the structure of the GDLs. Few examples are given. Banerjee at al. [177] investigated the effect of compression on the porosity distribution of the GDL using means of X-ray computed tomography. They found that rib compression has almost no impact on the microporous layer. Nitta et al. [178] studied the effect of compression on the GDL thermal conductivity and the contact resistance between GDLs and graphite plates. They showed that the GDL thermal conductivity is almost insensitive to the compression applied (0-5.5 MPa). Of particular interest is the impact of compression on the loading of the hydrophobic agent (e.g. PTFE). Of particular interest is the impact of compression on the loading of the hydrophobic agent (e.g. PTFE). The GDL should be reasonably hydrophobic in order to be capable of rejecting excess liquid water that may hinder the flow of the reacting gas to the catalysts layer.

It was shown in our previous work that the contact angle, which is a measure on how hydrophobic the GDL is, decreases by up to 10% after applying compressive stresses generated by a universal testing machine [179].This is probably partly due the PTFE layers being stripped from the carbon fibres of the GDL. To this end, it is of much interest to explore the effects of compression on the PTFE loading of the GDL in the absence/presence of sealing gaskets. Thermogravimetric analysis (TGA) has been successfully employed to quantify the amount of PTFE in various types of GDL materials [89], [180], [181].

In this chapter, an investigation, for the first time, on how the sealing gaskets could affect the mass transport properties of the GDL. Namely we focus on how the GDL gas permeability, which is more convenient to estimate compared to for example gas diffusivity, changes before and after compression and with/without sealing gaskets. Both the gas permeability and diffusivity of the GDL scale with porosity and therefore the changes in the gas diffusivity due to compression are expected to follow the same trends of the gas permeability. Further, to investigate the structural integrity of the GDL after applying compression in the presence/absence of sealing gaskets, TGA is performed. TGA is specifically used to quantify the amount of PTFE loss as a result of compression.

6.2 Methodology and Materials

6.2.1 Materials

Four different commercial GDL materials and two different types of gaskets were used in this study. The sheets of the selected two gasket materials have the same thickness, ~ 0.25 mm, but are made from different materials: Teflon and silicone HT-6135 (Rogers Corporation, USA). Table 6.1 shows the investigated GDL materials, their initial thicknesses, porosities and PTFE loadings (in the carbon substrate and, if applicable, the microporous layers or the MPLs). Each set mentioned in the table consists of 5 one-inch diameter GDL material samples and the numbers 1, 2 and 3 refer to the set of samples being tested: without using gaskets, with Teflon and silicone gaskets, respectively.

Table 6.1 Initial thickness (measured), PTFE loading and porosity (as reported in the literature) of the tested GDL materials.

Manufacturer type	Initial Thickness[(a)] (µm)	PTFE Loading (%)	PTFE Loading of MPL (%)	Porosity (%)
SGL-34-BA	set 1: 265.8 ± 4.0 set 2: 268.3 ± 3.7 set 3: 266.0 ± 4.4	5	NA	81 [182]
SGL-34-BC	set 1: 306.0 ± 3.2 set 2: 301.3 ± 4.2 set 3: 303.8 ± 3.3	5	25	75 [182]
SGL-39-BA	set 1: 251.8 ± 3.4 set 2: 253.5 ± 3.4 set 3: 253.5 ± 3.6	5	NA	89 [182]
SGL-39-BC	set 1: 300.0 ± 2.9 set 2: 286.5 ± 2.9 set 3: 297.0 ± 3.3	5	25	82 [182]

(a) Thickness measurments are based on 95% confidence average of all three GDL sets

It should be noted that SGL 34BA and SGL 39BA are both non-woven carbon substrates; however, they are, as implied by their porosity values, of different structures. SGL 34BA is probably, with the lower-porosity, more suitable for low-humidity operating conditions than the SGL 39BA [183].

6.2.2 Mechanical characterisation

The compression test for both the GDLs and gaskets was conducted using a universal testing machine, Shimadzu EZ-LX (Shimadzu Corporation, Japan). The readings obtained were corrected for machine compliance as described in [109]. To investigate the effects of the gaskets on the compressibility of the GDL materials, the GDL samples of the first set (i.e. Set 1) and the gasket samples were separately tested for compression. The GDL samples of the second or the third set (i.e. Set 2 or Set 3) were then tested for compression in combination with the Teflon or silicone gasket materials; see Figure 6.1. The diameter of the GDL sample is 1.0 inch and the outer diameter of the annular gasket sample encircling the GDL sample is around 1.5 inch. As detailed in [12], the test was designed to simulate the various compression types that the GDL materials subjected to inside the housing of the fuel cell, namely: (i) the assembling compression and (ii) the cyclic loading and unloading compressions arising from the hydration and the dehydration of the membrane electrolyte. It should be noted that the compression on the GDL due to the swelling of the membrane could be up to 2 MPa [179], [184]. To this end, the total compression applied to the GDL samples was set to 3 MPa (1 MPa representing assembling compression plus 2 MPa due to membrane swelling). Figure 6.2 shows the sequence of the compression test with time: the first third of the loading stroke (0 to 1 MPa) represents the assembling compression and the following 1 to 3 MPa cyclic compressive strokes represent the loading and the unloading compressions the GDL undergoes due to the swelling (due to

hydration) and the shrinkage (due to dehydration) of the membrane electrolyte.

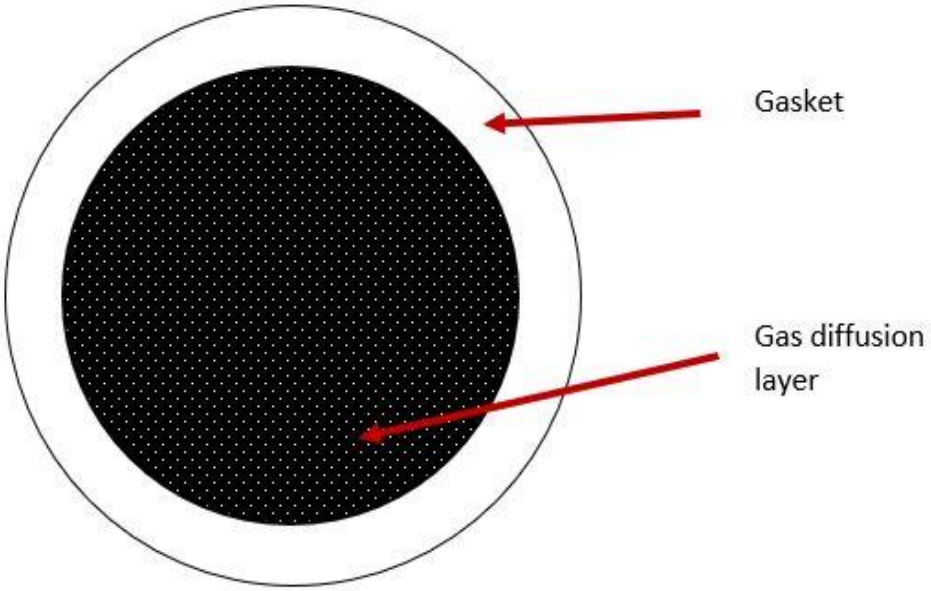

Figure 6.1 A schematic showing the top view of the combination of the circular GDL sample and the annular gasket sample.

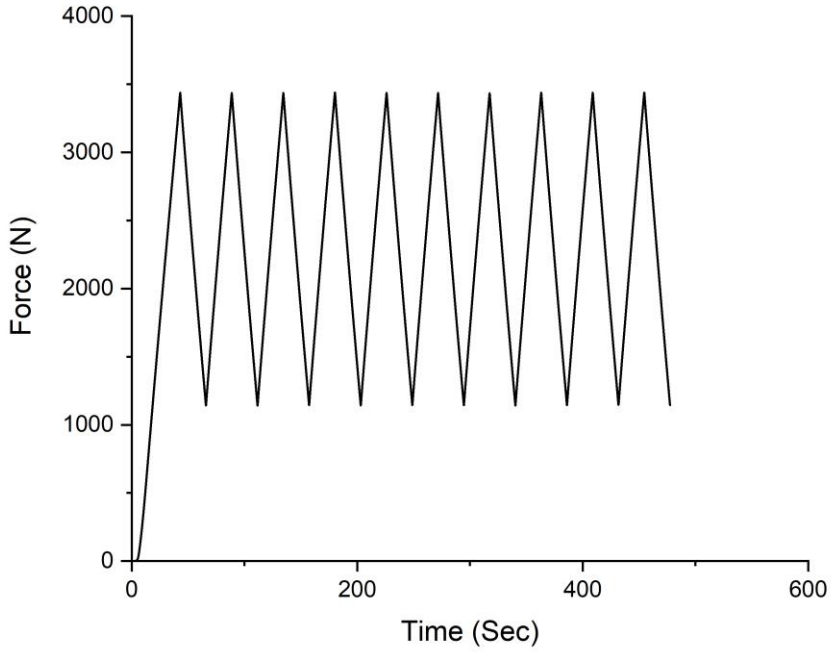

Figure 6.2 The pattern of the compression test as a function of force used on the tested GDLs and gaskets.

6.2.3 Through-plane gas permeability test

As described in Chapter 4 and Chapter 5, the in-house built gas permeability setup comprises of two main parts, namely lower and upper fixtures. A size of 25.4 mm diameter GDL sample is placed between the two fixtures [148], [149], [151], [153], [154]. A flowing Nitrogen gas is introduced to the GDL sample with different flowrates to measure the permeability of the samples. A minimum of 5 flowrates were used to measure the gas permeability for each sample. The flow controller used in the setup is (HFC-202, Teledyne Hastings, UK) with a range of 0.0–0.1 SLPM to adjust the flowrate of the nitrogen gas. Finally, in order to obtain the pressure difference across each GDL sample, a differential pressure sensor (PX653, Omega, UK) with a range of ±12.5 Pa. According to the low flowrates used, the assumption of minimal inertial losses is valid. As a result, the through-plane gas permeability of the GDL samples could be obtained using Darcy's law by applying the following equations:

$$\frac{\Delta P}{L} = \frac{\mu}{K} u \tag{6.1}$$

$$u = \frac{Q}{\pi D^2/4} \tag{6.2}$$

where ΔP is the pressure difference across the GDL sample, L is the measured thickness of the sample, μ is the dynamic viscosity of the flowing gas (i.e. nitrogen) which is about 1.8 × 105 Pa.s at 20 °C, K is the gas permeability of the GDL sample, u is the velocity of the flowing gas, Q is the volumetric flow rate and D is the diameter of the GDL sample.

The pressure gradient as a function of the flowing Nitrogen gas is shown in Fig 6.3 for: SGL-34-BA (a) set 1, (b) set 2, and (c) set 3, Fig 6.4 for: SGL-34-BC (a) set 1, (b) set 2, and (c) set 3, Fig 6.5 for: SGL-39-BA (a) set 1, (b) set 2, and (c) set 3, Fig 6.6 for: SGL-39-BC (a) set 1, (b) set 2, and (c) set 3. A number of five samples for each set were measured before and after the applied compression level. The average values were calculated with 95% confidence intervals, in which they are linearly curve fitted to measure the slope equation. Finally, the slope values are used to calculate for the gas permeability of the GDL materials using Eq. (6.1), and (6.2).

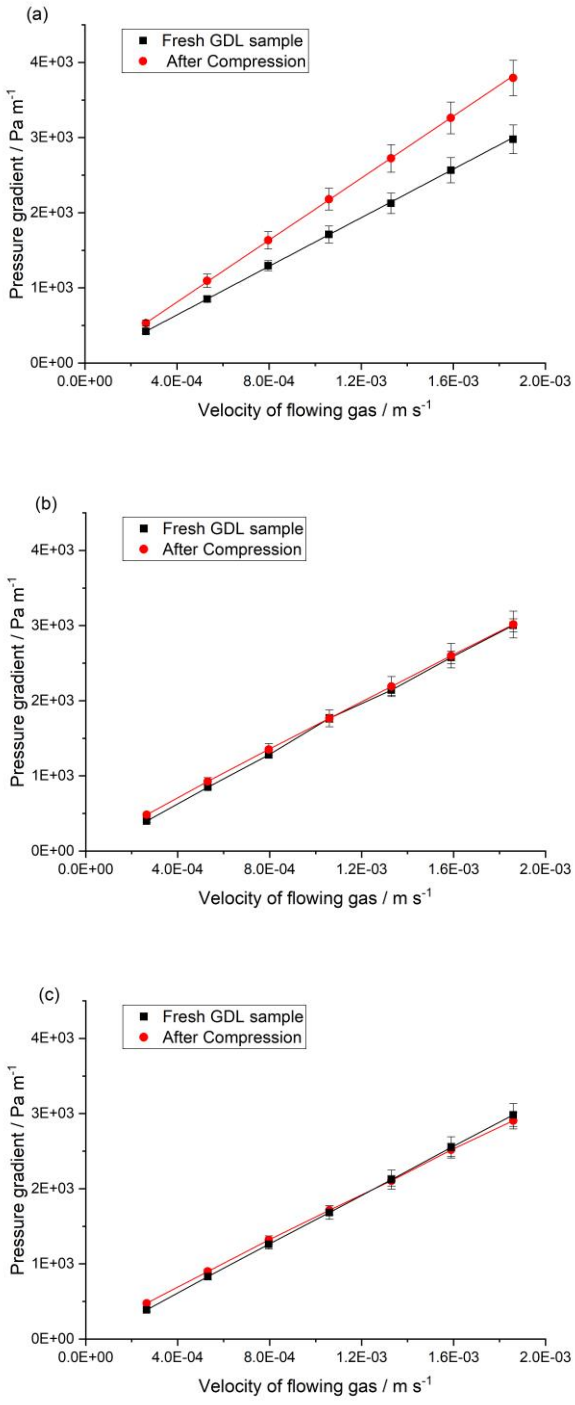

Figure 6.3 Pressure gradient versus gas velocity experimental data before and after compression for SGL-34-BA samples before and after compression: (a) without using gaskets (b) with Teflon gaskets and (c) with silicone gaskets.

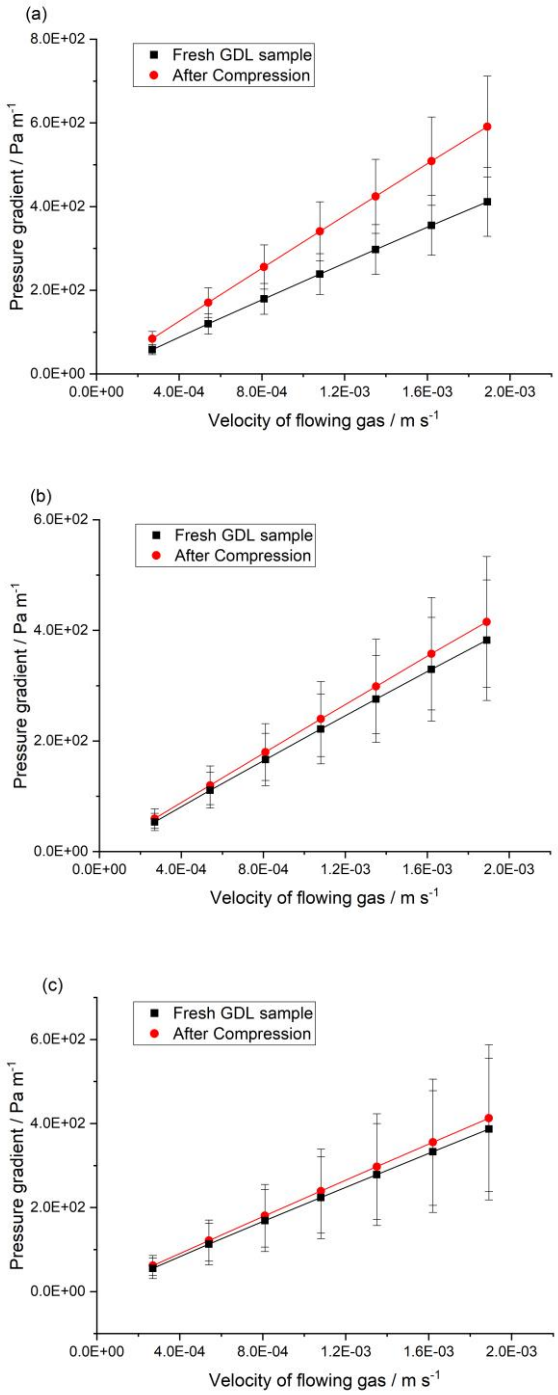

Figure 6.4 Pressure gradient versus gas velocity experimental data before and after compression for SGL-34-BC samples before and after compression: (a) without using gaskets (b) with Teflon gaskets and (c) with silicone gaskets.

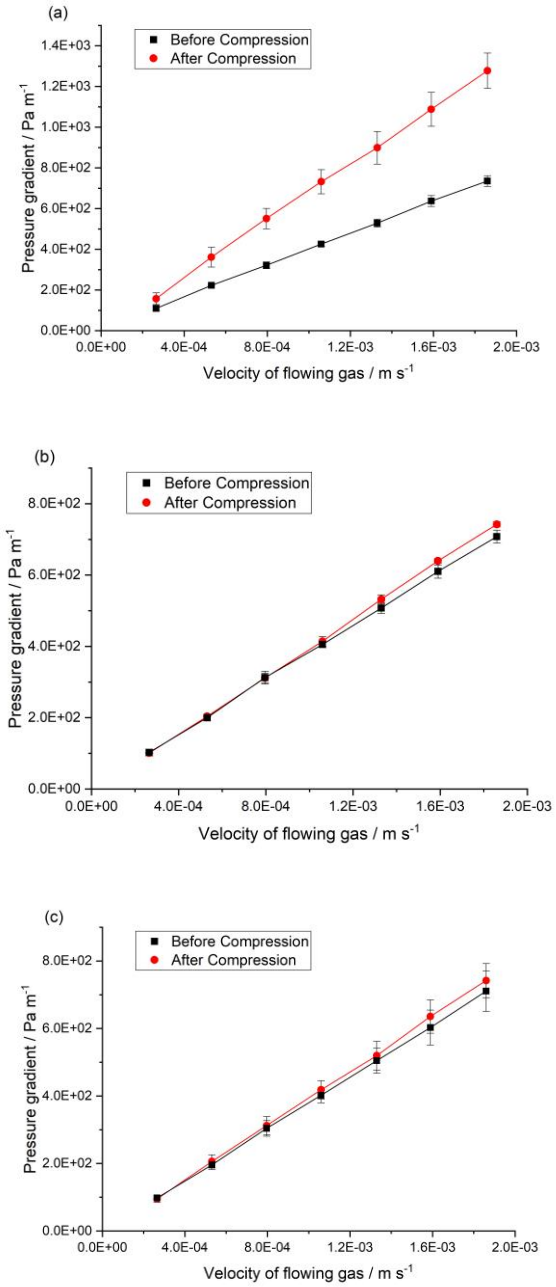

Figure 6.5 Pressure gradient versus gas velocity experimental data before and after compression for SGL-39-BA samples before and after compression: (a) without using gaskets (b) with Teflon gaskets and (c) with silicone gaskets.

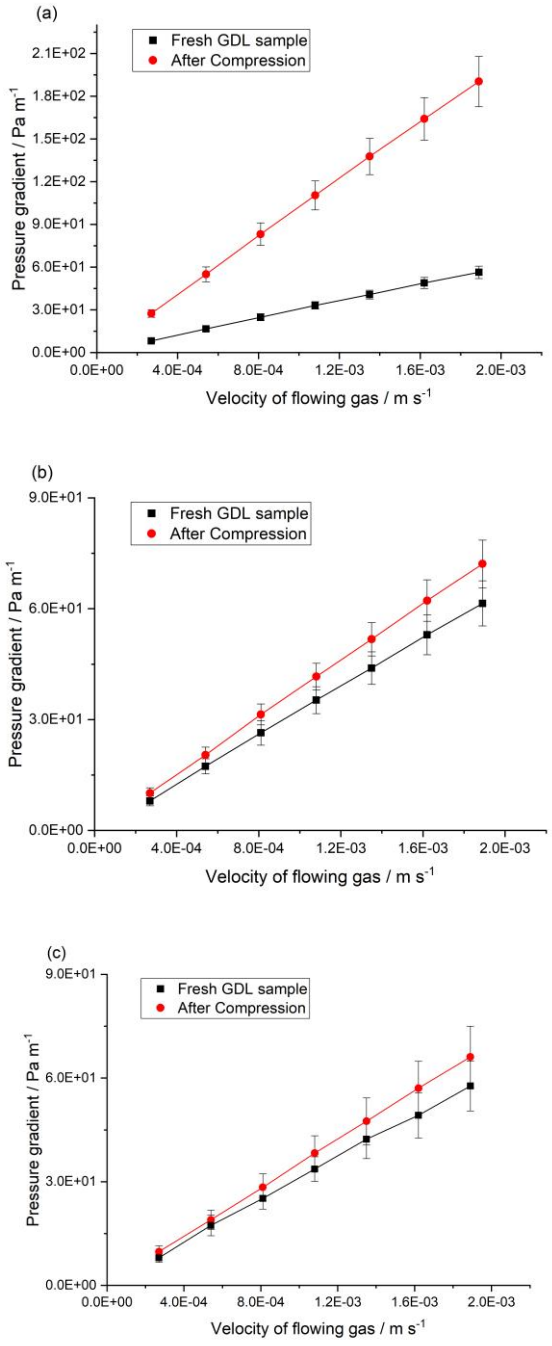

Figure 6.6 Pressure gradient versus gas velocity experimental data before and after compression for SGL-39-BC samples before and after compression: (a) without using gaskets (b) with Teflon gaskets and (c) with silicone gaskets.

6.2.4 Thermogravimetric Analysis (TGA)

Thermal stability of the materials used in PEM fuel cells can improve its performance and could give an indication of the durability during operation. Therefore, such an information can provide the limitation of the used materials, as well as can give indication of the hydrophobicity losses or degradation during operation. PTFE content in GDLs is responsible of the hydrophobicity property, in which it can assist in expelling excess water and avoid any blockage in of reacting gases during operation [185]. As previously explained in Section 3.3.1, TGA is used to quantify how much PTEF and any other decomposable materials (carbon powder, bindings resins, etc.) are lost from the investigated GDLs after compression campaigns. Such tests give an indication how the wettability of the GDL, which is an essential characteristic for water management within the fuel cell, is affected as a result of compression. Pyris 1 TGA Thermogravimetric Analyzer (PerkinElmer, USA) was used at a heating rate of 10 °C/min and under a nitrogen flow rate of 20 ml/min. This step was conducted to ensure that oxidation of the tested samples does not take place. The samples were initially exposed to nitrogen flow for 15 minutes at a temperature of 30 °C. The TGA analysis is then performed as the sample is heated from 30°C to 900°C at the above-mentioned rate (i.e., 10 °C/min).

6.3 Results and discussion

6.3.1 Compression test

Fig. 6.7, Fig. 6.8, Fig. 6.9, and Fig 6.10 show the stress-strain curves for the investigated GDL materials SGL 34 BA, SGL 34 BC, SGL-39 BA and SGL 39 BC, respectively as they were (a) without a gasket, (b) with Teflon gasket and (c) with a silicone gasket. Namely, the hysteresis (i.e., the difference between the forward curve (loading) and backward curve (unloading) is significant for the first cycle and becomes much less significant for the subsequent cycles. As explained in [12], this means that the first compression, caused by cell assembling, is responsible for most of the GDL deformation. This also means that the amount of heat dissipation resulting from the internal friction (the area enclosed between the forward and backward paths) in the first cycle is the maximum [90]. Subsequent cycles of loading (due to membrane hydration) and unloading (due to membrane dehydration) contribute much less to the deformation of the GDL, resulting in much less energy dissipation and signalling that the tested material has almost mechanically reached the equilibrium (or saturation) state [179]. As shown in Fig. 6.7(b,c), Fig. 6.8(b,c), Fig. 6.9(b,c), and Fig. 6.10(b,c), the gaskets have an effect on the mechanical behavior of the GDL material. Namely, the GDL material in general becomes more resistive to the compression in the presence of the gaskets; for example, the strain at the maximum applied stress, i.e. 3 MPa, for SGL 34BA is less than 0.4 in the presence of the gaskets whereas it is around 0.45 in the absence of the gaskets. This is, compared to the GDL materials, obviously due to the high mechanical resistance demonstrated by the tested gasket materials; see Fig. 6.7-Fig. 6.10.

Notably, the GDL samples with Teflon gaskets show less hysteresis than those with silicone gaskets; this is in accordance with the stress-strain curves of the investigated gaskets where the Teflon gaskets demonstrate less hysteresis compared to silicone gaskets (Fig. 6.11). It should be noted that the thicknesses of used gaskets did not change after the compression test. It can be seen from Figs. 6.7-6.10 that the MPL-coated GDL materials are more resistive than their corresponding carbon substrates; to illustrate, the strain displayed by SGL 34BA at 3 MPa is around 0.45 whereas it is around 0.37 for SGL 34BC at the same stress. This is mainly attributed to the fact that the MPL-coated GDL represent a system of two mechanical resistances in series and therefore the mechanical resistance is expected to increase. Further, an "inter-phase" layer is formed between the carbon substrate and the MPL as a result of MPL penetration into the substrate [30]. This layer is made up from the MPL material and carbon fibers and acts as a reinforcing material. Consequently, this is expected to improve the overall stiffness of the GDL [109].

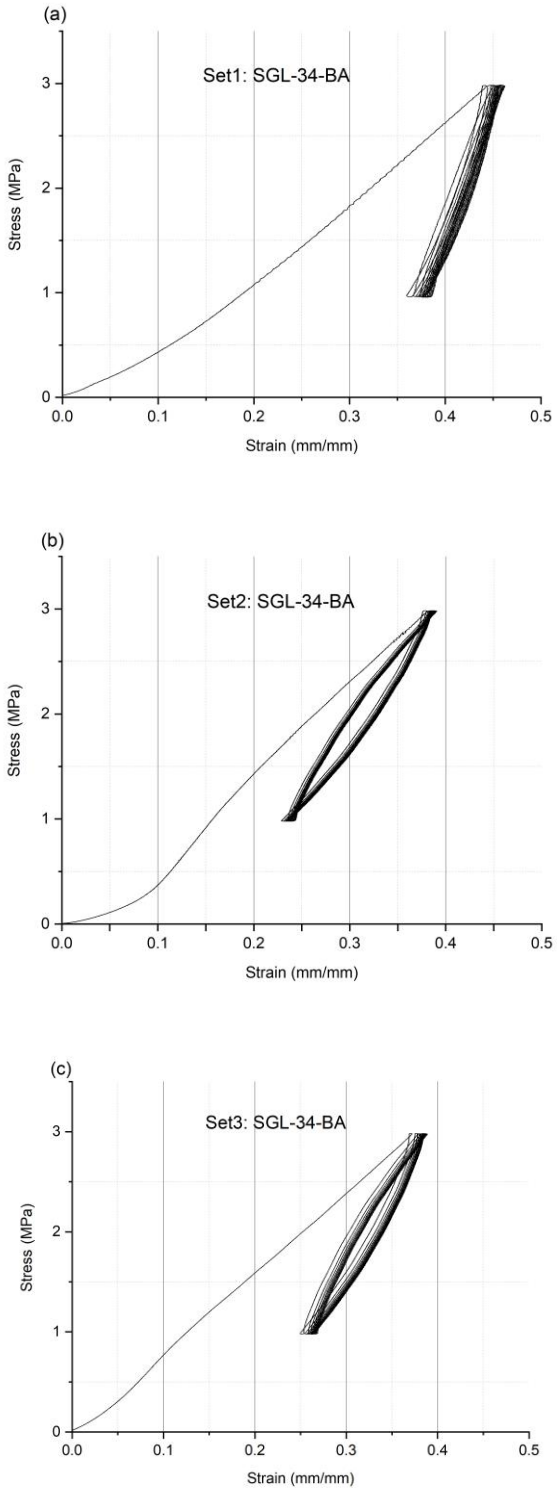

Figure 6.7 The stress-strain curves of SGL-34-BA (a) without gaskets, with (c) Teflon gaskets and (d) silicone gaskets.

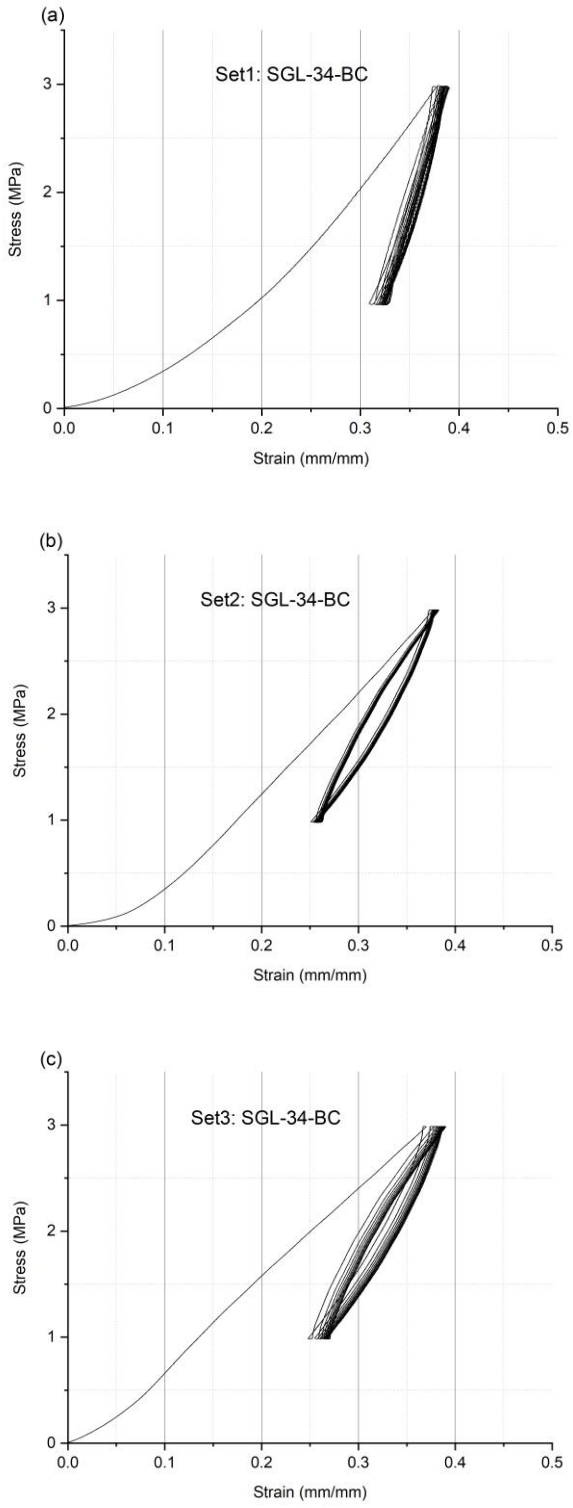

Figure 6.8 The stress-strain curves of SGL-34-BC (a) without gaskets, with (c) Teflon gaskets and (d) silicone gaskets.

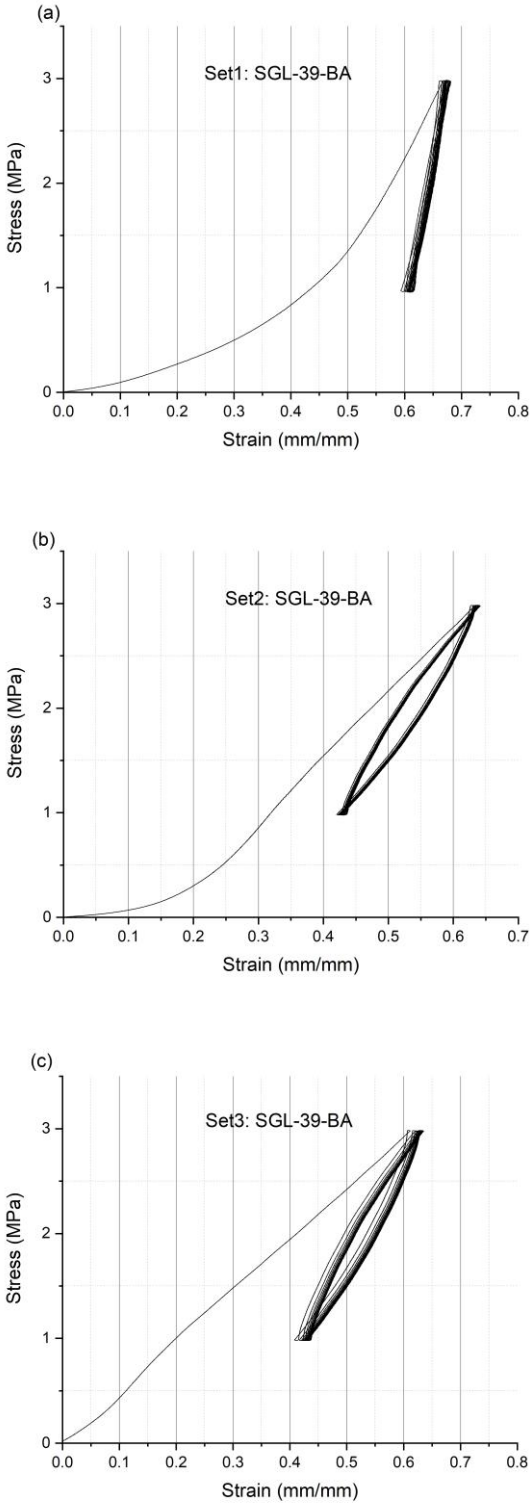

Figure 6.9 The stress-strain curves of SGL-39-BA (a) without gaskets, with (c) Teflon gaskets and (d) silicone gaskets.

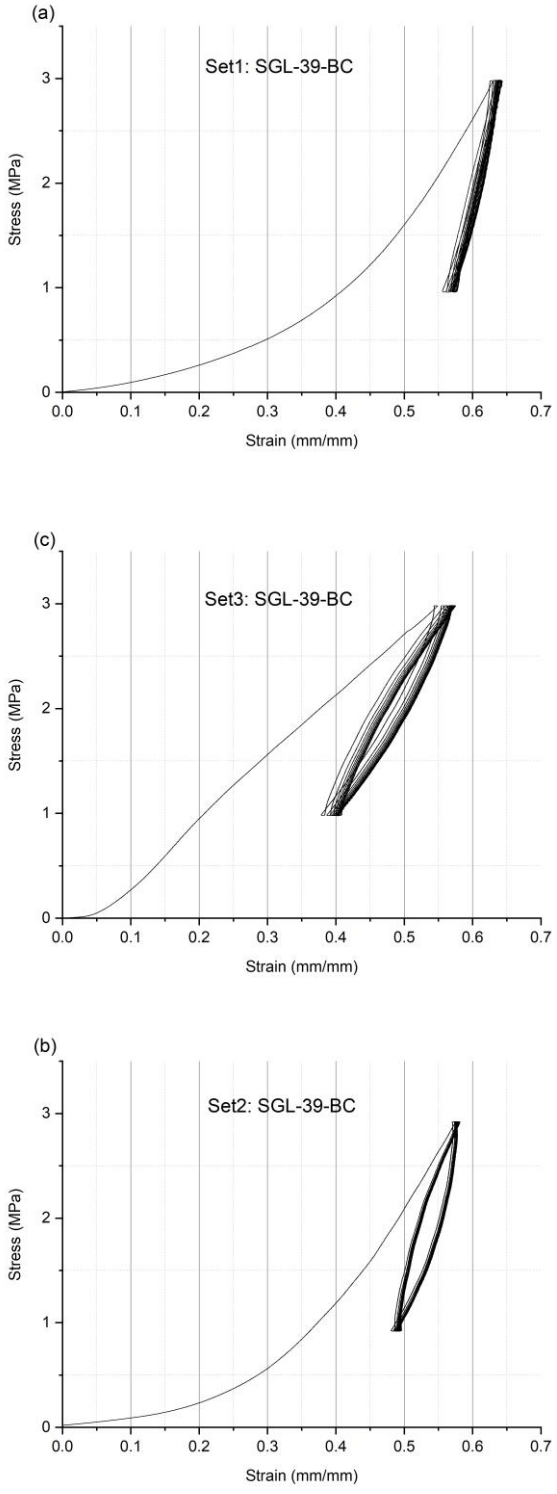

Figure 6.10 The stress-strain curves of SGL-39-BC (a) without gaskets, with (c) Teflon gaskets and (d) silicone gaskets.

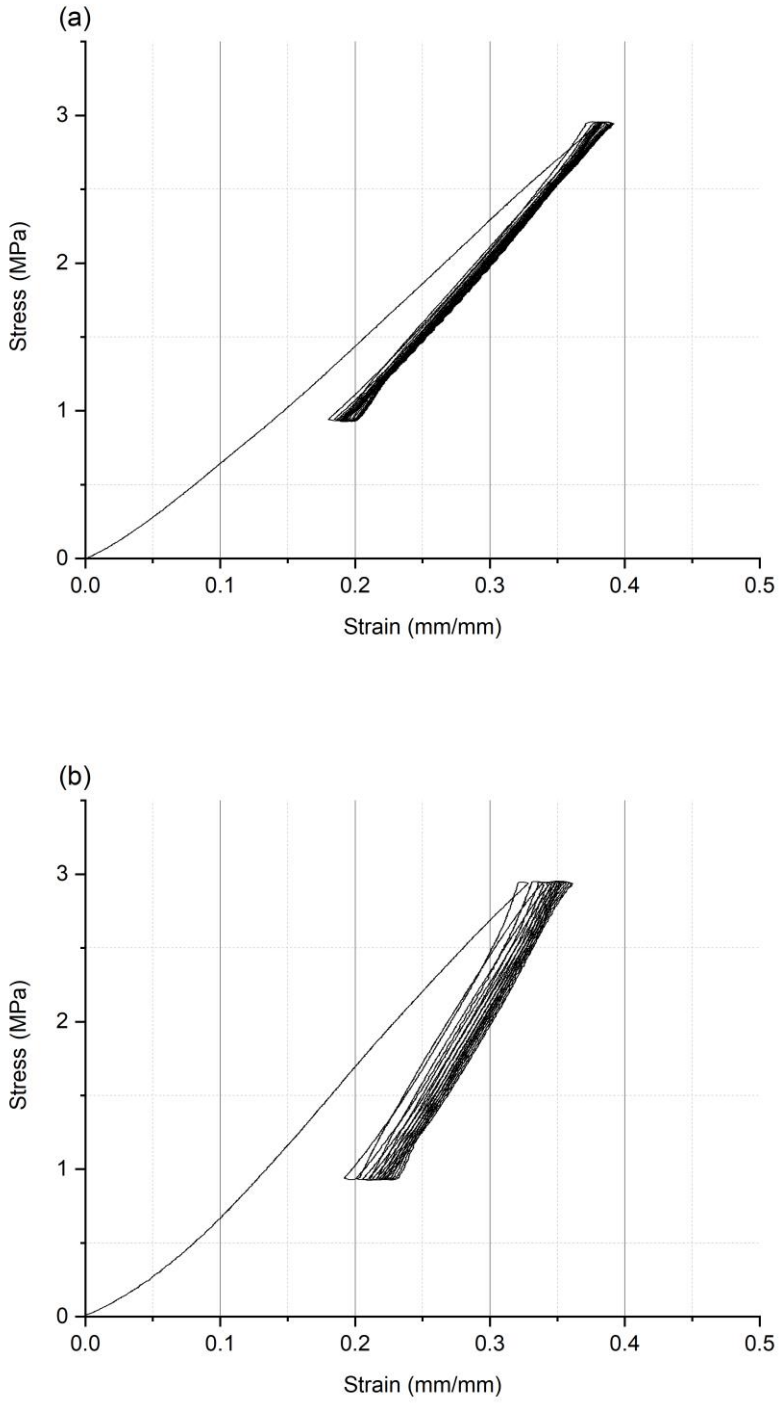

Figure 6.11 The stress-strain curves for typical samples of (a) Teflon and (b) silicon gaskets.

6.3.2 Gas permeability

The gas permeability of the tested GDL samples were experimentally estimated before and after compression tests in order to primarily evaluate the effects of the presence of the sealing gaskets. Table 6.2 shows the gas permeability of the samples before and after the compression tests. It also shows the amount of the reduction in permeability and thickness after performing the compression tests. Further, bar charts were generated for the gas permeability values to allow the readers to readily recognise the impact of compression on the gas permeability of the GDL samples (Fig. 6.12). As expected, the permeability and the thickness of the GDL samples that were subject to compression without encircling gaskets (i.e. Set 1) demonstrate significantly higher reduction in thickness and gas permeability compared to those encircled with Teflon and silicone gaskets respectively (i.e. Sets 2 and 3). This is evidently because the gaskets, owing to their higher stiffness relative to the GDL samples, limit the extent to which the GDL samples are compressed. For example, the mean thickness and permeability of the SGL 34BA samples, which were not encircled by annular gaskets when subjected to compression, have reduced by about 16 and 18%, respectively, after compression. On the other hand, the mean thickness of the GDL samples, encircled by silicone gaskets when subjected to compression tests (i.e. Set 3), have slightly reduced (slightly above 3%) and their mean gas permeability has hardly changed after compression. Fig. 6.13-Fig 6.16 show the cross-section SEM images of the investigated GDL samples (a) before compression (b) and after being exposed to compression without gaskets, (c) with Teflon gaskets and (d) with silicone

gaskets. These micrographs clearly show the controlling effect of the used gaskets on the final thicknesses of the GDL samples; compare the images listed in column (b) with those listed in columns (c) and (d). The second observation is that the silicone gaskets, although they have more or less the same thickness as the Teflon gaskets, renders the thickness and the gas permeability of the GDL samples to be less reduced compared to those tested with Teflon gaskets. This is, as could be inferred from Fig. 6.11 (a,b), attributed to the higher mechanical resistance featured by the silicone gaskets compared to Teflon gaskets. The third observation is that the MPL-coated GDL materials (i.e. SGL 34BC and SGL 39BC) demonstrate higher reductions in the mean thickness and gas permeability compared to their counterpart carbon substrates (i.e. SGL 34BA and SGL 39BA). This is more to do with the fact that the coated GDLs (SGL 34BC and SGL 39BC) experience, as a result of compression, the penetration of the MPL into the body of the carbon substrate. The MPL is much lower in porosity than the hosting carbon substrates and hence a good portion of the void fraction in the carbon substrate is replaced with the compression-induced penetrating MPL material, thus resulting in a much reduced gas permeability compared to the uncoated GDLs. Notably, one of the tested carbon substrates (i.e. SGL 39BA) is more compressible than the other (i.e. SGL 34BA) and this is due the lower density and higher porosity characterising the former carbon substrates [183], [186]; this could be also deduced from the superficial SEM images of the above two carbon substrates, namely: larger pores at the surfaces displayed by SGL 39BA; see Fig. 6.17. As expected, the MPL-coated GDLs follow the same trend as the corresponding carbon

substrates: SGL 39BC is more compressible than SGL 34BC. It should be noted that SEM surface images for the tested GDL materials before and after compression were not presented as there were no noticeable differences in the superficial morphology of the GDL sample before and after applying the compression. This is most likely due to the use of flat and smooth compressing plates and that most of the deformation is internal.

Table 6.2 Through-plane permeability before and after compression, and the percentage of both reduction in thickness and permeability. Set 1: without gaskets; Set 2: with Teflon gaskets; Set 3: with silicone gaskets.

GDL Type	Through-plane permeability before compression (m^2)	Through-plane permeability after compression (m^2)	Thickness before and after compression (μm)	Reduction in permeability (%)	Reduction in thickness (%)
SGL-34-BA					
set 1:	$(1.20 \pm 0.09) \times 10^{-11}$	$(9.88 \pm 1.94) \times 10^{-12}$	265.8 ± 4.0 / 233.8 ± 4.3	17.7	15.8
set 2:	$(1.11 \pm 0.04) \times 10^{-11}$	$(1.10 \pm 0.09) \times 10^{-11}$	268.3 ± 3.7 / 253.8 ± 2.8	0.9	5.55
set 3:	$(1.13 \pm 0.08) \times 10^{-11}$	$(1.13 \pm 0.05) \times 10^{-11}$	266.0 ± 4.4 / 257.3 ± 3.2	0	3.29
SGL-34-BC					
set 1:	$(2.63 \pm 0.90) \times 10^{-14}$	$(1.58 \pm 0.59) \times 10^{-14}$	306.0 ± 3.1 / 262.3 ± 3.8	39.9	14.3
set 2:	$(2.90 \pm 1.29) \times 10^{-14}$	$(2.48 \pm 1.08) \times 10^{-14}$	301.3 ± 4.2 / 279.0 ± 3.0	14.5	7.39
set 3:	$(3.05 \pm 1.40) \times 10^{-14}$	$(2.67 \pm 1.20) \times 10^{-14}$	303.8 ± 3.3 / 286.3 ± 3.1	12.5	5.76
SGL-39-BA					
set 1:	$(4.51 \pm 0.20) \times 10^{-11}$	$(2.65 \pm 0.26) \times 10^{-11}$	251.8 ± 3.4 / 164.0 ± 4.7	41.2	34.9
set 2:	$(4.71 \pm 0.16) \times 10^{-11}$	$(4.52 \pm 0.09) \times 10^{-11}$	253.5 ± 3.4 / 241.8 ± 3.5	4.03	4.64
set 3:	$(4.76 \pm 0.49) \times 10^{-11}$	$(4.57 \pm 0.44) \times 10^{-11}$	253.5 ± 3.6 / 245.3 ± 2.9	3.99	3.25
SGL-39-BC					
set 1:	$(1.80 \pm 0.18) \times 10^{-13}$	$(3.77 \pm 0.47) \times 10^{-14}$	300.0 ± 2.8 / 210.8 ± 3.3	79.1	79.1
set 2:	$(1.60 \pm 0.19) \times 10^{-13}$	$(1.26 \pm 0.14) \times 10^{-13}$	286.5 ± 2.9 / 266.3 ± 3.6	21.3	21.3
set 3:	$(1.76 \pm 0.29) \times 10^{-13}$	$(1.45 \pm 0.27) \times 10^{-13}$	297.0 ± 3.3 / 277.8 ± 2.9	17.6	17.6

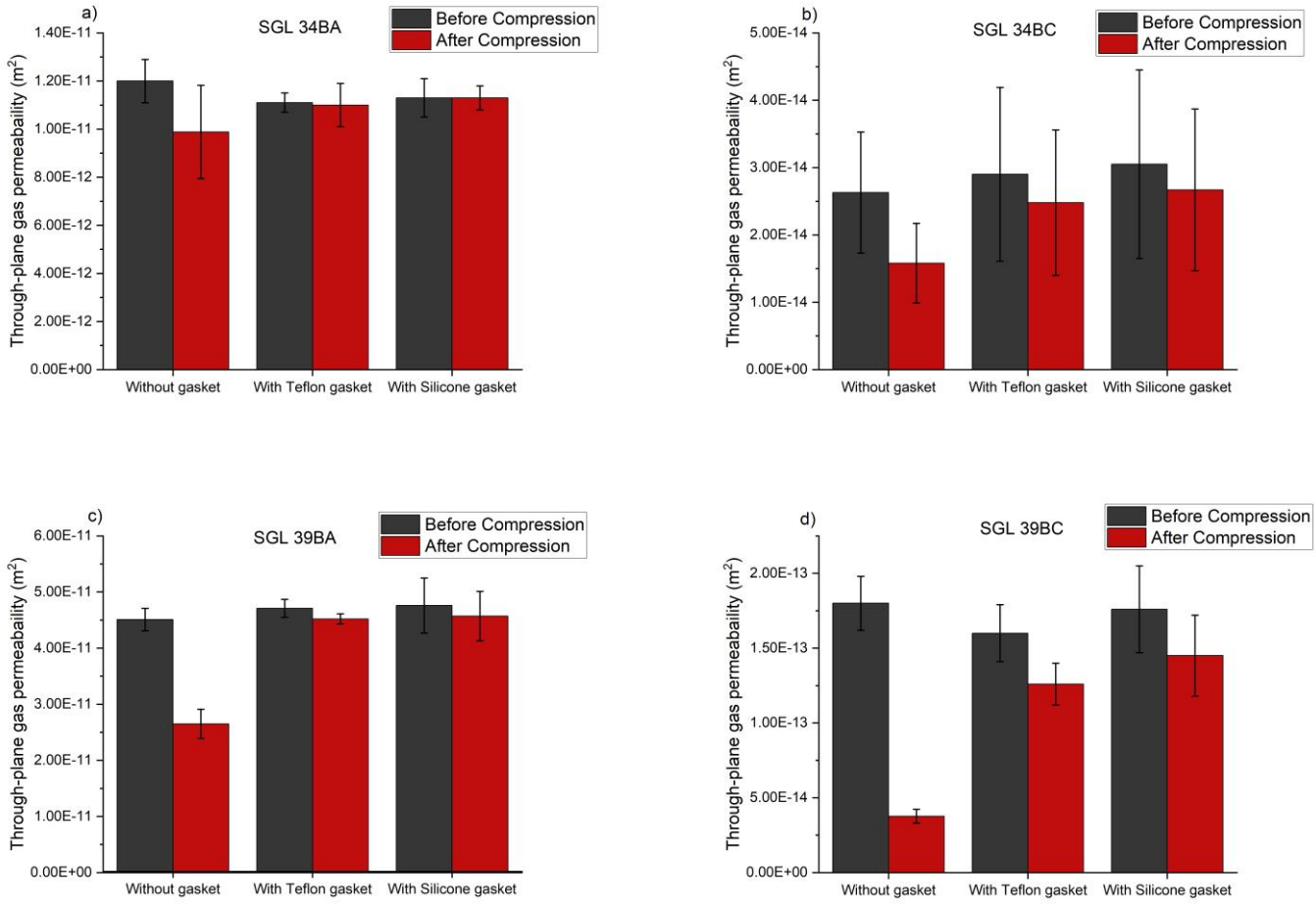

Figure 6.12 The through-plane gas permeability of the invetigated GDL materials before and after compression.

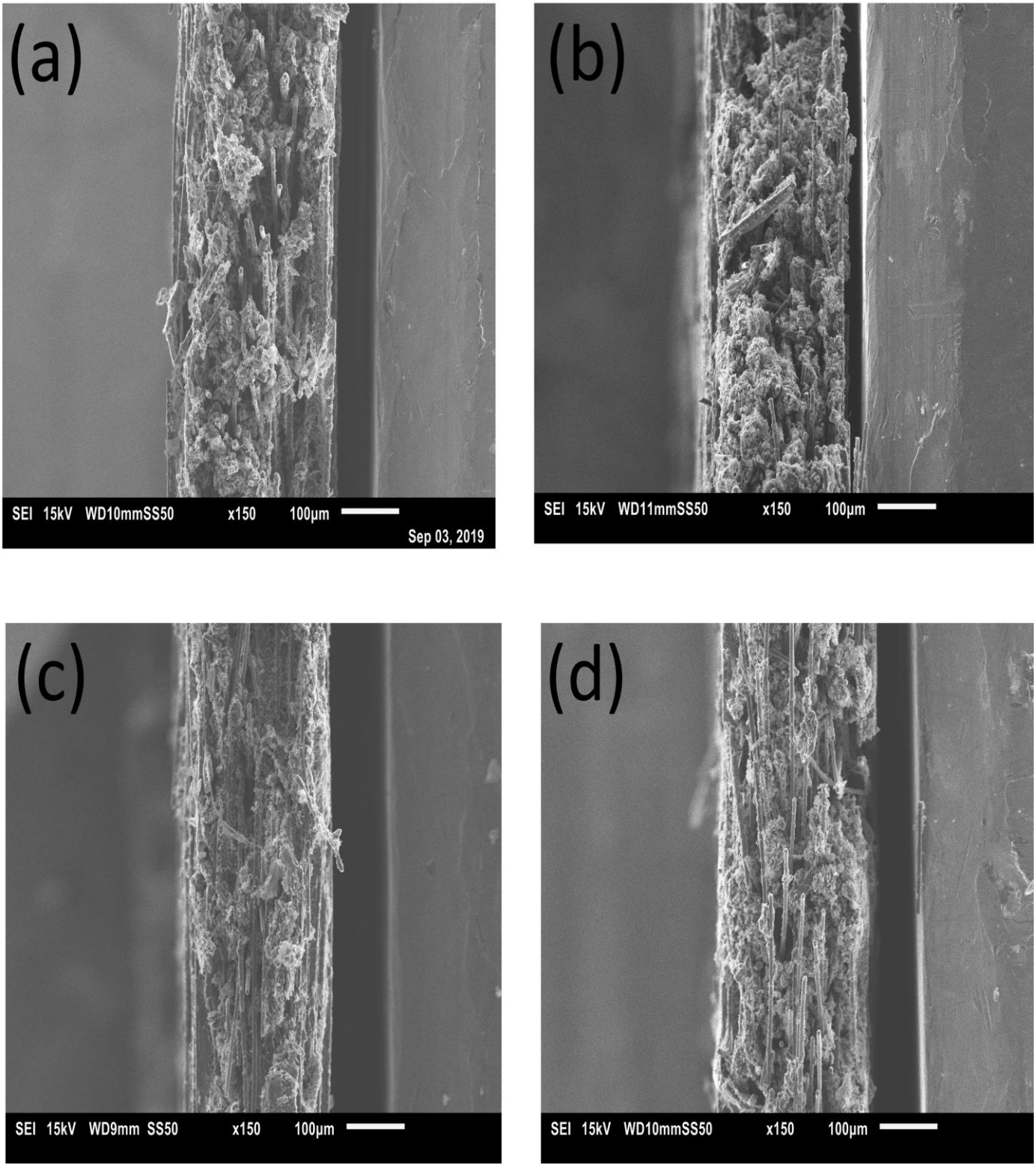

Figure 6.13 Cross-section SEM images of SGL-34-BA (a) before compression (b) after being exposed to compression without gaskets, (c) with Teflon gaskets and (d) with silicone gaskets.

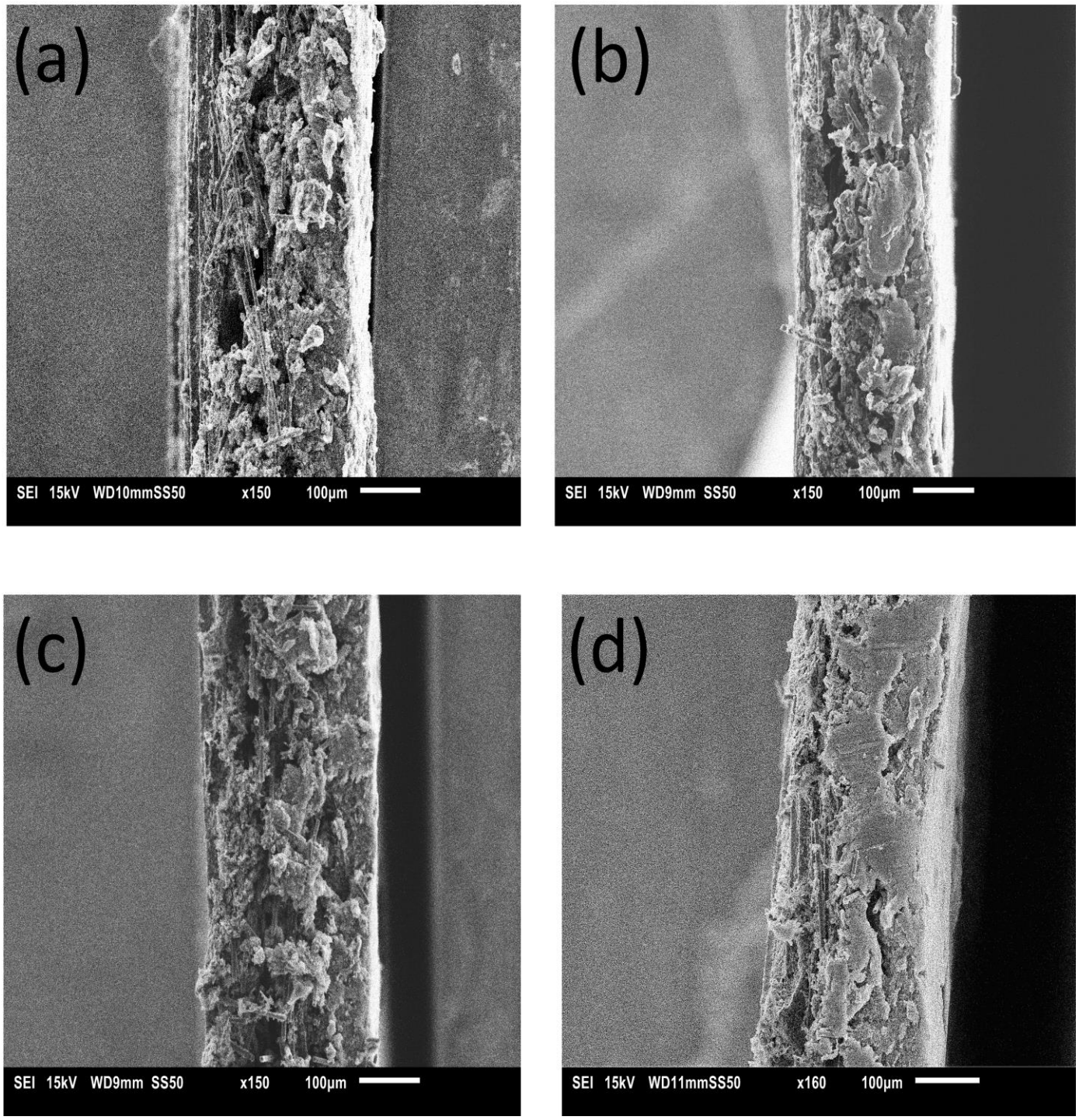

Figure 6.14 Cross-section SEM images of SGL-34-BC (a) before compression (b) after being exposed to compression without gaskets, (c) with Teflon gaskets and (d) with silicone gaskets.

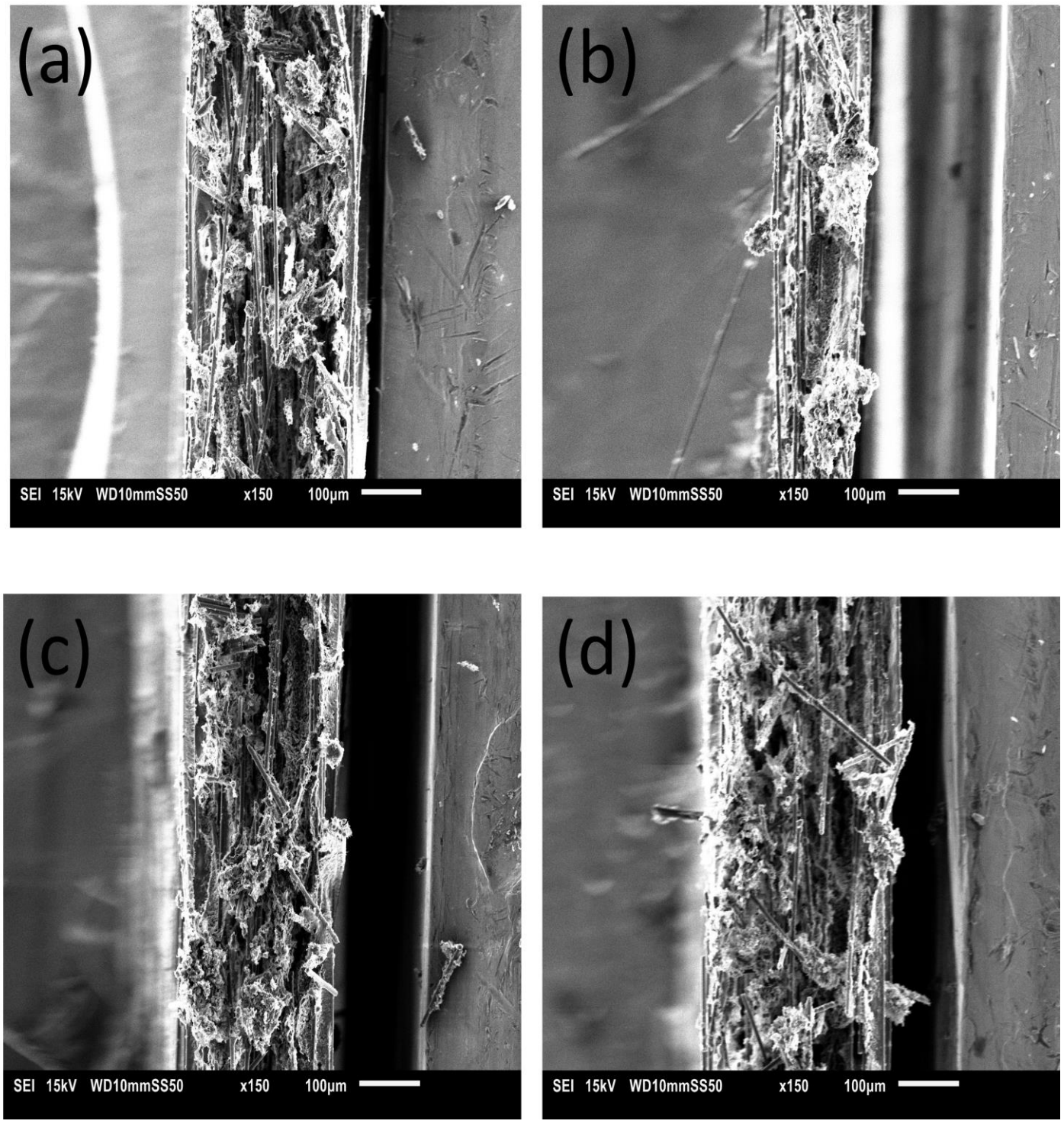

Figure 6.15 Cross-section SEM images of SGL-39-BA (a) before compression (b) after being exposed to compression without gaskets, (c) with Teflon gaskets and (d) with silicone gaskets.

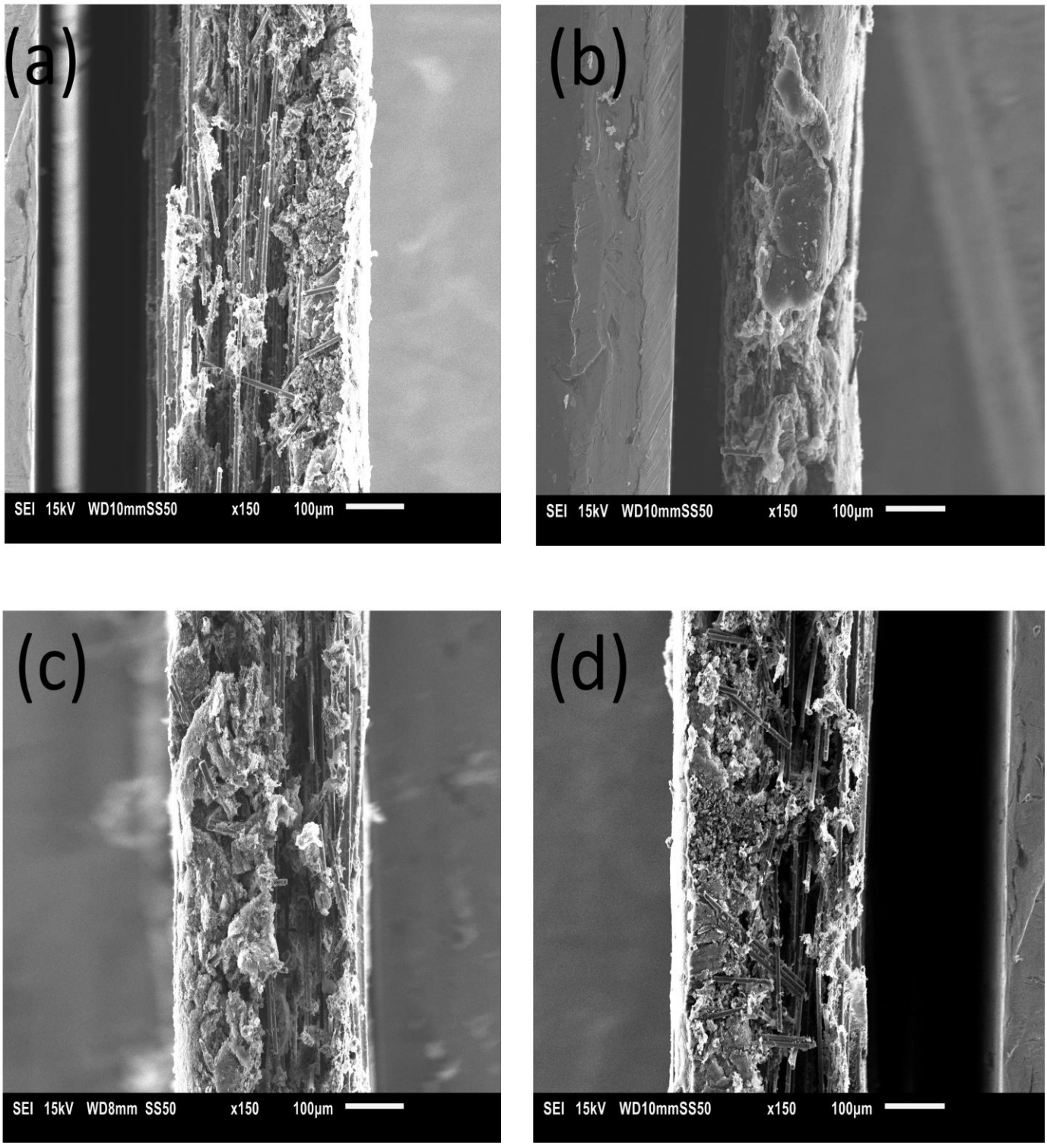

Figure 6.16 Cross-section SEM images of SGL-39-BC (a) before compression (b) after being exposed to compression without gaskets, (c) with Teflon gaskets and (d) with silicone gaskets.

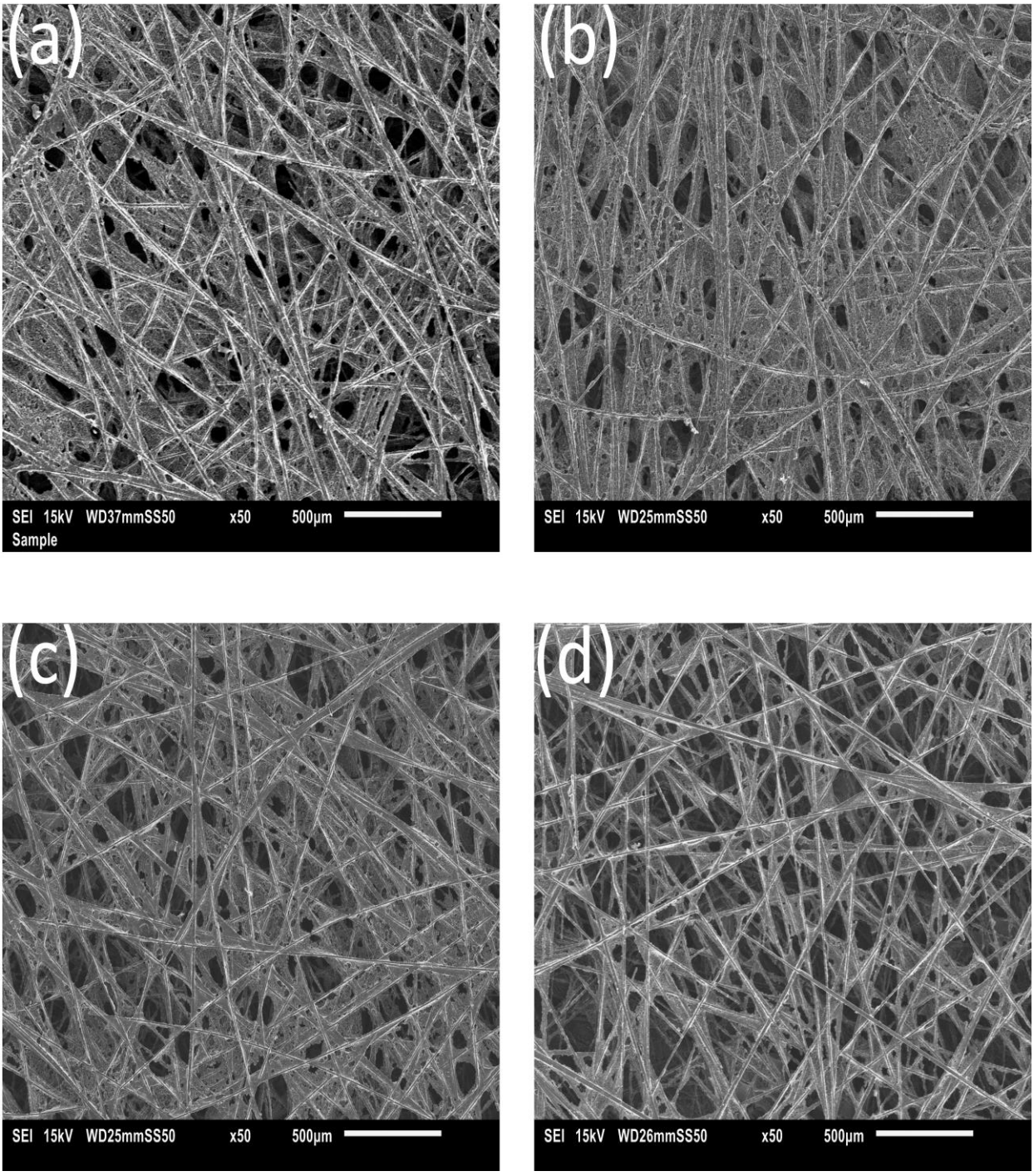

Figure 6.17 SEM surface images for (a) SGL-34-BA, (b) SGL-34-BC, (c) SGL-39-BA, (d) SGL-39-BC at a magnification of 50x.

6.3.3 Thermal stability

Fig. 6.18-6.20 show the TGA results for the tested GDL materials before and after compression. The PTFE material normally decomposes at around 600 °C [13] and therefore TGA could give an estimate of the amount of PTFE available in the tested GDL materials. Assuming that all the materials decomposing at ~ 600° is PTFE, the TGA of the uncompressed carbon substrates SGL 34BA and SGL 39BA suggests that the amount of PTFE in these GDL is around 12 wt. % (Fig. 6.18 (a) and Fig. 6.19 (a)). Following the same assumption, the amount of PTFE in the uncompressed MPL-coated GDL materials SGL 34BC and SGL 39BC is slightly higher: ~ 15 wt. % (Fig. 6.18 (b) and Fig 6.19 (b)) and this is apparently due to the presence of further PTFE material in the MPLs. The amount of PTFE in the carbon substrates SGL 34BA and SGL 39 BA, after compression, reduce from 12 wt. % to around 7 wt. % signaling that some PTFE material was lost during the compression; this observation is applicable to all the sets of samples (i.e. compression in the absence of gaskets or compression in the presence of Teflon/silicone gaskets). This is in line with some previous findings (e.g. [187] [188]) where the compression was found to cause the PTFE amount in the GDL to be reduced and this due to the breakage of carbon fibres and/or the PTFE layers coating these fibres, particularly those located under the ribs of the bipolar plates. However, the MPL-coated GDL materials behave differently; their PTFE loading is almost maintained after compression. This is probably due to the positive impact of the MPL in terms of absorbing the compressive forces and subsequently mitigating the breakage of the PTFE bonds. This is in accordance with the findings of [177] where it was found that

the compression has almost no effect on the MPL, thus corroborating our previous thought that the MPL acts as an absorbing and protective layer to the GDL sandwich.

For a given temperature above 600 °C, the weight loss of the compressed samples is less than that of the uncompressed samples; this is most likely to be due to that the compression making the GDL samples lose more decomposable materials (e.g. the binding resin [25]). This statement is supported by the observation that, for a given temperature above 600 °C, the weight loss of the GDL samples compressed with silicone gaskets is in general more than those compressed with the Teflon gaskets and this is apparently due to the higher stiffness demonstrated by the former gaskets which allows for less breakage and subsequent less loss of the decomposable material.

The TGA test was also performed for the tested gaskets (Fig. 6.20). The results confirmed that the Teflon gaskets used are pure as there was no material left above 600 °C. They also show that the Teflon gaskets are more thermally stable than the silicone gaskets in the range between 200 and 600 °C. This signifies the suitability of the Teflon gaskets for the fuel cells that operate within the above temperature range, such as phosphoric acid fuel cells (PAFCs). It is important to note that the operating temperature of PEM fuel cells is normally less than 100 °C, and therefore the thermal stability of either Teflon or silicone gaskets is not an issue.

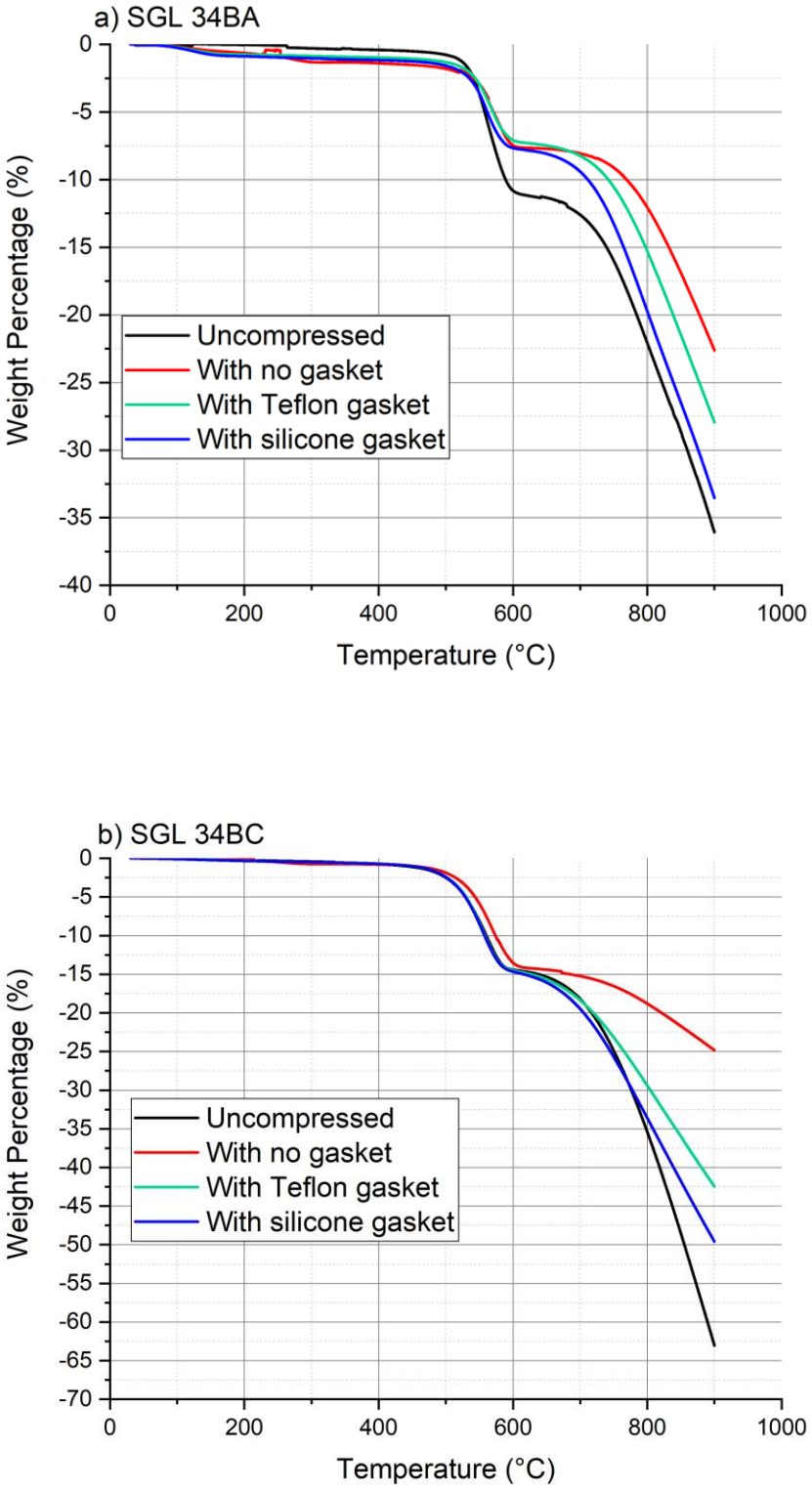

Figure 6.18 TGA data for (a) SGL 34BA, (b) SGL 34BC.

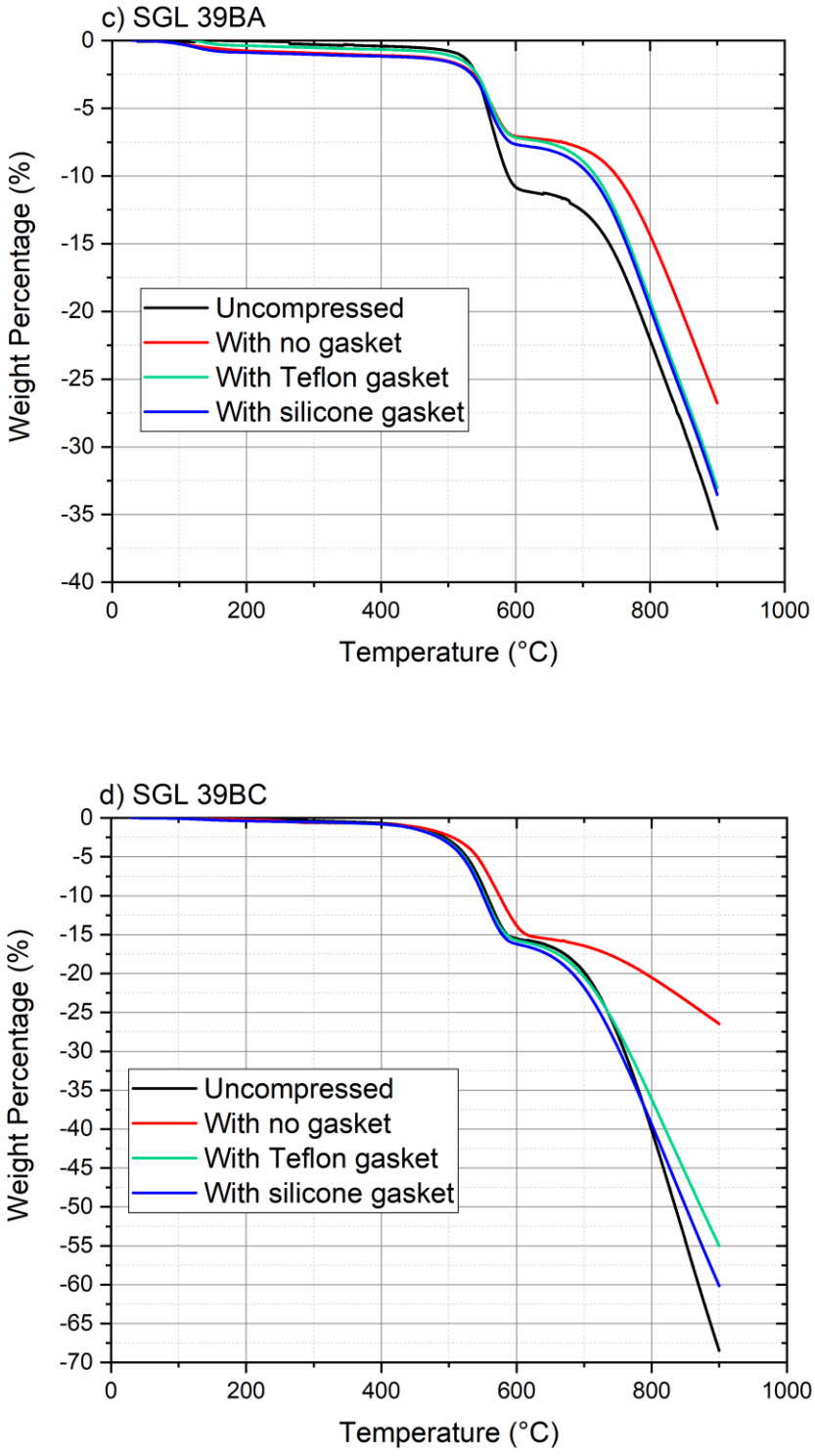

Figure 6.19 TGA data for (c) SGL 39BA, (d) SGL 39BC.

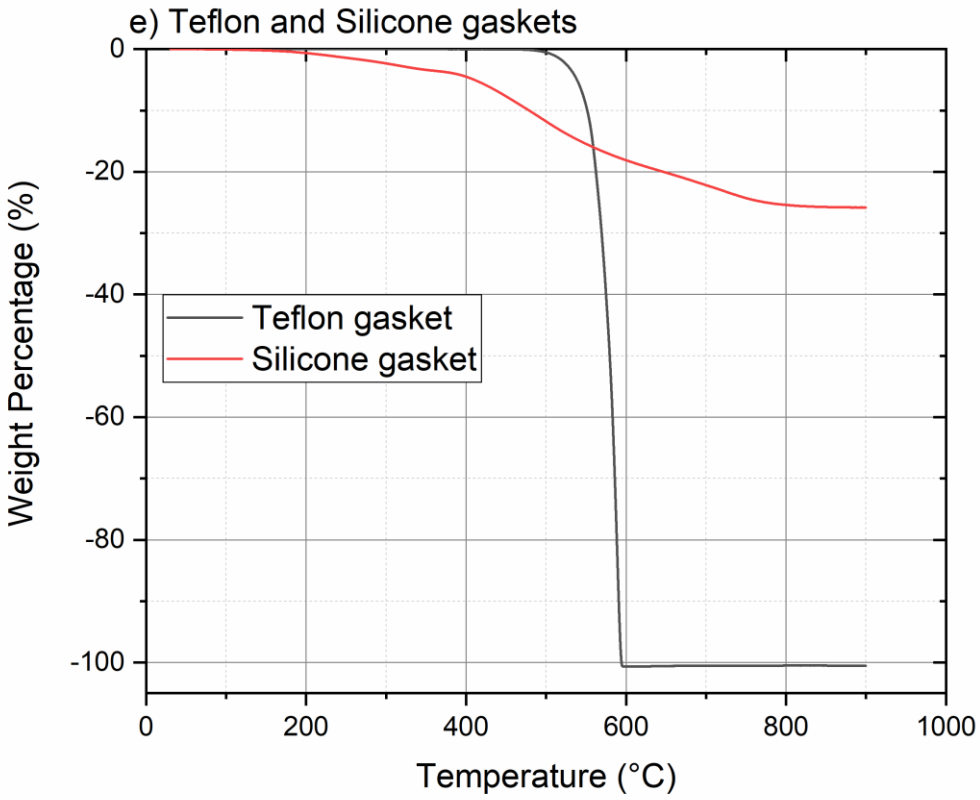

Figure 6.20 TGA data for (e) Teflon gasket, and Silicon gasket.

6.4 Conclusions

The compressibility, the gas permeability and the thermal stability of two uncoated GDLs (or carbon substrates) and two MPL-coated GDLs have been investigated before and after preforming ex-situ realistic compression tests (mimicking the compressive stresses the GDL experience within the fuel cell housing) in the absence/presence of two commercial sealing gaskets (Teflon and silicone gaskets). The following are the main findings of the study:

- The tested GDL materials are expectedly less deformed in the presence of the gaskets. They are also sensitive to the type of the gasket: they are less deformed with silicone gaskets than with Teflon gaskets and this is due to higher stiffness of the former type of gaskets.

- The reduction in the gas permeability and the thickness of the tested GDL materials with Teflon gaskets are higher than that with the silicone gasket and this is evidently due to the relatively higher stiffness of the latter gaskets.

- The MPL-coated GDL samples feature more reduction in their gas permeability and thickness compared to the corresponding bare carbon substrates; this is due to the penetration of the MPLs into the body of the carbon substrates as a result of compression.

- The TGA data shows the PTFE loading of the tested carbon substrates, either without or with gaskets, reduces by about 40% after performing the compression test, thus indicating that some PTFE material is stripped off as a result of the applied compressive forces. The MPL-coated GDLs behave differently as they appear to lose no PTFE material after compression.

- The GDL samples, subject to compression, show less weight loss above 600 °C compared to uncompressed samples and this is most likely due to the presence of less binding materials that are probably lost due to the compression. This is corroborated by the observation that more weight loss is observed for the GDL samples compressed along with the silicone gaskets that are mechanically stronger than the Teflon gaskets.

7 PEM FUEL CELL MODELLING

7.1 Introduction

In general, numerical modelling has many benefits in terms of optimisation and materials design and their specifications. Further, mathematical modelling reduces costs and shortens the design cycle. One of the most powerful pieces of software for the modelling of PEM fuel cells is the Fuel Cell modules within ANSYS Fluent. The PEM fuel cell is an electrochemical system that converts a chemical energy stored in hydrogen fuel into electricity and this involves many physical processes that represent mass, heat, and charge transfer. The detailed understanding of the interactions between these transport phenomena often requires sophisticated mathematical modelling. Therefore, the effects of the GDL gas permeability and wettability (in the form of the contact angle) of the GDLs on the PEM fuel cell performance are numerically investigated in this chapter. The gas permeability and the contact angle were experimentally estimated and presented in Chapters 5 and 6. The motivation behind undertaking of this investigation is to study the effects of the experimentally estimated through-plane gas permeability and the contact angle of the gas diffusion layers on the overall performance of the PEM fuel cell. Further, a parametric study is conducted to investigate how sensitive the fuel cell performance and the local distribution of the key variables are to substantial changes in the gas permeability and the contact angle. Also, the sensitivity of the fuel cell performance to the absence (a single phase model) or presence (i.e. a multiphase model) of liquid water is investigated. To this end, this investigation will provide much better insights on (i) the contribution

of convective flow to the transport of gases in the GDLs (ii) the role of the hydrophobicity of the GDL (in the form of contact angles) in driving excess water away from the catalyst layers and (iii) how the presence of liquid water impacts the fuel cell performance (it turns out that the impact is positive as will be shown in Section 7.3.1). It should be noted in-house fuel cell tests were not performed due to inability to access fuel cell laboratory during the lockdown. Therefore, the model has been validated using some well-known and reliable fuel cell performance data from the literature.

7.2 Model formulation

Figure 7.1a shows the section of the fuel cell that was modelled in this study, and Figure 7.1b shows the dimensions of the modelled section of the PEM fuel cell. The entire fuel cell was not modelled as it would be computationally very expensive to do so. The modelled section of the fuel cell should be representative of the key physics that is taking place within the fuel cell and this has been simplified by taking into account the symmetry in the geometry. In addition, Table 7.1 presents the dimensions of the components of the computational domain which are the dimensions of the real-life fuel cell reported in [189].

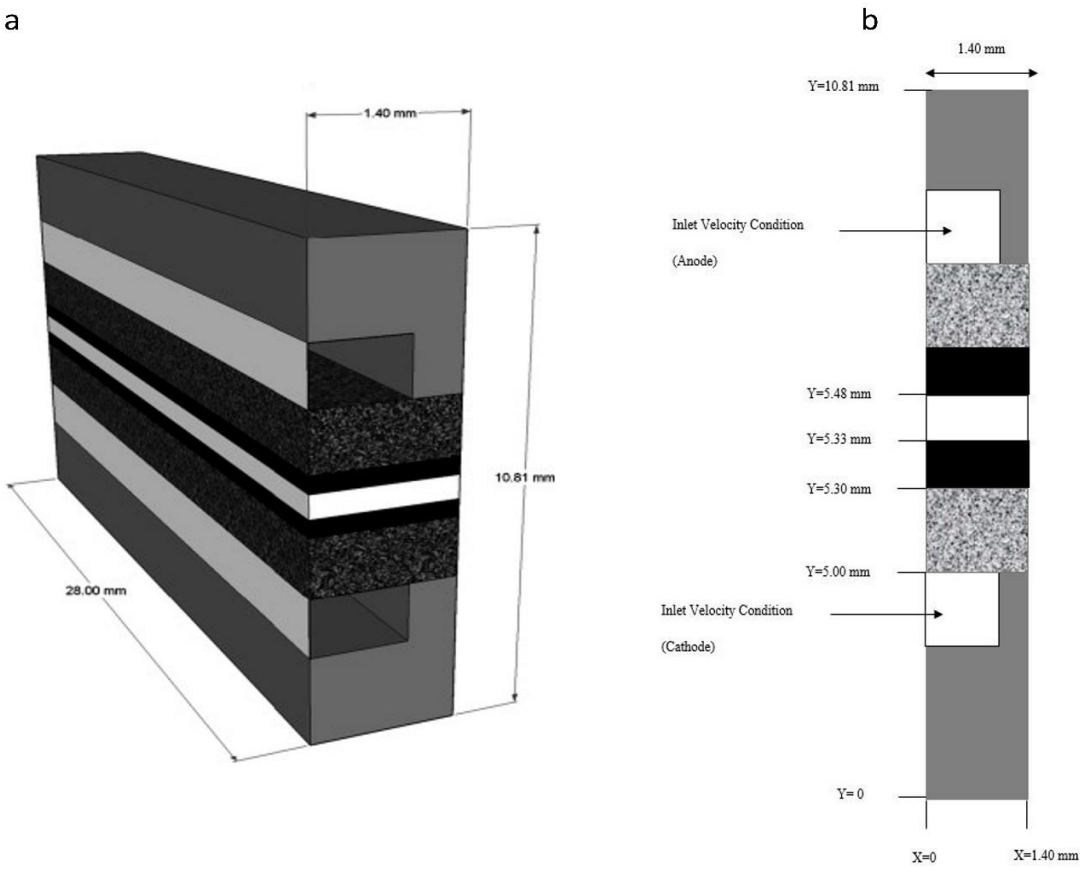

Figure 7.1 a) The section of the fuel cell modelled in the study, b) the dimensions of the modelled PEM fuel cell section.

Table 7.1 The dimensions of the components of the computational domain [189].

Dimension	Value
Channel length	2.8×10^{-2} m
Channel height	2.0×10^{-3} m
Channel width	2.0×10^{-3} m
Land area width	8.0×10^{-4} m
GDL thickness	3.0×10^{-4} m
Catalyst layer thickness	3.0×10^{-5} m
Membrane thickness	1.5×10^{-4} m

7.1.1 Model assumptions and simplifications:

- Fuel cell operates under steady-state conditions.
- The flow in the channels is laminar due to the low Reynolds numbers.
- The membrane is impermeable to the gases.

7.1.2 Governing equations

The three-dimensional (3D) model takes into account the different PEM fuel cell physics: transfer of mass, momentum, chemical species, charge (protonic or electronic) and heat. Also, it accounts for the electrochemical reactions in the catalyst layer (CL). The transport phenomena in the PEM fuel cell are expressed in the form of conservation equations [26], [177], [178] and these equations are mathematically described as follows:

Conservation of mass, momentum and species equations

Mass Conservation	$\nabla \cdot (\varepsilon \rho \vec{v}) = 0$	(7.1)
Momentum Conservation	$\nabla \cdot (\varepsilon \rho \vec{v}\vec{v}) = -\varepsilon \nabla P + \nabla \cdot (\mu \nabla \varepsilon \vec{v}) + \frac{\varepsilon^2 \mu \vec{v}}{K}$	(7.2)
Species Conservation	$\nabla \cdot (\varepsilon \rho \vec{v} Y_i) = \nabla \cdot (\rho D_i^{eff} \nabla Y_i) + S_i$	(7.3)

where ρ is the fluid density, P is the pressure, μ is the dynamic viscosity of the fluid, $\vec{v}$ is the fluid velocity vector, ε and K are the porosity and the permeability of the porous medium, respectively, Y_i and D_i^{eff} are the mass fraction and the effective mass diffusivity of the species i, respectively, and S_i is the source term

of species i (hydrogen, oxygen or water) involved in the electrochemical reactions which are given as follows:

$$S_{H_2} = -\frac{i_a a_a}{2F} M_{H_2} \tag{7.4}$$

$$S_{O_2} = -\frac{i_c a_c}{4F} M_{O_2} \tag{7.5}$$

$$S_{H_2O} = \frac{i_c a_c}{2F} M_{H_2O} \tag{7.6}$$

where i_a and i_c are, respectively, the anodic and cathodic current densities, a_a and a_c are, respectively, the anodic and cathodic specific surface areas, F is the Faraday's constant (96485 C/mol) and M is the molecular weight. The effective mass diffusivity, D_i^{eff}, is calculated using the Bruggmann's correlation [179], [180]:

$$D_i^{eff} = \varepsilon^{\tau} D_i \tag{7.7}$$

where τ is the tortuosity of the porous medium and D_i is the bulk diffusion coefficient of the species i.

Conservation of energy equation

$$\nabla \cdot \left(\rho c_p \vec{v} T\right) = \nabla \cdot \left(\mathrm{K}_{eff} \nabla T\right) + S_e \tag{7.8}$$

where c_p is the specific heat capacity of the gas mixtures, S_e is the energy source term, and K_{eff} is the effective thermal conductivity calculated using the Dagan correlation [106]:

$$\mathrm{K}_{eff} = -2\mathrm{K}_{sol} + [\frac{\varepsilon}{2\mathrm{K}_{sol}+\mathrm{K}_F} + \frac{1-\varepsilon}{3\mathrm{K}_{sol}}]^{-1} \quad (7.9)$$

where K_{sol} and K_F are the thermal conductivities for the solid-phase and gaseous (fluid) phase conductivities, respectively.

Conservation of charge equations

The electronic and protonic charges are conserved and governed using the following equations [190]:

$$\nabla \cdot (\sigma_s \nabla \phi_s) = \quad (7.10)$$

$$\begin{cases} j_a = i_{0,a}^{ref} a_a \left(\frac{c_{H_2}}{c_{H_2}^{ref}}\right)^{0.5} \left[exp\left(\frac{\alpha_{a,a}F}{RT}\eta_{act,a}\right) - exp\left(\frac{\alpha_{a,c}F}{RT}\eta_{act,c}\right)\right] \\ j_C = i_{0,c}^{ref} a_c \left(\frac{c_{O_2}}{c_{O_2}^{ref}}\right) \left[exp\left(\frac{\alpha_{c,a}F}{RT}\eta_{act,c}\right) - exp\left(\frac{\alpha_{c,c}F}{RT}\eta_{act,c}\right)\right] \end{cases}$$

$$\nabla \cdot (\sigma_m \nabla \phi_m) = \quad (7.11)$$

$$\begin{cases} j_a = -i_{0,a}^{ref} a_a \left(\frac{c_{H_2}}{c_{H_2}^{ref}}\right)^{0.5} \left[exp\left(\frac{\alpha_{a,a}F}{RT}\eta_{act,a}\right) - exp\left(\frac{\alpha_{a,c}F}{RT}\eta_{act,c}\right)\right] \\ j_C = i_{0,c}^{ref} a_c \left(\frac{c_{O_2}}{c_{O_2}^{ref}}\right) \left[exp\left(\frac{\alpha_{c,a}F}{RT}\eta_{act,c}\right) - exp\left(\frac{\alpha_{c,c}F}{RT}\eta_{act,c}\right)\right] \end{cases}$$

where ϕ_s and ϕ_m are, respectively, the solid and membrane phase potentials, σ_s and σ_m are, respectively, the solid and membrane phase conductivities potential, j_a and j_c are the volumetric current densities for the reactions at the anode and cathode electrodes, respectively, a_a and a_c are the specific areas of the anode and cathode electrodes, respectively, and F is the Faraday's constant (96485 C/mol). Also, c_{H_2} , c_{O_2} , are the concenrtrations of the hydrogne and oxygen, respectively, and $c_{H_2}^{ref}$, $c_{O_2}^{ref}$ are the reference concentrations of hydrogen and oxygen, respectively. The specific surrface area (a_c or a_a) is given as follows [26]:

$$a = \frac{Catalyst\ loading\ \times\ Surface\ area}{Catalyst\ layer\ thickness} \tag{7.12}$$

where i^{ref} in Equations (7.10) and (7.11) is the reference exchange current density, and $\alpha_{a,a}$ and $\alpha_{a,c}$ are the anodic and the cathodic transfer coefficients for the reaction at the anode, respectively, and $\alpha_{c,a}$ and $\alpha_{c,c}$ are the anodic and the cathodic transfer coefficients for the reaction at the cathode, respectively. The activiation overpotential η can be calculated as follows [26], [190] :

$$\eta_{=\phi_s-\phi_m-E_o}\ (\text{for cathode catalyst}) \tag{7.13}$$

$$\eta_{=\phi_s-\phi_m}\ (\text{for anode catalyst}) \tag{7.14}$$

where E_o in Eq. (7.13) is the theoretical potential of the fuel cell and it is given as follows [142]:

$$E_r = 1.482 - 0.000845T + 0.0000431T \ln\left(p_{H_2} p_{O_2}^{0.5}\right) \tag{7.15}$$

Where p_{H_2} is the partial pressure of hydrogen and p_{O_2} is the partial pressure of oxygen. σ_s is the electrical coductivity of the electrically-conduting components and σ_m is the membrane coductivity σ_m and is given as follows [142]:

$$\sigma_m = (0.005139\lambda - 0.00326)\exp\left[1268\left(\frac{1}{303} - \frac{1}{T}\right)\right] \tag{7.16}$$

where λ is the water conent:

$$\lambda = \begin{cases} 0.043 + 17.18ac - 39.85ac^2 36.09ac^3 & for\ 0 < ac \leq 1 \\ 14 + 1.4(ac - 1) & for\ 1 < ac \leq 3 \\ 16.8 & for\ ac > 3 \end{cases} \quad (7.17)$$

where ac is the water activity, which is given as follows:

$$ac = \frac{P_v}{P_{sat}} \quad (7.18)$$

where P_v is the partial pressure of the water vapour, and P_{sat} is the saturation pressure of the water which is given as follows [72]:

$$\log P_{sat} = -2.1794 + 0.02953(T - 273.15) - 9.1837 \times 10^{-5} (T - 273.15)^2 + 1.4454 \times 10^{-7}(T - 273.15)^3 \quad (7.19)$$

The model is multiphase and as such the transport of liquid water is taken into account through the water saturation or s (i.e. the volume fraction of the liquid water) which is obtained using the conservation equation:

$$\frac{\partial(\varepsilon\, \rho_l s)}{\partial_t} + \nabla.(\rho_l \overrightarrow{v_l} s) = r_w \quad (7.20)$$

where ρ_l is the density of liquid water, $\overrightarrow{v_l}$ is the velocity of liquid water and r_w is the condensation rate of water which is given by:

$$r_w = c_r \max([(1 - s)\frac{P_{wv} - P_{sat}}{RT} M_w, H_2O, [-s\rho_l]) \quad (7.21)$$

where c_r is the condensation rate constant (100 s^{-1}). The capillary pressure can be calculated as a function of s and given as follows:

$$P_c = \begin{cases} \frac{\sigma cos\theta_c}{\left(\frac{K}{\varepsilon}\right)^{0.5}}(1.417(1-s) - 2.12(1-s)^2 + 1.263(1-s)^3 \,, \theta_c < 90° \\ \frac{\sigma cos\theta_c}{\left(\frac{K}{\varepsilon}\right)^{0.5}}(1.417s - 2.12s^2 + 1.263s^3) \qquad\qquad , \theta_c > 90° \end{cases} \tag{7.22}$$

where ε is the porosity, σ is the surface tension (N/m^2), θ_c is the contact angle and K the absolute permeability. Table 7.2 shows the physical parameters used in the model. where ε is the porosity, σ is the surface tension (N/m^2), θ_c is the contact angle and K the absolute permeability. Table 7.2 shows the physical parameters used in the model which were taken from the fuel cell experiments reported in[189], [191].It should be noted that the model has been validated with the experimental data reported in [191] as they were, compared to those reported in [189], closer to the performance data of the fuel cells available in the market. To this end, the physical parameters were first looked for in [191] and, if missing, taken from [189] where similar materials for the fuel cell components to those of [191] were used.

Table 7.2 The physical parameters used in the model.

Property	Value
Operating temperature	353 K [191]
pressure at anode	3 atm [191]
pressure at cathode	5 atm [191]
Relative humidity of inlet gases	100%
Oxygen/nitrogen molar ratio in air	0.79 /0.21 [191]
Catalyst layer porosity	0.4 [189]

GDL porosity	0.7 [189]
GDL permeability	4.97×10^{-13} m^2 [189]
Electrical conductivity of solid phase	4000 S/m [189]
Ionic conductivity of the membrane	0.6 S/m [191]
Catalyst layer permeability	1×10^{-13} m^2 [189]
Membrane permeability	1.8×10^{-18} m^2 [189]
Thermal conductivity of electrodes	75 W/(m-K) [191]
Thermal conductivity of Bipolar plates	75 W/(m-K) [191]
Thermal conductivity of the membrane	0.67 W/(m-K) [191]
Faraday constant	96485 C/mol
Universal gas constant	8.314 J/(mol-K)
Active area	11.56×10^{-4} m^2 [189]
Anode inlet gas velocity	0.42 m/s [189]
Cathode inlet gas velocity	1.06 m/s [189]
Anode inlet mass fraction of hydrogen	0.37 [189]
Anode inlet mass fraction of water	0.63 [189]
Cathode inlet mass fraction of oxygen	0.22 [189]
Cathode inlet mass fraction of water	0.06 [189]
Cathode inlet mass fraction of nitrogen	0.72 [189]
Anode concentration exponents	0.5 [191]
Cathode concentration exponents	1 [191]
Anode reference exchange current density, $i_{0,a}^{ref}$	6000 A/m² [191]

Cathode reference exchange current density, $i_{0,c}^{ref}$	0.0044 A/m² [191]
Transfer coefficients for anode reaction	0.5 [191]
Transfer coefficients for cathode reaction	1 [191]

7.1.3 Boundary conditions and meshing

The velocities of the gas mixtures (humidified air and humidified hydrogen) were prescribed at the inlets and the outlets were set to have zero pressure boundary conditions. The symmetry boundary conditions were imposed on the right and left sides (at x=0, x=1.4 mm); see Figure 7.1 and constant temperature boundary conditions were imposed at the surfaces of the current collectors (i.e. at y=0 and y= 10.81mm). The computational domain was meshed using the arrangement shown in Table 7.3 and Figure 7.2 where it should be noted that the number of elements in the z-direction (i.e. the direction along the length of the channel) is 722. To ensure having mesh-independent solutions, the number of meshes shown in Table 7.3 were increased by a factor of 2. The variation between the solutions of the two meshes was found to be negligible (around 0.32% in the average current density at 0.55 V). Therefore, the computational domain with the original smaller number of mesh was used for the study in order to save computation time.

Table 7.3 Number of mesh in the x- and y-directions for all the fuel cell components. The number of mesh in the z-direction is 722.

Component	x-direction	y-direction
GDL	49	10
Catalyst layer	49	1
Membrane	49	5
Flow channel	36	65
Current collector	13	176

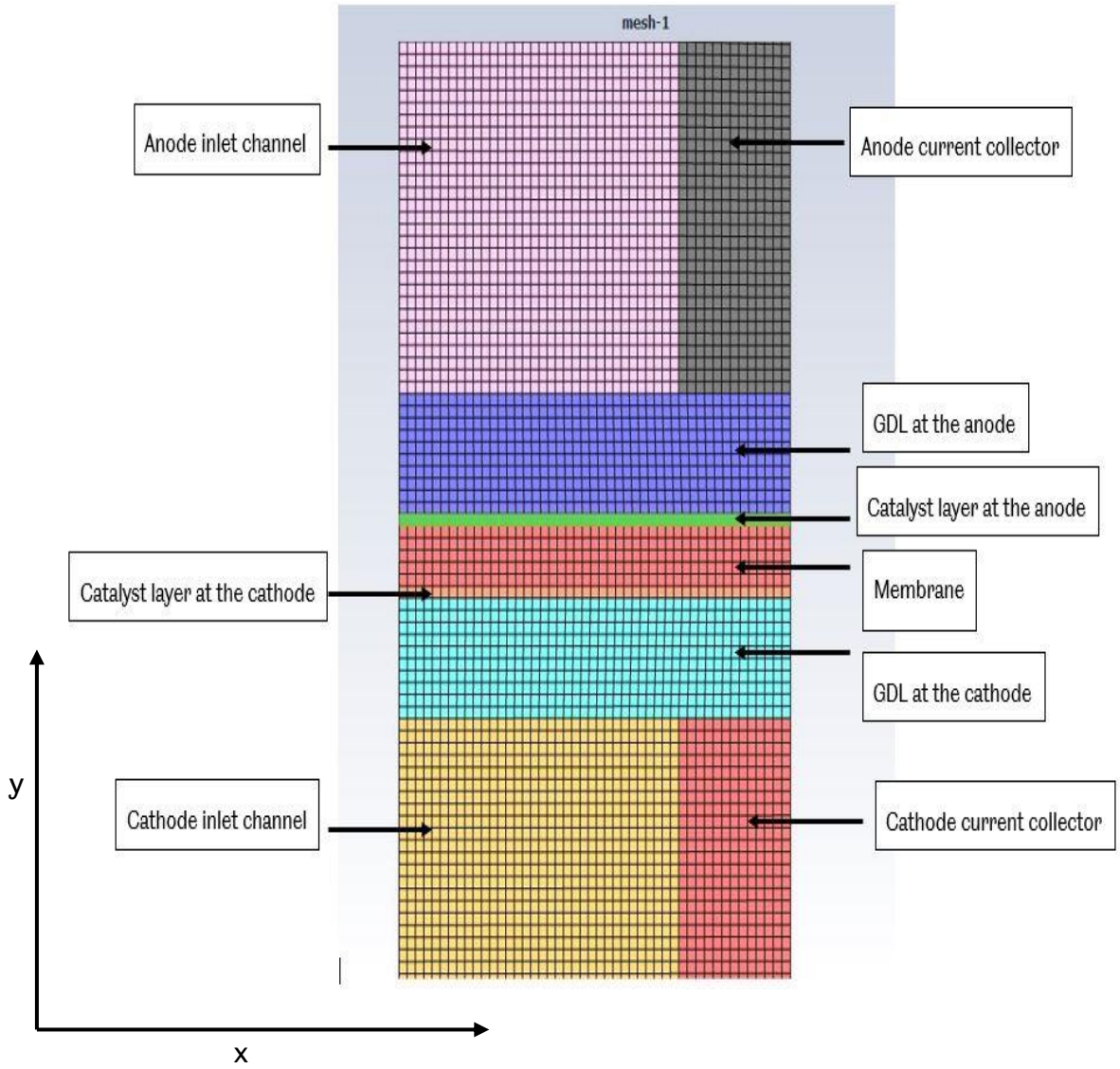

Figure 7.2 The front view of the mesh of the computational domain. Note that the upper parts of the collectors are not shown in order to clearly present the mesh of the MEA components.

7.2 Model Validation

7.2.1 Operating and physical properties for the base case model

For validation, the key outcome of the model (i.e. the polarisation curve) was compared with the corresponding experimental data reported by Ticianelli et al.

[192]. Figure 7.3 shows that the modelling and experimental data are in very good agreement, imparting confidence in the accuracy of the predictions of the model.

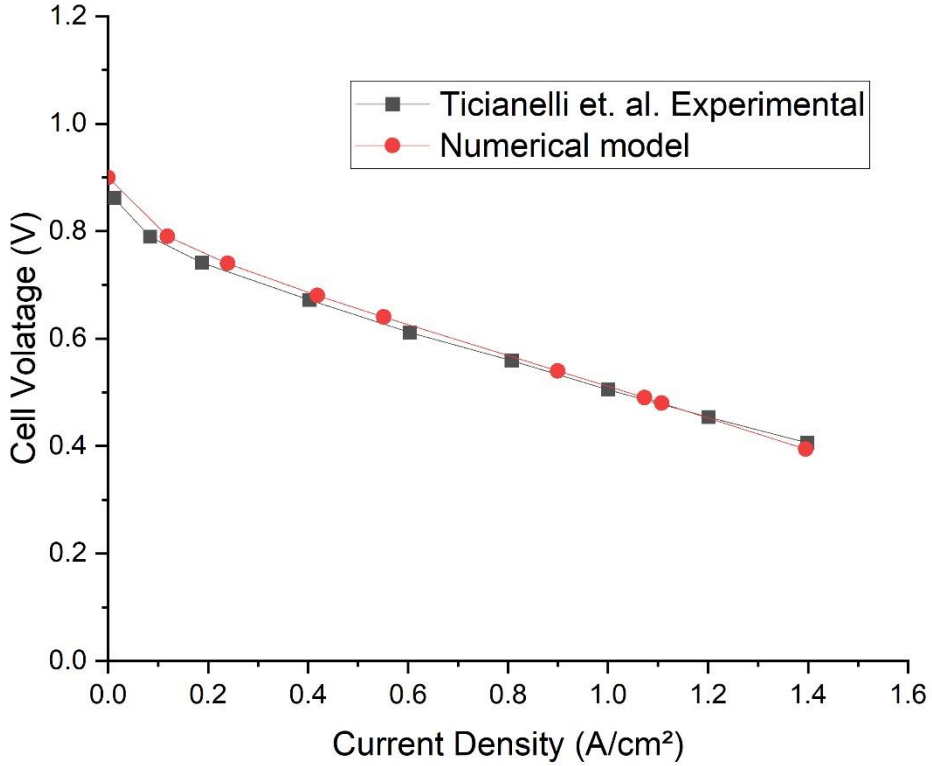

Figure 7.3 The modelling data (generated from the present model) and the experimental data as reported in [192] **for the polarisation curve of the fuel cell.**

7.3 Results and Discussions

7.3.1 Single phase model vs. multiphase model

Water is often assumed to be in a vapour form. However, in reality water may exist in either vapour or liquid form. To investigate how the nature of the water affects the results, the simulations were also run by first assuming single phase flow (only water vapour exists). Fig 7.4 shows the polarisation curves for the

single phase and multiphase models and Fig 7.5 and 7.6 show the local distribution of the current density and oxygen mole fraction at the mid-thickness of the cathode GDL, respectively. It may be clearly observed from the polarisation curves and the local distributions of current density and oxygen mole fraction that a single phase model underestimates the PEM fuel cell performance. This is mainly due to the neglect of the positive effect of the liquid water in terms of improving the ionic conductivity of the membrane: the mean ionic conductivity of the membrane for the single phase model is 8.129 S/m whereas it is 10.351 S/m for the multiphase model at 0.55 V. As stated in the earlier sections, the multiphase model was used for the investigations.

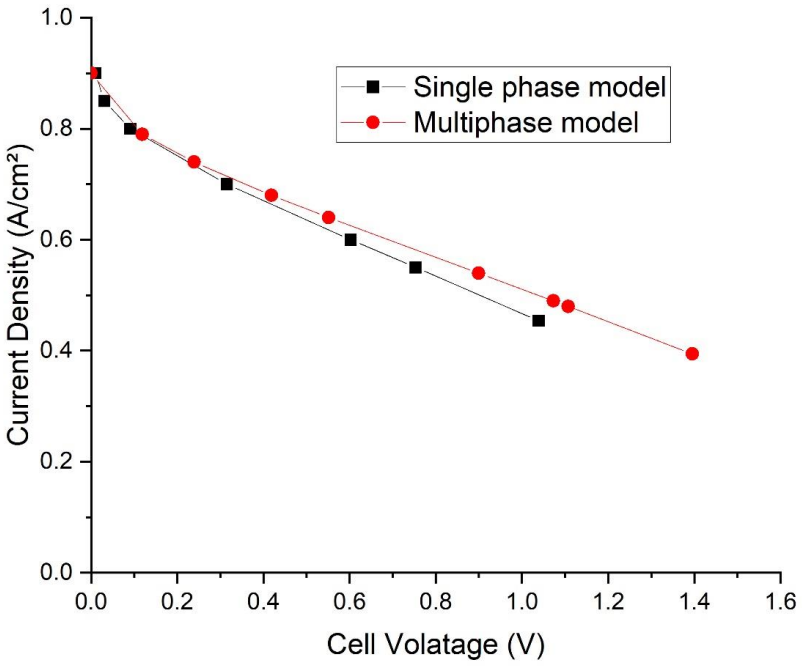

Figure 7.4 Polarisation curves as generated by the single and multiphase models.

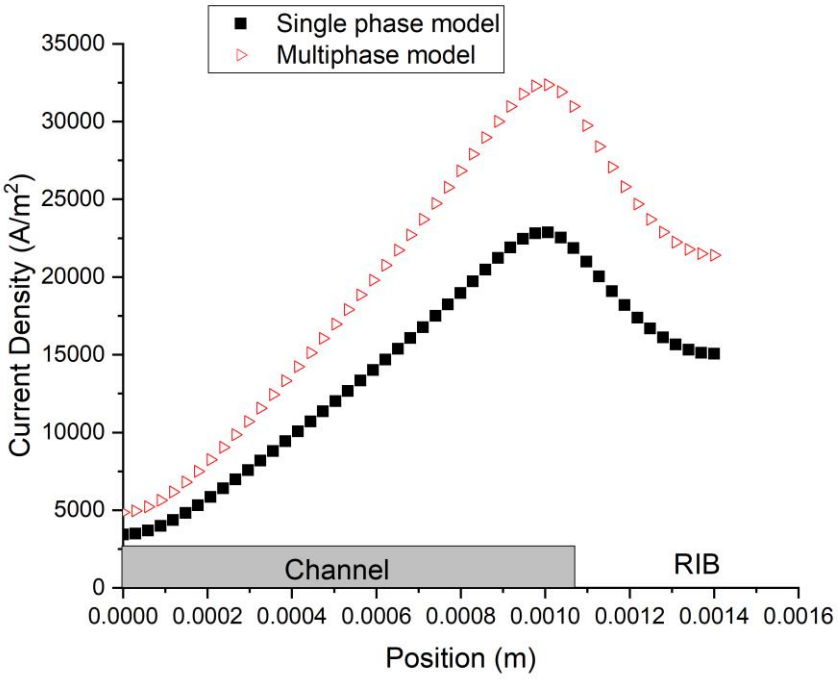

Figure 7.5 Current density distribution at the mid-thickness of the cathode GDL for both the single-phase and multiphase models.

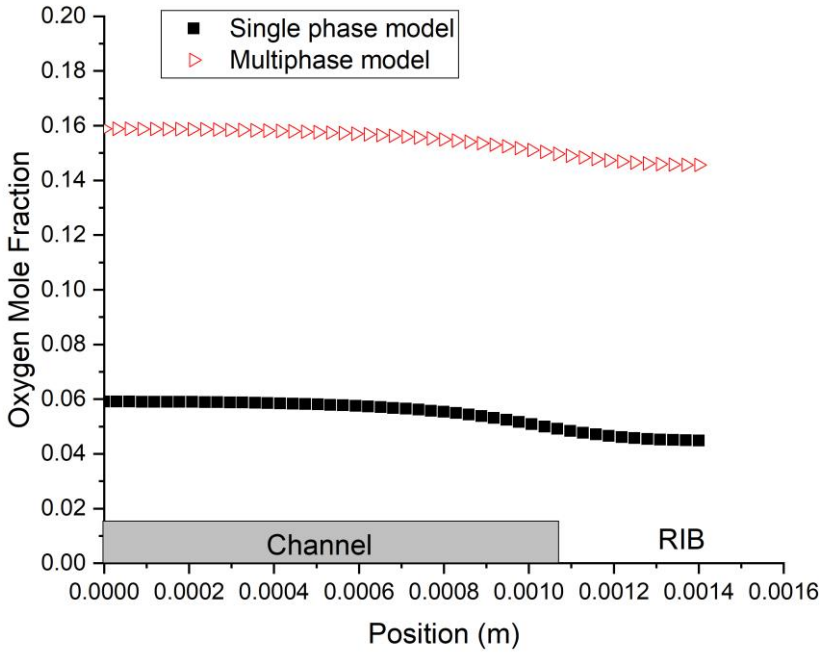

Figure 7.6 Oxygen mole fraction distribution at the mid-thickness of the cathode GDL for both the single-phase and multiphase models.

7.3.2 The effect of the anisotropy of the GDL gas permeability

The GDL gas permeability is anisotropic, i.e. it has different values for the in-plane and through-plane directions. Therefore, it is of interest to investigate the effect of the anisotropy of the GDL gas permeability. In order to investigate the anisotropy effect of the GDL gas permeability, the experimentally-estimated gas permeability for all the three principal directions, i.e. the in plane directions (0° and 90 ° directions) and the through-plane direction were employed into the model. In the first case, the permeability of the GDL was assumed to be isotropic and having the value of the through-plane gas permeability before compression (that was experimentally determined as described in Chapter 5): 2.38×10^{-11} m^2. On the other hand, in the second case, the GDL permeability was considered to be anisotropic and, in addition to the through-plane permeability, the in-plane gas permeability in the 0° and 90 ° directions are 9.29×10^{-11} and 1.16×10^{-10} m^2, respectively. The latter in-plane permeability values were, assuming zero reduction in the GDL thickness, computed from the curve-fitting equations used for the experimentally-measured in-plane permeabilities reported in [79]. Fig 7.7 shows the polarisation curves for the above two cases and Fig 7.8 and 7.9 show the distributions of the current and the oxygen mole fraction at the mid-thickness of the cathode GDL for these two cases.

The results show that the anisotropy in the GDL gas permeability has virtually no effect on the performance of the fuel cell. This is most likely due to the fact that, for the given range of the gas permeability, the convection is not the main mode of transport of gases; the main mode of transport is diffusion [189]. As

the sensitivity of the performance of the modelled fuel cell to the anisotropy of the GDL permeability is negligible, the further investigations assume that the gas permeability of the GDL is isotropic.

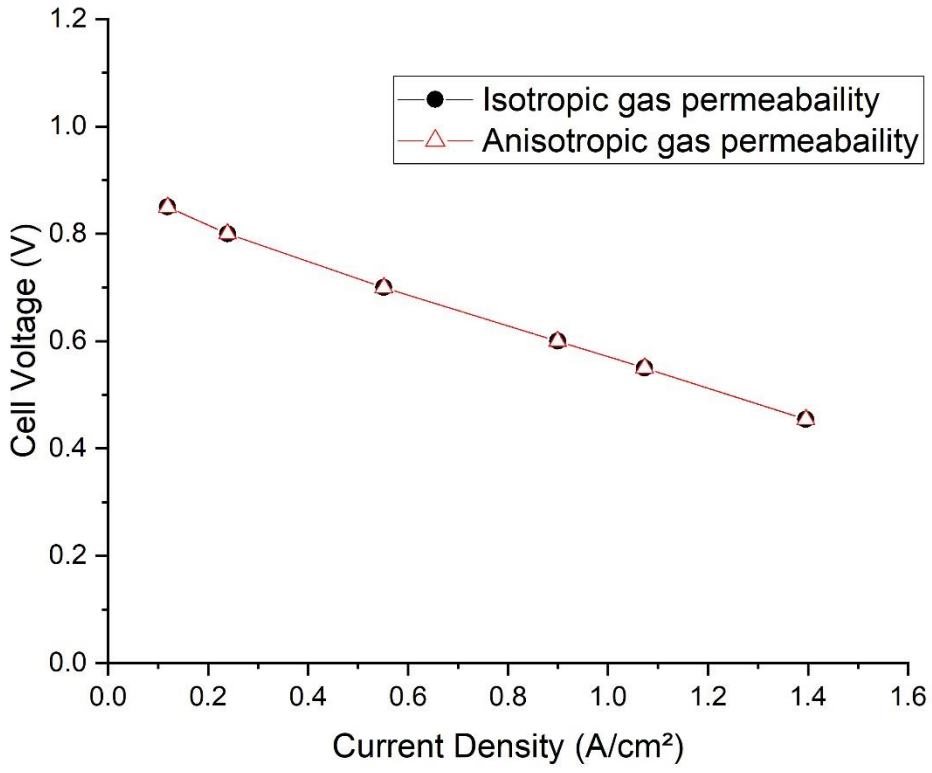

Figure 7.7 The polarisation curves of the modelled fuel cell with isotropic and anisotropic GDL gas permeability.

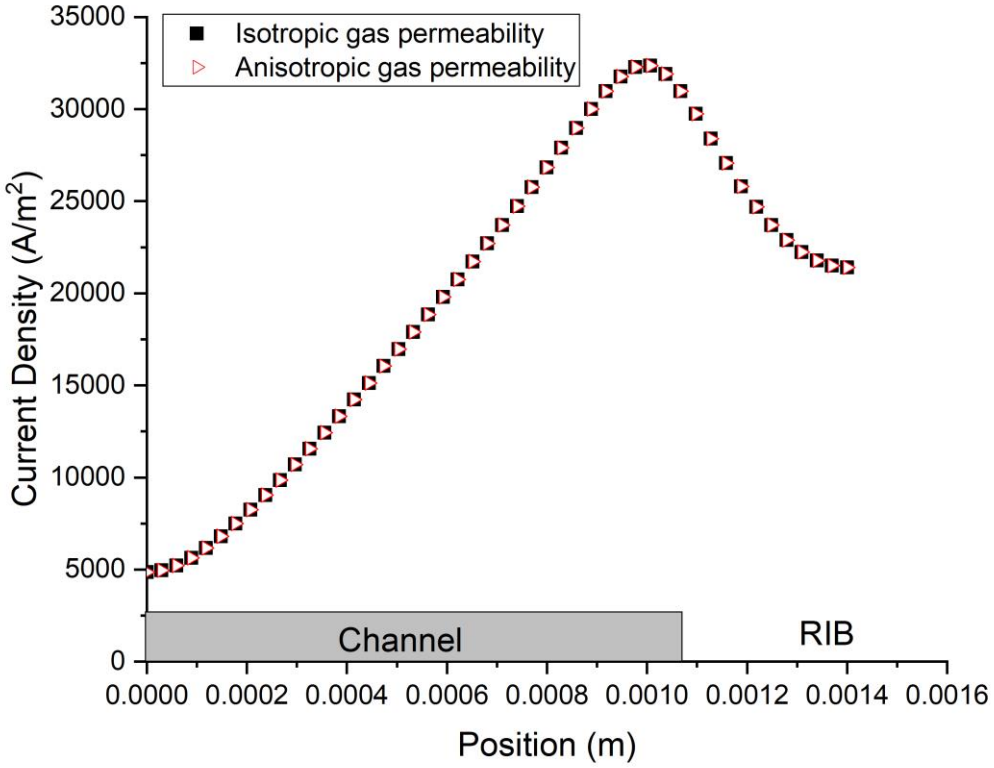

Figure 7.8 The local distribution current density at the mid-thickness of the cathode GDL with isotropic and anisotropic GDL gas permeability.

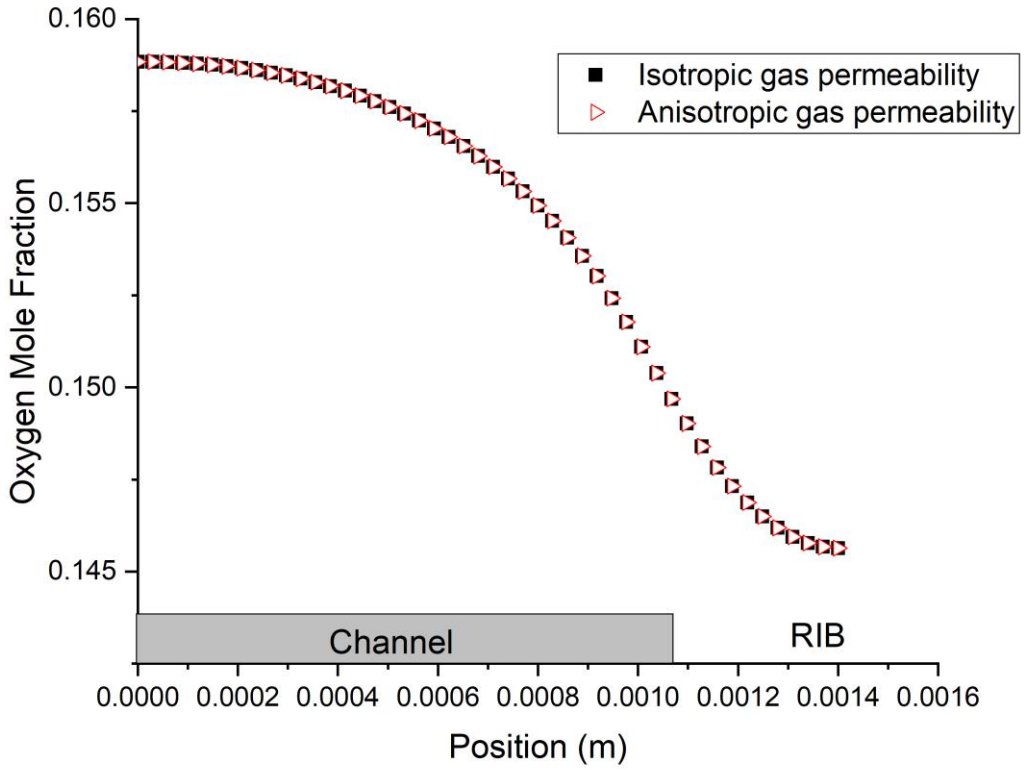

Figure 7.9 The local distribution of oxygen mole fraction at the mid-thickness of the cathode GDL with isotropic and anisotropic GDL gas permeability.

7.3.3 The effect of gas permeability before and after compression

In Chapter 5, an experimental study was conducted to investigate the effects of the combined compression (the constant assembling compression and the cyclic compression that is induced due to the swelling/shrinkage of the membrane) on the GDL gas permeability. Therefore, the effects of the GDL gas permeability before (2.38×10^{-11} m²) and after (1.31×10^{-11} m²) compression on the global and local performance of the fuel cell are investigated in this section.

As with the anisotropic GDL gas permeability investigation, that was presented in the previous section, it is clear from Figures 7.10, 7.11 and 7.12 that the variation in the GDL gas permeability as a result of compression has virtually

no effect on the polarisation curve and the local distribution of the key variables of the fuel cell. This is, as mentioned in the previous section, due to the minimal contribution of the convection in the transport of the gases in the GDL.

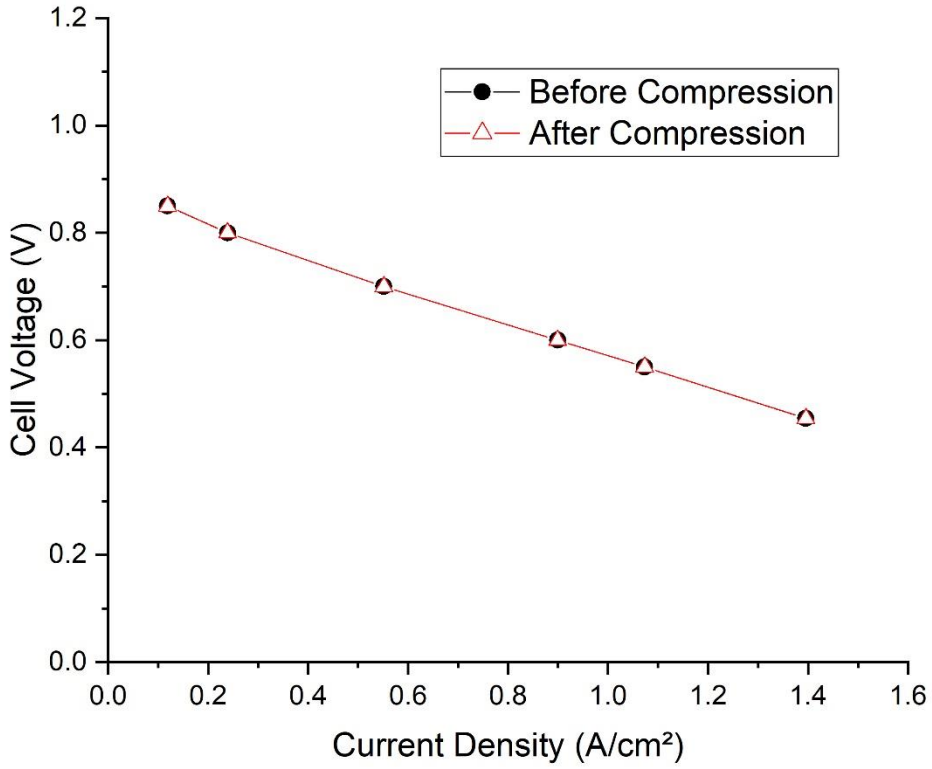

Figure 7.10 The polarisation curves of the modelled fuel cell with the GDL gas permeability before and after compression.

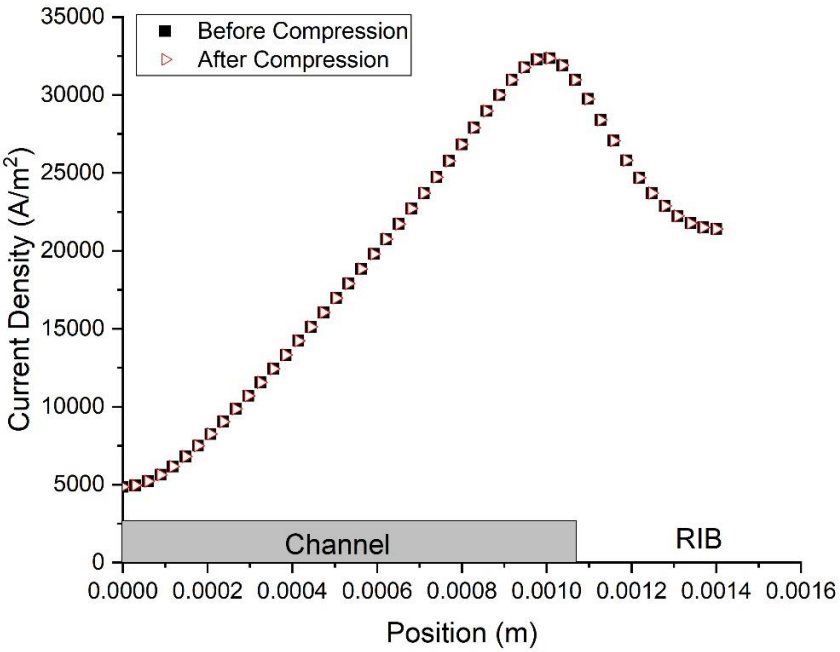

Figure 7.11 The local distribution current density at the mid-thickness of the cathode GDL with the GDL gas permeability before and after compression.

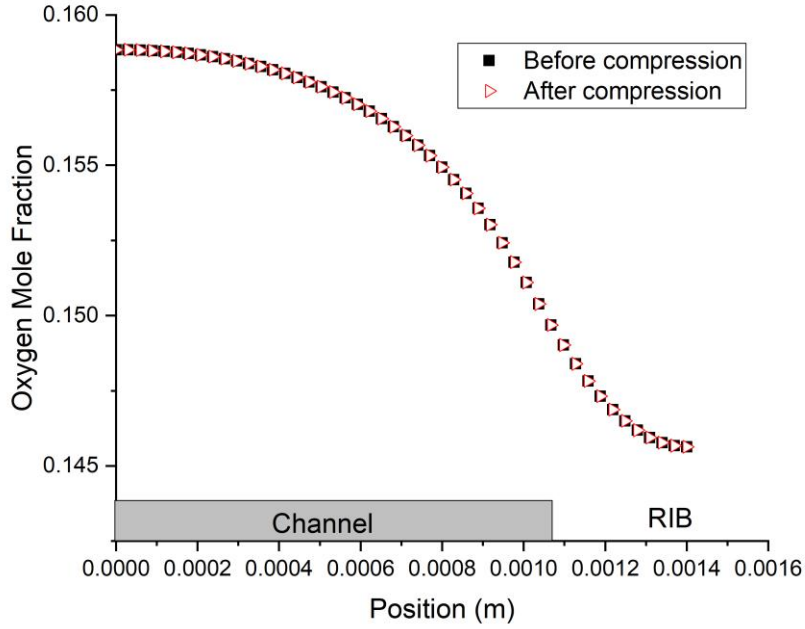

Figure 7.12 The local distribution of oxygen mole fraction at the mid-thickness of the cathode GDL with the GDL gas permeability before and after compression.

To investigate as to when the convection plays a more important role in transporting the reacting gases in the GDL, the GDL gas permeability was systematically increased by orders of magnitude (see for example the legends of Figure 7.13). It is observed in Fig.7.13 that even if the GDL gas permeability is increased by fours orders of magnitude, the positive effect on the performance of the PEM fuel cell either globally (Figure 7.13) or locally (Figure 7.14) is minimal. However, as expected, the fuel cell performance improves with increasing the GDL gas permeability and this is due to the increased ability of the latter to transport more oxygen to the cathode catalyst layer (Figure 7.15).

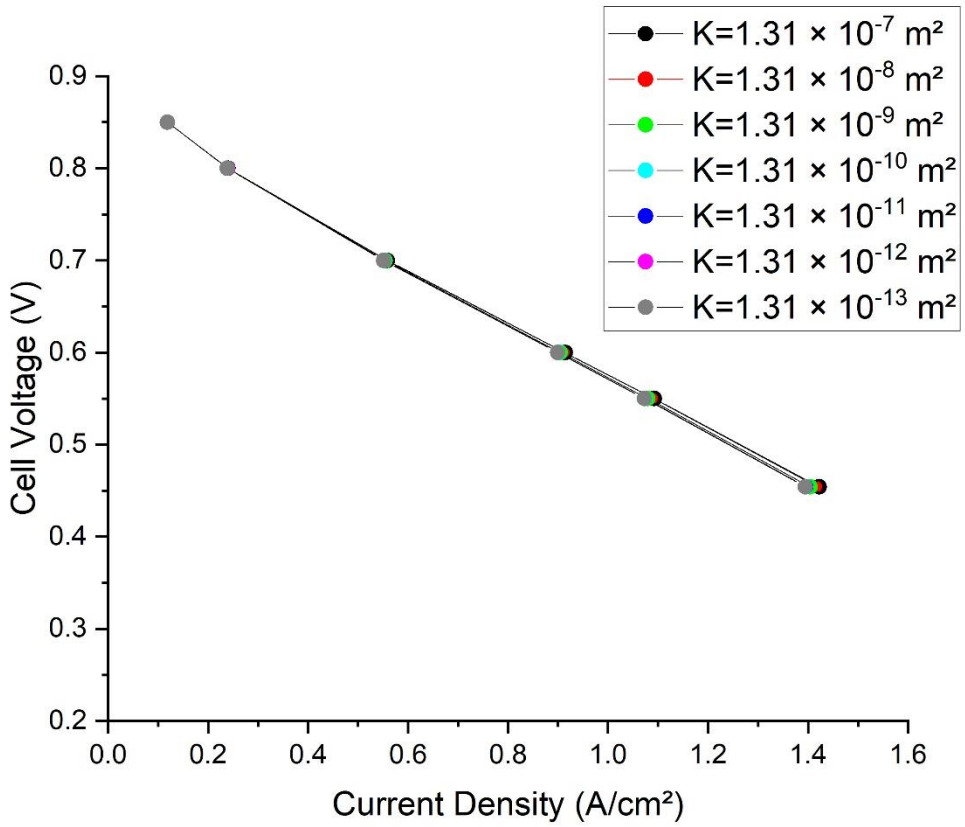

Figure 7.13 The polarisation curves of the modelled fuel cell as the GDL gas permeability changes by orders of magnitudes.

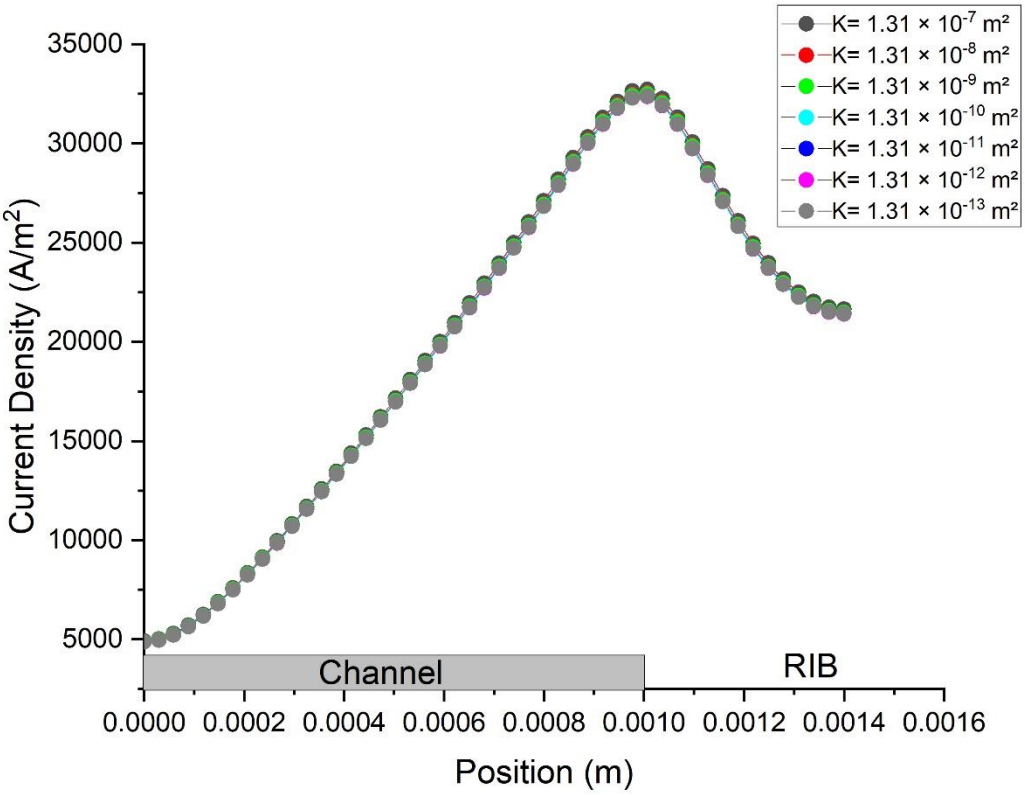

Figure 7.14 The local distribution current density at the mid-thickness of the cathode GDL as the GDL gas permeability changes by orders of magnitudes.

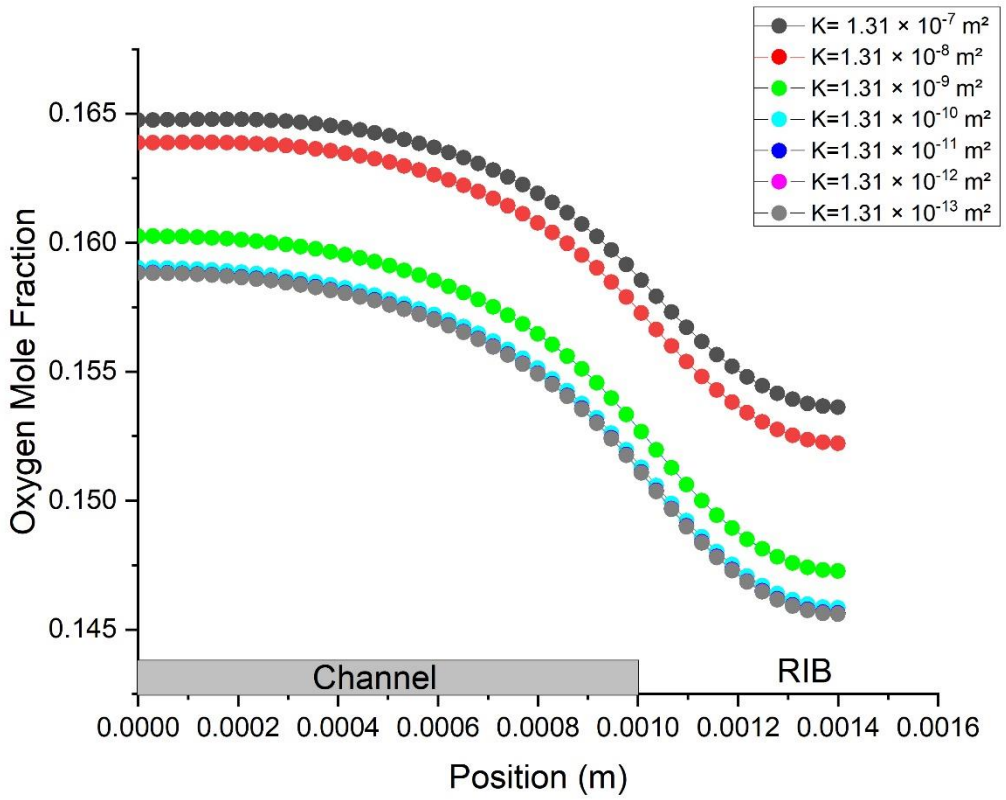

Figure 7.15 The local distribution of the oxygen mole fraction at the mid-thickness of the cathode GDL as the GDL gas permeability changes by orders of magnitudes.

7.3.4 The effect of the contact angle before and after compression

The contact angles for the SGL-10-BA GDL before (126.1°) and after (113.7°) compression have been, as shown in Chapter 5, measured and these values are employed in this study. The hydrophobicity of the GDL, represented here in the form of the contact angles, plays an important role in managing excess liquid water inside the fuel cell. Figures 7.16, 7.17 and 7.18 show the polarisation curve of the fuel cell, the local distribution of the current density and oxygen mole fraction across the mid-thickness of the GDL of the fuel cell as the contact angle of the cathode GDL changes as a result of compression, respectively.

Figure 7.16 shows that the fuel cell performance slightly degrades with the contact angle of the GDL after compression (i.e. 113.7°). This is clearly due to the decreased ability of the GDL to reject liquid water with the above contact angle. The global performance is mirrored at a local level and this is shown through the local distribution of the current density within the GDL (Figure 7.17). The decreased ability of the GDL to reject liquid water allows for less oxygen to reach the cathode catalyst layer or, in other words, more oxygen to be available in the cathode GDL (Figure 7.18).

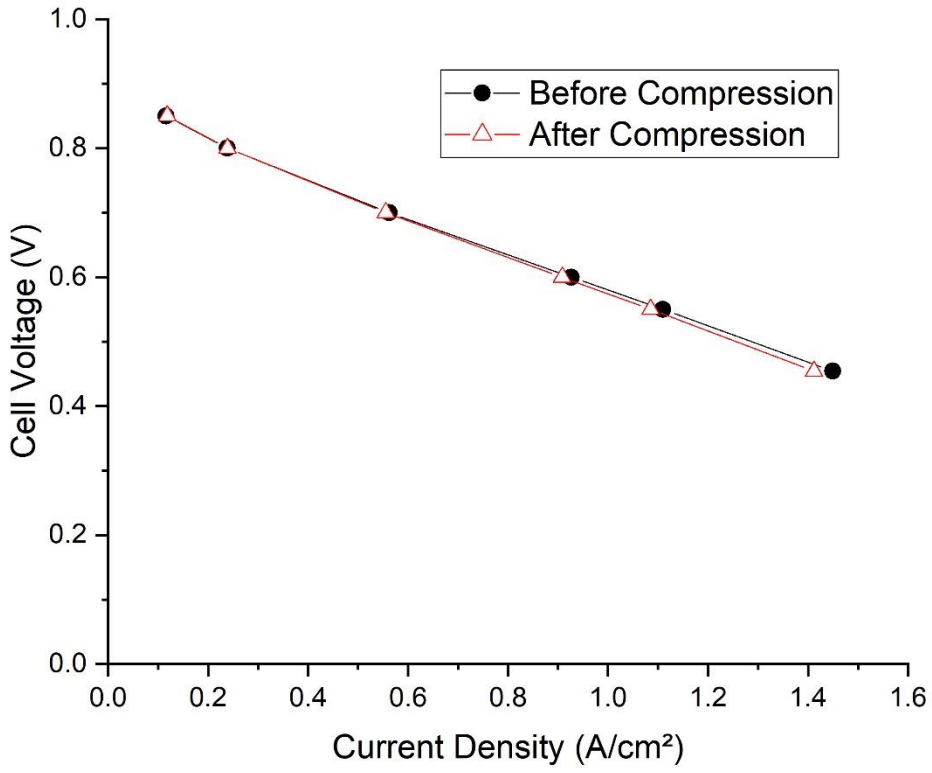

Figure 7.16 The polarisation curves of the modelled fuel cell with the GDL contact angle before and after compression.

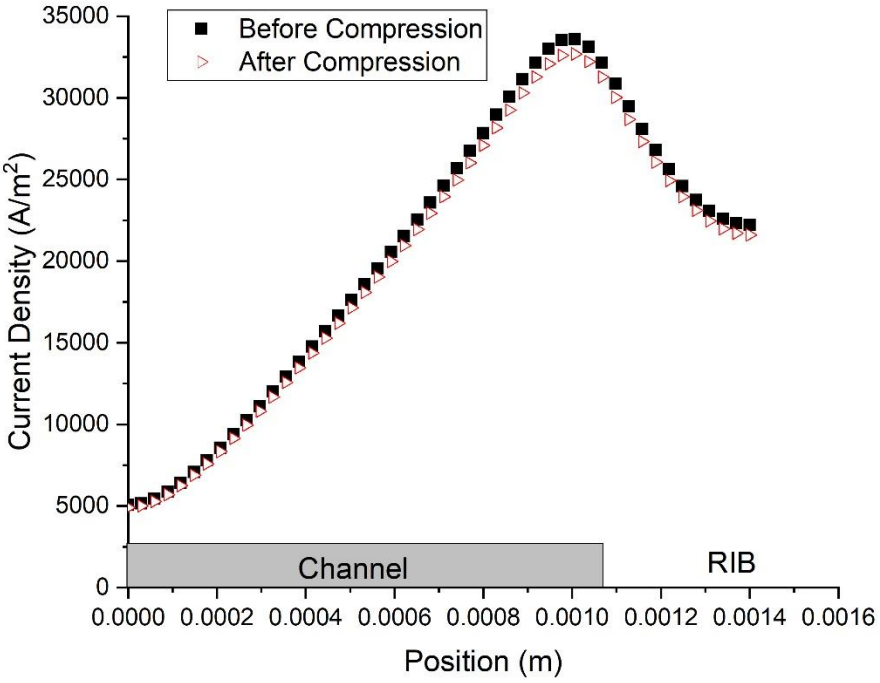

Figure 7.17 The local distribution current density at the mid-thickness of the cathode GDL with the GDL contact angle before and after compression.

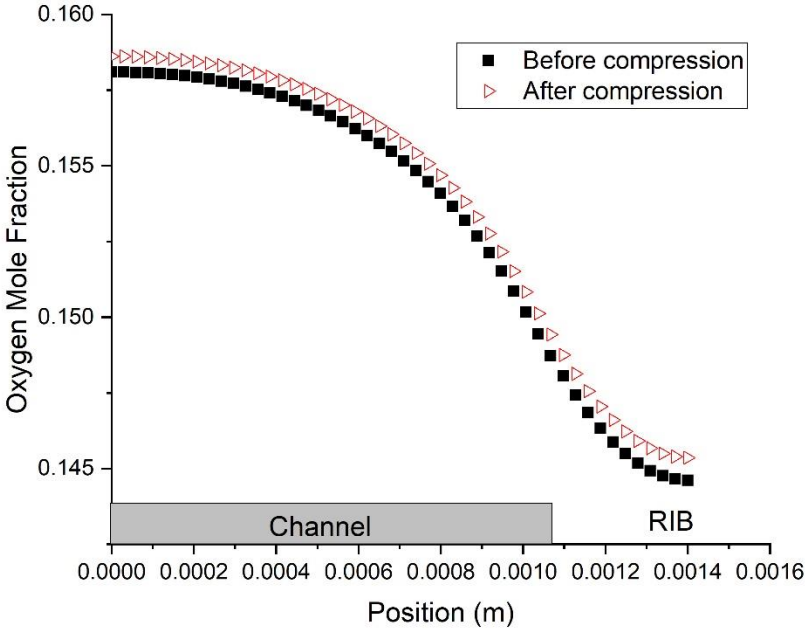

Figure 7.18 The local distribution of the oxygen mole fraction at the mid-thickness of the cathode GDL with the GDL contact angle before and after compression.

In order to further investigate the effects of the GDL contact angle and attempt to determine optimum values of the contact angle, a set of cathode GDL contact angles, changing in intervals of 10°, are employed in this study.

Figure 7.19 shows that there appears to be an optimum value for the GDL contact angle at which the fuel cell performance is a maximum, namely 136.1°. Accordingly, this contact angle gives the maximum current density (Figure 7.20) and the minimum oxygen concentration (Figure 7.21) within the cathode GDL. Also, one may observe that the fuel cell performance improves more profoundly in the range 96.1-116.1° and then this performance becomes much less apparent as the contact angle increases beyond 116.1°. These results indicate that the highest contact angle (176.1°) does not necessarily give the best fuel cell performance. The above results may be attributed to the impact

of the GDL contact angle on both the membrane conductivity and the ability of the GDL to reject liquid water. From Table 7.4, it may be inferred that the cathode GDL contact angle of 136.1° collectively provides a reasonable membrane conductivity and water rejection ability at the same time. For example, the membrane conductivity with a 96.1° contact angle is less than that of 136.1° by about 24%. On the other hand, the water removal with a 176.1° contact angle is very slightly less than that of 136.1° by about 1%.

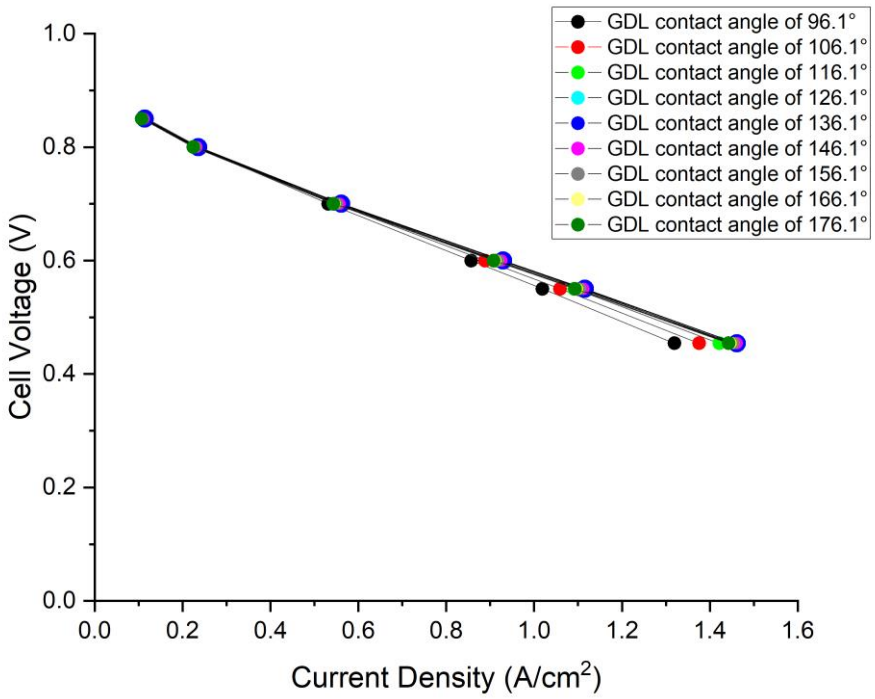

Figure 7.19 The polarisation curves of the modelled fuel cell as the cathode GDL contact angle changes in intervals of 10° from 96.1 to 176.1°.

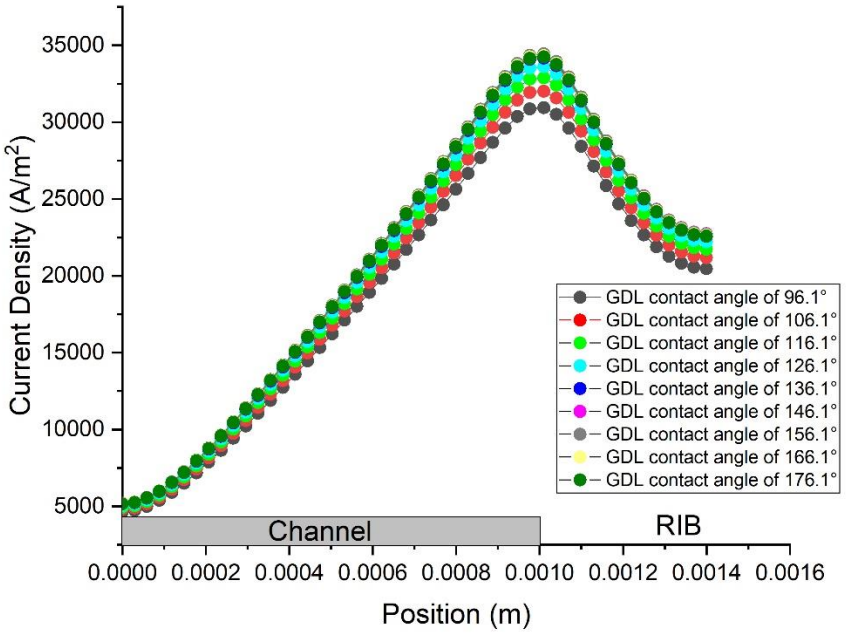

Figure 7.20 The local distribution current density at the mid-thickness of the cathode GDL as the cathode GDL contact angle changes in intervals of 10° from 96.1 to 176.1°.

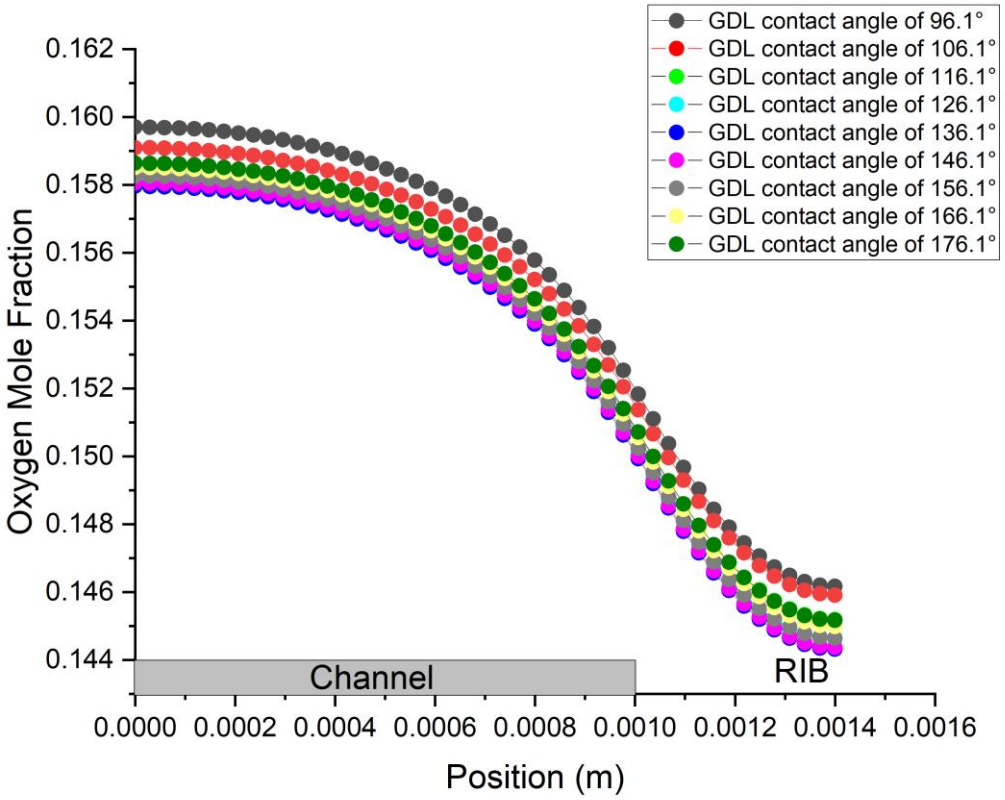

Figure 7.21 The local distribution of the oxygen mole fraction at the mid-thickness of the cathode GDL as the cathode GDL contact angle changes in intervals of 10° from 96.1 to 176.1°.

Table 7.4 The variation of the membrane conductivity and liquid water removal with GDL contact angles at 0.55 V.

GDL contact angle (°)	Membrane conductivity (S/m)	GDL liquid removal
96.1	8.714	-2.235
106.1	9.290	-2.267
113.7 (after comp.)	9.719	-2.275
116.1	10.529	-2.276
126.1 (before comp.)	10.351	-2.274
136.1	10.771	-2.267
146.1	11.096	-2.261
156.1	11.326	-2.256
166.1	11.468	-2.252
176.1	11.532	-2.249

7.4 Conclusions

In this chapter, the effects of compression being applied to the GDL in terms of reduced gas permeability and contact angle have been numerically investigated with the assistance of a three-dimensional multiphase model for a PEM fuel cell. The sensitivity of the fuel cell performance to (i) the assumption that water only exists as a vapour in the fuel cell and (ii) the anisotropy in the GDL gas permeability has been also explored. Further, the GDL gas permeability and contact angle were substantially changed to evaluate the limits of the impact of these two parameters. The main findings of this chapter may be summarized as follows:

- The single phase model underestimates the PEM fuel cell performance due to the exclusion of the positive effect of the liquid water on the membrane conductivity.

- The anisotropy of the gas permeability has almost, for the realistic given range of permeability, no effect on the performance of the PEM fuel cell and this is due to the minimal contribution of convection to the transport of the gases in the GDLs; the main mode of transport of gases is diffusion. For the same reason, the variation in the GDL gas permeability as a result of compression was found to have no impact on the fuel cell performance.

- The GDL permeability needs to be substantially increased (by 3-4 orders of magnitudes) to realise a positive impact on the fuel cell performance.

- The reduction in the contact angle of the GDL as a result of compression was shown to slightly decrease the fuel cell performance and this is mainly due to the decreased ability of the GDL to reject liquid water.
- For the given set of different magnitudes of contact angle used in the study, there exists an optimum value for the contact angle of the cathode GDL that maximises the fuel cell performance (~ 136°). This contact angle reasonably achieves the appropriate membrane conductivity and has the ability to reject liquid water.

8 CONCLUSIONS AND FUTURE WORK

8.1 Conclusions

The gas diffusion layers (GDLs) are subjected to assembling and cyclic compressions (due swelling and shrinkage of membrane electrolytes as a result of hydration/dehydration cycles) that may have detrimental effects of the overall performance of the proton exchange membrane (PEM) fuel cells. In this thesis, the effects of the above compressions on some of the key physical properties of the GDLs were investigated. The compressions (or stresses) that the GDLs are subject to were performed using a universal testing machine, mimicking the assembling and cyclic stresses that the GDL normally undergoes within an operating PEM fuel cell. The gas permeability, the morphology, the wettability and the thermal stability of the carefully-selected commercially-available uncoated and microporous layer (MPL)-coated GDLs were investigated before and after the compression tests (Chapter 5). The gas permeability was transversely measured using an in-house setup; the morphology was examined by analysing SEM images; the wettability was assessed measuring the contact angle of water droplets on the GDL surface; and the thermal stability was studied using TGA tests. These tests were then performed again but in presence of sealing gaskets this time in order to evaluate the sensitivity of all the above GDL properties to compressions in presence of this key component: sealing gaskets (Chapter 6). Finally, the measured gas permeability and contact angle of the GDLs, before and after compressions, were fed into a three-dimensional non-isothermal multi-phase

model representing a typical PEM fuel cell (Chapter 7). The geometry of the model was created and meshed. The model was run (with the relevant conservation equations for mass, momentum, heat, charge and chemical species) and mesh-independent solution was generated. The model was used to investigate the sensitivity of the fuel cell performance (either globally in the form of polarisation curves or locally in the form current density and oxygen concentration distributions within the GDL) to the single-phase (i.e. water only exists as vapour) assumption. Then, it (i.e. the model) was used to investigate the sensitivity of the fuel cell to the changes in the gas permeability and contact angle of the GDL as a result of compressions that the latter layer undergoes. The model was next used to investigate the effects of extreme values for GDL gas permeability and contact angle on the performance of the fuel cell. The below are the key findings withdrawn from all the technical chapters of the thesis (i.e. Chapters, 5, 6 and 7):

- The investigated MPL-coated GDLs are more resistive to mechanical deformation than the uncoated GDLs (i.e. carbon substrates) and this is attributed to the addition of higher-in-density layer to the uncoated GDL: the MPL. However, the reduction in thickness and gas permeability of the coated GDLs were shown to higher than those of the uncoated GDLs and this is apparently due to the penetration of the MPL into the carbon substrate of the former type of the GDLs.
- One of the commercial tested uncoated GDLs (i.e. Toray) was found to be mechanically stronger (and subsequently less deformable) than the tested SGL carbon substrates and this is due lower porosity and higher

density demonstrated by Toray carbon substrate. This results in less reduction in thickness and gas permeability of Toray samples.

- The tested coated GDLs show different levels of penetration of MPL layer into the carbon substrate. To this end, one of the tested MPL-coated GDLs (SGL 35BC) demonstrates substantially higher reduction in thickness and gas permeability compared to the other tested MPL-coated GDL (SGL 34BC).
- The contact angle of the tested GDLs was found to reduce by 3°-15° after compression; this is (as evidenced from the respective SEM images) mainly due to the increased smoothness surface of the GDL after compression.
- As expected, the tested GDLs were found to be less deformed in presence of sealing gaskets. However, they (i.e. the GDLs) are sensitive to the type of the gaskets used; GDLs tested with silicone gaskets appear to be less deformed than those tested with Teflon gaskets and this is due to higher stiffness of the former type of gaskets. As a consequence, the reduction in thickness and gas permeability (as a result of compression test) of the GDL samples tested with silicone gaskets were found to be less than that with Teflon gaskets.
- The TGA data of the tested carbon substrates compressed with/without gaskets shows around 40% reduction in PTFE loading, indicating that some of the PTFE material is stripped off due to the compressive forces. On the hand, the respective TGA data shows that the MPL-coated GDLs appear to lose no PTFE material after

compression and this is probably due to the malleability of the added MPL layer.

- The compressed GDL samples show less weight loss after 600 °C compared to the uncompressed GDL samples; this is most likely due to presence of less "decomposable" binding materials as a result of compression.
- The fuel cell performance of the modelled PEM fuel cell is underestimated if single phase is assumed and this is due to the neglect of the positive impact of liquid water on the conductivity of the membrane electrolyte.
- The modelled fuel cell performance was found to be almost insensitive to the anisotropy in the gas permeability of the GDL or the variation in the GDL gas permeability as a result of compression; this is due to the minimal contribution of convection to the transport of gases within the GDL where the main mode of transport is diffusion.
- The reduction of the contact angle of the GDL as a result of compression was shown to impose a slight decrease in the performance of the modelled fuel cell and this is due the degraded ability of the GDL to reject excess liquid water.
- There exists an optimum value for the contact angle of the GDL at which the modelled fuel cell performance is maximised (~ 136 °). With this contact angle, appropriate membrane conductivity and liquid water rejection ability are realised.

Overall, this work provides insights in terms of GDL design and development. One of the key insights is related to the hydrophobic agent (i.e. PTFE) added to the GDL material. As shown in the study, the carbon substrates lose considerable amount of PTFE after cycles of compression which reflects badly on the ability of these carbon substrates to reject liquid water. To remedy this issue, more robust application techniques should be implemented to ensure intimate contact between the PTFE particles and the carbon fibres of the carbon substrates. Another insight is related to the use of sealing gaskets inside the fuel cell. As demonstrated in the present work, one of the tested gaskets leads to more deformation and mass transport resistance than the other. Therefore, the selection of the sealing gaskets should be handled with care in order to ensure minimal damage to the GDL material. Lastly, as shown from the modelling investigation, the contact angle appears to require optimisation to ensure a maximum fuel cell performance.

8.2 Recommendations and Future work

To fully realise the effects of compressions on the physical properties of GDLs (and subsequently on the performance of the fuel cell), some other investigations are recommended to be performed:

- Different arrangements for the compression test could be attempted to see whether final findings of the present work are affected/unaffected. For example, fully loading and unloading cycles of compression (i.e. from/to 0 to/from 3 MPa) or a constant loading (e.g. 3.2 MPa) for a considerable amount of time (e.g. 1 hour) could be considered.
- Further, conditioning procedures from different protocols (e.g. the protocol used in [150]) could be considered to fully ensure that hysteresis-related strains are eliminated before conducting the post-compression tests
- Other key GDL transport properties need to be evaluated before and after compression: the gas diffusivity, the thermal conductivity and the electrical conductivity. In addition to gas permeability values provided by the present study, these investigations will provide realistic values for all the above transport properties that will eventually enhance the predictions of the modelled PEM fuel cell.
- More types of sealing gaskets are recommended to be taken into account when investigating the effects of presence of sealing gaskets on the compressed GDLs. This will provide more comprehensive insights

in terms of selection of gaskets that simultaneously ensure less deformation to the GDL materials and good contact with the flow-field plates. The chemical stability of the sealing gaskets need to be also investigated.

- The effects of the freeze-thaw cycles on the mechanical integrity of the GDLs are recommended to be investigated. This study will provide insights on the lifetime of the GDLs and how they perform in harsh environments which is an essential criteria for the automotive fuel cell systems.

REFERENCE

[1] C. Philibert, “Technology Penetration and Capital Stock Turnover: Lessons from IEA Scenario Analysis,” 2007. [Online]. Available: https://www.iea.org/publications/freepublications/publication/capital_stock.pdf%

[2] C. S. Mattick, E. Williams, and B. R. Allenby, “Historical trends in global energy consumption,” *IEEE Technol. Soc. Mag.*, vol. 29, no. 3, pp. 22–30, 2010.

[3] S. O. Ladislaw, “A report of the csis project on U.S. leadership in development: Energy and Development Trends,” 2011. [Online]. Available: www.csis.org.

[4] H. Hafeznia, A. Aslani, S. Anwar, and M. Yousefjamali, “Analysis of the effectiveness of national renewable energy policies: A case of photovoltaic policies,” *Renew. Sustain. Energy Rev.*, vol. 79, no. May 2016, pp. 669–680, 2017, doi: 10.1016/j.rser.2017.05.033.

[5] EIA, “International Energy Outlook 2017 Overview,” 2017. doi: www.eia.gov/forecasts/ieo/pdf/0484(2016).pdf.

[6] I. Lazkano, L. Nøstbakken, and M. Pelli, “From fossil fuels to renewables: The role of electricity storage,” *Eur. Econ. Rev.*, vol. 99, pp. 113–129, 2017, doi: 10.1016/j.euroecorev.2017.03.013.

[7] A. Coram and D. W. Katzner, “Reducing fossil-fuel emissions: Dynamic paths for alternative energy-producing technologies,” *Energy Econ.*, vol. 70, pp. 179–189, 2018, doi: 10.1016/j.eneco.2017.12.028.

[8] L. Gao, J. Huang, X. Chen, Y. Chen, and M. Liu, “Contributions of natural climate changes and human activities to the trend of extreme precipitation,” *Atmos. Res.*, vol. 205, no. August 2017, pp. 60–69, 2018, doi: 10.1016/j.atmosres.2018.02.006.

[9] IEA (2020), Global CO_2 emissions in 2019, IEA, Paris https://www.iea.org/articles/global-co2-emissions-in-2019.

[10] S. H. Schneider and M. D. Mastrandrea, "Probabilistic assessment of 'dangerous' climate change and emissions pathways," *Proc. Natl. Acad. Sci.*, vol. 102, no. 44, pp. 15728–15735, 2005, doi: 10.1073/pnas.0506356102.

[11] S. J. Peighambardoust, S. Rowshanzamir, and M. Amjadi, "Review of the proton exchange membranes for fuel cell applications," *Int. J. Hydrogen Energy*, vol. 35, no. 17, pp. 9349–9384, 2010, doi: 10.1016/j.ijhydene.2010.05.017.

[12] G. Hoogers, *Fuel Cell Technology Handbook*, 1st Edition. Boca Raton: CRC Press LLC, 2003.

[13] P. G. Grimes, "Historical pathways for fuel cells," *IEEE Aerosp. Electron. Syst. Mag.*, vol. 15, no. 12, pp. 1–10, 2000, doi: 10.1109/62.891972.

[14] J. Larminie and A. Dicks, *Fuel cell systems explained*, Second Edition. John Wiley & Sons Ltd, 2003.

[15] R. Lan, P. I. Cowin, S. Sengodan, and S. Tao, "A perovskite oxide with high conductivities in both air and reducing atmosphere for use as electrode for solid oxide fuel cells," *Sci. Rep.*, vol. 6, p. 31839, Aug. 2016, [Online]. Available: http://dx.doi.org/10.1038/srep31839.

[16] H. A. Taroco, J. A. F. Santos, R. Z. Domingues, and T. Matencio, "Ceramic Materials for Solid Oxide Fuel Cells," in *Advances in Ceramics Synthesis and Characterization, Processing and Specific Applications*, InTech, 2011, pp. 423–441.

[17] X. Li, *Principles of fuel cells*. Taylor & Francis, 2006.

[18] Y. S. Ye, J. Rick, and B. J. Hwang, "Water Soluble Polymers as Proton Exchange

Membranes for Fuel Cells," *Polymers*, vol. 4, no. 2. 2012, doi: 10.3390/polym4020913.

[19] O. T. Holton and J. W. Stevenson, "The Role of Platinum in Proton Exchange Membrane Fuel Cells Evaluation of platinum's unique properties for use in both the anode and cathode of a proton exchange membrane fuel cell," *Platin. Met. Rev.*, vol. 57, no. 4, pp. 259–271, 2013, doi: 10.1595/147106713X671222.

[20] S. M. Haile, "Fuel cell materials and components," *Acta Mater.*, vol. 51, no. 19, pp. 5981–6000, 2003, doi: 10.1016/j.actamat.2003.08.004.

[21] S. Srinivasan, L. Krishnan, and C. Marozzi, "FUEL CELL PRINCIPLES," in *Fuel Cells*, Boston, MA: Springer US, 2006, pp. 189–233.

[22] M. L. Perry and T. F. Fuller, "A Historical Perspective of Fuel Cell Technology in the 20th Century," *J. Electrochem. Soc.*, vol. 149, no. 7, p. S59, 2002, doi: 10.1149/1.1488651.

[23] K. D. Kreuer, "On the development of proton conducting polymer membranes for hydrogen and methanol fuel cells," vol. 185, pp. 29–39, 2001.

[24] J. M. Tang, K. Jensen, M. Waje, W. Li, P. Larsen, K. Pauley, Z. Chen, P. Ramesh, M. E. Itkis, Y. Yan, and R. C. Haddon, "High Performance Hydrogen Fuel Cells with Ultralow Pt Loading Carbon Nanotube Thin Film Catalysts High Performance Hydrogen Fuel Cells with Ultralow Pt Loading Carbon Nanotube Thin," *Phys. Chem.*, pp. 17901–17904, 2007, doi: 10.1021/jp071469k.

[25] R. P. O'Hayre, S. Cha, W. G. Colella, and F. B. Prinz, *Fuel cell fundamentals*, 3rd ed. New Jersey: Wiley, 2006.

[26] F. Barbir, "PEM Fuel Cells," in *Fuel Cell Technology*, Springer, 2006, pp. 27–51.

[27] X Z. Yuan and H. Wang, “PEM Fuel Cell Fundamentals,” in *PEM Fuel Cell Electrocatalysts and Catalyst Layer*, J. Zhang, 1st Edition. Springer, 2008, pp. 1–79.

[28] X. Li, I. Sabir, and J. Park, “A flow channel design procedure for PEM fuel cells with effective water removal,” *J. Power Sources*, vol. 163, no. 2, pp. 933–942, 2007, doi: 10.1016/j.jpowsour.2006.10.015.

[29] M. F. Mathias, J. Roth, J. Fleming, and W. Lehnert, “Diffusion media materials and characterisation,” in *Handbook of Fuel Cells*, vol. 3, 2010, pp. 517–537.

[30] C. Lim and C. Y. Wang, “Effects of hydrophobic polymer content in GDL on power performance of a PEM fuel cell,” *Electrochim. Acta*, vol. 49, no. 24, pp. 4149–4156, 2004, doi: 10.1016/j.electacta.2004.04.009.

[31] A. Ozden, I. E. Alaefour, S. Shahgaldi, X. Li, C. Ozgur Colpan, and F. Hamdullahpur, “Gas Diffusion Layers for PEM Fuel Cells,” in *Exergetic, Energetic and Environmental Dimensions*, Elsevier, 2018, pp. 695–727.

[32] P. T. Nguyen, T. Berning, and N. Djilali, “Computational model of a PEM fuel cell with serpentine gas flow channels,” *J. Power Sources*, vol. 130, no. 1–2, pp. 149–157, 2004, doi: 10.1016/j.jpowsour.2003.12.027.

[33] T. Berning and N. Djilali, “A 3D, Multiphase, Multicomponent Model of the Cathode and Anode of a PEM Fuel Cell,” *J. Electrochem. Soc.*, vol. 150, no. 12, p. A1589, 2003, doi: 10.1149/1.1621412.

[34] U. Pasaogullari and C. Y. Wang, “Two-phase transport and the role of micro-porous layer in polymer electrolyte fuel cells,” *Electrochim. Acta*, vol. 49, no. 25, pp. 4359–4369, 2004, doi: 10.1016/j.electacta.2004.04.027.

[35] J. H. Nam, K. J. Lee, G. S. Hwang, C. J. Kim, and M. Kaviany, “Microporous layer

for water morphology control in PEMFC," *Int. J. Heat Mass Transf.*, vol. 52, no. 11–12, pp. 2779–2791, 2009, doi: 10.1016/j.ijheatmasstransfer.2009.01.002.

[36] A. El-Kharouf, "Understanding GDL Properties and Performance in Polymer Electrolyte Fuel Cells," Ph.D thesis, School Of Chemical Engineering, University Of Birmingham, 2014.

[37] Y. S. Hwang, H. Choi, G. Y. Cho, Y. H. Lee, and S. Cha, "Effect of compression thickness on performance of gas diffusion layer of direct methanol fuel cells," *Int. J. Precis. Eng. Manuf. Technol.*, vol. 1, no. 3, pp. 215–221, 2014, doi: 10.1007/s40684-014-0027-y.

[38] A. Nabovati, J. Hinebaugh, A. Bazylak, and C. H. Amon, "Effect of porosity heterogeneity on the permeability and tortuosity of gas diffusion layers in polymer electrolyte membrane fuel cells," *J. Power Sources*, vol. 248, pp. 83–90, 2014, doi: 10.1016/j.jpowsour.2013.09.061.

[39] J. Farmer, B. Duong, S. Seraphin, S. Shimpalee, M. J. Martínez-Rodríguez, and J. W. Van Zee, "Assessing porosity of proton exchange membrane fuel cell gas diffusion layers by scanning electron microscope image analysis," *J. Power Sources*, vol. 197, pp. 1–11, 2012, doi: 10.1016/j.jpowsour.2011.08.064.

[40] J. Hinebaugh and A. Bazylak, "FuelCell2011-54 PEM fuel cell gas diffusion layer modelling of pore structure and predicted liquid water saturation," *Proc. ASME 9th fuel cell Sci. Eng. Technol. Conf.*, pp. 1–8, 2011.

[41] Z. Fishman, J. Hinebaugh, and A. Bazylak, "Microscale Tomography Investigations of Heterogeneous Porosity Distributions of PEMFC GDLs," *J. Electrochem. Soc.*, vol. 157, no. 11, p. B1643, 2010, doi: 10.1149/1.3481443.

[42] N. Rajalakshmi, G. Velayutham, K. Ramya, C. K. Subramaniyam, and K. S. Dhathathreyan, “Characterisation and Optimisation of Low Cost Activated Carbon Fabric as a Substrate Layer for PEMFC Electrodes.” ASME, Ypsilanti, Michigan, pp. 169–173, 2005, doi: 10.1115/FUELCELL2005-74182.

[43] Y. Hiramitsu, H. Sato, and M. Hori, “Prevention of the water flooding by micronizing the pore structure of gas diffusion layer for polymer electrolyte fuel cell,” *J. Power Sources*, vol. 195, no. 17, pp. 5543–5549, 2010, doi: 10.1016/j.jpowsour.2010.03.039.

[44] G. Luo, Y. Ji, C. Y. Wang, and P. K. Sinha, “Modeling liquid water transport in gas diffusion layers by topologically equivalent pore network,” *Electrochim. Acta*, vol. 55, no. 19, pp. 5332–5341, 2010, doi: 10.1016/j.electacta.2010.04.078.

[45] W. M. Yan, C. Y. Soong, F. Chen, and H. S. Chu, “Effects of flow distributor geometry and diffusion layer porosity on reactant gas transport and performance of proton exchange membrane fuel cells,” *J. Power Sources*, vol. 125, no. 1, pp. 27–39, 2004, doi: 10.1016/j.jpowsour.2003.07.017.

[46] R. Thiedmann, F. Fleischer, C. Hartnig, W. Lehnert, and V. Schmidt, “Stochastic 3D Modeling of the GDL Structure in PEMFCs Based on Thin Section Detection,” *J. Electrochem. Soc.*, vol. 155, no. 4, p. B391, 2008, doi: 10.1149/1.2839570.

[47] S. Obayopo, T. Bello-Ochende, and J. Meyer, “Performance enhancement of a PEM fuel cell through reactant gas channel and gas diffusion layer optimisation.,” Nov. 2011.

[48] C. S. Kong, D. Y. Kim, H. K. Lee, Y. G. Shul, and T. H. Lee, “Influence of pore-size distribution of diffusion layer on mass-transport problems of proton exchange

membrane fuel cells," *J. Power Sources*, vol. 108, no. 1–2, pp. 185–191, 2002, doi: 10.1016/S0378-7753(02)00028-9.

[49] L. R. Jordan, A. K. Shukla, T. Behrsing, N. R. Avery, B. C. Muddle, and M. Forsyth, "Effect of diffusion-layer morphology on the performance of polymer electrolyte fuel cells operating at atmospheric pressure," *J. Appl. Electrochem.*, vol. 30, pp. 641–646, 2000.

[50] E. Sadeghi, N. Djilali, and M. Bahrami, "Effective thermal conductivity and thermal contact resistance of gas diffusion layers in proton exchange membrane fuel cells. Part 2: Hysteresis effect under cyclic compressive load," *J. Power Sources*, vol. 195, no. 24, pp. 8104–8109, 2010, doi: 10.1016/j.jpowsour.2010.07.051.

[51] T. Frey and M. Linardi, "Effects of membrane electrode assembly preparation on the polymer electrolyte membrane fuel cell performance," *Electrochim. Acta*, vol. 50, no. 1, pp. 99–105, 2004, doi: 10.1016/j.electacta.2004.07.017.

[52] Y. Wang, C. Y. Wang, and K. S. Chen, "Elucidating differences between carbon paper and carbon cloth in polymer electrolyte fuel cells," *Electrochim. Acta*, vol. 52, no. 12, pp. 3965–3975, 2007, doi: 10.1016/j.electacta.2006.11.012.

[53] O. A. Obeisun, D. P. Finegan, E. Engebretsen, J. B. Robinson, O. O. Taiwo, G. Hinds, P. R. Shearing, and J. L. D. Brett, "Ex-situ characterisation of water droplet dynamics on the surface of a fuel cell gas diffusion layer through wettability analysis and thermal characterisation," *Int. J. Hydrogen Energy*, vol. 42, no. 7, pp. 4404–4414, 2017, doi: 10.1016/j.ijhydene.2017.01.003.

[54] V. Gurau, M. J. Bluemle, E. S. De Castro, Y. M. Tsou, J. A. Mann, and T. A. Zawodzinski, "Characterization of transport properties in gas diffusion layers for

proton exchange membrane fuel cells. 1. Wettability (internal contact angle to water and surface energy of GDL fibers)," *J. Power Sources*, vol. 160, no. 2 SPEC. ISS., pp. 1156–1162, 2006, doi: 10.1016/j.jpowsour.2006.03.016.

[55] I. Cabasso, Y. Yuan, and X. Xu, "Gas Diffusion Electrodes Based On Polyovinylidene Fluoride) Carbon Blends," US Patent 5,783,325, Jul. 21, 1998.

[56] P. Staiti, Z. Poltarzewsky, S. Lucia, V. Alderucci, G. Maggio, and N. Giordano, "Influence of electrodic properties on water management in a solid polymer electrolyte fuel cell," *J. Appl. Electrochem.*, vol. 22, pp. 663–667, 1992.

[57] S. Latorrata, C. Cristiani, and G. Dotelli, "Performance Evaluation and Durability Enhancement of FEP-Based Gas Diffusion Media for PEM Fuel Cells," *Energies*, vol. 10, no. 12, p. 17, 2017, doi: 10.3390/en10122063.

[58] F. B. Weng, C. Y. Hsu, and M. C. Su, "Experimental study of micro-porous layers for PEMFC with gradient hydrophobicity under various humidity conditions," *Int. J. Hydrogen Energy*, vol. 36, no. 21, pp. 13708–13714, 2011, doi: 10.1016/j.ijhydene.2011.07.141.

[59] G. Lin and T. Van Nguyen, "Effect of Thickness and Hydrophobic Polymer Content of the Gas Diffusion Layer on Electrode Flooding Level in a PEMFC," *J. Electrochem. Soc.*, vol. 152, no. 10, p. A1942, 2005, doi: 10.1149/1.2006487.

[60] S. Park, J. W. Lee, and B. N. Popov, "A review of gas diffusion layer in PEM fuel cells: Materials and designs," *Int. J. Hydrogen Energy*, vol. 37, no. 7, pp. 5850–5865, 2012, doi: 10.1016/j.ijhydene.2011.12.148.

[61] J. C. Tsai and C. K. Lin, "Effect of PTFE content in gas diffusion layer based on Nafion®/PTFE membrane for low humidity proton exchange membrane fuel cell," *J.*

Taiwan Inst. Chem. Eng., vol. 42, no. 6, pp. 945–951, 2011, doi: 10.1016/j.jtice.2011.05.008.

[62] G. Velayutham, J. Kaushik, N. Rajalakshmi, and K. S. Dhathathreyan, "Effect of PTFE content in gas diffusion media and microlayer on the performance of PEMFC tested under ambient pressure," *Fuel Cells*, vol. 7, no. 4, pp. 314–318, 2007, doi: 10.1002/fuce.200600032.

[63] P. K. Sow, S. Prass, P. Kalisvaart, and W. Mérida, "Deconvolution of electrical contact and bulk resistance of gas diffusion layers for fuel cell applications," *Int. J. Hydrogen Energy*, vol. 40, no. 6, pp. 2850–2861, 2015, doi: 10.1016/j.ijhydene.2014.12.110.

[64] G. Lin and T. Van Nguyen, "Effect of Thickness and Hydrophobic Polymer Content of the Gas Diffusion Layer on Electrode Flooding Level in a PEMFC," *J. Electrochem. Soc.*, vol. 152, no. 10, p. A1942, 2005, doi: 10.1149/1.2006487.

[65] S. Park, J. W. Lee, and B. N. Popov, "Effect of carbon loading in microporous layer on PEM fuel cell performance," *J. Power Sources*, vol. 163, no. 1 SPEC. ISS., pp. 357–363, 2006, doi: 10.1016/j.jpowsour.2006.09.020.

[66] S. Park and B. N. Popov, "Effect of a GDL based on carbon paper or carbon cloth on PEM fuel cell performance," *Fuel*, vol. 90, no. 1, pp. 436–440, 2011, doi: 10.1016/j.fuel.2010.09.003.

[67] Z. Qi and A. Kaufman, "Improvement of water management by a microporous sublayer for PEM fuel cells," *J. Power Sources*, vol. 109, no. 1, pp. 38–46, 2002, doi: 10.1016/S0378-7753(02)00058-7.

[68] J. Chen, T. Matsuura, and M. Hori, "Novel gas diffusion layer with water management

function for PEMFC," *J. Power Sources*, vol. 131, no. 1–2, pp. 155–161, 2004, doi: 10.1016/j.jpowsour.2004.01.007.

[69] J. H. Nam and M. Kaviany, "Effective diffusivity and water-saturation distribution in single- and two-layer PEMFC diffusion medium," *Int. J. Heat Mass Transf.*, vol. 46, no. 24, pp. 4595–4611, 2003, doi: 10.1016/S0017-9310(03)00305-3.

[70] A. Z. Weber and J. Newman, "Effects of Microporous Layers in Polymer Electrolyte Fuel Cells," *J. Electrochem. Soc.*, vol. 152, no. 4, p. A677, 2005, doi: 10.1149/1.1861194.

[71] Y. Zhou, G. Lin, A. J. Shih, and S. J. Hu, "Assembly pressure and membrane swelling in PEM fuel cells," *J. Power Sources*, vol. 192, no. 2, pp. 544–551, 2009, doi: 10.1016/j.jpowsour.2009.01.085.

[72] J. Park, H. Oh, T. Ha, Y. Il Lee, and K. Min, "A review of the gas diffusion layer in proton exchange membrane fuel cells: Durability and degradation," *Appl. Energy*, vol. 155, pp. 866–880, 2015, doi: 10.1016/j.apenergy.2015.06.068.

[73] W. Schmittinger and A. Vahidi, "A review of the main parameters influencing long-term performance and durability of PEM fuel cells," *J. Power Sources*, vol. 180, no. 1, pp. 1–14, 2008, doi: 10.1016/j.jpowsour.2008.01.070.

[74] G. Diloyan, M. Sobel, K. Das, and P. Hutapea, "Effect of mechanical vibration on platinum particle agglomeration and growth in Polymer Electrolyte Membrane Fuel Cell catalyst layers," *J. Power Sources*, vol. 214, pp. 59–67, 2012, doi: 10.1016/j.jpowsour.2012.04.027.

[75] P. Zhou, C. W. Wu, and G. J. Ma, "Contact resistance prediction and structure optimization of bipolar plates," *J. Power Sources*, vol. 159, no. 2, pp. 1115–1122,

2006, doi: 10.1016/j.jpowsour.2005.12.080.

[76] W. K. Lee, C. H. Ho, J. W. Van Zee, and M. Murthy, “The effects of compression and gas diffusion layers on the performance of a PEM fuel cell,” *J. Power Sources*, vol. 84, no. 1, pp. 45–51, 1999, doi: 10.1016/S0378-7753(99)00298-0.

[77] J. Ihonen, F. Jaouen, G. Lindbergh, and G. Sundholm, “A novel polymer electrolyte fuel cell for laboratory investigations and in-situ contact resistance measurements,” *Electrochim. Acta*, vol. 46, no. 19, pp. 2899–2911, 2001, doi: 10.1016/S0013-4686(01)00510-2.

[78] G. Karimi, X. Li, and P. Teertstra, “Measurement of through-plane effective thermal conductivity and contact resistance in PEM fuel cell diffusion media,” *Electrochim. Acta*, vol. 55, no. 5, pp. 1619–1625, 2010, doi: 10.1016/j.electacta.2009.10.035.

[79] M. S. Ismail, T. Damjanovic, D. B. Ingham, M. Pourkashanian, and A. Westwood, “Effect of polytetrafluoroethylene-treatment and microporous layer-coating on the electrical conductivity of gas diffusion layers used in proton exchange membrane fuel cells,” *J. Power Sources*, vol. 195, no. 9, pp. 2700–2708, 2010, doi: 10.1016/j.jpowsour.2009.11.069.

[80] X. Lai, D. Liu, L. Peng, and J. Ni, “A mechanical-electrical finite element method model for predicting contact resistance between bipolar plate and gas diffusion layer in PEM fuel cells,” *J. Power Sources*, vol. 182, no. 1, pp. 153–159, 2008, doi: 10.1016/j.jpowsour.2008.03.069.

[81] I. Nitta, T. Hottinen, O. Himanen, and M. Mikkola, “Inhomogeneous compression of PEMFC gas diffusion layer. Part I. Experimental,” *J. Power Sources*, vol. 171, no. 1, pp. 26–36, 2007, doi: 10.1016/j.jpowsour.2006.11.018.

[82] P. A. García-Salaberri, M. Vera, and R. Zaera, “Nonlinear orthotropic model of the inhomogeneous assembly compression of PEM fuel cell gas diffusion layers,” *Int. J. Hydrogen Energy*, vol. 36, no. 18, pp. 11856–11870, 2011, doi: 10.1016/j.ijhydene.2011.05.152.

[83] W. Sun, B. A. Peppley, and K. Karan, “Modeling the Influence of GDL and flow-field plate parameters on the reaction distribution in the PEMFC cathode catalyst layer,” *J. Power Sources*, vol. 144, no. 1, pp. 42–53, 2005, doi: 10.1016/j.jpowsour.2004.11.035.

[84] A. Kumar and R. G. Reddy, “Materials and design development for bipolar/end plates in fuel cells,” *J. Power Sources*, vol. 129, no. 1 SPEC. ISS., pp. 62–67, 2004, doi: 10.1016/j.jpowsour.2003.11.011.

[85] P. M. Wilde, M. Mändle, M. Murata, and N. Berg, “Structural and physical properties of GDL and GDL/BPP combinations and their influence on PEMFC performance,” *Fuel Cells*, vol. 4, no. 3, pp. 180–184, 2004, doi: 10.1002/fuce.200400022.

[86] S. Escribano, J. F. Blachot, J. Ethève, A. Morin, and R. Mosdale, “Characterization of PEMFCs gas diffusion layers properties,” *J. Power Sources*, vol. 156, no. 1 SPEC. ISS., pp. 8–13, 2006, doi: 10.1016/j.jpowsour.2005.08.013.

[87] T. Matsuura, M. Kato, and M. Hori, “Study on metallic bipolar plate for proton exchange membrane fuel cell,” *J. Power Sources*, vol. 161, no. 1, pp. 74–78, 2006, doi: 10.1016/j.jpowsour.2006.04.064.

[88] Z. Lu, C. Kim, A. M. Karlsson, J. C. Cross, and M. H. Santare, “Effect of gas diffusion layer modulus and land-groove geometry on membrane stresses in proton exchange membrane fuel cells,” *J. Power Sources*, vol. 196, no. 10, pp. 4646–4654, 2011, doi:

10.1016/j.jpowsour.2011.01.028.

[89] J. C. Tsai and C. K. Lin, “Effect of PTFE content in gas diffusion layer based on Nafion®/PTFE membrane for low humidity proton exchange membrane fuel cell,” *J. Taiwan Inst. Chem. Eng.*, vol. 42, no. 6, pp. 945–951, 2011, doi: 10.1016/j.jtice.2011.05.008.

[90] H. Pang, P. Huang, W. Zhuo, M. Li, C. Gao, and D. Guo, “Hysteresis and its impact on characterization of mechanical properties of suspended monolayer molybdenum-disulfide sheets,” *Phys. Chem. Chem. Phys.*, vol. 21, no. 14, pp. 7454–7461, 2019, doi: 10.1039/c8cp07158f.

[91] V. Mishra, F. Yang, and R. Pitchumani, “Measurement and Prediction of Electrical Contact Resistance Between Gas Diffusion Layers and Bipolar Plate for Applications to PEM Fuel Cells,” *J. Fuel Cell Sci. Technol.*, vol. 1, no. 1, p. 2, 2004, doi: 10.1115/1.1782917.

[92] N. de las Heras, E. P. L. Roberts, R. Langton, and D. R. Hodgson, “A review of metal separator plate materials suitable for automotive PEMfuel cells,” *Energy Environ. Sci.*, vol. 2, no. 2, pp. 206–214, 2009, doi: 10.1039/B813231N.

[93] G. G. Park, Y. J. Sohn, T. H. Yang, Y. G. Yoon, W. Y. Lee, and C. S. Kim, “Effect of PTFE contents in the gas diffusion media on the performance of PEMFC,” *J. Power Sources*, vol. 131, no. 1–2, pp. 182–187, 2004, doi: 10.1016/j.jpowsour.2003.12.037.

[94] W. Yoon, X. Huang, P. Fazzino, K. L. Reifsnider, and M. A. Akkaoui, “Evaluation of coated metallic bipolar plates for polymer electrolyte membrane fuel cells,” *J. Power Sources*, vol. 179, no. 1, pp. 265–273, 2008, doi: 10.1016/j.jpowsour.2007.12.034.

[95] W. R. Chang, J. J. Hwang, F. B. Weng, and S. H. Chan, “Effect of clamping pressure on the performance of a PEM fuel cell,” *J. Power Sources*, vol. 166, no. 1, pp. 149–154, 2007, doi: 10.1016/j.jpowsour.2007.01.015.

[96] W. Zhang and C. Wu, “Effect of Clamping Load on the Performance of Proton Exchange Membrane Fuel Cell Stack and Its Optimization Design: A Review of Modeling and Experimental Research,” *J. Fuel Cell Sci. Technol.*, vol. 11, no. 2, pp. 1–11, 2013, doi: 10.1115/1.4026070.

[97] J. Kleemann, F. Finsterwalder, and W. Tillmetz, “Characterisation of mechanical behaviour and coupled electrical properties of polymer electrolyte membrane fuel cell gas diffusion layers,” *J. Power Sources*, vol. 190, no. 1, pp. 92–102, 2009, doi: 10.1016/j.jpowsour.2008.09.026.

[98] X. Q. Xing, K. W. Lum, H. J. Poh, and Y. L. Wu, “Optimization of assembly clamping pressure on performance of proton-exchange membrane fuel cells,” *J. Power Sources*, vol. 195, no. 1, pp. 62–68, 2010, doi: 10.1016/j.jpowsour.2009.06.107.

[99] I. Taymaz and M. Benli, “Numerical study of assembly pressure effect on the performance of proton exchange membrane fuel cell,” *Energy*, vol. 35, no. 5, pp. 2134–2140, 2010, doi: 10.1016/j.energy.2010.01.032.

[100] C. Y. Wen, Y. S. Lin, and C. H. Lu, “Experimental study of clamping effects on the performances of a single proton exchange membrane fuel cell and a 10-cell stack,” *J. Power Sources*, vol. 192, no. 2, pp. 475–485, 2009, doi: 10.1016/j.jpowsour.2009.03.058.

[101] H. Mehboob, P. M. Kyun, K. An-soo, B. A. Zai, and R. Ali, “Analysis of the Clamping Pressure Effect in PEM Fuel Cell Structure by FEM and Experiment Introduction :,”

Fuel Cell, pp. 1–6, 2009.

[102] R. Solasi, Y. Zou, X. Huang, K. Reifsnider, and D. Condit, "On mechanical behavior and in-plane modeling of constrained PEM fuel cell membranes subjected to hydration and temperature cycles," *J. Power Sources*, vol. 167, no. 2, pp. 366–377, 2007, doi: 10.1016/j.jpowsour.2007.02.025.

[103] A. Tamayol and M. Bahrami, "In-plane gas permeability of proton exchange membrane fuel cell gas diffusion layers," *J. Power Sources*, vol. 196, no. 7, pp. 3559–3564, 2011, doi: 10.1016/j.jpowsour.2010.11.109.

[104] V. Radhakrishnan and P. Haridoss, "Effect of GDL compression on pressure drop and pressure distribution in PEMFC flow field," *Int. J. Hydrogen Energy*, vol. 36, no. 22, pp. 14823–14828, 2011, doi: 10.1016/j.ijhydene.2011.05.185.

[105] M. V. Williams, E. Begg, L. Bonville, H. R. Kunz, and J. M. Fenton, "Characterization of Gas Diffusion Layers for PEMFC," *J. Electrochem. Soc.*, vol. 151, no. 8, pp. A1173–A1180, 2004, doi: 10.1149/1.1764779.

[106] J. P. Feser, A. K. Prasad, and S. G. Advani, "Experimental characterization of in-plane permeability of gas diffusion layers," *J. Power Sources*, vol. 162, no. 2 SPEC. ISS., pp. 1226–1231, 2006, doi: 10.1016/j.jpowsour.2006.07.058.

[107] J. G. Pharoah, "On the permeability of gas diffusion media used in PEM fuel cells," *J. Power Sources*, vol. 144, no. 1, pp. 77–82, 2005, doi: 10.1016/j.jpowsour.2004.11.069.

[108] J. T. Gostick, M. W. Fowler, M. D. Pritzker, M. A. Ioannidis, and L. M. Behra, "In-plane and through-plane gas permeability of carbon fiber electrode backing layers," *J. Power Sources*, vol. 162, no. 1, pp. 228–238, 2006, doi:

10.1016/j.jpowsour.2006.06.096.

[109] M. S. Ismail, A. Hassanpour, D. B. Ingham, L. Ma, and M. Pourkashanian, “On the compressibility of gas diffusion layers in proton exchange membrane fuel cells,” *Fuel Cells*, vol. 12, no. 3, pp. 391–397, 2012, doi: 10.1002/fuce.201100054.

[110] J. H. Lin, W. H. Chen, Y. J. Su, and T. H. Ko, “Effect of gas diffusion layer compression on the performance in a proton exchange membrane fuel cell,” *Fuel*, vol. 87, no. 12, pp. 2420–2424, 2008, doi: 10.1016/j.fuel.2008.03.001.

[111] T. J. Mason, J. Millichamp, T. P. Neville, A. El-Kharouf, B. G. Pollet, and D. J. L. Brett, “Effect of clamping pressure on ohmic resistance and compression of gas diffusion layers for polymer electrolyte fuel cells,” *J. Power Sources*, vol. 219, pp. 52–59, 2012, doi: 10.1016/j.jpowsour.2012.07.021.

[112] V. Radhakrishnan and P. Haridoss, “Effect of GDL compression on pressure drop and pressure distribution in PEMFC flow field,” *Int. J. Hydrogen Energy*, vol. 36, no. 22, pp. 14823–14828, 2011, doi: 10.1016/j.ijhydene.2011.05.185.

[113] S. D. Yim, B. J. Kim, Y. J. Sohn, Y. G. Yoon, G. G. Park, W. Y. Lee, C. S. Kim, and Y. C. Kim, “The influence of stack clamping pressure on the performance of PEM fuel cell stack,” *Curr. Appl. Phys.*, vol. 10, no. 2 SUPPL., pp. S59–S61, 2010, doi: 10.1016/j.cap.2009.11.042.

[114] I.-S. Han, S.-K. Park, and C.-B. Chung, “Effect of gas diffusion layer compression on the polarization curves of a polymer electrolyte membrane fuel cell: Analysis using a polarization curve-fitting model,” *Korean J. Chem. Eng.*, vol. 33, no. 11, pp. 3121–3127, 2016, doi: 10.1007/s11814-016-0157-8.

[115] P. A. Gigos, Y. Faydi, and Y. Meyer, “Mechanical characterization and analytical

modeling of gas diffusion layers under cyclic compression," *Int. J. Hydrogen Energy*, vol. 40, no. 17, pp. 5958–5965, 2015, doi: 10.1016/j.ijhydene.2015.02.136.

[116] C. W. Lin, C. H. Chien, J. Tan, Y. J. Chao, and J. W. Van Zee, "Dynamic mechanical characteristics of five elastomeric gasket materials aged in a simulated and an accelerated PEM fuel cell environment," *Int. J. Hydrogen Energy*, vol. 36, no. 11, pp. 6756–6767, 2011, doi: 10.1016/j.ijhydene.2011.02.112.

[117] M. Habibnia, M. Shakeri, and S. Nourouzi, "Determination of the effective parameters on the fuel cell efficiency, based on sealing behavior of the system," *Int. J. Hydrogen Energy*, vol. 41, no. 40, pp. 18147–18156, 2016, doi: 10.1016/j.ijhydene.2016.06.258.

[118] G. Li, J. Tan, and J. Gong, "Degradation of the elastomeric gasket material in a simulated and four accelerated proton exchange membrane fuel cell environments," *J. Power Sources*, vol. 205, pp. 244–251, 2012, doi: 10.1016/j.jpowsour.2011.06.092.

[119] J. Tan, Y. J. Chao, J. W. Van Zee, and W. K. Lee, "Degradation of elastomeric gasket materials in PEM fuel cells," *Mater. Sci. Eng. A*, vol. 445–446, pp. 669–675, 2007, doi: 10.1016/j.msea.2006.09.098.

[120] J. Zhang, H. Zhang, J. Wu, and J. Zhang, "Design and Fabrication of PEM Fuel Cell MEA, Single Cell, and Stack," *Pem Fuel Cell Test. Diagnosis*, pp. 43–80, Jan. 2013, doi: 10.1016/B978-0-444-53688-4.00002-4.

[121] L. Frisch, "PEM fuel cell stack sealing using silicone elastomers," *Seal. Technol.*, vol. 2001, no. 93, pp. 7–9, 2001, doi: 10.1016/S1350-4789(01)80085-4.

[122] P. C. Ghosh, "Influences of Contact Pressure on the Performances of Polymer Electrolyte Fuel Cells," *J. Energy*, vol. 2013, pp. 1–11, 2013, doi:

10.1155/2013/571389.

[123] D. Yang, J. Zheng, B. Li, and J. Ma, “Degradation of Other Components,” in *PEM Fuel Cell Failure Mode Analysis*, 1st ed., H. Wang, H. Li, and X.-Z. Yuan, Eds. CRC Press, 2011, pp. 265–304.

[124] R. Bieringer, M. Adler, S. Geiss, and M. Viol, “Gaskets: Important Durability Issues,” in *Polymer Electrolyte Fuel Cell Durability*, 1st ed., F. N. Büchi, M. Inaba, and T. J. Schmidt, Eds. NY,USA: Springer US, 2009, pp. 271–281.

[125] S. Damdar and J. Drago, “Advanced Fuel Cell Technology,” vol. 15, no. 8. pp.1-15,2011,[Online].Available:https://www.garlock.com/sites/default/files/files/technical_articles/Advanced Fuel Cell Technology.pdf.

[126] S. Sarangapani and F. J. Luczak, “Experimental Methods In Low Temperature Fuel Cells,” in *Fuel cells: from fundamentals to applications*, S. Srinivasan, 1st ed. New York: Springer, 2006, pp. 267–308.

[127] V. Radhakrishnan and P. Haridoss, “Effect of cyclic compression on structure and properties of a Gas Diffusion Layer used in PEM fuel cells,” *Int. J. Hydrogen Energy*, vol. 35, no. 20, pp. 11107–11118, 2010, doi: 10.1016/j.ijhydene.2010.07.009.

[128] M. Ismail, “On the Transport Properties of Gas Diffusion Layers used in Proton Exchange Membrane Fuel Cells,” Ph.D thesis, School Of Process, Environmental and Materials Engineering, University Of Leeds, 2011.

[129] A. B. Abell, K. L. Willis, and D. A. Lange, “Mercury intrusion porosimetry and image analysis of cement-based materials,” *J. Colloid Interface Sci.*, vol. 211, no. 1, pp. 39–44, 1999, doi: 10.1006/jcis.1998.5986.

[130] B. Münch and L. Holzer, “Contradicting geometrical concepts in pore size analysis

attained with electron microscopy and mercury intrusion," *J. Am. Ceram. Soc.*, vol. 91, no. 12, pp. 4059–4067, 2008, doi: 10.1111/j.1551-2916.2008.02736.x.

[131] P. Rama, R. Chen, and J. Andrews, "A review of performance degradation and failure modes for hydrogen-fuelled polymer electrolyte fuel cells," *Proc. Inst. Mech. Eng. Part A J. Power Energy*, vol. 222, no. 5, pp. 4214–441, 2008, doi: 10.1243/09576509JPE603.

[132] C. Wang, M. Waje, X. Wang, J. M. Tang, R. C. Haddon, and Y. S. Yan, "Proton exchange membrane fuel cells with carbon nanotube based electrodes," *Nano Lett.*, vol. 4, no. 2, pp. 345–348, 2004, doi: 10.1021/nl034952p.

[133] H. Zamora, P. Cañizares, M. A. Rodrigo, and J. Lobato, "Improving of micro porous layer based on advanced carbon materials for high temperature proton exchange membrane fuel cell electrodes," *Fuel Cells*, vol. 15, no. 2, pp. 375–383, 2015, doi: 10.1002/fuce.201400139.

[134] S. Litster and G. McLean, "PEM fuel cell electrodes," *J. Power Sources*, vol. 130, no. 1–2, pp. 61–76, 2004, doi: 10.1016/j.jpowsour.2003.12.055.

[135] X.-Z. Yuan and H. Wang, "PEM Fuel Cell Fundamentals," in *PEM Fuel Cell Electrocatalysts and Catalyst Layers*, London: Springer London, 2008, pp. 1–87.

[136] S. Subramaniam, G. Rajaram, K. Palaniswamy, and V. R. Jothi, "Comparison of perforated and serpentine flow fields on the performance of proton exchange membrane fuel cell," *J. Energy Inst.*, vol. 90, no. 3, pp. 363–371, 2017, doi: 10.1016/j.joei.2016.04.006.

[137] J. Millichamp, T. J. Mason, T. P. Neville, N. Rajalakshmi, R. Jervis, P. R. Shearing, and D. J. L. Brett, "Mechanisms and effects of mechanical compression and

dimensional change in polymer electrolyte fuel cells - A review," *J. Power Sources*, vol. 284, pp. 305–320, 2015, doi: 10.1016/j.jpowsour.2015.02.111.

[138] J. Ge, A. Higier, and H. Liu, "Effect of gas diffusion layer compression on PEM fuel cell performance," *J. Power Sources*, vol. 159, no. 2, pp. 922–927, 2006, doi: 10.1016/j.jpowsour.2005.11.069.

[139] S. S. L. Rao, A. Shaija, and S. Jayaraj, "Performance analysis of a transparent PEM fuel cell at theoptimized clamping pressure applied on its bolts," in *Materials Today: Proceedings*, 2018, vol. 5, no. 1, pp. 58–65, doi: 10.1016/j.matpr.2017.11.053.

[140] A. H. Mahmoudi, A. Ramiar, and Q. Esmaili, "Effect of inhomogeneous compression of gas diffusion layer on the performance of PEMFC with interdigitated flow field," *Energy Convers. Manag.*, vol. 110, pp. 78–89, 2016, doi: 10.1016/j.enconman.2015.12.012.

[141] J. Wang, J. Yuan, and B. Sundén, "On electric resistance effects of non-homogeneous GDL deformation in a PEM fuel cell," *Int. J. Hydrogen Energy*, vol. 42, no. 47, pp. 28537–28548, 2017, doi: 10.1016/j.ijhydene.2017.09.119.

[142] S. Tanaka and T. Shudo, "Experimental and numerical modeling study of the electrical resistance of gas diffusion layer-less polymer electrolyte membrane fuel cells," *J. Power Sources*, vol. 278, pp. 382–395, 2015, doi: 10.1016/j.jpowsour.2014.12.077.

[143] C. J. Netwall, B. D. Gould, J. A. Rodgers, N. J. Nasello, and K. E. Swider-Lyons, "Decreasing contact resistance in proton-exchange membrane fuel cells with metal bipolar plates," *J. Power Sources*, vol. 227, pp. 137–144, 2013, doi: 10.1016/j.jpowsour.2012.11.012.

[144] P. Liang, D. Qiu, L. Peng, P. Yi, X. Lai, and J. Ni, “Contact resistance prediction of proton exchange membrane fuel cell considering fabrication characteristics of metallic bipolar plates,” *Energy Convers. Manag.*, vol. 169, no. April, pp. 334–344, 2018, doi: 10.1016/j.enconman.2018.05.069.

[145] N. De Las Heras, E. P. L. Roberts, R. Langton, and D. R. Hodgson, “A review of metal separator plate materials suitable for automotive PEM fuel cells,” *Energy Environ. Sci.*, vol. 2, no. 2, pp. 206–214, 2009, doi: 10.1039/b813231n.

[146] N. Kulkarni, J. I. S. Cho, L. Rasha, R. E. Owen, Y. Wu, R. Ziesche, J. Hack, T. Neville, M. Whiteley,, N. Karddjilov, H. Markotter, I. Manke, P. R. Shearing, and D. J. L. Brett, “Effect of cell compression on the water dynamics of a polymer electrolyte fuel cell using in-plane and through-plane in-operando neutron radiography,” vol. 439, no. May, 2019, doi: 10.1016/j.jpowsour.2019.227074.

[147] Y. Wu, J. I. S. Cho, X. Lu, L. Rasha, T. P. Neville, J. Millichamp, R. Ziesche, N. Kardjilov, H. Markotter, P. Shearing, and D. J. L. Brett, “Effect of compression on the water management of polymer electrolyte fuel cells : An in-operando neutron radiography study,” vol. 412, no. November 2018, pp. 597–605, 2019, doi: 10.1016/j.jpowsour.2018.11.048.

[148] O. M. Orogbemi, D. B. Ingham, M. S. Ismail, K. J. Hughes, L. Ma, and M. Pourkashanian, “On the gas permeability of the microporous layer used in polymer electrolyte fuel cells,” *J. Energy Inst.*, vol. 41, no. 46, pp. 21345–21351, 2017, doi: doi: 10.1016/j.joei.2017.09.006.

[149] O. M. Orogbemi, D. B. Ingham, M. S. Ismail, K. J. Hughes, L. Ma, and M. Pourkashanian, “Through-plane gas permeability of gas diffusion layers and microporous layer: Effects of carbon loading and sintering,” *J. Energy Inst.*, vol. 91,

no. 2, pp. 270–278, 2018, doi: 10.1016/j.joei.2016.11.008.

[150] A. El-Kharouf, T. J. Mason, D. J. L. Brett, and B. G. Pollet, “Ex-situ characterisation of gas diffusion layers for proton exchange membrane fuel cells,” *J. Power Sources*, vol. 218, pp. 393–404, 2012, doi: 10.1016/j.jpowsour.2012.06.099.

[151] M. S. Ismail, T. Damjanovic, K. Hughes, D. B. Ingham, L. Ma, M. Pourkashanian, and M. Rosli, “Through-Plane Permeability for Untreated and PTFE-Treated Gas Diffusion Layers in Proton Exchange Membrane Fuel Cells,” *J. Fuel Cell Sci. Technol.*, vol. 7, no. 5, p. 051016, 2010, doi: 10.1115/1.4000685.

[152] M. S. Ismail, T. Damjanovic, D. B. Ingham, L. Ma, and M. Pourkashanian, “Effect of polytetrafluoroethylene-treatment and microporous layer-coating on the in-plane permeability of gas diffusion layers used in proton exchange membrane fuel cells,” *J. Power Sources*, vol. 195, no. 19, pp. 6619–6628, 2010, doi: 10.1016/j.jpowsour.2010.04.036.

[153] M. S. Ismail, D. Borman, T. Damjanovic, D. B. Ingham, and M. Pourkashanian, “On the through-plane permeability of microporous layer-coated gas diffusion layers used in proton exchange membrane fuel cells,” *Int. J. Hydrogen Energy*, vol. 36, no. 16, pp. 10392–10402, 2010, doi: 10.1016/j.ijhydene.2010.09.012.

[154] O. M. Orogbemi, D. B. Ingham, M. S. Ismail, K. J. Hughes, L. Ma, and M. Pourkashanian, “The effects of the composition of microporous layers on the permeability of gas diffusion layers used in polymer electrolyte fuel cells,” *Int. J. Hydrogen Energy*, vol. 41, no. 46, pp. 21345–21351, 2016, doi: 10.1016/j.ijhydene.2016.09.160.

[155] M. S. Ismail, K. . Hughes, D. B. Ingham, L. Ma, and M. Pourkashanian, “Effect of

PTFE loading of gas diffusion layers on the performance of proton exchange membrane fuel cells running at high-efficiency operating conditions," *Int. J. ENERGY Res.*, vol. 37, no. 13, pp. 1592–1599, 2013, doi: 10.1002/er.

[156] M. S. Ismail, D. B. Ingham, L. Ma, and M. Pourkashanian, "The contact resistance between gas diffusion layers and bipolar plates as they are assembled in proton exchange membrane fuel cells," *Renew. Energy*, vol. 52, pp. 40–45, 2013, doi: 10.1016/j.renene.2012.10.025.

[157] T. Chen, S. Liu, J. Zhang, and M. Tang, "Study on the characteristics of GDL with different PTFE content and its effect on the performance of PEMFC," *Int. J. Heat Mass Transf.*, vol. 128, pp. 1168–1174, 2019, doi: 10.1016/j.ijheatmasstransfer.2018.09.097.

[158] R. John Felix Kumar, V. Radhakrishnan, and P. Haridoss, "Enhanced mechanical and electrochemical durability of multistage PTFE treated gas diffusion layers for proton exchange membrane fuel cells," *Int. J. Hydrogen Energy*, vol. 37, no. 14, pp. 10830–10835, 2012, doi: 10.1016/j.ijhydene.2012.04.092.

[159] J. H. Chun, D. H. Jo, S. G. Kim, S. H. Park, C. H. Lee, and S. H. Kim, "Improvement of the mechanical durability of micro porous layer in a proton exchange membrane fuel cell by elimination of surface cracks," *Renew. Energy*, vol. 48, pp. 35–41, 2012, doi: 10.1016/j.renene.2012.04.011.

[160] A. Ozden, S. Shahgaldi, X. Li, and F. Hamdullahpur, "A graphene-based microporous layer for proton exchange membrane fuel cells: Characterization and performance comparison," *Renew. Energy*, vol. 126, pp. 485–494, 2018, doi: 10.1016/j.renene.2018.03.065.

[161] V. V. Atrazhev, T. Y. Astakhova, D. V. Dmitriev, N. S. Erikhman, V. I. Sultanov, T. Patterson, and S. F. Burlatsky, “The Model of Stress Distribution in Polymer Electrolyte Membrane,” *J. Electrochem. Soc.*, vol. 160, no. 10, pp. F1129–F1137, 2013, doi: 10.1149/2.079310jes.

[162] S. G. Kandlikar, M. L. Garofalo, and Z. Lu, “Water management in a PEMFC: Water transport mechanism and material degradation in gas diffusion layers,” *Fuel Cells*, vol. 11, no. 6, pp. 814–823, 2011, doi: 10.1002/fuce.201000172.

[163] A. El-Kharouf and R. Steinberger-Wilckens, “The Effect of Clamping Pressure on Gas Diffusion Layer Performance in Polymer Electrolyte Fuel Cells,” *Fuel Cells*, vol. 15, no. 6, pp. 802–812, 2015, doi: 10.1002/fuce.201500088.

[164] M. Mortazavi and K. Tajiri, “Effect of the PTFE content in the gas diffusion layer on water transport in polymer electrolyte fuel cells (PEFCs),” *J. Power Sources*, vol. 245, pp. 236–244, 2014, doi: 10.1016/j.jpowsour.2013.06.138.

[165] L. Chen, H. Luan, Y. L. He, and W. Q. Tao, “Effects of roughness of gas diffusion layer surface on liquid water transport in micro gas channels of a proton exchange membrane fuel cell,” *Numer. Heat Transf. Part A Appl.*, vol. 62, no. 4, pp. 295–318, 2012, doi: 10.1080/10407782.2012.670586.

[166] V. Gurau, M. J. Bluemle, E. S. De Castro, Y. Tsou, T. A. Zawodzinski, and J. A. Mann, “Characterization of transport properties in gas diffusion layers for proton exchange membrane fuel cells 2 . Absolute permeability,” vol. 165, pp. 793–802, 2007, doi: 10.1016/j.jpowsour.2006.12.068.

[167] C. Robin, M. Gerard, A. A. Franco, and P. Schott, “Multi-scale coupling between two dynamical models for PEMFC aging prediction,” *Int. J. Hydrogen Energy*, vol. 38,

no. 11, pp. 4675–4688, 2013, doi: 10.1016/j.ijhydene.2013.01.040.

[168] P. R. Pathapati, X. Xue, and J. Ã. Tang, “A new dynamic model for predicting transient phenomena in a PEM fuel cell system,” vol. 30, pp. 1–22, 2005, doi: 10.1016/j.renene.2004.05.001.

[169] E. Carcadea, M. Varlam, M. Ismail, D. B. Ingham, A. Marinoiu, M. Raceanu, C. Jianu, L. Patularu, and D. Ion-Ebrasu, “PEM fuel cell performance improvement through numerical optimization of the parameters of the porous layers,” *Int. J. Hydrogen Energy*, vol. 45, no. 14, pp. 7968–7980, 2020, doi: 10.1016/j.ijhydene.2019.08.219.

[170] E. Nishiyama and T. Murahashi, “Water transport characteristics in the gas diffusion media of proton exchange membrane fuel cell - Role of the microporous layer,” *J. Power Sources*, vol. 196, no. 4, pp. 1847–1854, 2011, doi: 10.1016/j.jpowsour.2010.09.055.

[171] R. Li, Y. Cai, U. Reimer, K. Wippermann, Z. Shao, and W. Lehnert, “CrN / Cr-Coated Steel Plates for High-Temperature Polymer Electrolyte Fuel Cells : Performance and Durability,” *J. Electrochem. Soc.*, vol. 167, 2020, doi: 10.1149/1945-7111/abc76c.

[172] F. J. Luczak and S. Sarangapani, “Experimental Methods In Low Temperature Fuel Ccells BT - Fuel Cells: From Fundamentals to Applications,” 1st ed., S. Srinivasan, Ed. Boston, MA: Springer US, 2006, pp. 267–308.

[173] D. Qiu, L. Peng, P. Yi, X. Lai, H. Janßen, and W. Lehnert, “Contact behavior modelling and its size effect on proton exchange membrane fuel cell,” *J. Power Sources*, vol. 365, pp. 190–200, 2017, doi: 10.1016/j.jpowsour.2017.08.088.

[174] H. Tang, Z. Qi, M. Ramani, and J. F. Elter, “PEM fuel cell cathode carbon corrosion due to the formation of air/fuel boundary at the anode,” *J. Power Sources*, vol. 158,

no. 2 SPEC. ISS., pp. 1306–1312, 2006, doi: 10.1016/j.jpowsour.2005.10.059.

[175] J. Tan, Y. J. Chao, X. Li, and J. W. Van Zee, “Degradation of silicone rubber under compression in a simulated PEM fuel cell environment,” *J. Power Sources*, vol. 172, no. 2, pp. 782–789, 2007, doi: 10.1016/j.jpowsour.2007.05.026.

[176] P. C. Ghosh, “Influences of Contact Pressure on the Performances of Polymer Electrolyte Fuel Cells,” *J. Energy*, vol. 2013, pp. 1–11, 2013, doi: 10.1155/2013/571389.

[177] R. Banerjee, J. Hinebaugh, H. Liu, R. Yip, N. Ge, and A. Bazylak, “Heterogeneous porosity distributions of polymer electrolyte membrane fuel cell gas diffusion layer materials with rib-channel compression,” *Int. J. Hydrogen Energy*, vol. 1, no. 416, pp. 14886–14896, 2016, doi: 10.1016/j.ijhydene.2016.06.147.

[178] I. Nitta, O. Himanen, and M. Mikkola, “Thermal conductivity and contact resistance of compressed gas diffusion layer of PEM fuel cell,” *Fuel Cells*, vol. 8, no. 2, pp. 111–119, 2008, doi: 10.1002/fuce.200700054.

[179] F. Aldakheel, M. S. Ismail, K. J. Hughes, D. B. Ingham, L.Ma, M. Pourkashanian, D. Cumming, and R. Smith, “Gas permeability, wettability and morphology of gas diffusion layers before and after performing a realistic ex-situ compression test,” *Renew. Energy*, vol. 151, pp. 1082–1091, 2020, doi: 10.1016/j.renene.2019.11.109.

[180] R. R. Rashapov, J. Unno, and J. T. Gostick, “Characterization of PEMFC Gas Diffusion Layer Porosity,” *J. Electrochem. Soc.*, vol. 162, no. 6, pp. F603–F612, 2015, doi: 10.1149/2.0921506jes.

[181] T. Ha, J. Cho, J. Park, K. Min, H. S. Kim, E. Lee, and J. Y. Jyoung, “Experimental study of the effect of dissolution on the gas diffusion layer in polymer electrolyte

membrane fuel cells," *Int. J. Hydrogen Energy*, vol. 36, no. 19, pp. 12427–12435, 2011, doi: 10.1016/j.ijhydene.2011.06.096.

[182] S. Shukla, F. Wei, M. Mandal, J. Stumper, and M. Secanell, "Determination of PEFC Gas Diffusion Layer and Catalyst Layer Porosity Utilizing Archimedes Principle," *J. Electrochem. Soc.*, vol. 166, no. 15, pp. F1142–F1147, 2019, doi: 10.1149/2.0251915jes.

[183] "Sigracet 34 and 35 Series Carbon Paper GDL Properties Sheet." https://www.fuelcellstore.com/spec-sheets/SGL-GDL_34-35.pdf.

[184] V. V. Atrazhev, T. Y. Astakhova, D. V. Dmitriev, N. S. Erikhman, V. I. Sultanov, T. Patterson, and S. F. Burlatsky, "The Model of Stress Distribution in Polymer Electrolyte Membrane," *J. Electrochem. Soc.*, vol. 160, no. 10, pp. F1129–F1137, 2013, doi: 10.1149/2.079310jes.

[185] A. H. Kakaee, G. R. Molaeimanesh, and M. H. Elyasi Garmaroudi, "Impact of PTFE distribution across the GDL on the water droplet removal from a PEM fuel cell electrode containing binder," *Int. J. Hydrogen Energy*, vol. 43, no. 32, pp. 15481–15491, 2018, doi: 10.1016/j.ijhydene.2018.06.111.

[186] "Gas Diffusion Layer non-woven fabric Material type : GDL -39BA-," 2014. https://www.fuelcellstore.com/spec-sheets/sigracet-39ba-spec-sheet.pdf.

[187] S. Yu, X. Li, J. Li, S. Liu, W. Lu, Z. Shao, and B. Yi, "Study on hydrophobicity degradation of gas diffusion layer in proton exchange membrane fuel cells," *Energy Convers. Manag.*, vol. 76, pp. 301–306, 2013, doi: 10.1016/j.enconman.2013.07.034.

[188] Y. Ira, Y. Bakhshan, and J. Khorshidimalahmadi, "Effect of wettability heterogeneity and compression on liquid water transport in gas diffusion layer coated with

microporous layer of PEMFC," *Int. J. Hydrogen Energy*, vol. 46, no. 33, pp. 17397–17413, 2021, doi: 10.1016/j.ijhydene.2021.02.160.

[189] M. S. Ismail, K. J. Hughes, D. B. Ingham, L. Ma, and M. Pourkashanian, "Effects of anisotropic permeability and electrical conductivity of gas diffusion layers on the performance of proton exchange membrane fuel cells," vol. 95, pp. 50–63, 2012, doi: 10.1016/j.apenergy.2012.02.003.

[190] H. W. Wu, "A review of recent development: Transport and performance modeling of PEM fuel cells," *Appl. Energy*, vol. 165, pp. 81–106, 2016, doi: 10.1016/j.apenergy.2015.12.075.

[191] T. Berning, D. M. Lu, and N. Djilali, "Three-dimensional computational analysis of transport phenomena in a PEM fuel cell," *J. Power Sources*, vol. 106, no. 1–2, pp. 284–294, 2002, doi: 10.1016/S0378-7753(01)01057-6.

[192] E. A. Ticianelli, C. R. Derouin, A. Redondo, and S. Srinivasan, "Methods to Advance Technology of Proton Exchange Membrane Fuel Cells," *J. Electrochem. Soc.*, vol. 135, no. 9, pp. 2209–2214, 1988, doi: 10.1149/1.2096240.

APPENDIX A: KYUSHU UNIVERSITY COLLABRATION (JAPAN)

Research Collaboration between Energy 2050 & I^{2}CNER

18th/July/2019- 10th/Aug/2019

Fahad Aldakheel

PhD student

University of Sheffield

Energy 2050

Introduction

The research collabration between the University of Sheffield and Kyushu University is part of a research grant between the Energy 2050 fuel cell group and the Next generation fuel cell technology lab in the International Instituate for Carbon-Netural Energy Research (I^{2}CNER) group. The trip duration was

from 18th/July/2019 to 10th/Aug/2019, and was based in the I^2CNER research facilities at Kyushu University Ito Campus in Fukuoka, Japan.

As part of the research collaboration, researchers from both institutions organise workshops to share the latest progress in their research. Another essential part of the collaboration is to give the opportunity of PhD students to share knowledge and get experience in different labs. Therefore, I was selected to be part of this exchange opportunity and be able to do experimental work at I^2CNER.

Objectives

- To be trained on the electrochemical analysis machine (3-electrode cyclic voltammetry)
- Fabrication of non-Pt catalyst (Fe-N-C) and Pt/C catalyst inks.
- To conduct experiments on the gas diffusion layers, which includes:
  - Electrical resistance before and after a compression test
  - BET analysis for surface area
  - Thermogravimetric analysis (TGA) for GDL and gasket samples

Research & Experimental work

1) Electrochemical Analysis

Cyclic voltammetry is an electrochemical method that measures the current of the working electrode under an excess voltage of that calculated using Nernst Equation.

Machine setup and preparation:

Catalyst ink preparation:

1) Non-pt-catalyst [Fe-N-C]

In order to make the ink, we have to use a ratio of the elements

Notes:

- Rule of thumb: For any catalyst, always start it water and then start pouring the ethanol .

3:3:1 ⟶ DI:Ethonal:Nafion(5 wt%)

150ml:150ml:50ml

Now, by having the powder catalyst of (Fe-N-C), we start the mixing process: [Check Fig.1]

Figure 0.1 The materials used for creating the catalyst ink.

- You can use either a bath type or a probe sonicator. In this, experimental work a probe sonicator was used. [Check Fig. 2]

- Clean the probe with ethanol as shown in Fig. 2a, then use a plastic beaker or container filled with ice to place your ink sample.
- Place the probe inside the sample ink as shown in Fig. 3b for 30 mins to mix, and wrap the tip of the vial with a parafilm.
- Using a pipette with 8 µl and carefully cast your ink on the glassy carbon on the electrode.
- Finally, place your electrodes in an oven with 65°C for at least 10 mins to dry and be ready to use.

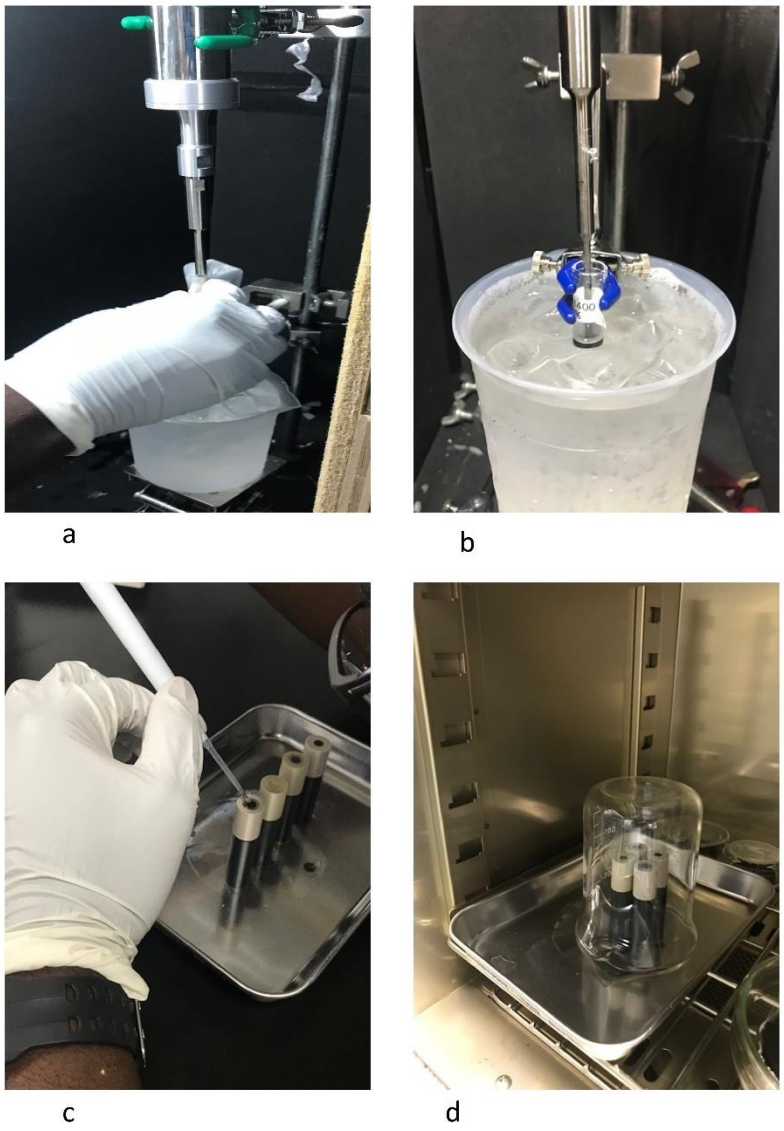

Figure 0.2 The procedure of a) cleaning the probe, b) sonicating the ample in the clod bath, c) casting your ink on the working electrode, and d) drying your ample in an oven.

2) Pt/c catalyst

The carbon used is Ketjen black with platinum; the ratios of making the ink as follows:

- Pt/CB: the Pt% in Pt/CB= 46.4%
- Electrode surface area= 0.196 cm^2.
- A) Amount of Pt on electrode should be = 17.3 $\mu g/cm^2$

- B) calculating how many grams of Pt you need: 17.3 * 0.196= 3.3908 µg
- C) since the powder has a 46.4% of Pt, we need to calculate for the amount of the carbon+Pt on the electrode= $\frac{3.3908\ \mu g}{46.4\%}$= 7.3 µg
- D) calculating for the catalyst amount (Pt+Carbon) based on the ratio of volume:

$$\frac{Amount\ of\ catalsyt}{10\ \mu l\ (\text{the amount of ink on the surface of the electrode})} = \frac{x\ (Pt+carbon) in\ mg}{3\ ml\ (total\ of\ catalsyt)}$$

Acidic electrolyte solution preparation ($HCLO_4$):

In order to prepare the acidic electrolyte for the electrochemical measurement:

0.1 M of $HCLO_4$ (Perchloric Acid 60%):

- Using a 500 ml beaker (¾) filled with DI water.
- Then, using a 5.4538 µl of $HCLO_4$ into the DI water
- Finally, continue filling the beaker up to 500 ml with the DI water.

Electrochemical Testing and cell (a)

- First, Rinse the glassware with the counter and reference electrodes using acid.
- After having the electrode ready, you can start assembling the glassware with the reference and counter electrode. [Check Fig.3]

- Place the working electrode in position, and start flowing a Nitrogen gas for bubbling (saturation for 30 mins at 100 ml/min).

- Switch the flowing gas to the other side of the glassware (on the surface) at rate of 50 ml/min, and make sure that that there is no bubble inside the solution or on the electrode surface.

- Run the software, and make sure you have the procedure protocol as follows:

N_2 bubble for 30 mins	Make sure that the gas is flowing from the right side of the cell
CV 50 cycles	Before this step, change the flowing gas to the left side
CV 3 cycles	save
LSV 2500 rpm	save
LSV 1600 rpm	save
LSV 900 rpm	save
LSV 400 rpm	save
O_2 bubble for 30 min	Make sure that the gas is flowing from the right side of the cell

CV 3 cycles	Before this step, change the flowing gas to the left side (save)
LSV 2500 rpm	save
LSV 1600 rpm	save
LSV 900 rpm	save
LSV 400 rpm	save

a b

Figure 0.3 a) the electrochemical dynamic electrode machine, and b) the glassware and the counter electrode

After running all the steps, start washing the cell as follows:

1) Clean the glassware after use with tap water and rinse with DI water.
2) Put glassware into a beaker, and add distilled water.
3) Heat at 350°C for 30mins, and wait for temperature to drop down to room temperature.

4) Pour water out of the beaker and add new distilled water.
5) Ultrasonicate for 30 mins; make sure the probe is less than 1 cm dip and seal with plastic wrap.
6) Cleaning the electrode: First, wipe the ink off the electrode with ethanol , then polish the electrode Using alumina paste either by using a rotating polishing disk with 4 different movement (90° for 4 times); or using the (8 movement-method for homogenous polishing). Clean it with hater and sonicate the electrodes with ethanol for 10 mins (they should face dwon the beaker in a diagonal position.
7) Dry the electrode for 10 mins.
8) Tip: before casting the ink on the electrode, it's better to make sure the electrode is dry and ready for casting, or just right after the sonication of the ink you can cast it homogenously.

<u>Acid washing every 3 months (1M sulfuric acid):</u>

1) Salt bridge and counter electrode don't need to acid ash; also avoid washing plastic, rubber parts with acid. [Only pour out distilled water after removing the glass].
2) Clean looping tube, glass seal, and reference electrode tube with water and rinse with deionized water. Wash the beaker and dry it with drying paper.
3) Put glass into a large beaker (make sure it becomes stable and add acid.
4) Finally, Seal with plastic wrap.

2) Thermogravimetric analysis (TGA)

As the temperature is increasing with time, the TGA analysis measures the mass loss and shows any endothermic or exothermic reactions that happen during the process. This information is essential for the thermal stability of the material used.

All the samples were carried out using a Rigaku (Thermo Plus-EVO2), and the sample holder used is $Al2O_3$

Sample preparations and Analysis

- First, start cutting your sample into small pieces, and measure a 5 mg mass.
- Then, open the chamber and put the sample holder (empty) and close the chamber.
- Zero the mass measurement in the software.
- Open the chamber and place your sample inside the Alumina sample holder and place carefully place back inside the chamber.
- In order to ensure an inert atmosphere, flow Nitrogen gas for 2 hours before running the experiment.
- The measurement of mass loss was taken at room temperature to 1000°C at 10°C/min heating rate.
- Note: The Alumina sample holder can be used multiple times after cleaning with ethanol after each use.

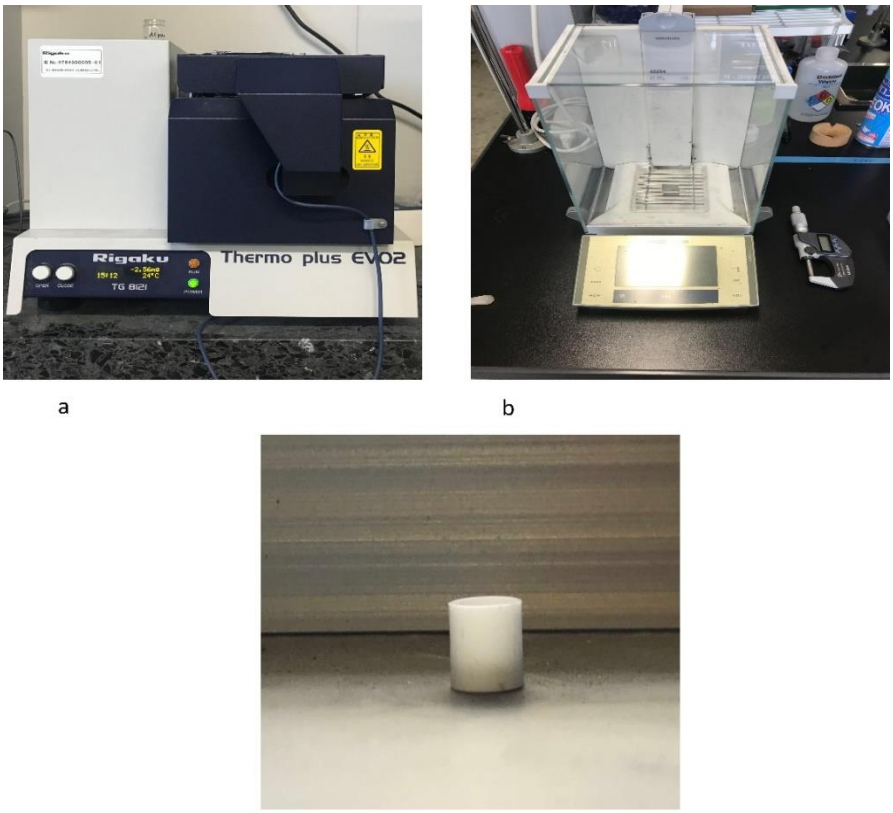

a b

Figure 0.4 a) Rigaku Thermo Plus EVO0.5 machine, b) micro scale, and c) Alumina ample holder

Initial results

Figure 5 shows the thermal stability of the SGL-34-BA before and after compression:

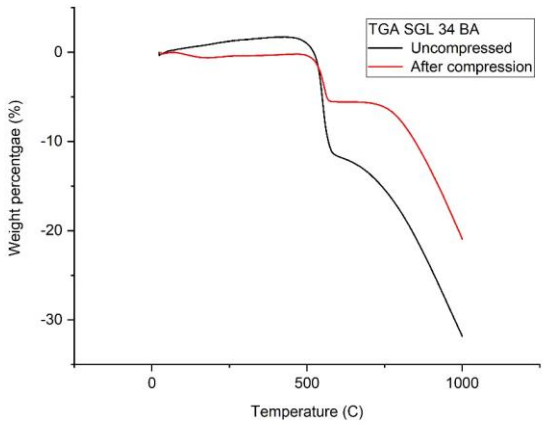

Figure 5 Weight percentage vs. the temperature for uncompressed and compressed SGL-34-BA GDL sample.

3) Brunauer–Emmett–Teller (BET)

The BET method is used to calculate the surface area of materials by flowing a gas, Typically Nitrogen gas, and being adsorbed by the material. The amount of the adsorbed gas is calculated to determine the surface area, and the pore size distribution.

Preparation and Procedure:

a) Open N_2 and He gases, by switching both valves on device, then turn on the machine.
b) Assemble the glass tube by first inserting the glass rod in a horizontal direction, to avoid breaking the tube and close it with a filter.
c) Mount the glass tube into Port 1, 2,3, if you are measuring only one ample, just press on port 1 and 2. [Usually port 2 used empty as a reference]
d) Turn on the pump:

- Press the VAC-for vacuum until it reaches 10^{-2} KPa (green light is on)
- Stop vacuum when it reaches 10^{-2}, and press PURGE.

e) Demount the glass tube and take to balance the sample holder tube empty for 3 times and take the average value.
f) Now, weigh the sample 3 times when placed inside the glass tube and calculate the avg.
g) Mount the glass tube with sample to device and change probes to stage with reference tube.
h) Press VAC and fast vacuum appear and wait for it to reach 10^{-2} Kpa (green).

i) Set the Temperature to 200°C, then press HEAT (red light flashes), and wait for 2 hours.

j) After 2 hours of heating stop HEAT, and change glass tube to stage 1 and wait to cool down

k) When the glass tube cools down, stop VAC and press PURGE.

l) Demount the sample tubes and take to balance for weighing 3 times and take average (This average will be subtracted from the empty tubes average for mass input).

m) Now, stop the degassing device and the pump (including all three ports)

n) Turn on the BET machine and PC:

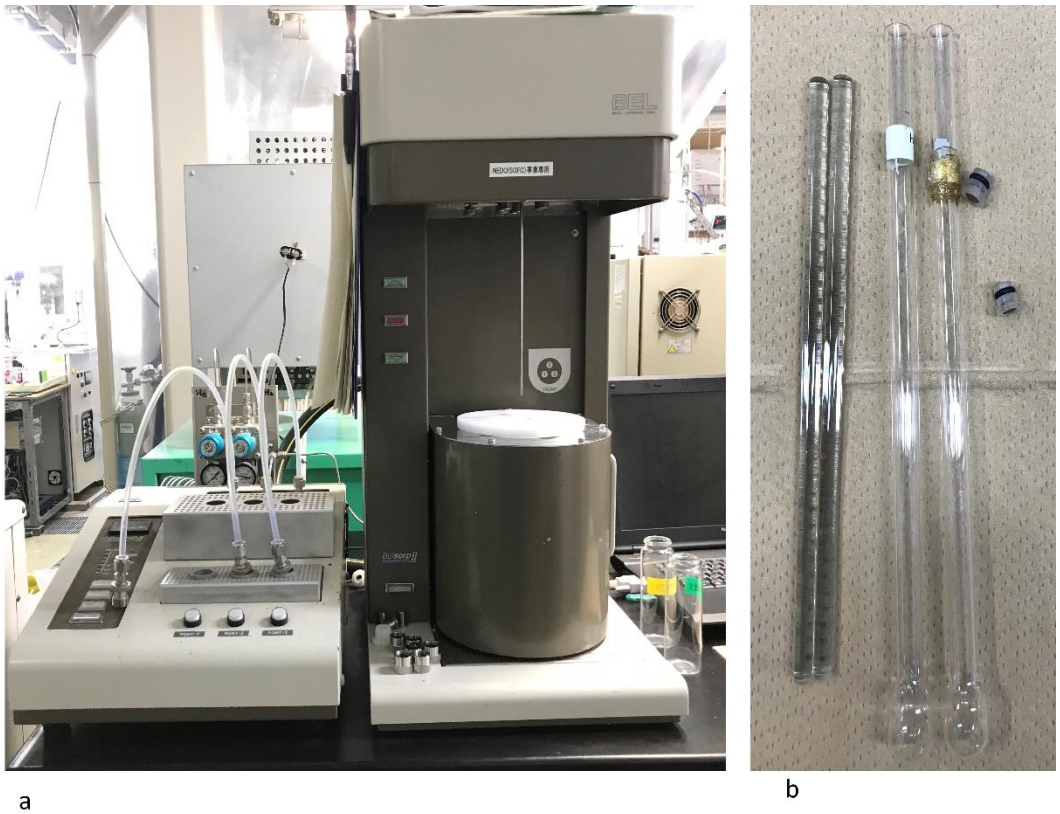

a b

Figure 6 a) The degassing device at left and the BET machine on right b) the glass tube with rods and filters for measurement.

Initial results

Figure 7 shows the BET result of SGL-34-BA surface area which is 4.40 m^2 g^{-1}

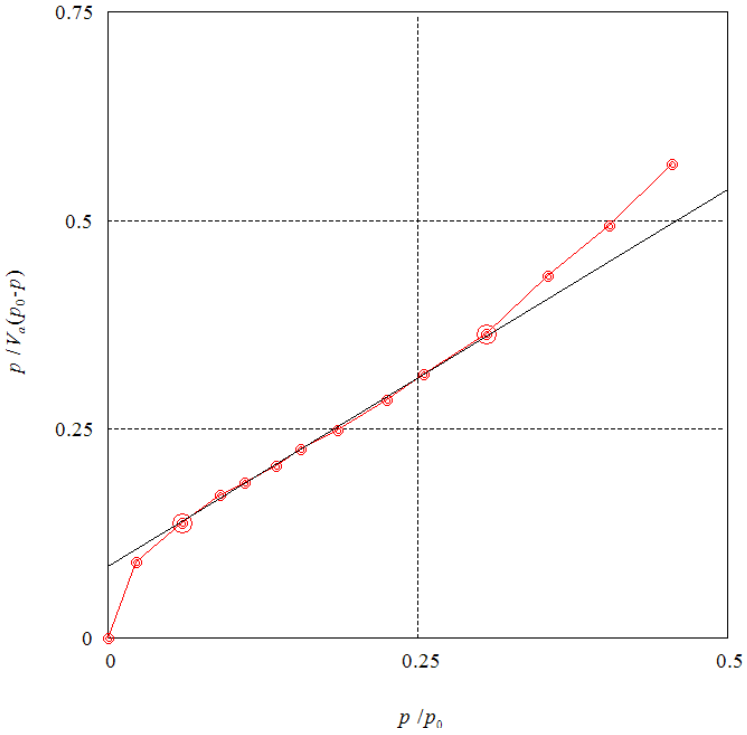

Figure 7 The nitrogen adsorption process of SGL-34-BA GDL sample

4) Electrical Resistance

In order to measure the electrical resistance of the GDL samples, a cell with a 5 cm^2 active area used without a membrane electrode assembly during the resistance measurement. A GDL is between two graphite bipolar plates. The cell used is shown in Fig.8 and it is connected to a potentiostat/galvanostat device. Electrical resistance measurements were carried out by an Autolab PGSTAT128N potentiostat/galvanostat. The electrical resistance measurements were controlled by a frequency range of 100KHz and 0.1 Hz, with an amplitude of 0.005 V using a single sinusoidal sweeping.

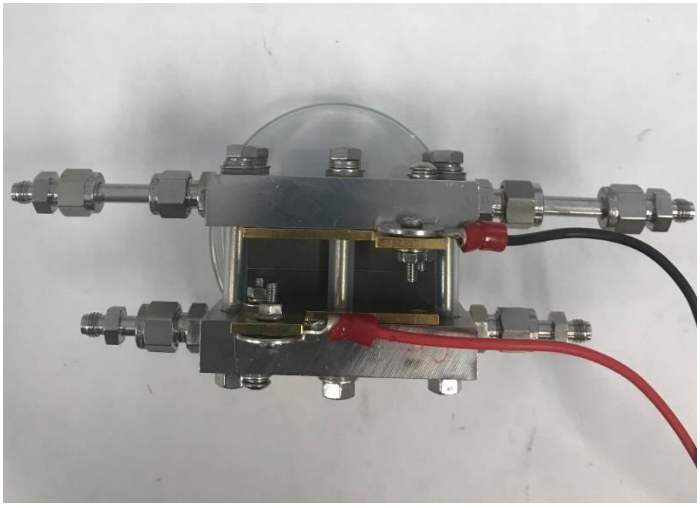

Figure 8 A fuel cell assembled and connected to the potentiostat/galvanostat

The tested GDL samples are two uncoated and two MPL-coated GDLs. GDL samples were tested before and after applying a steady-state and cyclic compression test. The following table shows the results obtained from the Frequency-response analysis by electrochemical impedance spectroscopy.

Sample Type	Uncompressed	Compressed w/o gasket	Compressed w/Teflon gasket	Compressed w/Silicon gasket
SGL-34BA	0.101 Ω	0.085 Ω	0.089 Ω	0.079 Ω
SGL-34BC	0.145 Ω	0.105 Ω	0.110 Ω	0.104 Ω
SGL-39BA	0.148 Ω	0.074 Ω	0.080 Ω	0.083 Ω
SGL-39BC	0.142 Ω	0.103 Ω	0.092 Ω	0.082 Ω

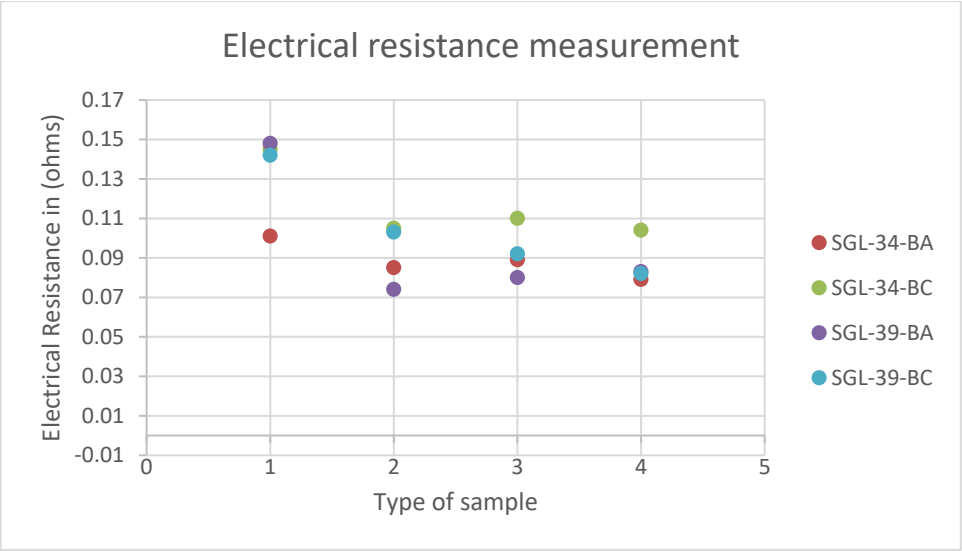

Figure 9 Electrical resistance measurement vs. different types of compressed GDL sample, 1: uncompressed sample, 2: compressed w/o gasket, 3: compressed w/PTFE gasket, 4: compressed w/Silicon gasket.

An example of the actual impedance FRA measurement:

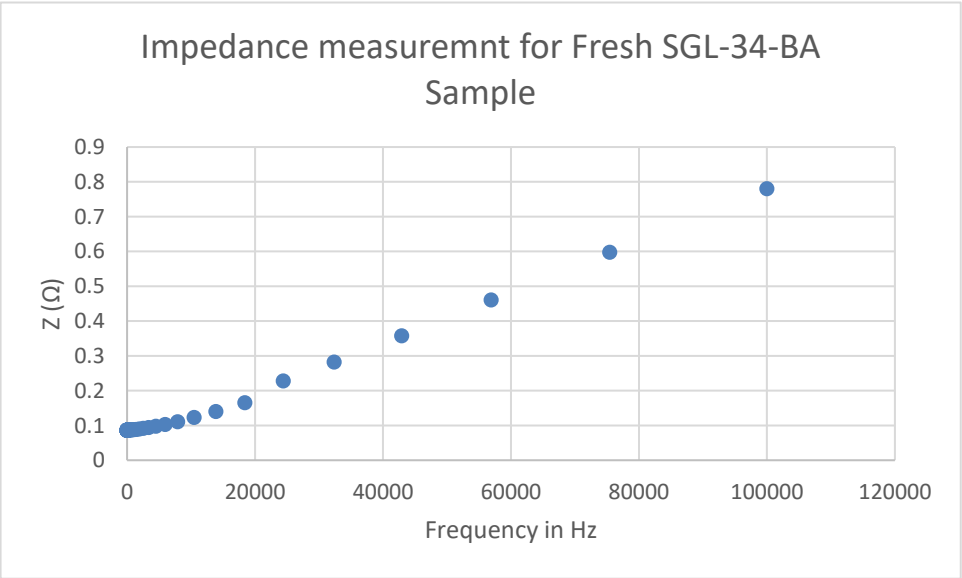

Figure 10 Electrical resistance measurements vs a range of high to low frequencies.

Seminars

I^2CNER group hosts research seminars where members of the department and visiting researchers present their present their work. I have attended and presented my PhD project in a workshop seminar hosted by the fuel cell group in I^2CNER.

Conclusions and Personal Reflection

In conclusion, the opportunity of sharing experience and being able to work in the fuel cell laboratories at Kyushu University was very productive.

Dr. Lyth's fuel cell group is specialised in fabricating and characterising different types of membrane electrolyte assemblies and novel non-platinum catalysts. The outcome of this trip collaboration allowed me to be introduced to different characterisation techniques for gas diffusion layers used in PEM fuel cell. Also, I had the opportunity to attend the fuel cell seminars, where different PhD students share their work. I really appreciate such an opportunity that helped me to broaden my thoughts, ideas and experience in fuel cell related topics.